UNIVERSITÀ DEGLI STUDI DELL'AQUILA
DIPARTIMENTO DI INGEGNERIA INDUSTRIALE E DELL'INFORMAZIONE E DI ECONOMIA

Dottorato di Ricerca in Ingegneria Industriale e dell'Informazione e di Economia

Curriculum Ingegneria Chimica e Materiali

XXXVII ciclo

Titolo della tesi

Applicazioni green alla conversione di oli di origine biologica/

Green applications to the conversion of oils with biological origin

SSD ING/IND-27
ICHI-02/B

Dottoranda

Stefania Lucantonio

Coordinatrice del corso

Prof.ssa Katia Gallucci

Tutor

Dott. Andrea Di Giuliano

Co-Tutor

Prof.ssa Katia Gallucci

A.A. 2023/2024

A nonno Sergio e nonna Antonina, le stelle più brillanti del firmamento.
Nonostante la vostra assenza sia assordante, vi sento vicini ogni giorno.

A mamma e papà, pilastri fondamentali della mia esistenza.

A Stefano, la mia àncora e il mio ancòra.

ABSTRACT

This PhD thesis focuses on renewable energy, with a particular focus on the development of innovative catalysts for the catalytic deoxygenation (DO) of vegetable oils to produce green diesel—a biofuel capable of replacing conventional petrodiesel.

One of the most pressing challenges today is global warming, primarily driven by the rise in atmospheric greenhouse gases, largely due to the overuse of fossil fuels. Achieving carbon neutrality, or net-zero CO_2 emissions, is a critical global goal that requires a shift from non-renewable to renewable energy sources. The transportation sector, as one of the largest consumers of fossil fuels and a major contributor to greenhouse gas emissions, urgently needs greener fuel alternatives to facilitate this energy transition.

Biofuels, derived from renewable biomass, offer a sustainable and carbon-neutral alternative to fossil fuels. While biodiesel is widely used, it has drawbacks such as high oxygen content, low heating value, and poor stability. A more effective option is green diesel, made via catalytic DO of vegetable oils, which produces n-alkanes similar to fossil fuels. This process, involving hydrodeoxygenation (HDO), decarbonylation (DCO), and decarboxylation (DCO_2) reactions, results in green diesel with a high heating value, good cold properties, and full compatibility with petroleum diesel engines. However, current production methods rely on high temperatures, pressures, and expensive or sulfur-polluting catalysts.

This PhD research focuses on developing cost-effective and "*green*" catalysts to promote DO under milder conditions, enabling more sustainable green diesel production.

In particular, two catalysts, NiCoMo and ZnCoMo were sourced from the literature (Velasques et al. 2013, *Ind. Eng. Chem. Res.*, 52, p. 5582-5586): the aim is to repurpose Velasquez et al.'s catalysts, replicating their synthesis and unprecedently testing them for green diesel production through the DO process.

The third catalyst was developed based on Green Chemistry principles. This nickel-molybdenum-aluminum catalyst (Ni-Mo-Al) is synthesized using a solvent-free method aimed at simplifying production while adhering to Green Chemistry and Green Engineering principles.

The overall goal of this PhD research is to demonstrate the feasibility of producing green diesel from vegetable oils with high efficiency using faster, more cost-effective and greener catalyst synthesis methods compared to conventional approaches.

Catalyst characterization techniques were applied to assess the physical and chemical properties of the catalysts before and after the DO reactions, including Inductively Coupled Plasma Mass Spectrometry (ICP-MS), Laser diffractometry, Fourier Transform Infrared Spectroscopy (FT-IR), Scanning Electron Microscopy coupled with Energy Dispersive X-ray Spectroscopy (SEM-EDS) at University of L'Aquila, and X-Ray Diffraction (XRD), Temperature Programmed Reduction (TPR) and Temperature Programmed Desorption (TPD-H_2) performed and elaborated by the Institut de Chimie et procédés pour l'énergie, l'environnement et la santé (ICPEES) - unité mixte de recherche (UMR 7515) CNRS-Université de Strasbourg (France).

The successful synthesis of NiCoMo and ZnCoMo was confirmed by catalyst characterizations and compared with the findings of Velasquez et al., while a comprehensive characterization was also provided for the Ni-Mo-Al catalyst.

The catalytic DO tests were conducted using rapeseed oil as feedstock in a PARR® mini batch reactor, focusing on the effects of various experimental

parameters on reaction outcomes. Catalysts, NiCoMo, ZnCoMo, and Ni-Mo-Al, were activated through in-situ pre-reduction before testing. A 2^3 factorial design of experiments (DoE) was employed, varying temperature (280°C and 320°C), catalyst-to-oil weight ratio ($4\%_{w/w}$ and $10\%_{w/w}$), and reaction time (2 and 6 hours). Recycling tests assessed catalyst reusability over four runs under optimal conditions. A face-centered central composite design (FCCCD) further explored the influence of stirring speed on the Ni-Mo-Al catalyst's performance. Results from this investigation provide insights to choice conditions for effective DO of rapeseed oil and contribute to understanding empirically the catalyst behavior under varying operational parameters.

Additional tests conducted with preliminary form in the concluding phase of the doctoral program studied: (i) the influence of stirring speed on the DO performance of the NiCoMo catalyst; and (ii) the usage of waste cooking oil (WCO) as feedstock for DO.

The repurposing of NiCoMo and ZnCoMo catalysts from propane oxidative dehydrogenation to DO for green diesel production were confirmed by experimental DO tests. The DoEs aimed to identify key factors and provide preliminary characterization of the process, revealing that a pre-reduction step is crucial for optimizing catalyst activity. Results showed that the significant factors affecting the DO performances, including temperature (T), catalyst-to-oil ratio (Υ), and reaction time (t), along with their interactions. In addition, the catalysts maintained stable performance during recycling tests, achieving complete TG conversion and high diesel yields across four cycles, with ZnCoMo showing slightly superior activity and stability.

In contrast, the Ni-Mo-Al catalyst exhibited notable catalytic activity without pre-reduction (i.e., χ = 86.04% and Y_{diesel} = 55.15%). Statistical evaluations indicated significant influences of T, Υ, and t on DO performance. Although the established models fit several performance parameters, the potential for overfitting emerged, emphasizing the need for second-order regression models to accurately represent the data.

Analysis of the Face-Centered Central Composite Design (FCCCD) data highlighted the significance of T, Υ, and stirring speed (ω) on key performance parameters, showing that higher values of these factors enhance conversion. However, the proposed model explained significant trends, it displayed issues with external validity, indicating that its applicability may be limited beyond the tested conditions.

In conclusion, this PhD research demonstrates the successful repurposing of NiCoMo and ZnCoMo catalysts for green diesel production via DO, highlighting the critical role various operational parameters on catalyst performance. The promising results from the recycling tests indicate the potential for these catalysts in industrial applications. Additionally, the Ni-Mo-Al catalyst synthesized by solvent-free synthesis, in agreement with the principles of Green Chemistry and Green Engineering, has proven to be a good catalyst for the production of green diesel, paving the way for further investigations and improvements.

Overall, this study provides insights into the complex interactions governing the DO process and establishes a foundation for further research aimed at improving catalyst efficiency in the production of sustainable fuels.

SOMMARIO

La presente tesi di dottorato è incentrata sulle energie rinnovabili, con particolare attenzione allo sviluppo di catalizzatori innovativi per la deossigenazione catalitica (DO) di oli vegetali per produrre green diesel, un biocarburante in grado di sostituire il petrodiesel convenzionale.

Ad oggi, una delle sfide più urgenti è il riscaldamento globale, determinato principalmente dall'aumento dei gas serra nell'atmosfera, in gran parte dovuto all'uso eccessivo di combustibili fossili. Il raggiungimento della neutralità del carbonio, o emissioni nette di CO_2, è un obiettivo globale cruciale che richiede il passaggio da fonti energetiche non rinnovabili a fonti rinnovabili. Il settore dei trasporti, uno dei maggiori consumatori di combustibili fossili e uno dei principali responsabili delle emissioni di gas serra, ha urgentemente bisogno di alternative di carburante più ecologiche per facilitare questa transizione energetica.

I biocarburanti, derivati da biomasse rinnovabili, offrono un'alternativa sostenibile e a zero emissioni di carbonio rispetto ai carburanti fossili. Sebbene il biodiesel sia ampiamente utilizzato, presenta inconvenienti quali l'elevato contenuto di ossigeno, il basso potere calorifico e la scarsa stabilità. Un'opzione più efficace è il green diesel, prodotto attraverso la deossigenazione catalitica di oli vegetali, che produce n-alcani simili ai combustibili fossili. Questo processo, che prevede reazioni di idrodeossigenazione (HDO), decarbonilazione (DCO) e decarbossilazione

(DCO_2), consente di ottenere un green diesel con un elevato potere calorifico, buone proprietà a freddo e piena compatibilità con i motori diesel a petrolio. Tuttavia, gli attuali metodi di produzione si basano su temperature e pressioni elevate e su catalizzatori costosi o zolfo inquinanti.

Questa ricerca di dottorato si concentra sullo sviluppo di catalizzatori economici e "*verdi*" per promuovere la DO in condizioni più blande, consentendo una produzione di green diesel più sostenibile.

In particolare, due catalizzatori, NiCoMo e ZnCoMo, sono stati reperiti in letteratura: l'obiettivo è quello di riproporre i catalizzatori di Velasquez et al. replicandone la sintesi e testandoli senza precedenti per la produzione di green diesel attraverso il processo DO.

Il terzo catalizzatore è stato sviluppato sulla base dei principi della "*Chimica Verde*". Questo catalizzatore a base di nichel-molibdeno-alluminio (Ni-Mo-Al) è sintetizzato con un metodo senza utilizzo di solventi, volto a semplificare la produzione e a rispettare i principi della "*Chimica Verde e dell'Ingegneria Verde*".

L'obiettivo generale di questa ricerca di dottorato è quindi quello di dimostrare la fattibilità della produzione di green diesel da oli vegetali con un'elevata efficienza utilizzando metodi di sintesi dei catalizzatori più rapidi ed economici rispetto agli approcci convenzionali.

Per valutare le proprietà fisiche e chimiche dei catalizzatori prima e dopo le reazioni DO sono state applicate tecniche di caratterizzazione dei catalizzatori, tra cui la spettrometria di massa al plasma ad accoppiamento induttivo (ICP-MS), la diffrattometria laser, la spettroscopia infrarossa in trasformata di Fourier (FT-IR), la microscopia elettronica a scansione accoppiata alla spettroscopia a raggi X a dispersione di energia (SEM-EDS) condotte presso l'Università dell'Aquila, e diffrazione dei raggi X (XRD), riduzione a temperatura programmata (TPR) e desorbimento a temperatura programmata (TPD-H_2) eseguiti ed elaborati dall'Institut de Chimie et procédés pour l'énergie, l'environnement et la santé (ICPEES) - unité mixte de recherche (UMR 7515) CNRS-Université de Strasbourg (Francia).

Il successo della sintesi di NiCoMo e ZnCoMo è stato confermato dalla caratterizzazione dei catalizzatori e confrontato con i risultati ottenuti da Velasquez et al.

I test preliminari condotti nella fase conclusiva del programma di dottorato hanno evidenziato i risultati relativi all'influenza della velocità di agitazione sulle prestazioni DO del catalizzatore NiCoMo. Inoltre, sono stati presentati anche i risultati dei test preliminari di DO eseguiti utilizzando come materia prima l'olio esausto da cucina (WCO).

I test catalitici di deossigenazione sono stati condotti utilizzando olio di colza come materia prima in un mini-reattore batch PARR®, concentrandosi sugli effetti di vari parametri sperimentali sui risultati della reazione. I catalizzatori, NiCoMo, ZnCoMo e Ni-Mo-Al, sono stati attivati mediante pre-riduzione in situ prima dei test. È stato utilizzato un disegno sperimentale 2^3, variando la temperatura (280°C e 320°C), il rapporto di peso catalizzatore/olio (4%$_{w/w}$ e 10%$_{w/w}$) e il tempo di reazione (2 e 6 ore). I test di riciclo hanno valutato la riutilizzabilità del catalizzatore su quattro cicli di reazione successivi in condizioni ottimali. Un disegno composito centrale a facce centrate (FCCCD) ha esplorato ulteriormente l'influenza della velocità di agitazione sulle prestazioni del catalizzatore Ni-Mo-Al. I risultati di questa indagine completa forniscono indicazioni sulle condizioni ottimali per un efficace DO dell'olio di colza e contribuiscono alla comprensione del comportamento del catalizzatore in presenza di diversi parametri operativi.

Il riutilizzo dei catalizzatori NiCoMo e ZnCoMo dalla deidrogenazione ossidativa del propano alla DO per la produzione di green diesel è stato confermato da prove sperimentali di DO. I DoE miravano a identificare i fattori chiave e a fornire una caratterizzazione preliminare del processo, rivelando che una fase di pre-riduzione è cruciale per ottimizzare l'attività del catalizzatore. I risultati hanno mostrato che i fattori significativi che influenzano le prestazioni del DO, sono la temperatura (T), il rapporto catalizzatore-olio (Υ) e il tempo di reazione (t), e le loro interazioni. Inoltre, i catalizzatori hanno mostrato prestazioni stabili durante i test di riciclo, ottenendo una conversione completa del TG e alti rendimenti di green diesel

per quattro cicli, con ZnCoMo che ha mostrato attività e stabilità leggermente superiori.

Al contrario, il catalizzatore Ni-Mo-Al ha mostrato una notevole attività catalitica senza pre-riduzione (χ = 86.04% and Y_{diesel} = 55.15%), suggerendo un'autoriduzione durante il processo. Le valutazioni statistiche hanno indicato influenze significative di *T*, Υ e *t* sulle prestazioni di DO. Sebbene i modelli stabiliti si adattino a diversi parametri di prestazione, il potenziale di overfitting è evidente, sottolineando la necessità di modelli di regressione del secondo ordine per rappresentare accuratamente i dati.

L'analisi dei dati del disegno sperimentale cubico a facce centrate (FCCCD) ha evidenziato l'importanza di *T*, Υ e della velocità di agitazione (ω) sui parametri chiave delle prestazioni, dimostrando che valori più elevati di questi fattori migliorano la conversione. Tuttavia, il modello proposto ha spiegato tendenze significative, ma ha mostrato problemi di validità esterna, indicando che la sua applicabilità può essere limitata al di là delle condizioni testate.

In conclusione, questa ricerca di dottorato dimostra il successo del reimpiego dei catalizzatori NiCoMo e ZnCoMo per la produzione di green diesel, evidenziando il ruolo critico dei vari parametri operativi sulle prestazioni del catalizzatore. I risultati promettenti dei test di riciclo indicano il potenziale di questi catalizzatori nelle applicazioni industriali. Inoltre, il catalizzatore Ni-Mo-Al sintetizzato mediante sintesi senza solventi, secondo i principi "*della Chimica Verde e dell'Ingegneria Verde*", si è dimostrato un buon catalizzatore per la produzione di green diesel, aprendo la strada a ulteriori indagini e miglioramenti.

Nel complesso, questo studio fornisce indicazioni sulle complesse interazioni che regolano il processo DO e getta le basi per ulteriori ricerche volte a migliorare l'efficienza dei catalizzatori nella produzione di carburanti sostenibili.

CONTENTS

List of figures vi

List of tables xii

List of abbreviations xv

Nomenclature xviii

Latin xviii

Greek xx

1. Literature review 1

1.1 Environmental issues 1

1.1.1 Climate change and Greenhouse gas emissions 1

1.1.2 Global and local policies against climate change 4

1.1.3 The energy issue 7

1.2 Principles of Green Chemistry and Green Engineering 10

1.3 The future of renewable fuels: from Biofuels to E-fuels and E-biofuels 13

1.3.1 Biofuels 13

1.3.2 E-Fuels and E-Biofuels 16

1.4 Biodiesel and Green Diesel 17

1.4.1 Biodiesel 17

1.4.2 Green Diesel 19

1.4.3 A comparison between green diesel and biodiesel 22

1.4.4 Industrial green diesel production 24

1.5 Green diesel production: deoxygenation reactions 26
1.5.1 Primary liquid phase reactions 26
1.5.2 Gas phase reactions 32
1.6 Factors influencing the catalytic DO process 33
1.6.1 Feedstock for DO 34
1.6.2 Influence of temperature and H_2-pressure 37
1.6.3 Effects of other parameters 38
1.6.4 Reactor type 39
1.6.5 Impact of mass transfer 41
1.6.6 Catalyst choice 43
1.7 Aim and Structure of this work 48
2. Materials and methods 51
2.1 Catalysts synthesis 51
2.1.1 NiCoMo and ZnCoMo catalyst synthesis 51
2.1.2 Solventless synthesis of Ni-Mo-Al catalyst 52
2.2 Catalysts characterizations 54
2.2.1 Inductively Coupled Plasma-Mass Spectrometry (ICP-MS) 55
2.2.2 CHNS elemental analysis 57
2.2.3 Fourier Transform Infrared Spectroscopy (FT-IR) 58
2.2.4 Laser diffractometry for determination of particle size distribution (PSD) 59
2.2.5 X-Ray Diffraction (XRD) 60
2.2.6 N_2-Physisorption 62
2.2.7 Scanning Electron Microscopy and Energy Dispersive X-ray Spectroscopy (SEM-EDS) 65
2.2.8 Transmission Electron Microscopy (TEM) 66
2.2.9 Temperature Programmed Reduction (TPR) 67
2.2.10 H_2-Temperature Programmed Desorption (TPD-H_2) 68
2.3 Feedstocks for DO tests 69
2.3.1 Feedstock characterization 69
2.4 Deoxygenation tests 71
2.4.1 2^3 factorial Design of Experiment 72

2.4.2 Recycling tests 74

2.4.3 Assessing the effect of stirring speed on the efficiency of DO 74

2.5 Characterization of the reaction product and data analysis 76

2.5.1 Product composition analysis using FT-IR in ATR mode 76

2.5.2 Product characterization: Gas Chromatography with Flame Ionization Detection (GC-FID) 77

2.5.3 Product characterization: Gas Chromatography Mass Spectrometry (GC-MS) 79

2.5.4 Evaluation of DO performances 80

2.6 Preliminary experimental studies-awaiting completion 87

2.6.1 Preliminary mixing tests on NiCoMo catalyst 87

2.6.2 DO tests with WCO 88

3. Results of as-synthesized catalysts characterizations 89

3.1 NiCoMo and ZnCoMo catalyst characterization results 90

3.1.1 ICP-MS results 90

3.1.2 FT-IR results 90

3.1.3 PSD measurements 91

3.1.4 XRD spectra of NiCoMo and ZnCoMo 93

3.1.5 Results of pore analyses 94

3.1.6 NiCoMo and ZnCoMo SEM-EDS 96

3.1.7 TPR Results 97

3.1.8 TPD-H_2 Results 98

3.2 Ni-Mo-Al catalyst characterization results 101

3.2.1 Ni-Mo-Al ICP-MS results 101

3.2.2 FT-IR spectrum of Ni-Mo-Al 101

3.2.3 PSD of Ni-Mo-Al catalyst 102

3.2.4 Ni-Mo-Al XRD results 103

3.2.5 Results of pore analysis of Ni-Mo-Al 105

3.2.6 Results of SEM-EDS analysis for Ni-Mo-Al 106

3.2.7 Ni-Mo-Al TPR Results 108

3.2.8 Results of TPD-H_2 analysis 109

3.3 Conclusions 112

4. Results of feedstocks characterization 116

4.1 Rapeseed oil characterization 116

4.2 WCO characterization 117

5. Results of DO tests 119

5.1 DO test results for NiCoMo and ZnCoMo catalysts 119

5.1.1 Results of 2^3 factorial design experiments 120

5.1.2 Results of NiCoMo and ZnCoMo recycling test 130

5.2 Ni-Mo-Al DO test results 134

5.2.1 Results of the Ni-Mo-Al 2^3 experimental campaign 134

5.2.2 Results of recycling tests 143

5.2.3 Impact of Stirring Speed on DO Efficiency 145

5.3 Final remarks 153

6. Catalysts characterizations post test 156

6.1 NiCoMo and ZnCoMo post tests 156

6.1.1 ICP-MS results 157

6.1.2 CHNS results for NiCoMo and ZnCoMo 158

6.1.3 NiCoMo and ZnCoMo XRD post tests 159

6.1.4 SEM post tests 160

6.2 Characterization of Ni-Mo-Al post tests 162

6.2.1 Ni-Mo-Al ICP-MS post tests 162

6.2.2 CHNS results for Ni-Mo-Al 163

6.2.3 XRD of Ni-Mo-Al post tests 164

6.2.4 SEM of Ni-Mo-Al post tests 164

6.2.5 Results of TEM analysis 166

6.3 Final remarks 169

7. Results of additional preliminary investigations 171

7.1 Preliminary test results on the influence of stirring speed on DO performance for NiCoMo 172

7.2 Results of DO tests on WCO 174

7.2.1 Overall results of WCO experiments 174

7.2.2 Performance Comparison: WCO vs. rapeseed oil 176

8. General conclusions and future outlooks 180

Addendum A 185

Addendum B 186

Addendum C 190

Addendum D 198

Bibliography 239

Ringraziamenti 261

LIST OF FIGURES

Figure 1 Global temperature anomaly charts, taken from [7]. 2

Figure 2 Global GHGEs per country in 2022. Data taken from [15]. 4

Figure 3 Warming scenarios and global GHGs taken from [30]. 6

Figure 4 Total Energy consumption in 2023, expressed in Mtoe (i.e., Million Tons of Oil Equivalent), taken from [33]. 8

Figure 5 World Energy Consumption by source in 2023. Data taken from [34]. 8

Figure 6 The 12 principles of Green Chemistry. Figure taken from [44]. 10

Figure 7 Planetary Monomill "PULVERISETTE 6" used for Ni-Mo-Al catalyst synthesis. 54

Figure 8 iCAP-TQ and ICP-MS used for catalysts characterization. 57

Figure 9 CHNS analyzer used for catalysts elemental analyses. 58

Figure 10 PerkinElmer Spectrum instrument with ATR unit. 59

Figure 11 Malvern Mastersizer 2000 for PSD measurements. 60

Figure 12 Bragg's law, taken from [270]. 61

Figure 13 Bragg-Brentano geometry, taken from [271]. 61

Figure 14 MICROMERITICS ASAP 2420 analyzer for N_2-physisorption measurements. 64

Figure 15 TPR/TPD-H_2 equipment used for catalysts characterization. 68

Figure 16 Thermo Trace GC-FID used for FAMEs identification in transesterified samples. 71

Figure 17 PARR® batch reactor used for DO tests. 72

Figure 18 Graphical representation of FCCCD. Taken from [286]. 75

Figure 19 Comparison of IR spectra between rapeseed oil and reaction product, taken from [172]. 77

Figure 20 Agilent GC/7820A gas chromatograph. 78

Figure 21 GC-MS. Varian star 3400cx (GC model), Varian Saturn 2000 (MS model). 80

Figure 22 FT-IR results of NiCoMo and ZnCoMo catalyst. 91

Figure 23 Average and cumulative PSD of (a) NiCoMo and (b) ZnCoMo catalysts 92

Figure 24 XRD patterns of NiCoMo and ZnCoMo catalysts. 93

Figure 25 N_2-physisorption isotherm of NiCoMo catalyst. 94

Figure 26 N_2-physisorption isotherm of ZnCoMo catalyst. 95

Figure 27 SEM micrographs at 3000x magnification of as-synthesized catalysts: (a) NiCoMo and (b) ZnCoMo. 96

Figure 28 SEM-EDS analyses with elemental maps of as-synthesized catalysts: (a) NiCoMo (Ni = magenta; Co = blue; Mo = yellow) and (b) ZnCoMo (Zn = magenta; Co = blue; Mo = yellow). 97

Figure 29 TPR profiles of NiCoMo and ZnCoMo catalysts. 97

Figure 30 Time profiles of TPR preparative procedure (i.e., 320 °C, 4 h) for NiCoMo and ZnCoMo before TPD-H_2. 98

Figure 31 Results of TPD-H_2: (a) time profiles of TPD-H_2 for NiCoMo and ZnCoMo; (b) temperatures profiles of TPD-H_2 for NiCoMo and ZnCoMo. 100

Figure 32 FT-IR spectra of Ni-Mo-Al catalyst and single oxides (NiO, MoO_3 and Al_2O_3). 102

Figure 33 Average and cumulative PSD of Ni-Mo-Al catalyst. 103

Figure 34 XRD pattern of Ni-Mo-Al catalyst and single oxides (Al_2O_3, MoO_3, and NiO). 104

Figure 35 N_2-physisorption isotherm of Ni-Mo-Al catalyst. 105

Figure 36 SEM analysis of: (a) calcined NiO at 10kx magnification; (b) calcined Al_2O_3 at 10kx magnification; (c) calcined MoO_3 at 10kx magnification; (d) as-synthesized Ni-Mo-Al catalyst at 150x magnification; (e) as-synthesized Ni-Mo-Al catalyst at 10kx magnification; and (f) SEM-EDS analysis at 10kx magnification. 107

Figure 37 TPR profiles of NiO, MoO_3 and Ni-Mo-Al catalyst samples. 109

Figure 38 TPR profile of Ni-Mo-Al sample as a preparative step before TPD-H_2 (i.e., 320°C, 4 h). 110

Figure 39 Results of Ni-Mo-Al TPD-H_2: (a) time profiles of TPD-H_2; (b) temperatures profiles of TPD-H_2 111

Figure 40 $Y_{product}$, χ, and Y_{diesel} of DO test for (a) NiCoMo and (b) ZnCoMo catalyst. Values are taken from Table 19. 121

Figure 41 $S_{HDO/DCOx}$ of DO tests for (a) NiCoMo and (b) ZnCoMo catalyst. Values are taken from Table 19. 123

Figure 42 Surface responses of $A\%_{Ci}$ (with $15 \leq i \leq 18$) for NiCoMo at (a) t=-1, (b) t=1 and ZnCoMo at (c) t=-1 and (d) t=1. 126

Figure 43 Comparison of $Y_{product}$, χ, Y_{diesel} of recycling test for NiCoMo and ZnCoMo catalyst. Values are taken from Table 21. 131

Figure 44 FT-IR spectra of recycling tests reaction product of (a) NiCoMo and (b) ZnCoMo catalyst. 132

Figure 45 $Y_{product}$, χ, Y_{diesel} of DO tests for Ni-Mo-Al catalyst. Values are taken from Table 22. 135

Figure 46 $S_{HDO/DCOx}$ for 2^3 experimental DO tests for Ni-Mo-Al catalyst. Data are taken from Table 22. 136

Figure 47 Surface responses of χ for Ni-Mo-Al DO tests at (a) t=-1 and (b) t=1. Regression coefficients are taken from Table 23. 138

Figure 48 Surface responses of $S_{HDO/DCOx}$ for Ni-Mo-Al DO tests at (a) t=-1 and (b) t=1. Regression coefficients are taken from Table 23. 140

Figure 49 Results of Ni-Mo-Al recycling tests, in terms of $Y_{product}$, χ, and Y_{diesel}. Data are taken from Table 24. 143

Figure 50 $S_{HDO/DCOx}$ for Ni-Mo-Al recycling tests. 144

Figure 51 FT-IR spectra of reaction products from recycling tests of Ni-Mo-Al catalyst. 145

Figure 52 XRD of NiCoMo catalyst post test with reference to as-synthesized form: (i) NiCoMo post treatment (1); (ii) NiCoMo post treatment “ab”; and (iii) catalyst post recycling test (Test_R4). Experimental conditions of tests are reported in Table 8. 159

Figure 53 XRD of ZnCoMo catalyst post test with reference to as-synthesized form: (i) ZnCoMo post treatment (1); (ii) ZnCoMo post treatment “ab”; and (iii) catalyst post recycling test (Test_R4). Experimental conditions of tests are reported in Table 8. 160

Figure 54 SEM micrographs at 3kx magnification of post-test NiCoMo and ZnCoMo: (a) NiCoMo after treatment “ab”; (b) ZnCoMo after treatment “ab”; (c) NiCoMo after treatment (1); (d) ZnCoMo after treatment (1); (e) NiCoMo after Test_R4; (f) ZnCoMo after Test_R4. 161

Figure 55 XRD results of Ni-Mo-Al catalyst post tests with reference to as-synthesized form: (i) catalyst post treatment “abc”; (ii) catalyst post Test_R4. 164

Figure 56 SEM micrographs of Ni-Mo-Al after DO test at 150x magnification: (a) Ni-Mo-Al post treatment “abc”; (b) Ni-Mo-Al post treatment (1); (c) Ni-Mo-Al post Test_R4; (d) Ni-Mo-Al post Test_R4 with measurements of diameter. 165

Figure 57 TEM micrographs of as-synthesized Ni-Mo-Al catalyst: (a) at 200 nm; (b) 0.5 µm. 166

Figure 58 TEM micrographs of Ni-Mo-Al post TPR: (a) at 10 nm; (b) at 500nm. 167

Figure 59 TEM micrographs of post DO tests: (a) post treatment "abc" (320°C, 10% catalyst-to-oil, 6 h) at 10nm; (b) post treatment "abc" (320°C, 10% catalyst-to-oil, 6 h) at 20 nm; (c)

C-deposit taken from [327]; (d) post Test_R4 (320°C, 10% catalyst-to-oil, 6 h) at 10 nm; (e) post Test_R4 (320°C, 10% catalyst-to-oil, 6 h) at 20 nm. 168

Figure 60 Detail of TEM image post Test_R4 circled in red in Figure 59 (d). 169

Figure 61 FT-IR spectra of reaction product from tests at 200, 300, 400, 500, 600 and 700 rpm for NiCoMo catalyst. 173

Figure 62 FT-IR spectra of product of DO test on WCO. 174

Figure 63 Comparison between DO test of WCO and Rapeseed Oil, in terms of product composition at 320°C (a) and 280°C (c), and DO performance parameters (i.e., Y_{diesel}, χ and $Y_{product}$) at 320°C (b) and 280°C (c). *WCO and RO indicate tests performed with WCO and rapeseed oil at the same conditions. 179

Figure B 1 C_{14}-C_{22} FAME MIX standard injected into Thermo Trace GC-FID. 187

Figure B 2 C_7-C_{40} n-alkanes reference standard used for Agilent GC-FID. 188

Figure B 3 Example of GC-MS analysis of two unidentified peaks. 189

Figure C 1 High-magnification SEM micrograph illustrating the lamellar structure of the catalysts: (a) NiCoMo at 10kx magnification; and (b) ZnCoMo at 36.94kx magnification. 190

Figure C 2 EDS spectra of NiCoMo catalysts: (a) the SEM image at 1kx magnification, (b) Spectrum 17, (c) Spectrum 18, (d) Spectrum 19, (e) Spectrum 20, (f) Spectrum 21. 192

Figure C 3 EDS spectra of ZnCoMo catalysts (a) the SEM image at 1kx magnification, (b) Spectrum 87, (c) Spectrum 88, (d) Spectrum 89, (e) Spectrum 90, (f) Spectrum 91. 194

Figure C 4 SEM images of: (i) NiO at 20kx magnification; (b) Al_2O_3 at 150x magnification; (c) MoO_3 at 20kx magnification; (d) Ni-Mo-Al catalyst at 500x magnification. 195

Figure C 5 EDS spectra of Ni-Mo-Al catalysts: (a) the SEM image at 1kx magnification, (b) Spectrum 1, (c) Spectrum 2, (d) Spectrum 3, (e) Spectrum 4, (f) Spectrum 5. 197

Figure D 1 Response surface of DO process parameters for NiCoMo catalyst derived from the regression model of 2^3 experimental DoE, with coefficients in Table 20, at t=±1: (a) $Y_{product}$ (Equation 2.9) at t=-1; (b) $Y_{product}$ (Equation 2.9) at t=1; (c) χ (Equation 2.10) at t=-1; (d) χ (Equation 2.10) at t=1; (e) Y_{diesel} (Equation 2.11) at t=-1; (f) Y_{diesel} (Equation 2.11) at t=1; (g) $S_{HDO/DCOx}$ (Equation 2.12) at t=-1; (e) $S_{HDO/DCOx}$ (Equation 2.12) at t=1. 200

Figure D 2 Contour plots of DO process parameters for NiCoMo catalyst derived from the regression model of 2^3 experimental DoE, with coefficients in Table 20, at t=±1: (a) $Y_{product}$ (Equation 2.9) at t=-1; (b) $Y_{product}$ (Equation 2.9) at t=1; (c) χ (Equation 2.10) at t=-1; (d) χ (Equation 2.10) at t=1; (e) Y_{diesel} (Equation 2.11) at t=-1; (f) Y_{diesel} (Equation 2.11) at t=1; (g) $S_{HDO/DCOx}$ (Equation 2.12) at t=-1; (e) $S_{HDO/DCOx}$ (Equation 2.12) at t=1. 202

Figure D 3 Response surface of DO product composition for NiCoMo catalyst derived from the regression model of 2^3 experimental DoE, with coefficients in Table 20, at t=±1: (a) $A\%_{Ci}$

(with $C_8 \leq i \leq C_{14}$) at t=-1; (b) $A\%_{Ci}$ (with $C_8 \leq i \leq C_{14}$) at t=1; (c) $A\%_{Ci}$ (with $C_{15} \leq i \leq C_{18}$) at t=-1; (d) $A\%_{Ci}$ (with $C_{15} \leq i \leq C_{18}$) t=1; (e) $A\%_{Ci}$ (with $C_{19} \leq i \leq C_{30}$) at t=-1; (f) $A\%_{Ci}$ (with $C_{19} \leq i \leq C_{30}$) at t=1; (g) $A\%_{BHC}$ at t=-1; (h) $A\%_{BHC}$ at t=1; (i) $A\%_{UHC}$ at t=-1; (l) $A\%_{UHC}$ at t=1; (m) $A\%_{Others}$ at t=-1; (n) $A\%_{Others}$ at t=1; (p) $A\%_{FAME}$ at t=-1; (q) $A\%_{FAME}$ at t=1..... 205

Figure D 4 Contour plots of DO product composition for NiCoMo catalyst derived from the regression model of 2^3 experimental DoE, with coefficients in Table 20, at t=±1: (a) $A\%_{Ci}$ (with $C_8 \leq i \leq C_{14}$) at t=-1; (b) $A\%_{Ci}$ (with $C_8 \leq i \leq C_{14}$) at t=1; (c) $A\%_{Ci}$ (with $C_{15} \leq i \leq C_{18}$) at t=-1; (d) $A\%_{Ci}$ (with $C_{15} \leq i \leq C_{18}$) at t=1; (e) $A\%_{Ci}$ (with $C_{19} \leq i \leq C_{30}$) at t=-1; (f) $A\%_{Ci}$ (with $C_{19} \leq i \leq C_{30}$) at t=1; (g) $A\%_{BHC}$ at t=-1; (h) $A\%_{BHC}$ at t=1; (i) $A\%_{UHC}$ at t=-1; (l) $A\%_{UHC}$ at t=1; (m) $A\%_{Others}$ at t=-1; (n) $A\%_{Others}$ at t=1; (p) $A\%_{FAME}$ at t=-1; (q) $A\%_{FAME}$ at t=1..... 208

Figure D 5 Response surface of DO process parameters for ZnCoMo catalyst derived from the regression model of 2^3 experimental DoE, with coefficients in Table 20, at t=±1: (a) $Y_{product}$ (Equation 2.9) at t=-1; (b) $Y_{product}$ (Equation 2.9) at t=1; (c) χ (Equation 2.10) at t=-1; (d) χ (Equation 2.10) at t=1; (e) Y_{diesel} (Equation 2.11) at t=-1; (f) Y_{diesel} (Equation 2.11) at t=1; (g) $S_{HDO/DCOx}$ (Equation 2.12) at t=-1; (e) $S_{HDO/DCOx}$ (Equation 2.12) at t=1. 210

Figure D 6 Contour plots of DO process parameters for ZnCoMo catalyst derived from the regression model of 2^3 experimental DoE, with coefficients in Table 20, at t=±1: (a) $Y_{product}$ (Equation 2.9) at t=-1; (b) $Y_{product}$ (Equation 2.9) at t=1; (c) χ (Equation 2.10) at t=-1; (d) χ (Equation 2.10) at t=1; (e) Y_{diesel} (Equation 2.11) at t=-1; (f) Y_{diesel} (Equation 2.11) at t=1; (g) $S_{HDO/DCOx}$ (Equation 2.12) at t=-1; (e) $S_{HDO/DCOx}$ (Equation 2.12) at t=1. 212

Figure D 7 Response surface of DO product composition for ZnCoMo catalyst derived from the regression model of 2^3 experimental DoE, with coefficients in Table 20, at t=±1: (a) $A\%_{Ci}$ (with $C_8 \leq i \leq C_{14}$) at t=-1; (b) $A\%_{Ci}$ (with $C_8 \leq i \leq C_{14}$) at t=1; (c) $A\%_{Ci}$ (with $C_{15} \leq i \leq C_{18}$) at t=-1; (d) $A\%_{Ci}$ (with $C_{15} \leq i \leq C_{18}$) at t=1; (e) $A\%_{Ci}$ (with $C_{19} \leq i \leq C_{30}$) at t=-1; (f) $A\%_{Ci}$ (with $C_{19} \leq i \leq C_{30}$) at t=1; (g) $A\%_{BHC}$ at t=-1; (h) $A\%_{BHC}$ at t=1; (i) $A\%_{UHC}$ at t=-1; (l) $A\%_{UHC}$ at t=1; (m) $A\%_{Others}$ at t=-1; (n) $A\%_{Others}$ at t=1; (p) $A\%_{FAME}$ at t=-1; (q) $A\%_{FAME}$ at t=1..... 215

Figure D 8 Contour plots of DO product composition for ZnCoMo catalyst derived from the regression model of 2^3 experimental DoE, with coefficients in Table 20, at t=±1: (a) $A\%_{Ci}$ (with $C_8 \leq i \leq C_{14}$) at t=-1; (b) $A\%_{Ci}$ (with $C_8 \leq i \leq C_{14}$) at t=1; (c) $A\%_{Ci}$ (with $C_{15} \leq i \leq C_{18}$) at t=-1; (d) $A\%_{Ci}$ (with $C_{15} \leq i \leq C_{18}$) at t=1; (e) $A\%_{Ci}$ (with $C_{19} \leq i \leq C_{30}$) at t=-1; (f) $A\%_{Ci}$ (with $C_{19} \leq i \leq C_{30}$) at t=1; (g) $A\%_{BHC}$ at t=-1; (h) $A\%_{BHC}$ at t=1; (i) $A\%_{UHC}$ at t=-1; (l) $A\%_{UHC}$ at t=1; (m) $A\%_{Others}$ at t=-1; (n) $A\%_{Others}$ at t=1; (p) $A\%_{FAME}$ at t=-1; (q) $A\%_{FAME}$ at t=1..... 218

Figure D 9 Response surface of DO process parameters for Ni-Mo-Al catalyst derived from the regression model of 2^3 experimental DoE, with coefficients in Table 23, at t=±1: (a) $Y_{product}$ (Equation 2.9) at t=-1; (b) $Y_{product}$ (Equation 2.9) at t=1; (c) χ (Equation 2.10) at t=-1; (d) χ (Equation 2.10) at t=1; (e) Y_{diesel} (Equation 2.11) at t=-1; (f) Y_{diesel} (Equation 2.11) at t=1; (g) $S_{HDO/DCOx}$ (Equation 2.12) at t=-1; (e) $S_{HDO/DCOx}$ (Equation 2.12) at t=1. 220

Figure D 10 Contour plots of DO process parameters for Ni-Mo-Al catalyst derived from the regression model of 2^3 experimental DoE, with coefficients in Table 23, at t=±1: (a) $Y_{product}$ (Equation 2.9) at t=-1; (b) $Y_{product}$ (Equation 2.9) at t=1; (c) χ (Equation 2.10) at t=-1; (d) χ (Equation 2.10) at t=1; (e) Y_{diesel} (Equation 2.11) at t=-1; (f) Y_{diesel} (Equation 2.11) at t=1; (g) $S_{HDO/DCOx}$ (Equation 2.12) at t=-1; (e) $S_{HDO/DCOx}$ (Equation 2.12) at t=1. 222

Figure D 11 Surface responses of DO product composition for Ni-Mo-Al catalyst derived from the regression model of 2^3 experimental DoE, with coefficients in Table 23, at t=±1: (a) $A\%_{Ci}$ (with $C_8 \leq i \leq C_{14}$) at t=-1; (b) $A\%_{Ci}$ (with $C_8 \leq i \leq C_{14}$) at t=1; (c) $A\%_{Ci}$ (with $C_{15} \leq i \leq C_{18}$) at t=-1; (d) $A\%_{Ci}$ (with $C_{15} \leq i \leq C_{18}$) at t=1; (e) $A\%_{Ci}$ (with $C_{19} \leq i \leq C_{30}$) at t=-1;

(f) $A\%_{Ci}$ (with $C_{19} \leq i \leq C_{30}$) at t=1; (g) $A\%_{BHC}$ at t=-1; (h) $A\%_{BHC}$ at t=1; (i) $A\%_{UHC}$ at t=-1; (l) $A\%_{UHC}$ at t=1; (m) $A\%_{Others}$ at t=-1; (n) $A\%_{Others}$ at t=1; (p) $A\%_{FAME}$ at t=-1; (q) $A\%_{FAME}$ at t=1..... 225

Figure D 12 Contour plots of DO product composition for Ni-Mo-Al catalyst derived from the regression model of 2^3 experimental DoE, with coefficients in Table 23, at t=±1: (a) $A\%_{Ci}$ (with $C_8 \leq i \leq C_{14}$) at t=-1; (b) $A\%_{Ci}$ (with $C_8 \leq i \leq C_{14}$) at t=1; (c) $A\%_{Ci}$ (with $C_{15} \leq i \leq C_{18}$) at t=-1; (d) $A\%_{Ci}$ (with $C_{15} \leq i \leq C_{18}$) at t=1; (e) $A\%_{Ci}$ (with $C_{19} \leq i \leq C_{30}$) at t=-1; (f) $A\%_{Ci}$ (with $C_{19} \leq i \leq C_{30}$) at t=1; (g) $A\%_{BHC}$ at t=-1; (h) $A\%_{BHC}$ at t=1; (i) $A\%_{UHC}$ at t=-1; (l) $A\%_{UHC}$ at t=1; (m) $A\%_{Others}$ at t=-1; (n) $A\%_{Others}$ at t=1; (p) $A\%_{FAME}$ at t=-1; (q) $A\%_{FAME}$ at t=1..... 228

Figure D 13 Surface responses of DO process parameters for Ni-Mo-Al catalyst derived from the regression model of FCCCD, with coefficients in Table 26, at $\Upsilon=\pm1$: (a) $Y_{product}$ (Equation 2.9) at Υ=-1; (b) $Y_{product}$ (Equation 2.9) at Υ=1; (c) χ (Equation 2.10) at Υ=-1; (d) χ (Equation 2.10) at Υ=1; (e) Y_{diesel} (Equation 2.11) at Υ=-1; (f) Y_{diesel} (Equation 2.11) at Υ=1; (g) $S_{HDO/DCOx}$ (Equation 2.12) at Υ=-1; (e) $S_{HDO/DCOx}$ (Equation 2.12) at Υ=1..... 230

Figure D 14 Contour plots of DO process parameters for Ni-Mo-Al catalyst derived from the regression model of FCCCD, with coefficients in Table 26, at $\Upsilon=\pm1$: (a) $Y_{product}$ (Equation 2.9) at Υ=-1; (b) $Y_{product}$ (Equation 2.9) at Υ=1; (c) χ (Equation 2.10) at Υ=-1; (d) χ (Equation 2.10) at Υ=1; (e) Y_{diesel} (Equation 2.11) at Υ=-1; (f) Y_{diesel} (Equation 2.11) at Υ=1; (g) $S_{HDO/DCOx}$ (Equation 2.12) at Υ=-1; (e) $S_{HDO/DCOx}$ (Equation 2.12) at Υ=1..... 232

Figure D 15 Response surfaces of DO product composition for Ni-Mo-Al catalyst derived from the regression model of FCCCD, with coefficients in Table 26, at $\Upsilon=\pm1$: (a) $A\%_{Ci}$ (with $C_8 \leq i \leq C_{14}$) at Υ =-1; (b) $A\%_{Ci}$ (with $C_8 \leq i \leq C_{14}$) at Υ =1; (c) $A\%_{Ci}$ (with $C_{15} \leq i \leq C_{18}$) at Υ =-1; (d) $A\%_{Ci}$ (with $C_{15} \leq i \leq C_{18}$) at Υ =1; (e) $A\%_{Ci}$ (with $C_{19} \leq i \leq C_{30}$) at Υ =-1; (f) $A\%_{Ci}$ (with $C_{19} \leq i \leq C_{30}$) at Υ =1; (g) $A\%_{BHC}$ at Υ =-1; (h) $A\%_{BHC}$ at Υ =1; (i) $A\%_{UHC}$ at Υ =-1; (l) $A\%_{UHC}$ at Υ =1; (m) $A\%_{Others}$ at Υ =-1; (n) $A\%_{Others}$ at Υ =1; (p) $A\%_{FAME}$ at Υ =-1; (q) $A\%_{FAME}$ at Υ =1. 235

Figure D 16 Contour plots of DO product composition for Ni-Mo-Al catalyst derived from the regression model of FCCCD, with coefficients in Table 26, at $\Upsilon=\pm1$: (a) $A\%_{Ci}$ (with $C_8 \leq i \leq C_{14}$) at Υ =-1; (b) $A\%_{Ci}$ (with $C_8 \leq i \leq C_{14}$) at Υ =1; (c) $A\%_{Ci}$ (with $C_{15} \leq i \leq C_{18}$) at Υ =-1; (d) $A\%_{Ci}$ (with $C_{15} \leq i \leq C_{18}$) at Υ =1; (e) $A\%_{Ci}$ (with $C_{19} \leq i \leq C_{30}$) at Υ =-1; (f) $A\%_{Ci}$ (with $C_{19} \leq i \leq C_{30}$) at Υ =1; (g) $A\%_{BHC}$ at Υ =-1; (h) $A\%_{BHC}$ at Υ =1; (i) $A\%_{UHC}$ at Υ =-1; (l) $A\%_{UHC}$ at Υ =1; (m) $A\%_{Others}$ at Υ =-1; (n) $A\%_{Others}$ at Υ =1; (p) $A\%_{FAME}$ at Υ =-1; (q) $A\%_{FAME}$ at Υ =1. 238

LIST OF TABLES

Table 1 The 12 principles of Green Chemistry divided in three categories, adapted from [45]. 11

Table 2 The 12 principles of Green Engineering from [51]. 12

Table 3 Comparison between petrodiesel, biodiesel and green diesel. Data adapted from sources in the "Ref." column. 22

Table 4 Feedstock typically used for catalytic DO: data taken from [35, 59, 140, 142]..... 35

Table 5 Fatty acid composition of some edible and non-edible biomasses. Data adapted from [59, 113, 145-148]. $C_{n:m}$: n is the number of carbon atoms and m is the number of double bonds in the fatty acid. 36

Table 6 Cost of some raw material for DO process; data taken from [35, 149]. 36

Table 7 Summary of principal supports, and active metals typically used for DO in the production of green diesel. 44

Table 8 DO experimental conditions: all listed tests carried out at H_2 initial partial pressure of 40 bar, 200 rpm, with 2 g of rapeseed oil and 20 g of n-hexane. 74

Table 9 List of FCCCD experiments. 75

Table 10 Results of NiCoMo and ZnCoMo analysis by ICP-MS in terms of elemental molar ratios. 90

Table 11 Statistical parameters of PSD of NiCoMo and ZnCoMo. 92

Table 12 S_{BET}, V_{BJH}, and d_{BJH} of NiCoMo and ZnCoMo. 95

Table 13 H_2 desorption during TPD-H_2 of NiCoMo and ZnCoMo samples. 100

Table 14 ICP-MS results of Ni-Mo-Al catalyst in as-synthetize form. 101

Table 15 Statistical parameters of PSD of Ni-Mo-Al catalyst. 103

Table 16 Crystalline particle size (D, expressed in nm) of NiO and MoO_3 in single and Ni-Mo-Al catalyst. 104

Table 17 Composition of commercial rapeseed oil in terms of A% of chromatographic peaks. $C_{n:m}$ is a fatty acid with n carbon atoms and m double bonds. 116

Table 18 WCO and high oleic sunflower oil fatty acid compositions, in terms of A% of chromatographic peaks. $C_{n:m}$ is a fatty acid with n carbon atoms and m double bonds. 117

Table 19 Experimental results of unreplicated 2^3 factorial DoE with 3 replicated central points (with treatments classified for ANOVA) and supplementary "blank" and "no-pre-red" tests. 128

Table 20 Regression coefficients, explained variance and explained variance in cross validation of main factors and interactions from experimental data of unreplicated 2^3 factorial DoE with 3 replicated central points and their significance (see Section 2.5.4.1); Significance P-value intervals: 0 < *** ≤ 0.001 < ** ≤ 0.01 < * ≤ 0.05 < . < 0.1 < no < 1. "N.v" means that the CV Expl. Var has negative value (no fitting). 129

Table 21 Results of recycling tests (320°C, 10 $\%_{w/w}$ catalyst-to-oil, 2 h) with (a) NiCoMo; (b) ZnCoMo, in terms of product composition (A%), $Y_{product}$ (Equation 2.9), χ (Equation 2.10), Y_{diesel} (Equation 2.11), and $S_{HDO/DCOx}$ (Equation 2.12). Test_Ni/Zn_CoMo_Rr is the r^{th} DO cycle on the same catalyst sample. 133

Table 22 Experimental results of unreplicated 2^3 factorial DoE with 3 replicated central points (with treatments classified for ANOVA) of Ni-Mo-Al catalyst, and supplementary "blank" and "no-pre-red" tests. 141

Table 23 Regression coefficients, explained variance and explained variance in cross validation of main factors and interactions from experimental data of unreplicated 2^3 factorial DoE for Ni-Mo-Al catalyst with 3 replicated central points and their significance (see Section 2.5.4.1); Significance P-value intervals: 0 < *** ≤ 0.001 < ** ≤ 0.01 < * ≤ 0.05 < . < 0.1 < no < 1. "N.v" means that CV Expl. Var has negative value (no fitting). 142

Table 24 Results of Ni-Mo-Al recycling tests (320°C, 10 $\%_{w/w}$ catalyst-to-oil, 6 h) in terms of product composition (A%), $Y_{product}$ (Equation 2.9), χ (Equation 2.10), Y_{diesel} (Equation 2.11), and $S_{HDO/DCOx}$ (Equation 2.12). Test_Rr is the r^{th} DO cycle on the same catalyst sample. 142

Table 25 Experimental results of unreplicated FCCCD of Ni-Mo-Al catalyst. 151

Table 26 Regression coefficients, explained variance and explained variance in cross validation of main factors and interactions from experimental data of unreplicated FCCCD for Ni-Mo-Al catalyst and their significance (see Section 2.4.3). Significance P-value intervals: 0 < *** ≤ 0.001 < ** ≤ 0.01 < * ≤ 0.05 < . < 0.1 < no < 1. "N.v" means that CV Expl. Var has negative value (no fitting). 152

Table 27 Results of NiCoMo and ZnCoMo analysis by ICP-MS in terms of elemental molar ratios; conditions of treatments (1) and "ab" are in Table 8. 157

Table 28 Results of CHNS analysis of NiCoMo and ZnCoMo samples: (i) as-synthesized; (ii) post treatment (1); (iii) post treatment "ab"; (iv) post recycling test. Conditions of treatments (1) and "ab" are in Table 8. 158

Table 29 ICP-MS results of Ni-Mo-Al catalyst in terms of elemental molar ratios; conditions of treatments (1) and "abc" are in Table 8. 163

Table 30 Results of CHNS analysis of Ni-Mo-Al samples: (i) as-synthesized; (ii) post treatment (1); (ii) post treatment "abc"; (iv) post recycling test. Conditions of treatments (1) and "abc" are in Table 8. 163

Table 31 Results of tests varying the reactor stirring speed (SS), conducted at 280°C, 4 $\%_{w/w}$ catalyst-to-oil and 2 h, in terms of product composition (A%), $Y_{product}$ (Equation 2.9), χ (Equation 2.10), Y_{diesel} (Equation 2.11), and $S_{HDO/DCOx}$ (Equation 2.12)..... 178

Table 32 Results of preliminary DO tests on WCO (280°C/320°C, 10 $\%_{w/w}$ catalyst-to-oil, 2 h and 200 rpm) in terms of product composition (A%), $Y_{product}$ (Equation 2.9), χ (Equation 2.10), Y_{diesel} (Equation 2.11), and $S_{HDO/DCOx}$ (Equation 2.12). 178

LIST OF ABBREVIATIONS

AE: Atom Economy

AOAC: Association of Official Agricultural Chemists

ATR: Attenuated Total Reflection

BET: Brunauer-Emmett-Teller

BHC: Branched Hydrocarbons

BJH: Barrett-Joyner-Halenda

BSD: Back Scatter Detector

CAT: Chemometric Agile Tool

CN: Cetane Number

COP: Conference of Parties

CSTR: Continuous Stirred Tank Reactor

CV Expl. Var: Explained Variance in Cross-Validation

DO: Deoxygenation

DoE: Design of Experiments

DCO: Decarbonylation

DCO_2: Decarboxylation

Expl. Var: Explained Variance

FAEE: Fatty Acid Ethyl Ester

FAME: Fatty Acid Methyl Ester

FCCCD: Face-Centered Central Composite Design

FFA: Free Fatty Acid

FT-IR: Fourier Transform Infrared Spectroscopy

FWHM: Full Width at Half Maximum

EU: European Union

GC: Gas Chromatograph

GC-FID: Gas Chromatography- Flame Ionization Detector

GC-MS: Gas Chromatography- Mass Spectrometry

GHG: GreenHouse Gas

GHGE: GreenHouse Gas Emission

GM: Genetically Modified

HC: Hydrocarbon

HDO: Hydrodeoxygenation

HVO: Hydrotreated Vegetable Oil

ICP: Inductively Coupled Plasma

ICP-MS: Inductively Coupled Plasma-Mass Spectrometry

IR: Infrared

LHSV: Liquid Hourly Space Velocity

LHV: Lower Heating Value

MCM: Mobil Composition of Matter

MLR: Multiple Linear Regression

MS: Mass Spectrometer

MS_E: Mean Square Error

ODH: Oxidative-Dehydrogenation

OLS: Ordinary Least Squares

PM: Particulate Matter

PSD: Particle Size Distribution

RE: Renewable Energy

RED II: Renewable Energy Directive II

RES: Renewable Energy Source

RI: Retention Index

RT: Room Temperature

SBA: Santa Barbara Amorphous

SEM-EDS: Scanning Electron Microscopy and Energy Dispersive X-ray Spectrometry

STEM: Scanning Transmission Electron Microscopy

TCD: Thermal Conductivity Detector

TEM: Transmission Electron Microscopy

TG: Triglyceride

TPD-H_2: H_2-Temperature Programmed Desorption

TPR: Temperature Programmed Reduction

TRL: Technology Readiness Level

UHC: Unsaturated Hydrocarbons

UNFCCC: United Nations Framework Convention on Climate Change

U.S.: United States

VOCs: Volatile Organic Compounds

WCO: Waste Cooking Oil

WO: Waste Oil

WGS: Water Gas Shift

XRD: X-Ray Diffraction

NOMENCLATURE

LATIN

$C_{n:m}$	fatty acid with n carbon atoms and m double bonds
$d(0,1)$	10th percentile of cumulative PSD curve
$d(0,5)$	50th percentile of cumulative PSD curve
$d(0,9)$	90th percentile of cumulative PSD curve
$d(3,2)$	Sauter mean diameter
d	Interplanar distance
n	Positive integer number
D	Crystalline particle size
k	Adimensional factor
v	Volume of gas adsorbed
v_m	Volume of gas adsorbed for a monolayer
c	BET constant
P	Adsorption pressure
P_0	Vapor pressure of adsorbate
E_m	Monolayer heat of adsorption
E_L	Heat of adsorption of others layer
R	Gas constant
T	Temperature
S_{BET}	BET surface area
N_A	Avogadro's number
m	Mass sample
v_t	Molar value
r_k	Kelvin radius

d_{BJH}	BJH pore diameter
V_{BJH}	BJH pore volume
t	Reaction time
$A\%$	Area % of chromatography peak
tr_i	Retention time of the unknown compound
tr_z	Retention time of the linear alkane eluting before the unknown peak
tr_{z+1}	Retention time of the linear alkane eluting after the unknown peak
z	Number of carbon atoms of the linear alkane eluting before the unknown peak
$Y_{product}$	Product yield
m_{oil}	Mass of oil
$m_{product}$	Mass of product
$A\%_{FAME}$	Area % of FAME
Y_{diesel}	Diesel yield
$A\%_{Ci}$	Area % of C_i for the n-alkane with i carbon atoms
$S_{HDO/DCOx}$	Catalyst Selectivity
x_n	Independent variable (with n=1, 2, 3, …., k)
Y	Dependent variable (response variable)
x_A	Temperature
x_B	Catalyst-to-oil weight ratio
x_C	Reaction time
$Expl.Var$	Explained Variance
R^2	Coefficient of determination
$CV\ Expl.Var$	Explained Variance in Cross-Validation

$SS_{pure\ quadratic}$	Single-degree-of-freedom sum of squares for pure quadratic curvature
H_0	Null hypothesis in hypothesis testing
H_1	Alternative hypothesis in hypothesis testing
MS_E	Pure error mean square
n_C	Number of replicated observations at central point
n_F	Number of unreplicated factorial observations = 2^3
y_{jC}	j^{th} observation of Y at center point (j = 1, …, n_C)
$\bar{y}_C$	Arithmetic mean of observations y_{jC}
$\bar{y}_F$	Arithmetic mean of unreplicated n_F factorial observations of y
x_D	Stirring speed

GREEK

λ	Wavelength of incident wave
θ	Scattering angle
β	Width at half height of the diffraction peak
σ_m	Molecular cross-sectional area
γ	Surface tension
Υ	Catalyst-to-oil weight ratio
ω	Reactor stirring speed
χ	Conversion of TGs
β_0	Intercept
β_n	Coefficients of independent variable (with z=1, 2, 3, …., k)
β_{nq}	Coefficients of half of interaction effect between factors
ε	Error term

$\beta_{A,B,C,D}$	Coefficients of the linear terms for the factors x_A, x_B, x_C *and* x_D
$\beta_{AB,AC,BC,AD,BD}$	Coefficients of two-way interaction
β_{nn}	Coefficients of quadratic terms of factors
$\beta_{AA,BB,DD}$	Coefficients of quadratic terms of factors A, B and D

1. LITERATURE REVIEW

1.1 ENVIRONMENTAL ISSUES

Environmental issues encompass a wide range of challenges that affect the natural world and human health. These include climate change, pollution, deforestation, loss of biodiversity, and the depletion of natural resources [1, 2]. Understanding these issues is crucial for developing strategies to mitigate their impacts and promote a sustainable future. This Section provides an overview of key environmental concerns and their implications for ecosystems and human societies.

1.1.1 CLIMATE CHANGE AND GREENHOUSE GAS EMISSIONS

Climate change involves long-term shifts in weather patterns, often caused by human-induced alterations to the Earth's atmosphere [3].

Its widespread impacts cross geographical boundaries, globally influencing ecosystems, economies, and the well-being of societies [4]. At the environmental level, consequences include melting of glaciers, rising sea levels, extreme weather events such as hurricanes, droughts, and floods, and increased ocean acidification, all of which adversely affect ecosystems, endangering biodiversity and potentially causing the extinction of animal and plant species [5].

The economic implications of climate change are significant. The severity and growing frequency of natural disasters result in high costs for repairing damages and adapting to new climate risks. In addition, sectors such as agriculture and tourism, vital to many economies, are particularly vulnerable to climate effects. Social inequalities can amplify the impact of climate change, with the poorest and most vulnerable communities suffering disproportionately.

Above all, climate change also affects human life, threatening the essential components of good health, among which clean air and water, nutritious food, and safe housing [6]. About 250.000 more deaths per year between 2030 and 2050 are expected from malnutrition, malaria, diarrhea and heat stress alone, in connection to climate change effects [6].

Overall, in 2023 the Earth was about +1.36°C warmer than the pre-industrial average of the late 19th century (see Figure 1) [7, 8]. The last 10 years are the warmest on record [7].

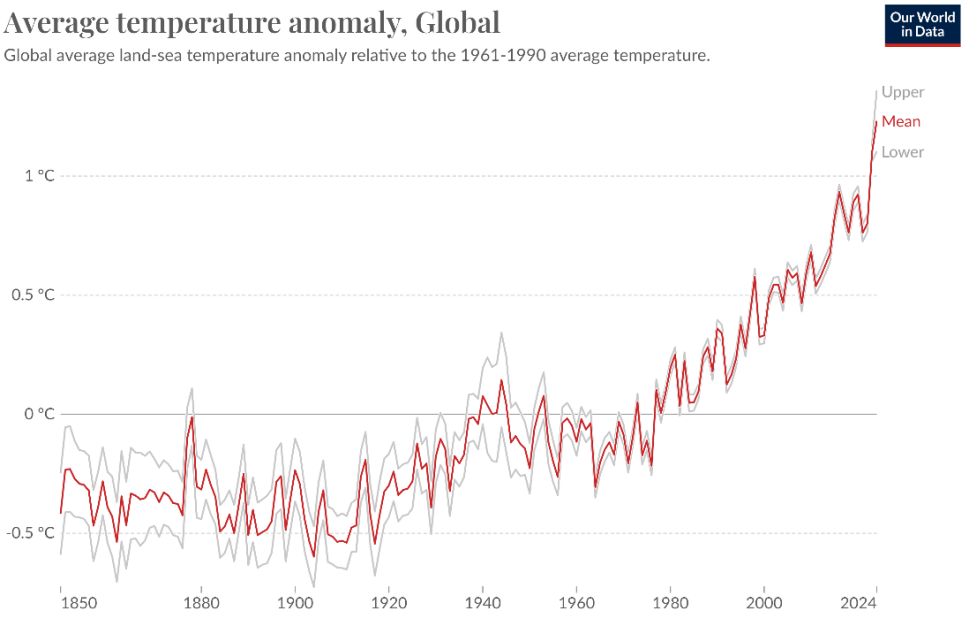


Figure 1 Global temperature anomaly charts, taken from [7].

The greenhouse effect is recognized as a major driver of climate change; 97% of climate scientists agree that the global warming observed in recent decades is mainly caused by human activities [9].

The natural greenhouse effect is a process that occurs in Earth's atmosphere and helps maintain a temperature suitable for life [10-12]. The Sun emits solar radiation, which reaches the Earth in the form of visible light and other types of energy [10-12]. The Earth absorbs some of this energy, warming its surface, while the rest is reflected into space [10-12]. As the Earth's surface warms, it also emits heat in the form of infrared radiation. Some of this infrared radiation escapes into space, but a portion is trapped by greenhouse gases (GHGs) in the atmosphere, such as carbon dioxide (CO_2), methane (CH_4), water vapor (H_2O), and nitrous oxide (N_2O) [10-12]. These gases act like the glass of a greenhouse, allowing sunlight to enter but preventing some of the heat from escaping. This trapped heat keeps the Earth's surface warmer than it would be if all the heat escaped into space [10-12]. The natural greenhouse effect is essential for life, as it keeps Earth's average temperature around 15°C [13, 14]. Without it, the planet would be much colder, around 18°C, making it inhospitable for most forms of life [13, 14]. However, human activities, such as industrial overproduction, fossil fuel combustion, fossil fuel use and energy production [3], are increasing the concentration of GHGs, enhancing this effect and leading to global warming.

In 2022, global greenhouse gas emissions (GHGEs) reached about 54 billion tons of equivalent CO_2 [15]. Figure 2 shows the global GHGEs in 2022.
China is the largest CO_2 producer globally, mainly due to its reliance on coal; United States (U.S.) remain one of the largest emitters per capita; India, with a growing economy and rapid urbanization, is also significantly increasing its emissions [16]. For these reasons, they are considered the largest contributors to worldwide GHGs.

Thus, it is necessary to adopt global and local policies to contain GHGs and mitigate climate change.

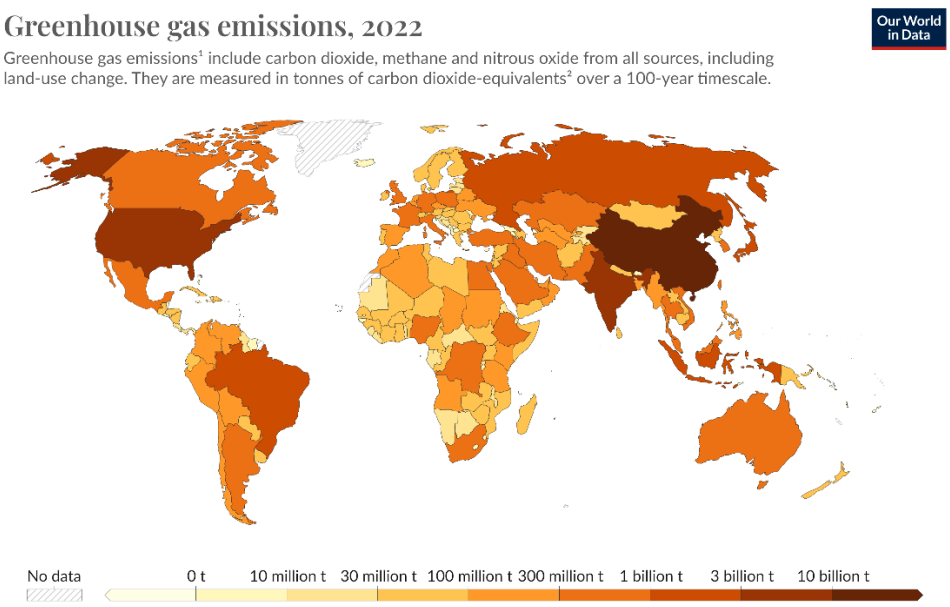


Figure 2 Global GHGEs per country in 2022. Data taken from [15].

1.1.2 Global and local policies against climate change

The Kyoto protocol was the first global policy adopted against climate change, promulgated in 1997 and entered into force in 2005 [17]. The protocol operationalized the United Nations Framework Convention on Climate Change (UNFCCC) by committing industrialized countries and transition economies to limit and reduce GHGEs according to agreed individual targets.

The Paris Agreement [18] is the subsequent relevant milestone, sealed in 2015 under the UNFCCC, which has aimed to limit global warming to well below +2°C compared to pre-industrial levels, with efforts to limit the increase to +1.5°C, with GHGEs peak by 2025 and fall by 43% by 2030.

Under the aegis of Paris Agreement, the most recent global policy initiative is COP 28 (Conference of Parties), the latest annual conference organized by the UNFCCC (in 2023) [19]. This conference acts as a forum for discussions and negotiations on global climate policy. The main objectives of COP 28 are to (i) continue to implement the Paris Agreement; (ii) strengthen national commitments to reduce GHGEs; and (iii) advance discussions on financing and support for developing countries [19].

In 2019, the European Union (EU) launched the European Green Deal [20], a comprehensive strategy to address climate change and promote sustainability across Europe. The European Green Deal aims to make EU the first climate-neutral continent by 2050. Its main goals are: (i) achieve net zero GHGEs by 2050; (ii) reduce GHGEs by at least 55% by 2030 compared to 1990 levels; (iii) foster sustainable economic growth through the transition to a low-carbon economy; and (iv) enhance biodiversity, reduce pollution, and promote the sustainable use of resources [20]. Thus, the main initiatives undertaken include: (i) promoting renewable energy sources (RES); (ii) phasing out coal and other high-emitting energy sources; (iii) promoting recycling and circular use of resources; (iv) mobilizing significant investment for green initiatives and transition efforts; (v) ensuring an equitable transition for regions and communities affected by the transition to a green economy [20]. The European Green Deal is also supported by a range of legislative and policy measures, including the European Climate Pact, which enshrines in law the 2050 climate neutrality goal [21].

In September 2020, China announced a commitment to peak carbon emissions by 2030 and achieve carbon neutrality by 2060 [22]. As the world's largest emitter of GHGs (as seen in Figure 2), China faces significant challenges in meeting this goal, particularly compared to developed nations. These challenges stem from its reliance on coal, rapid industrialization, and the scale of transformation required across its vast economy [22]. Nonetheless, China has laid out ambitious plans to shift toward renewable energy and reduce carbon intensity, though the path ahead remains complex and demanding [22].

India's key commitments made during the October 2015 Paris UNFCCC conference include reducing the emission intensity of its gross domestic product by 33-35% by 2030 from 2005 levels, achieving 40% of its installed electricity capacity from RES by 2030, and creating an additional carbon sink of 2.5 to 3 billion tons through increased forest cover [23]. At COP 26 in Glasgow, India further strengthened its climate commitments by introducing stricter carbon taxes to discourage energy consumption and attract

investments worth trillions of rupees in renewable energy by 2030, and achieve net zero emissions by 2070, reaffirmed during COP 28 [23].

In U.S., the President has pursued ambitious climate goals, aiming for a 50-52% reduction GHGs by 2030, 100% carbon pollution-free electricity by 2035, and a net-zero emissions economy by 2050 [24].

Some of other local policies that demonstrate the different approaches cities around the world are taking to address climate change, reduce emissions, and promote sustainability are: (i) London Environment Strategy [25], (ii) New York City Climate Mobilization Act [26], (iii) Melbourne Climate Change Mitigation Strategy [27], (iv) Oslo Climate and Energy Strategy [28], and (v) Seoul's One Less Nuclear Power Plant Initiative [29]. The abovementioned policies aim to reduce or at least slow down the growth of GHGs and will contribute to the containment of global warming.

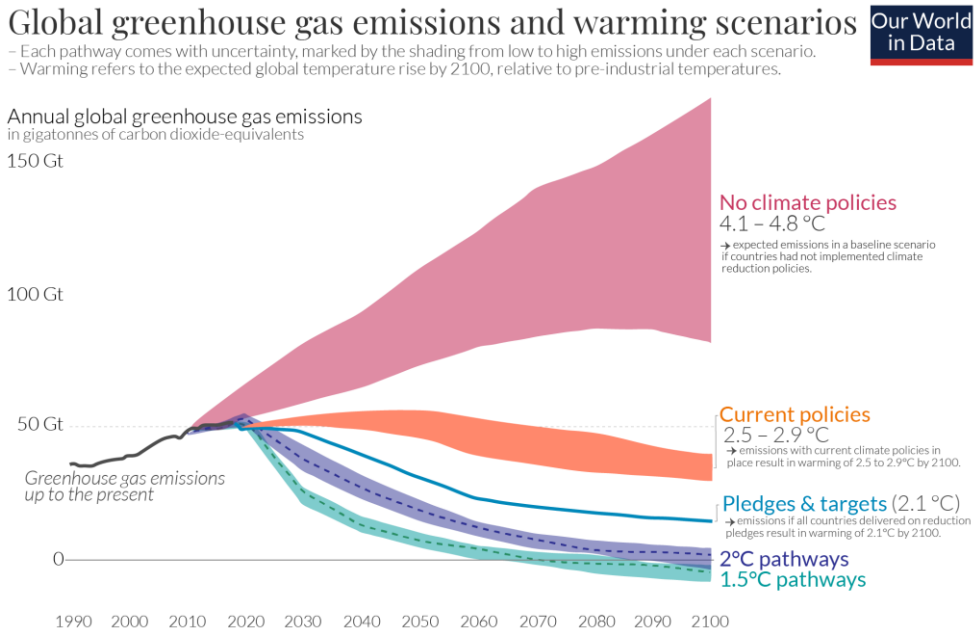


Figure 3 Warming scenarios and global GHGs taken from [30].

Figure 3 shows future GHG scenarios based on several assumptions: (i) if climate policies are not implemented; (ii) if current policies are implemented; (iii) whether all countries commit to meeting emission reduction targets; and (iv) whether the necessary actions are implemented to limit heating to +1.5°C or +2°C over the course of the century [30]. Figure 3 illustrates that existing

climate and energy policies (some of which above mentioned), encompassing both enacted legislation and executive orders, would lead to a global temperature rise of approximately 2.7°C by 2100 if no additional measures are taken. If countries fulfill their current pledges, this rise could be reduced to about 2.1°C. However, to meet the Paris Agreement's goal of limiting warming to "*well below 2°C*", current policies fall significantly short. To achieve this target, countries must enhance their commitments and align their policies accordingly. However, as seen in the Figure 3, climate and energy policies adopted and implemented would reduce warming compared to a world without climate policies.

For this reason, it is crucial to implement both global and local policies to drive effective progress and achieve sustainability goals.

1.1.3 THE ENERGY ISSUE

Energy indeed plays a crucial role in economic and social development, as well as in improving the quality of life. Economic growth in developing countries over the last decades and world population growth (8.1 billion people in 2024 [31]) has led to a rapid increase in energy demand. Figure 4 reports the world total energy consumption per country in 2023. As in Figure 2 for GHGEs in 2022, the nations with the highest energy consumption in 2023 were China, U.S., India, and Russia (see Figure 4). They are also countries with the largest population and with the highest rate of economic development [32]. This assesses the current correlation between energy demand, economic growth, population growth and GHGEs; the latter element should be pulled off that correlation by policies mentioned in Section 1.1.2.

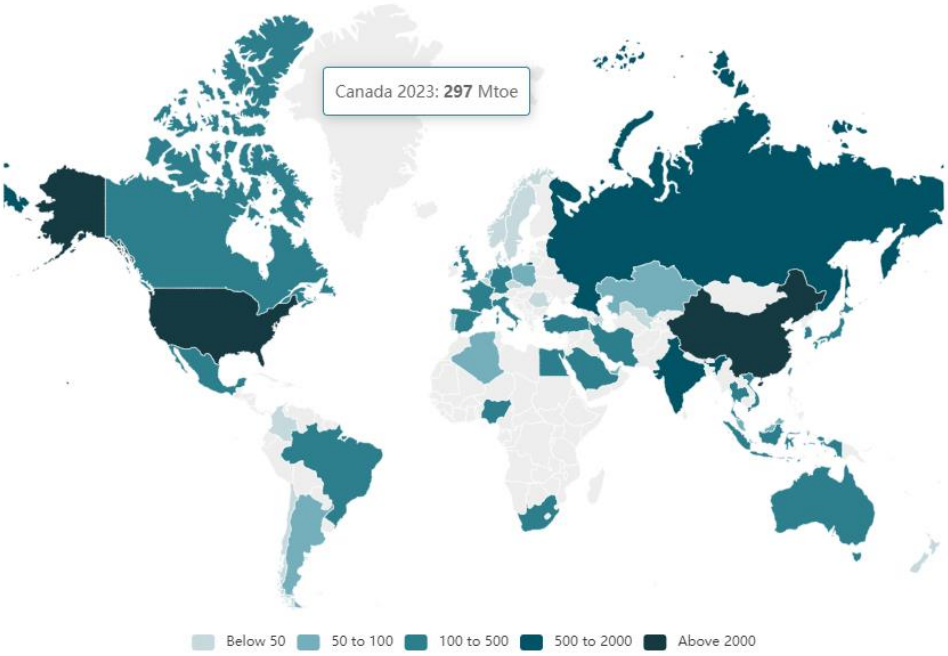


Figure 4 Total Energy consumption in 2023, expressed in Mtoe (i.e., Million Tons of Oil Equivalent), taken from [33].

The distribution of energy sources is given in Figure 5: in 2023 the main energy sources are still oil, coal, and natural gas (overall 82%), all fossil fuels.

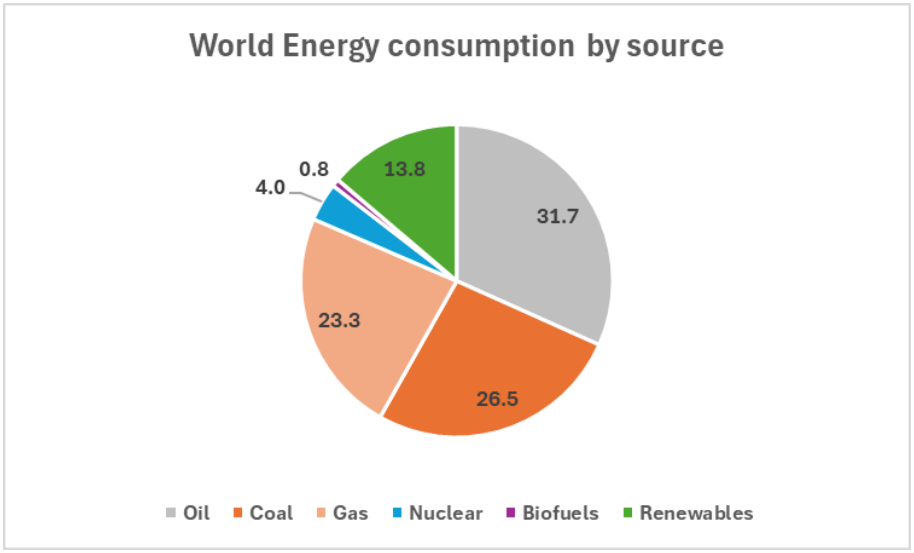


Figure 5 World Energy Consumption by source in 2023. Data taken from [34].

In addition to their limited availability and geopolitical dependencies, fossil fuels determine significant environmental consequences because of their combustion, that generates pollutants, including GHGs such as CO_2, CO,

nitrogen oxides, sulfur compounds, volatile organic compounds (VOCs), and particulate matter [35]. Consequently, a significant effect of fossil fuel consumption is global warming.

The implementation of global and local policies (listed in Section 1.1.2) is necessary to enable a rapid transition towards renewable energies (RE). For this reason, the EU has set a binding target of 32% of RE in the energy sector by 2030, through the Renewable Energies Directive II (RED II) [36]. This action should lead to a significant reduction of emissions and an increase in the use of RE sources in the energy and transport sectors. Currently, the transport sector is a significant consumer of non-renewable energy (fossil origin) and a major contributor to GHGEs. It accounted for 29% of total GHGEs in the U.S. in 2022 [37], 29% in the UE in 2021 [38], and 15.5% of global emissions in 2020 [39].

Achieving the ambitious targets set by climate policies and advancing the energy transition requires significant investment in and development of cutting-edge technologies for renewable fuel production. This includes improving methods for producing biofuels and emerging E-fuels and E-biofuels (the main differences between the three will be listed in Section 1.4), which are essential for reducing dependence on fossil fuels. Promoting innovation in these technologies will not only contribute to lowering emissions but also support the broader goal of creating a more sustainable, resilient, and diversified energy system, capable of meeting future demands while addressing environmental challenges.

Fostering innovation in these technologies, guided by the 12 principles of Green Chemistry and Green Engineering, will not only help reduce emissions but also optimize resource use and minimize the environmental impact of production processes. This approach supports the broader goal of creating a more sustainable, resilient, and diversified energy system.

1.2 Principles of Green Chemistry and Green Engineering

Green Chemistry and Engineering aim to enhance efficiency while reducing health and environmental hazards at every stage of chemical production [40]. The principles and metrics of Green Chemistry can impact on the entire life cycle of a process, regardless of its complexity.

Green Chemistry has a relatively recent history; Cathcart was likely the first to reference it in a scientific paper in 1990 [41]. However, it was in 1996, with the publication of “Green Chemistry: An Overview” by Anastas and Williamson [42], that the foundation for the modern "philosophy" of Green Chemistry was firmly established. The core idea of Green Chemistry is to apply chemical expertise and knowledge to minimize or eliminate the use and production of hazardous substances throughout the design, manufacturing, and application of chemicals, with the goal of reducing risks to both human health and the environment [42]. In 1998, Paul Anastas and John Warner [43] released the first “Green Chemistry handbook”, where they introduced 12 principles of Green Chemistry (Figure 6).

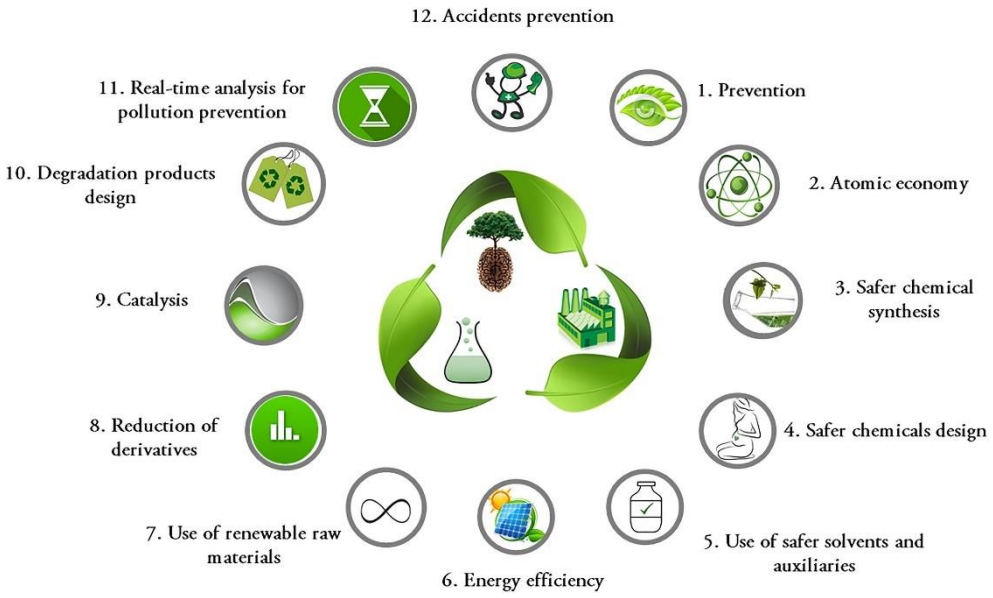


Figure 6 The 12 principles of Green Chemistry. Figure taken from [44].

The 12 principles of Green Chemistry focus on reducing or eliminating the use of toxic solvents in chemical processes and minimizing waste production. In Table 1, the 12 principles of Green Chemistry are categorized as follows: (i) those that enhance resource efficiency; (ii) those that improve process energy efficiency; and (iii) those that mitigate environmental and human health risks.

Table 1 The 12 principles of Green Chemistry divided in three categories, adapted from [45].

Improve resource use	**Increase energy efficiency**	**Reduce human and environmental hazards**
Principle 1: *Prevention*	***Principle 6***: *Design for energy efficiency*	***Principle 3***: *Less hazardous chemical synthesis*
Principle 2: *Atom Economy*		***Principle 4***: *Designing safer chemicals*
Principle 7: *Use of renewable feedstock*		***Principle 5***: *Safer solvents and auxiliaries*
Principle 8: *Reduce derivatives*		***Principle 10***: *Design for degradation*
Principle 9: *Catalysis*		***Principle 12***: *Inherently safer chemistry for accident prevention*
Principle 11: *Real-time analysis for pollution prevention*		

Key aspects include maximizing atomic and energy efficiency, using renewable and non-toxic raw materials, and accelerating reactions through catalysis to save energy and reduce waste. Another principle emphasizes designing chemicals that break down into harmless products after use, avoiding environmental harm and bioaccumulation. Overall, the principles aim to minimize environmental and occupational risks throughout a product's lifecycle, from synthesis to disposal. The 12 principles of Green Chemistry are thoroughly detailed and clearly explained in numerous publications [46-50]. Whereby, Green Chemistry should not be viewed as a distinct branch of chemistry but rather as a guiding "*philosophy*" that is seamlessly integrated into all existing fields of chemistry. The expectation is that, over time, Green Chemistry will become a fundamental part of every scientific discipline.

In addition to formulating the guidelines for the principles of Green Chemistry, Anastas and Zimmerman also authored and developed the 12

Principles of Green Engineering [51]. The 12 Principles (in Table 2) offer a framework for creating environmentally sustainable processes and products. They focus on minimizing hazardous materials, optimizing resource use, and prioritizing RES. The principles advocate waste reduction, designing for easy disassembly and recycling, and considering the full lifecycle of products.

Table 2 The 12 principles of Green Engineering from [51].

Principle 1:	Inherent rather than circumstantial
Principle 2:	Prevention instead of treatment
Principle 3:	Design for separation
Principle 4:	Maximize mass, energy, space, and time efficiency
Principle 5:	Output-pulled versus input-pushed
Principle 6:	Conserve complexity
Principle 7:	Durability rather than immortality
Principle 8:	Meet need, minimize excess
Principle 9:	Minimize material diversity.
Principle 10:	Integrate local material and energy flows
Principle 11:	Design for commercial "afterlife"
Principle 12:	Renewable rather than depleting

They emphasize simplicity, durability, responsible technological use, and promoting environmental justice. Ultimately, the goal is to develop systems that reduce environmental impact while ensuring efficiency and sustainability in engineering practices. The 12 principles of Green Engineering are extensively discussed and applied in various literature works [40, 52-55].

Kirchhoff [56] in her work said that: "*the engineer's job becomes easier when chemists develop products and processes that minimize or eliminate the use and creation of hazardous materials. Green Chemistry serves as the foundation for advancing Green Engineering*". This highlights the essential collaboration between chemists and engineers in achieving sustainable innovation. By integrating the principles of Green Chemistry, engineers can design more efficient, safer, and environmentally friendly processes, ultimately contributing to a more sustainable future in industrial practices.

1.3 THE FUTURE OF RENEWABLE FUELS: FROM BIOFUELS TO E-FUELS AND E-BIOFUELS

In this context, biofuels, E-fuels, and E-biofuels stand out as promising solutions. Biofuels, derived from biomass, have long been pioneers in providing alternatives to traditional fuels. However, increasing demand and sustainability concerns have led to the development of new technologies.

E-fuels, produced from renewable energy through synthetic processes, enable the creation of fuels without affecting food resources. In contrast, E-biofuels leverage both biomass and renewable energy, offering a synergistic approach that could revolutionize the energy sector.

This section will examine the characteristics, advantages, and challenges of each fuel type, highlighting their potential contributions to a cleaner and more sustainable energy future.

1.3.1 BIOFUELS

The UE has defined the term biofuels as: "*biofuels are liquid or gaseous transport fuels, such as biodiesel and bioethanol, made from biomass. They serve as a renewable alternative to fossil fuels in the EU's transport sector, helping to reduce GHGEs and improve the EU's security of supply*"[57].

Biofuels offer a renewable substitute for fossil fuels, capable of cutting GHGEs and bolstering energy security [58]. They are derived from renewable resources, with biomass — which includes materials from wood, crops, livestock, marine and industrial waste — being the principal source for producing solid, liquid, and gaseous biofuels [59]. Biomass encompasses all biological material and can be categorized into lignocellulosic or non-lignocellulosic types [60]. In contrast to fossil fuel combustion, which adds extra CO_2 to the atmosphere, burning biomass is regarded as a carbon-neutral process. This is because the CO_2 released during combustion is the same CO_2 that was absorbed by the plant during photosynthesis, resulting in no net increase in CO_2 [61], if no other net CO_2 emission occurs in the related life

cycle. Furthermore, biomass generally contains lower levels of sulfur and nitrogen, leading to reduced emissions of SO_x and NO_x compared to fossil fuels [61]. Furthermore, biomass is a RES with considerable growth potential, owing to its extensive global availability [62]. It can be derived from by-products of numerous industrial and agricultural activities, as well as from organic waste [62]. The global supply of biomass from agriculture and forestry is estimated at approximately 11.9 billion tons of dry matter per year; 61% of the total comes from agriculture and 39% from forestry [63]. Within this, agricultural crops represent 47%, while residues collected from above-ground sources account for 14% [63].

In 2023, the U.S. led the world in biofuel production, generating 1795 PJ. Brazil and Indonesia followed, producing approximately 1016 and 433 PJ, respectively [64]. Germany, with about 160 PJ of biofuel production, ranked among the top five global producers and was the leading producer in UE [64]. Global biofuel production has reached 1.9 million barrels of oil equivalent per day in 2022 [64].

Biofuels are categorized into four generations according to their feedstock and production processes: first, second, third, and fourth generation.

First-generation biofuels are made from edible biomass, including starches (e.g., potatoes, wheat, barley, corn) and sugars (e.g., sugar cane, sugar beet) [65].

These biofuels are typically produced by well-established processes such as fermentation and transesterification, and include products such as bioethanol and biodiesel [66]. The main advantage of first-generation biofuels is their relatively simple production process and well-established infrastructure. However, these biofuels raise ethical issues as they use edible crops as feedstocks and raise concerns about their impact on cultivated land, biodiversity and food supply, as well as water depletion [67].

Second-generation biofuels are produced from non-food biomass, including some by-products of agriculture (e.g., cereal straw, sugarcane bagasse, forest residues), waste (e.g., organic components of municipal solid waste), and dedicated feedstocks (e.g., purpose-grown vegetative grasses, short-rotation forests, and other energy crops) [68]. The key issues of producing second

generation biofuels include reducing overall energy costs, minimizing waste production, and creating biofuels with higher added value to ensure economic feasibility, and reducing GHGEs [69]. Second-generation liquid biofuels are typically produced using either biological or thermochemical processing of biomass [70]. A key advantage of utilizing inedible feedstocks for second-generation biofuels is the reduction of direct competition between food and fuel production, a significant issue with first-generation biofuels. In addition, second-generation biofuels are linked to increased land use efficiency and reduced pressure on biodiversity [70]. The disadvantages of second-generation fuels include the lower yield of inedible plants and the use of agricultural land for non-edible products, which directly impacts the economy and food production [71].

Third-generation biofuels, derived from oleaginous microorganisms such as microalgae, bacteria, yeast, and fungi, have recently attracted interest as a potential feedstock for energy fuel production [72]. Microalgal biomass exhibits a higher growth rate and greater biomass productivity compared to conventional biomass, and it can accumulate a substantial amount of cellular lipids, ranging from 20% to 77% of its dry weight [73]. In certain microalgal species, the oil content constitutes over 80% of the dry weight of the algal biomass [73], 20 to 300 times more oil compared to traditional biomass crops [74]. This high lipid accumulation enhances the potential of microalgae as a valuable feedstock for biofuel production. Additionally, microalgae require only light, CO_2, and other inorganic nutrients for their growth [75]. Biofuel production from microalgae primarily helps reduce CO_2 levels in the environment, as producing 1 kg of microalgae consumes approximately 1.8 kg of CO_2 [74]. For these reasons, third-generation biofuels are considered the most viable and sustainable solution to future energy needs, as they address the limitations of earlier generations of biofuels.

Fourth generation biofuels are produced from genetically modified (GM) algal biomass to enhance biofuel yields [76]. Common strategies for genetic modification of microalgae include: (i) improving photosynthetic efficiency; (ii) increasing light penetration; and (iii) reducing photoinhibition [76]. Additionally, metabolic engineering of microalgae can significantly boost

lipid or carbohydrate content [77]. GM microalgae have a high adaptability to extreme environmental conditions, including salinity, drought, photo-oxidation, osmotic pressure, anaerobic temperature, and ultraviolet radiation [77]. Moreover, as nutrients they use mainly nitrogen and the phosphorus [77]. The environmental benefits of GM microalgae include CO_2 sequestration and assimilation, simply wastewater treatment, and reduction of GHGs [78]. Fourth-generation biofuels are primarily focused on achieving a lower environmental impact compared to previous generations, although research and development in this area are still ongoing.

The production cost of biofuel is also a crucial factor in determining its sustainability. The total production cost of first-generation biofuels ranges from 0.49 $/L to 0.86 $/L [78]. The production cost of second-generation biofuel ranges from 0.31 $/L to 2.07 $/L of gasoline equivalent [78], while for the third-generation biofuel ranging from 0.44 $/L to 8.76 $/L [78]. These biofuels are not economically competitive with other fuels, because their cost also includes the costs of the microalgae cultivation, harvesting, dehydration and drying processes [78]. Therefore, despite their high costs, third- and fourth-generation biofuels are considered the best options for achieving sustainable development goals. However, these biofuels could also become economically sustainable with further research and development.

1.3.2 E-FUELS AND E-BIOFUELS

In addition to biofuels, E-fuels and E-biofuels emerge as promising renewable alternatives, particularly in sectors where biofuels may face limitations.

E-fuels (i.e., Electro-fuels) are synthetic fuels created by capturing CO_2, from the atmosphere or industrial emissions, and combining it with H_2 produced through electrolysis, using RES like wind, solar, or hydropower [79]. The key advantage of E-fuels lies in their potential for high sustainability, particularly when produced entirely with renewable electricity [80]. By using captured CO_2 as the primary raw material for their synthesis, E-fuels offer a carbon-neutral alternative to both traditional fossil fuels and conventional biofuels [79]. These fuels do not rely on biomass for their production. Technologies

involved in producing E-fuels, such as E-diesel, often utilize H_2 and CO_2, converted into liquid fuel through the Fischer-Tropsch synthesis process, a well-established method for generating hydrocarbons from syngas [79]. Although still in the early stages of large-scale implementation, E-fuels are increasingly recognized as a vital component in decarbonizing sectors. Their long-term potential lies in significantly reducing GHGEs by providing a carbon-neutral alternative to fossil fuels, especially for applications where electrification may not be feasible or efficient (e.g., aviation, shipping, and heavy industry) [81].

In E-biofuels, green hydrogen, typically derived from water electrolysis, is used for the hydrotreatment of renewable biomass feedstocks, making them a type of biofuel [82]. Being produced from biomass and using green hydrogen, E-biofuels can contribute to a closed carbon cycle, reducing environmental impact [82]. E-biofuels are still in the developmental phase, but they are gaining attraction as a promising solution for sustainable energy.

1.4 BIODIESEL AND GREEN DIESEL

Biodiesel and green diesel are considered the most promising alternatives to conventional petrodiesel, as they can be used in standard internal combustion diesel engines without major modifications, particularly in the case of green diesel [35].

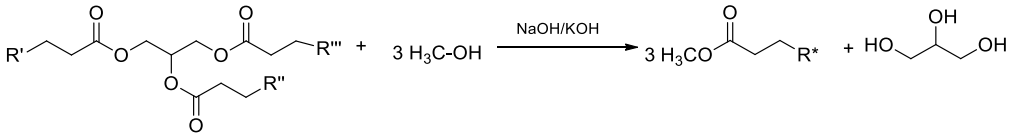
1.4.1 BIODIESEL

The term "*biodiesel*" refers to a fuel made up of mono-alkyl esters of long-chain fatty acids, known as "*B100*" according to the ASTM D6751 biodiesel standard [83]. Biodiesel, in the form of FAMEs (Fatty Acid Methyl Esters) and FAEEs (Fatty Acid Ethyl Esters), can be produced from a variety of sources, including edible oils, inedible oils, waste cooking oils (WCOs), animal fats, and microalgal lipids [84].The European biodiesel standard EN 14214 designates this fuel as FAME [85].

Biodiesel can be produced through various methods, such as thermal cracking, ultrasonic, and microwave techniques [59]. However, the most

widely used commercial process is the transesterification/esterification of vegetable oils, with homogeneous acid or base catalysis (i.e., H_2SO_4 or NaOH/KOH), in the presence of methanol or ethanol as esterifying agents [59]. When biodiesel is produced with methanol, the carbon atoms in the biofuel are only about 95% "*bio*" because, although methanol can be obtained from renewable resources, it is most derived from non-renewable natural gas [84]. When ethanol is used, resulting in the production of ethyl esters, the biodiesel is considered completely "*bio*" since ethanol is typically derived from renewable resources like corn and sugarcane [84]. When choosing between methanol and ethanol, methanol is cheaper and more reactive, and FAMEs are more volatile than FAEEs [86]. However, ethanol is less toxic [86].

Scheme 1 shows the transesterification reaction of the biomass triglycerides (TGs) with methanol, to obtain FAME.



Scheme 1 Transesterification reaction. With R= R', R'' and/or R'''.*

The transesterification process is primarily influenced by temperature, time or space velocity, pressure, alcohol-to-feedstock ratio, TG concentration, type of catalyst, mixing intensity, and type of feedstock [87]. Typical transesterification conditions include: (i) temperature range of 50 to 65°C; (ii) atmospheric pressure; (iii) reaction time of 1 to 4 hours; and (iv) alcohol-to-feed molar ratio between 6:1 and 12:1 [88, 89]. The use of biodiesel is beneficial because it is a non-toxic, biodegradable, and potentially renewable biofuel that can help reduce GHGEs [35]. Biodiesel can be used either pure or blended with petroleum-derived diesel. When used in its pure form, it is referred to as "*B100"*. However, this can lead to compatibility issues, as not all engines are designed to operate with pure biodiesel [90]. Consequently, biodiesel is mainly used in blends, typically at a $7\%_{v/v}$ with petroleum-derived diesel [90].

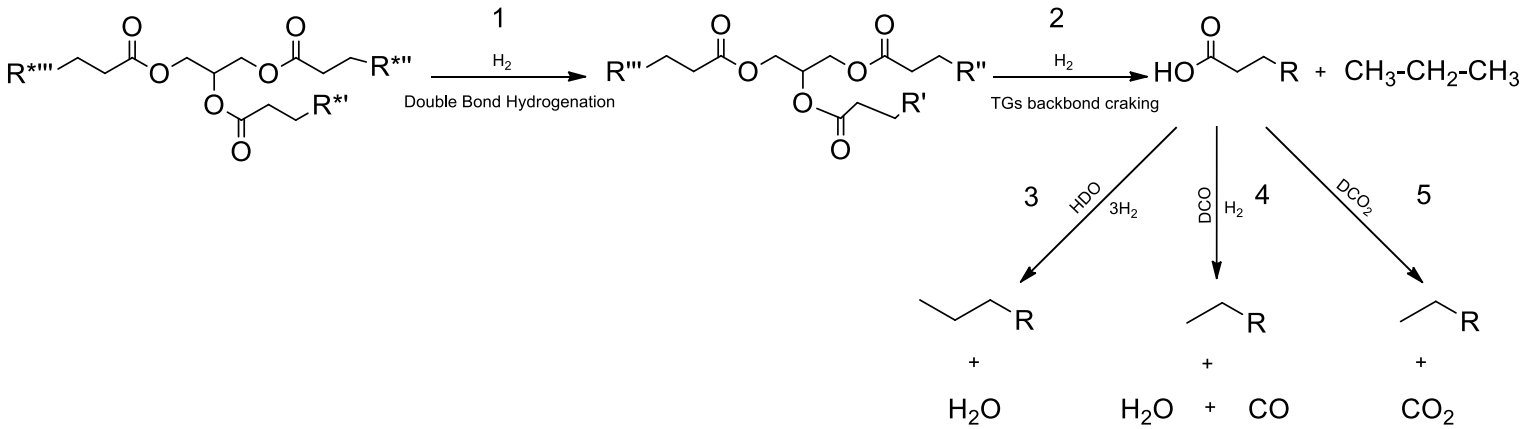
In addition to its overall favorable properties as transport fuel, biodiesel has numerous other potential applications. These include energy production, lubricants, plasticizers, high boiling point absorbers for cleaning industrial gaseous emissions, and various solvent applications [91].

Compared to petrodiesel, the main constraints of biodiesel usage and production are: (i) high cost of raw materials; (ii) reduced stability during storage, due to oxidation (see Table 3 in Section 1.4.3); (iii) lower energy content (see Table 3 in Section 1.4.3); (iv) higher NO_x emissions (see Table 3 in Section 1.4.3); and (v) limited miscibility with conventional fossil fuels [35]. Additionally, key issues in the commercial-scale production of biodiesel include socioeconomic and bioethical impacts, food security, land use, regional sustainability, biomass pretreatment, and production technology [35].

1.4.2 GREEN DIESEL

Green diesel, also known as "*Renewable Diesel*" or "*Hydrotreated Vegetable Oil (HVO)*" (when produced from vegetable oil feedstock) is an alternative to biodiesel and is produced through the catalytic deoxygenation reaction (DO) of fatty biomass [92]. In this process, fatty biomass TGs are heat-treated, usually in a hydrogen-rich environment in presence of heterogeneous catalyst, and converted into n-alkanes as main products in the C_{15}-C_{18} range [92].

The overall DO of TG is summarized in Scheme 2. In the first step, TGs are hydrogenated (reaction 1 of Scheme 2) and cleaved (reaction 2 of Scheme 2) to obtain free fatty acids (FFAs) and propane (as a by-product). FFAs are subsequently converted into n-alkanes through three main reactions: (i) hydrodeoxygenation (HDO, reaction 3 of Scheme 2), which produces n-alkanes with the same number of carbon as the starting FFA, with H_2O as the only by-product; (ii) decarbonylation (DCO, reaction 4 of Scheme 2) and (iii) decarboxylation (DCO_2, reaction 5 of Scheme 2), which produce n-alkanes with one carbon atom less than the starting FFA, with H_2O, CO, and CO_2 as by-products, respectively [59].



*Scheme 2 Formation of FFAs from TGs and HDO, DCO and DCO_2 reaction pathways. * = possibility of double bonds in acid tails; R, R', R'' and R''' groups could be equal or differ from each other.*

The catalytic DO reaction produces a biofuel that is chemically analogous to petroleum-derived diesel fuel, with comparable chemical and physical properties (see Table 3 in Section 1.4.3) [59]. Green diesel is an excellent renewable alternative fuel due to its high heating value, energy density, good cetane number (CN), high stability and low oxygen content (see Table 3 in Section 1.4.3) [35]. It also has superior physical properties, such as cloud point, flash point, viscosity, and lubricity, compared to both petrodiesel and biodiesel [93]. It has the chemical structure of C_nH_{2n+2} and is free of aromatics, oxygen, sulfur, and ash, which can be easily adapted to feedstock availability and meets the safety and quality standards of internal combustion engines, ranging from light to heavy-duty [94]. Green diesel has a high CN due to the low activation energy required for combustion compared to branched hydrocarbons (HCs) or aromatics. However, these HCs typically have poor cold flow properties and high freezing points above 15°C, which can make the liquid impractical for use as a fuel or blend [95]. To solve this problem, an isomerization process is required to lower the melting point [95]. Green diesel also possesses all the advantageous characteristics of biofuels: it is produced from renewable sources, is carbon neutral if it is produced from green hydrogen (see Section 1.3.2), and generates low emissions of GHGs, VOCs, and particulate matter (PM) [90]. If green diesel were produced from the DO of biomass using green hydrogen, it would qualify as an E-biofuel (see Section 1.3.2), making it a fully sustainable fuel. This approach not only enhances energy efficiency (in full agreement also with the principles of Green Chemistry and Green Engineering, Section 1.2), but also aligns with global efforts to reduce GHGEs and transition to a more sustainable energy system. Emphasizing the use of renewable resources in this process could significantly contribute to achieving climate goals and fostering a circular economy. Although green diesel (and E-green diesel) offers many benefits, traditional diesel and biodiesel remain predominant today due to its economic advantages.

1.4.3 A COMPARISON BETWEEN GREEN DIESEL AND BIODIESEL

A comparison between biodiesel and green diesel, with reference to petrodiesel, was reported in Table 3.

Table 3 Comparison between petrodiesel, biodiesel and green diesel. Data adapted from sources in the "Ref." column.

Properties	**Petrodiesel**	**Biodiesel**	**Green Diesel**	**Ref.**
Carbon content [% wt.]	86.8	76.2	84.9	[35]
Oxygen content [% wt.]	0	11	0	[35]
Hydrogen content [% wt.]	13.2	12.6	15.1	[35]
Sulfur content [ppm]	< 10	< 1	< 1	[59]
Water content [ppm]	59	410	46	[96]
NO_x emissions	baseline	+ 10%	–10 to 0%	[59]
Particulate Matter emissions [g/kW h]	0.077	0.044	0.056	[96]
Specific gravity	0.84	0.88	0.78	[59]
Cetane Number	44.5–67	50–65	70–90	[35]
Viscosity at 40 °C [mm^2/s]	3.18	4.6	3.43	[96]
Lower heating value [MJ/kg]	43	38	44	[35]
Density [g/mL]	0.84	0.88	0.78	[35]
Stability	Good	Marginal	Good	[92]
Flash Point [°C]	65	171	122.7	[96]
Cloud point [°C]	−5	−5, +15	−20, +20	[92]

Overall, green diesel has properties that closely resemble those of petrodiesel, this likeness stems from their largely similar chemical compositions. This means that the marketing of green diesel must adhere to the same ASTM and EN standards that apply to petrodiesel [97]. The high chemical similarity between green diesel and petrodiesel, both being composed of HC chains, suggests that green diesel could potentially replace petrodiesel in the future [93].

The high oxygen content in biodiesel (composed by FAME) compared to green diesel and petrodiesel, due to the ester functionality, leads to a lower carbon content and consequently a lower LHV (lower heating value) [98]. The LHV indicates the amount of heat released during the combustion of a

given amount of substance; so a higher LHV means higher energy density [98].

American and European standards require a minimum CN of 40 for diesel fuel, as the CN gauges the ignition quality of the fuel in diesel engines; higher CN indicate better fuel quality [99]. According to Table 3, both biodiesel and green diesel exceed this CN requirement, with green diesel having the highest CN of the three fuels. As the CN increases, the ignition delay in diesel engines decreases, allowing the engines to operate with greater thermal efficiency and reduced fuel consumption [99].

Biodiesel has several disadvantages compared to green diesel, including a higher cloud point (i.e., the temperature at which wax starts to separate from the liquid biofuel), greater corrosivity (presence of high content of water, see Table 3), and inferior thermal and chemical stability [100]. As to green diesel, some of n-alkanes can converted into branched HCs through subsequent hydroisomerization treatment, which enhances the cold properties of the biofuel (e.g., cloud point) [35].

Regarding the GHGEs, both green diesel and biodiesel contribute to reductions in CO_2, CO, NO_x, SO_x, and PM compared to fossil diesel. However, due to its higher combustion efficiency, green diesel generates lower levels of NO_x and CO compared to biodiesel [101]. The reduction in PM emissions related to green diesel combustion may be attributed to its negligible sulfur and aromatic content. Additionally, the higher CN of green diesel leads to a shorter ignition delay, which reduces soot formation during the premix phase and further contributes to the decrease in PM [96].

Green diesel fuel has lower viscosity, density, and flash point than biodiesel (see Table 3) because the oxygenated compounds in biodiesel (i.e., FAME) typically raise these properties [91].

Biodiesel is synthetically advantageous due to its production under mild reaction conditions (e.g., temperature between 50 and 65°C, atmospheric pressure. See Section 1.4.1 for further details) , even though the final product necessitates additional separation and purification processes to remove the homogeneous catalyst and by-products such as glycerol [102]. These

requirements lead to higher production costs. In contrast, green diesel is produced by processes such as catalytic DO of TG-based biomasses, which use heterogeneous catalysts. This greatly reduces the need for complex separation and purification steps for the final product, compared to biodiesel, which requires these steps. Additionally, 95% of biodiesel production relies on edible oils, as inedible oils, that typically containing more than 4% of water, require acid esterification pretreatment before they can be used for biodiesel production [59]. Instead, green diesel production processes are tolerant to crude oils with higher water content and high levels of impurities, thus reducing operating costs [103, 104]. For these reasons, compared to biodiesel, green diesel presents substantial benefits in terms of product quality, streamlined production processes, and full compatibility with existing infrastructure, making it a more efficient and flexible option for industrial use [103, 104]. Additionally, green diesel boasts lower production costs and reduced process complexity, positioning it as a more cost-effective and sustainable alternative to both biodiesel and petrodiesel [103, 104].

1.4.4 INDUSTRIAL GREEN DIESEL PRODUCTION

Technology readiness levels (TRLs) are a measurement system used to evaluate the maturity of a technology, with levels ranging from 1 to 9 [105]. Currently, the TRL for green diesel production reached 8 or 9 in some cases [35, 94].

Green diesel production through the catalytic DO of TGs and fatty-acid-based biomasses has been commercialized by companies such as Neste, Diamond Green Diesel, UOP/Eni, AltAir Fuels, TotalEnergies, Exxon Mobil, UPM Biofuels, Preem, Renewable Energy Group, Phillips 66, Marathon Petroleum and Repsol [35].

Neste has developed the NExBTL (next-generation biomass-to-liquid) technology, which utilizes catalytic HDO to produce pure HCs with high energy density [106]. Neste MY Renewable Diesel can reduce GHGEs (measured as $CO_{2,eq.}$) by up to 75% or even up to 95% [35, 106].

Diamond Green Diesel operates a production plant in the U.S. utilizing Ecofining™ technology, which involves hydrogenation and isomerization of animal fats, algal oils, and WCO to produce high-quality biofuels [35, 107]. This technology has achieved a reduction in GHGEs by up to 80%, recycled 2.3 billion pounds of waste, and produced approximately 1.2 billion gallons per year of green diesel [35, 107]. The resulting fuel has been commercialized in Europe, Canada, and California [107].

The Ecofining™ technology is also employed in Italy by UOP/Eni. Their plant uses vegetable oils, animal fats, and WCO as raw materials to produce green diesel [108]. By 2025, 3 million tons per year of biofuels are expected to be produced using Ecofining™ technology [35, 108].

Additionally, AltAir Fuels utilizes the same Ecofining™ technology at their plant in California [35].

TotalEnergies has converted several conventional refineries to produce green diesel using animal fats, residual oils, and used oils [109]. These biorefineries have a combined capacity to produce 500.000 tons of biofuels annually [109].

UPM Biofuels produces BioVerno green diesel from tall crude oil, a by-product of pulp production [35]. This green diesel is characterized by a high CN, low aromatic content, and is sulfur-free [35, 110]. BioVerno can be used on its own or blended with petrodiesel in varying concentrations and is compatible with all diesel engines and existing fuel distribution systems [35, 110]. Additionally, BioVerno green diesel results in GHGEs that are 80% lower than those of petrodiesel [110].

Exxon Mobil produces green diesel from bio-feedstock using its EMRD™ technology, which involves two stages: (i) catalytic HDO and (ii) isomerization of n-paraffins to iso-paraffins [35, 111]. This process improves the cold flow properties of the green diesel [35, 111].

Although many industrial companies, including those mentioned, already produce and market green diesel, global production is still insufficient to meet the daily demand for biofuel. Therefore, further advancements are necessary to enhance and increase green diesel production worldwide.

1.5 GREEN DIESEL PRODUCTION: DEOXYGENATION REACTIONS

In general, the DO process is a thermal process that produces n-alkanes by removing hydrogen, oxygen, and carbon atoms from TG biomasses, with the release of CO_2, CO, and H_2O [112]. This process typically operates under high pressure and high temperature conditions (see next Section 1.6.2) and involves the presence of a metal-based catalyst [113]. While the DO process is generally carried out in the presence of H_2, it can also be performed in an H_2-free environment or at low H_2 partial pressures. The products of the overall reaction can vary depending on the feedstock and reaction conditions.

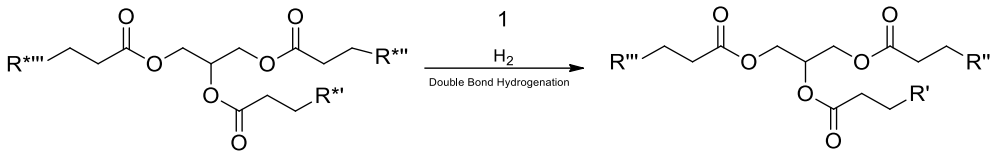
The DO process encompasses both primary reactions, which occur in the liquid phase, and secondary reactions, which primarily take place in the gas phase [114].
The overall reaction resulting in the production of green diesel from TGs, as mentioned in Section 1.4.2, is explained in detail in the following Sections.

1.5.1 PRIMARY LIQUID PHASE REACTIONS

The primary reactions occurring in the liquid phase initially involve the hydrogenation of TGs and their conversion into FFAs (see Scheme 3 and Scheme 4, respectively). Once these FFAs are produced, they are converted into n-alkanes through three main mechanisms: hydrodeoxygenation (HDO, see Scheme 6), decarbonylation (DCO, see Scheme 7), and decarboxylation (DCO_2, see Scheme 7), as mentioned in Section 1.4.2. Additional reactions that may follow n-alkanes formation include hydroisomerization and oligomerization (see Section 1.5.1.3).

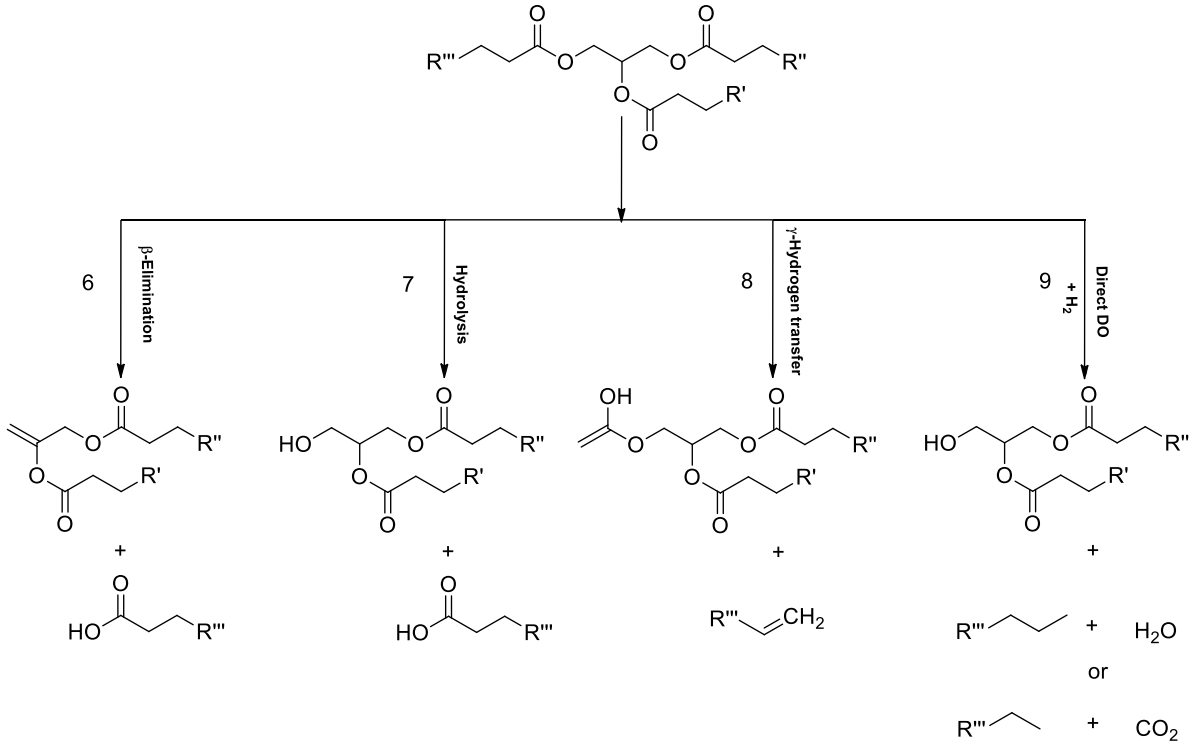
1.5.1.1 TRIGLYCERIDES HYDROGENATION AND FORMATION OF FFAS

The initial reaction in the liquid phase involves the hydrogenation of double bonds in TG chains, resulting in their saturation, as reported in Scheme 3 and in the overall reaction in Scheme 2 (see reaction 1).



*Scheme 3 Double Bond Hydrogenation reaction. *: Unsaturated Alkyl Chain; R', R'' and R''': Saturated Alkyl Chain that may be identical or differ from one another.*

At this stage, the saturated TG is decomposed through four possible mechanisms: (i) β-elimination (reaction 6 of Scheme 4); (ii) hydrolysis (reaction 7 of Scheme 4); (iii) γ-hydrogen transfer (reaction 8 of Scheme 4); and (iv) direct DO (reaction 9 of Scheme 4) [115]. The Scheme 4 reports the overall possible reaction mechanisms.



Scheme 4 Possible mechanism for breaking of saturated TG: (i) β-elimination; (ii) Hydrolysis; (iii) γ-hydrogen transfer; and (iv) direct DO. Adapted from [115].

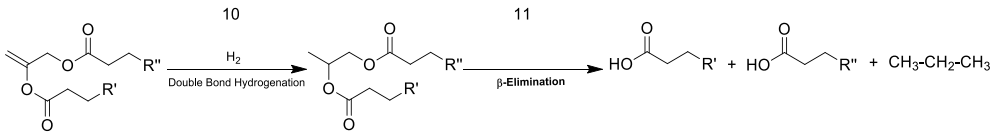
Reports on γ-hydrogen transfer (reaction 8 of Scheme 4) and direct DO (reaction 9 of Scheme 4) reaction mechanisms under typical DO conditions are very limited [116]. To produce n-alkanes with low H_2 consumption, the γ-hydrogen transfer mechanism appears promising. However, it is anticipated to be more prevalent in hydrocracking processes than in DO, as it occurs at higher temperatures [116].

Direct DO (reaction 9 of Scheme 4) is the reaction that converts TGs directly into n-alkanes and glycerol, without FFA as intermediates in the mixture [115-117]. The resulting n-alkanes are produced through direct HDO or direct DCO/DCO_2. The exact mechanisms of direct HDO, DCO, and DCO_2 are not yet well understood due to the absence of observable reaction intermediates and lack of quantifiable evidence supporting these as primary pathways [115-117].

In the case of hydrolysis (reaction 7 of Scheme 4), the TG is hydrolyzed, resulting in the release of three FFAs and one mole of glycerol [115]. This reaction mechanism is observed in hydrothermal reactions and with ester feedstock [115]. However, it has never been observed in reactions using vegetable oils because they lack H_2O [118].

For typical DO processes, β-elimination (reaction 6 of Scheme 4) remains the most predominant reaction mechanism reported for the breakdown of TGs during catalytic DO.

The β-elimination mechanism involves the removal of one fatty acid unit and the formation of an unsaturated diglyceride (see reaction 6 of Scheme 4) [119]. Subsequently, the unsaturated diglyceride may undergo double bond saturation (reaction 10 of Scheme 5) and another β-elimination (reaction 11 of Scheme 5), producing an additional fatty acid molecule [119]. A further step of hydrogenation and β-elimination leads to the formation of the final fatty acid unit and propane as a by-product, as in Scheme 5.

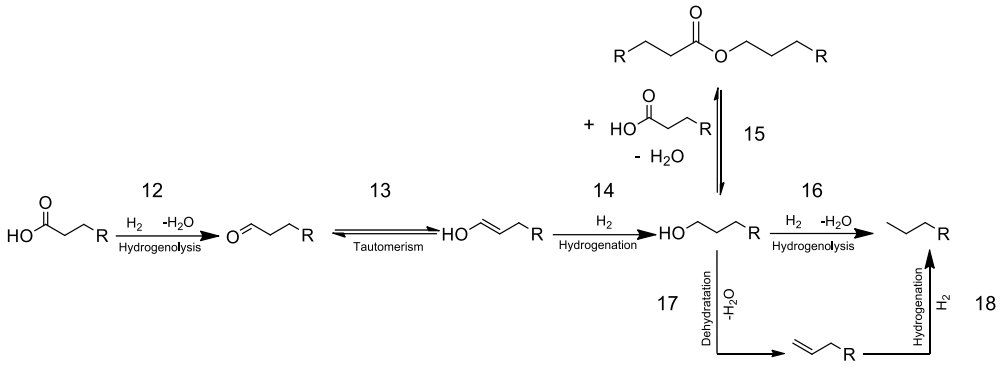


Scheme 5 Diglyceride double bond hydrogenation and β-Elimination.

1.5.1.2 HDO, DCO AND DCO_2 PATHWAYS

The FFAs produced can subsequently follow the three reaction mechanisms outlined in Section 1.4.2 (reaction 3, 4 and 5 of Scheme 2). Scheme 6 and Scheme 7 detail the reaction mechanisms of HDO, DCO and DCO_2 leading to the formation of n-alkanes, as mentioned in the overall reaction mechanisms in Scheme 2.

Scheme 6 presents the comprehensive reaction mechanism for HDO.



Scheme 6 HDO reaction mechanism. Adapted from [115].

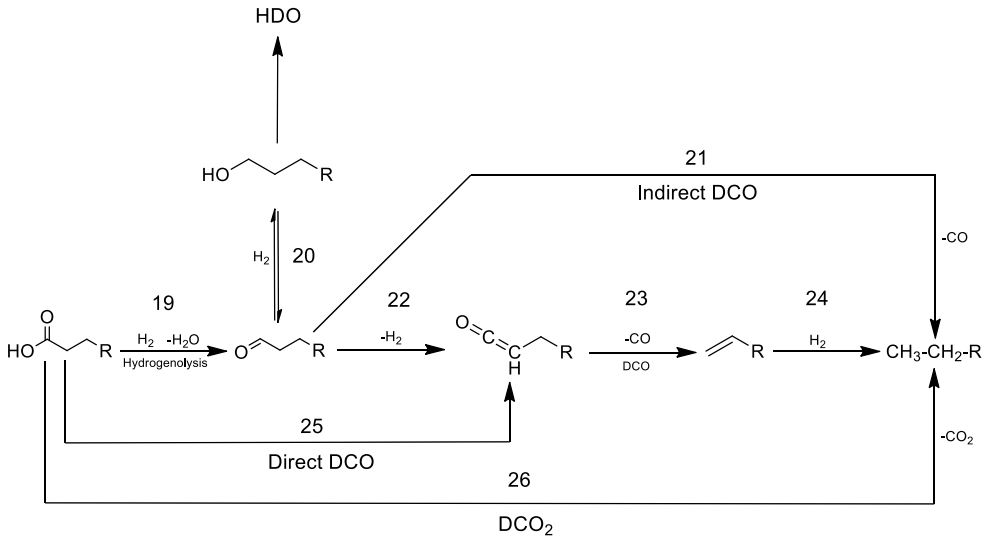
After β-elimination, FFAs undergo a hydrogenolysis reaction (reaction 12 of Scheme 6), where a C-C or C-heteroatom bond is broken by H_2, resulting in the formation of an aldehyde [120, 121]. This aldehyde is in equilibrium with its tautomer (reaction 13 of Scheme 6), which can be hydrogenated to produce a fatty alcohol (reaction 14 of Scheme 6). The fatty alcohol can then either undergo hydrogenolysis (reaction 16 of Scheme 6) to directly form a n-alkanes, or it can be dehydrated to form an alkene (reaction 17 of Scheme 6), which is subsequently hydrogenated to yield an n-alkane (reaction 18 of Scheme 6) [120]. Additionally, the alcohol can react with a FFA to form an ester (reaction 15 of Scheme 6), which exists in equilibrium [120, 121]. This ester can be cleaved to regenerate the alcohol (reverse reaction 15 of Scheme 6), which then continues the pathway to form the n-alkane.

The HDO pathway consumes high amount of H_2 and is an overall exothermic reaction [35, 115].

In Scheme 7 is reported the reaction mechanism of direct and indirect DCO and DCO_2.

In DCO, like HDO, the initial reaction step involves hydrogenolysis of the FFA (reaction 19 of Scheme 7), producing an aldehyde that is in equilibrium, in the presence of hydrogen, with its corresponding alcohol (reaction 20 of Scheme 7),. If the reaction selectively favors HDO, it proceeds as described in Scheme 6. However, if the reaction is more selective towards DCO_x, the

alcohol plays a secondary role, and the aldehyde undergoes decarbonylation, resulting in the formation of n-alkanes.



Scheme 7 DCO and DCO_2 reaction mechanism. Adapted from [115, 116].

Scheme 7 illustrates three proposed mechanisms for the formation of n-alkanes from FFA via DCO [115, 116].

The first mechanism involves the conversion of an FFA into an aldehyde through hydrogenolysis (reaction 19 of Scheme 7). This aldehyde then transforms into a ketene (reaction 22 of Scheme 7), which undergoes DCO to produce an alkene (reaction 23 of Scheme 7). Finally, the alkene is hydrogenated to form an alkane (reaction 24 of Scheme 7), resulting in a n-alkane with one less carbon atom than the original FFA.

The second mechanism is direct DCO (reaction 25 of Scheme 7), where the FFA bypasses the formation of an aldehyde, unlike in the previous mechanism. Instead, it is directly converted into the corresponding ketene through dehydration reaction (reaction 25 of Scheme 7). From the ketene stage onward, the mechanism proceeds as described earlier.

The final proposed mechanism is indirect DCO (reaction 21 of Scheme 7). In this mechanism, the FFA is first converted into an aldehyde through hydrogenolysis (reaction 19 of Scheme 7), that is then transformed into a n-alkane through decarbonylation (reaction 21 of Scheme 7).

Finally, the DCO_2 reaction pathway involves the cleavage of the C-C bond and the release of CO_2, to form n-alkanes (as indicated in reaction 26 of Scheme 7) [115].

DCO consumes less H_2 than HDO, while DCO_2 does not actually consume H_2 [115]. DCO and DCO_2 are overall endothermic reactions, whereas HDO is exothermic [35]. In terms of H_2 consumption, HDO is less desirable than DCO and DCO_2 because it requires more H_2, accounting for both saturation and TG cleavage. The DCO and DCO_2, compared to HDO, can be conducted at a lower H_2 partial pressure or even in an inert atmosphere, which can improve the overall yield of the process [122]. In contrast, HDO is preferable in terms of atom economy (AE) because it produces only H_2O as a by-product (see Scheme 6), whereas DCO_2 and DCO result in carbon loss through the production of CO_2 and CO (see Scheme 7), leading to lower AE [123]. Additionally, CO_2 and CO emissions can negatively impact catalyst activity and contribute to GHGEs, which is a significant drawback considering the environmental objectives outlined in previously sections [123].

1.5.1.3 Side reactions in liquid phase

In the catalytic DO process for green diesel production, various side reactions can impact both the efficiency and yield of the target product. These side reactions, which may take place in either the liquid or gas phase, often result in the generation of by-products.

One potential side reaction in liquid phase is hydroisomerization, in which n-alkanes are transformed into branched alkanes [35, 59]. Further details about hydroisomerization reaction mechanism are described in detail elsewhere [124-126]. Hydroisomerization has become essential reaction for producing high-quality biofuels because the presence of branched alkanes enhances the biofuel cold properties, thermal stability, and viscosity [127]. In general, hydroisomerization reactions depend on bifunctional catalysts that possess both hydrogenation-dehydrogenation and acid functions [127-129]. It is widely recognized that acid sites are effective in this process only when they are in their Brønsted form, rather than their Lewis form [127]. For this reaction to occur, the catalyst must possess specific compositional and

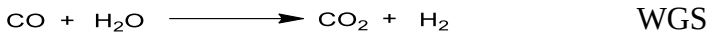
structural characteristics, including: (i) a suitable balance between metal and acid sites; (ii) medium pore size; (iii) high metal dispersion on the catalyst surface; (iv) mild acidity; and (v) a well-distributed presence of acid sites [130]. Catalysts with medium pore sizes and low acidity, especially those loaded with noble metals, are particularly effective in the hydroisomerization of long-chain normal paraffins [130, 131].

Another possible side reaction that occurs in the liquid phase, and often alongside hydroisomerization, is hydrocracking. Hydrocracking is a reaction that converts long-chain HCs into shorter once, in the presence of H_2 and a suitable catalyst [132]. Compared to thermal cracking, hydrocracking operates at relatively lower temperatures [132]. This reaction is often undesirable for producing green diesel fuel (C_{15} to C_{18} n-alkanes) because it breaks down n-alkanes into shorter alkanes; however, it can be useful for producing bio-gasoline and bio-jet fuel [133].

A highly undesirable reaction is the oligomerization of fatty acids, which leads to the formation of heavy products that can readily transform into coke, causing catalyst deactivation [134, 135]. Using high temperatures can cause oligomerization, which decreases the yield of diesel range n-alkanes [136].

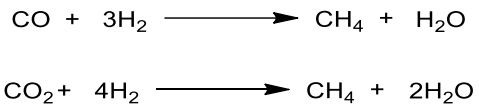
1.5.2 GAS PHASE REACTIONS

Gas-phase reactions may occur from the by-products generated by the HDO (i.e., H_2O, see Scheme 6), DCO, and DCO_2 reactions (i.e., CO and CO_2 respectively, see Scheme 7), and in presence of H_2. These gas-phase reactions include: (i) water gas shift (WGS, Scheme 8), (ii) methanation (Scheme 9), and (iii) Boudouard reaction (Scheme 10). These reactions can lead to several undesirable effects, including (i) the consumption of additional H_2, (ii) the production of other gaseous by-products like CH_4, CO, and CO_2, (iii) catalyst deactivation, and (iv) coke deposition or catalyst agglomeration [35].
The WGS reaction (Scheme 8) can reduce the concentration of CO in a gas mixture by reacting it with H_2O, resulting in the formation of CO_2 (a GHG) and H_2 [137].



Scheme 8 WGS reaction.

The methanation reactions (Scheme 9) occur when CO and/or CO_2 react with H_2, producing CH_4 and H_2O.



Scheme 9 Methanation reactions.

In addition to the previously secondary reactions, any carbon deposited on the catalyst surface (e.g., from coking) can react with CO_2 to produce CO via the Boudouard reaction.



Scheme 10 Boudouard reaction.

The Boudouard reaction is undesirable because it produces CO, a GHG, a reactant in methanation, and a potential cause of catalyst deactivation due to poisoning from irreversible CO adsorption [138].
The WGS, methanation, and reverse Boudouard reactions are all exothermic and become more favorable as the temperature decreases [35].

1.6 FACTORS INFLUENCING THE CATALYTIC DO PROCESS

The catalytic DO process is intricate and multifaceted, as discussed in the previous Section 1.5. Several factors can influence the production of green diesel, including the type of catalyst, feedstock, temperature, pressure, reactor type, and various other process parameters (i.e., reaction time, type of solvent, quantity of catalyst, H_2/feed ratio, and liquid hourly space velocity).

This section provides an overview of the factors that affect the production of green diesel through the catalytic DO process.

1.6.1 FEEDSTOCK FOR DO

Vegetable oils and animal fats are among the most utilized feedstocks for producing green diesel. Fats and oils are primarily water-insoluble, hydrophobic substances found in both plants and animals [139]. They consist mainly of TGs, which are glycerol esters of mono- or polyunsaturated fatty acids with alkyl chains typically ranging from C_{14} to C_{18} [59]. They also contain smaller amounts of fatty acids with up to 24 carbon atoms [35, 59]. Since DO can produce n-alkanes with the same number or one fewer carbon atom than the original fatty acid composition (refer to Section 1.5.1), selecting feedstocks primarily composed of fatty acids with more than 15 carbon atoms ensures that the resulting n-alkanes will fall within the diesel range (i.e., C_{15}-C_{18} alkanes). The composition and types of fatty acids vary depending on the specific raw material. The selection of raw materials is influenced by local cropping patterns. Choosing the appropriate raw materials can help lower transportation, storage, and procurement costs.

Feedstocks can be evaluated according to their availability and source type, whether edible, non-edible, or waste [140]. Table 4 presents the typical feedstocks used for green diesel production. Due to competition between the fuel sector and the food industry, it is advisable to use inedible oils and waste fatty materials as feedstocks for the DO process, instead of edible oils [35].

In the U.S., soybean oil is a promising feedstock due to its higher production rate, while in Europe, rapeseed oil, palm oil, and sunflower oil are the predominant sources for green diesel production [141]. The types and distribution of fatty acids in biomass are influenced by the nature of the originating feedstock. Moreover, the distribution of fatty acids in each type of feedstock can be affected by the specific crop variety, environmental conditions, harvesting practices, and processing methods [59]. Table 5 shows the fatty acid composition of various feedstocks commonly used in green diesel production.

Table 4 Feedstock typically used for catalytic DO: data taken from [35, 59, 140, 142].

Type of feedstock	***Name***
Edible	Sunflower Oil
	Palm Oil
	Soybean Oil
	Rapeseed Oil
	Peanut Oil
	Olive Oil
	Canola Oil
	Coconut Oil
	Corn Oil
	Mustard Oil
Non-Edible	Jatropha Oil
	Stillingia Oil
	Karanja Oil
	Neem Oil
	Castor Oil
	Linseed Oil
	Rubber Seed Oil
	Algae Oil
	Microalgae Oil
	Jojoba Oil
Waste	Waste Oil (WO)
	WCO
	Animal and Fish Fats
	Cashew Nutshell Liquid

For the DO process, it is preferred to use vegetable oils that are as saturated as possible. This preference is because saturated oils reduce H_2 consumption, allow the reaction to occur under milder conditions, and decrease the likelihood of undesirable reactions such as cracking, cyclization, and polymerization [59]. These undesirable reactions collectively lead to catalyst deactivation, decreased DO activity, and reduced diesel selectivity [143].

Using waste as feedstock for green diesel production is preferred because it not only repurposes waste into a source of RE but also reduces the environmental impact associated with waste disposal. For instance, WCO is

classified as hazardous waste, and improper disposal can lead to environmental pollution and the loss of valuable energy resources [144]. Converting WCO into green diesel is both an economical and environmentally friendly solution, offering a sustainable approach to managing and utilizing this waste [144].

Table 5 Fatty acid composition of some edible and non-edible biomasses. Data adapted from [59, 113, 145-148]. $C_{n:m}$: n is the number of carbon atoms and m is the number of double bonds in the fatty acid.

	Fatty Acid Composition (% wt.)									
	$C_{14:0}$	$C_{16:0}$	$C_{16:1}$	$C_{18:0}$	$C_{18:1}$	$C_{18:2}$	$C_{18:3}$	$C_{20:0}$	$C_{20:1}$	$C_{22:1}$
Chicken fat	0.2	25.5	0.1	11.9	36.5	6.2	0.2	0.0	0.2	0.0
Salmon fat	3.0	11.0	5.0	4.0	25.0	5.0	5.0	0.0	0.0	0.0
Jatropha oil	0.0	15.9	0.9	6.9	41.1	34.7	0.3	0.0	0.2	0.0
Karanja oil	0.0	9.8	0.0	6.2	72.2	11.8	0.0	0.0	0.0	0.0
Microalgae oil	0.6	27.8	0.0	0.9	28.2	9.3	23.9	0.0	0.0	0.0
Palm oil	2.5	40.8	0.0	3.6	45.2	7.9	0.0	0.0	0.0	0.0
Canola oil	0.1	4.3	0.3	2.4	64.4	17.4	9.6	0.8	0.0	0.5
Rapeseed oil	0.0	4.9	0.0	1.6	33.0	20.4	7.9	0.0	9.3	23.0
Rubber Seed oil	0.0	10.2	0.0	8.7	24.6	39.6	16.3	0.0	0.0	0.0
Soybean oil	0.0	11.5	0.0	4.0	24.5	53.0	7.0	0.0	0.0	0.0
Sunflower oil	0.0	6.5	0.2	5.8	27.0	60.0	0.2	0.3	0.0	0.0

The selection of raw material for the DO process is often influenced by its cost. Table 6 presents the prices of some raw materials listed in Table 4.

Table 6 Cost of some raw material for DO process; data taken from [35, 149].

Feedstock	***Cost [$/ton]***
Pork Fat	252
Palm oil	543
Rapeseed oil	456
Sunflower oil	929
Soybean oil	771
WOs	224

As shown in Table 6, the least expensive raw materials, which therefore have the smallest impact on the overall process cost, are waste products (e.g., pork fat and WOs). From a cost perspective, waste materials appear to be the most sustainable option.

1.6.2 INFLUENCE OF TEMPERATURE AND H_2-PRESSURE

DO studies of TGs, fatty acids, and fatty esters are typically conducted at temperatures ranging from 250 to 350°C [143]. The reaction temperature significantly influences the products; if the temperature is too high, hydrocracking reactions can occur, resulting in the formation of various alkanes in the lower diesel range [35]. Additionally, as the reaction temperature rises above 350°C, the endothermic DCO and DCO_2 reactions become thermodynamically favored over the exothermic HDO reaction (as described in Section 1.5.1.2), leading to different distributions of products [150]. On the other hand, lower temperatures favor HDO (as underlined in 1.5.1.2) but also promote methanation reactions, WGS, and the reverse Boudouard reaction, which are considered undesirable [35]. Several studies have demonstrated that raising the temperature increases DO yield, but at temperatures above 350°C, thermal cracking and hydrocracking reactions are favored (as discussed in Section 1.5.1.3) [151-154]. Moreover, the reaction temperature is crucial for achieving optimal catalyst activation and reducing the risk of catalyst sintering [155]. Excessively high temperatures can break down and alter the primary structure of catalysts, diminishing their effectiveness [155].

Regarding partial pressure of H_2, typical values range from 20 to 50 bars [59, 156]. Fluctuations in H_2 pressure significantly impact the contributions of both primary and secondary reactions [35]. High H_2 partial pressures favor HDO over DCO and DCO_2 [157], net of reactions leading to FFA formation (see Sections 1.5.1.1 and 1.5.1.2). In addition, high H_2 pressures tend to promote the methanation reactions and reverse WGS [157]. High pressure can also inhibits isomerization because the increased amount of H_2 adsorbed on the catalyst sites competes with the sites needed for isomerization [59]. On the other hand, an excess of H_2 can impair catalytic activity due to competitive adsorption between FFA and H_2 [143]. Atmospheres free of H_2 (e.g., N_2, He, Ar) have also been explored [158-162]. However, lacking H_2 in the DO process results in lower n-alkanes conversion rates [143]. To address the

drawbacks associated with excessive or absent H_2, diluting H_2 with inert gases (such as H_2-Ar, H_2-N_2, or H_2-He) has been considered [163-165].

1.6.3 EFFECTS OF OTHER PARAMETERS

The reaction time (i.e., batch process duration) is a critical factor in green diesel production, with optimal durations typically ranging from 3 to 6 hours [35]. An increase in reaction time leads to lighter products due to the occurrence of cracking reactions [166].

The presence of solvent significantly impacts reaction performance. Studies [167, 168] have shown that DO reactions conducted without a solvent did not yield alkanes. This lack of alkane formation may be attributed to the formation of macromolecules through coupling reactions between intermediates on the catalyst surface. Using organic solvents is advantageous for conducting DO experiments of fatty acids and related compounds, as it enhances DO activity. Solvents such as n-decane, n-dodecane, n-hexane and mesitylene, each with varying DO activities, are employed [143, 169]. For example, supercritical hexane enhances diffusivity, reducing mass transfer resistance by improving the contact between H_2, reactants, and the catalyst [143, 167, 169]. Additionally, it promotes the desorption of alkanes from catalyst surfaces due to its high solubility, which helps prevent coupling reactions between alkyl intermediates on active sites that could lead to macromolecule formation [143, 167, 169]. The variation in DO activities among solvents is not related to their chemical nature but rather to their boiling points and viscosities; solvents with lower boiling points generally exhibit better activity [170, 171]. On the other hand, excessive use of solvent in the DO process can slow down the reaction rate due to the occurrence of volume expansion reactions [143]. Indeed, one key operating parameter frequently adjusted to optimize process yield is the solvent-to-feed (oil or TG-biomass) ratio.

The quantity of catalysts employed for DO plays a crucial role in affecting both the reaction rate and the selectivity of the desired products. Studies have demonstrated that the reaction rate and conversion increase proportionally

with the catalyst amount, particularly within the 1-5%$_{w/w}$ range relative to the feedstock quantity [35, 169]. Using small amounts of catalyst can trigger polymerization, leading to a higher production of aromatics and other unwanted by-products [143].

The hydrogen-to-oil ratio (H_2/feed ratio) refers to the proportion of hydrogen to liquid feed introduced into the reactor and plays a significant role in determining the efficiency of HDO, DCO, and cracking reactions. Typical values of this ratio range from 0.01 to 20 Nm^3/m^3 [35, 172]. Raising this ratio generally reduces the conversion and selectivity for green diesel production, as it encourages cracking and hydrogenation reactions [173].

In continuous reactors, the liquid hourly space velocity (LHSV) is a key process variable, defined as the ratio of the liquid feed volumetric flow rate (in Nm^3/h) to the volume of catalyst in the reactor [174]. Typical values of LHSV range from 0.25 to 5 h^{-1} [35]. This parameter is crucial for regulating the catalyst effectiveness and lifespan by determining how long the feedstock remains in the reactor. Typically, increasing LHSV enhances the selectivity for green diesel, as it shortens retention time, boosts sulfur and nitrogen removal and increases oxygen removal capacity [173].

1.6.4 REACTOR TYPE

Batch and semi-batch reactors are commonly employed for small-scale processes, such as laboratory experiments, pilot studies, and small-scale industrial production, as well as for testing processes in development. These reactors can achieve high conversion rates when sufficient time is allowed for contact between the reactants and catalysts [175]. The semi-batch reactor enables the addition of reagents and/or the removal of products and by-products during the reaction, offering greater flexibility in process control and optimization of yields [176]. Mini-batch reactors are frequently used for studying reaction mechanisms, analyzing conversion kinetics, and screening catalysts [177]. The primary advantage of mini-batch reactors is their ability to handle extremely small volumes, typically just a few milliliters, which significantly reduces the amount of reactants required for experiments.

However, these reactors lack internal stirring, which limits mass transfer, and the small volumes involved make it difficult to obtain sufficient spent catalyst for characterization and reusability assessments [177].

In contrast, continuous reactors are typically employed for large-scale industrial production, where they develop a product with a consistent composition throughout the operation. A key difference between continuous and batch reactors is the handling of H_2. In batch reactors, H_2 is consumed during the reaction, leading to a decrease in H_2 fraction within the reactor [175]. This reduction often results in lower conversion rates and yields [178, 179]. As a result, the reduction in H_2 content in a batch reactor lowers the H_2/oil ratio, which increases the likelihood of DCO_2 pathways and cracking reactions [180, 181]. Thus, continuous reactors can achieve the same green diesel conversion results as batch reactors, but with lower H_2 pressure, because the H_2 partial pressure is continuously regulated and maintained through a steady flux [35]. The most commonly used continuous reactors for green diesel production include tubular reactors, fixed-bed reactors, trickle-bed reactors, and continuous stirred tank reactors (CSTR) [177]. The CSTR is the most widely used in industry, primarily due to its ease of operation and lower operating costs [35]. Continuous tubular reactors offer several advantages, including a relatively stable flow pattern, a large heat transfer area, and uniform space-time for all materials [177]. The use of continuous and semi-batch reactors offers the advantage of removing CO_x produced during the reaction [182, 183]. This approach provides dual benefits: it shifts the reaction equilibrium towards product formation and prevents catalyst poisoning caused by CO adsorption [182, 183]. However, in flow-through reactors, collecting catalysts can be difficult, and the extent of catalyst deactivation may vary across different positions [177]. Moreover, the lack of mixing restricts mass and heat transfer within the reactor [177]. For instance, compared to tubular reactors, CSTR can enhance mass transfer rates through active stirring [35, 177]. However, they typically have a smaller heat exchange area and exhibit variable space-time for different materials [35, 177]. To address mass transfer issues in reactors without stirring, baffles can be installed to create a stirring effect [177]. Fixed-bed and trickle-bed reactors

offer the key advantage of achieving a more uniform distribution of raw materials within the reactor, thereby maximizing the reaction rate per unit volume [35].

The selection of reactor types significantly impacts process control, reaction rate, residence time or batch duration, heat transfer rate, selectivity, and product yield.

1.6.5 IMPACT OF MASS TRANSFER

When considering mass transfer resistances, three key factors should be addressed: (i) at the gas-liquid interface, (ii) at the liquid-solid interface, and (iii) intraparticle diffusion [184]. These resistances are influenced by changes in hydrodynamic parameters, such as film thickness and velocity field distribution [184]. Typically, gas-liquid-solid mass transfer coefficients are estimated using either the series resistance model or the film model [184]. The mass transfer of TG molecules within the pore structure of the catalyst is a critical factor, particularly when designing and selecting catalysts.

Hachemi et al. [185] conducted a study to assess how process parameters affect mass transfer during the HDO of stearic acid using Ni-based catalysts. They investigated two types of catalysts: sulfur-free Ni-based catalysts supported by H-Y zeolites, γ-Al_2O_3, and SiO_2, and palladium supported on activated carbon. The experiments were performed in a semi-batch reactor at 300°C and 30 bars of H_2 for 6 hours, using catalysts with a mean particle radius of 63 μm. A preliminary study was conducted to find the optimal stirring speed (ranging from 100 to 1200 rpm) and catalyst amount (0.1 to 0.4 g). The results indicated that a stirring speed of 1200 rpm and 0.25 g of catalyst provided sufficient liquid/solid phase mixing.

The Weisz-Prater modulus, calculated as the ratio of the reaction rate to the diffusion rate within the pores [186], was used by Hachemi et al. [185] to estimate the influence of pore diffusion. These calculations revealed that significant internal mass transfer effects were not present, depending on the reaction order. Furthermore, at the highest reaction rate achieved (i.e., 5.8×10^{-7} mol L^{-1} s^{-1}) with the Ni/H-Y catalyst, the Weisz-Prater modulus values confirmed that mass transfer limitations of stearic acid and H_2 were minimal,

indicating that intraparticle diffusion did not impact the reaction rate. Finally, Hachemi et al. [185] concluded that for zeolite-supported catalysts, configurational diffusion must be considered, as this occurs when the size of the reactant molecules approaches that of the pores. Fatty acids are too large to diffuse through the smallest pores, while molecular diffusion occurs in larger channels and on the outer surface of the catalyst. They [185] concluded that their experimental data were obtained within the kinetic regime.

Zhou et al. [187] conducted a kinetic study on the DO of microalgae oil using a Pt-γAl_2O_3 catalyst to assess mass transfer limitations. The experiments were performed in a packed bed microreactor with 1% feedstock in dodecane at 360°C and 35.5 bars of H_2, with a residence time of 0.06 s and a H_2/feed ratio of 1000 SmL/mL. The catalyst particle size ranged from 75-150 μm, and data were collected in the Taylor flow regime (this regime occurs in laminar flows, where the fluid moves in parallel layers without turbulence), comprising alternate liquid slugs and gas bubbles. By varying gas and liquid flow rates and catalyst amounts, they determined that the space-time consumption of the feed was independent of surface flow velocity, indicating no external mass transfer limitations, even at lower flow velocities (0.49 m/s). The Weisz-Prater parameter confirmed that the reaction rate was lower than the diffusion rate, showing that internal mass transfer did not control the reaction. Additionally, they [187] found that in the gas-liquid reaction, H_2 adsorbed onto the catalyst surface without dissociating, differing from typical gas-phase reactions where dissociative adsorption of H_2 occurs.

Arora et al. [188] conducted a kinetic study on the HDO of stearic acid using a NiMoS catalyst in a stirred-batch reactor at 50 bars of H_2, temperatures ranging from 275-325°C, and stirring rates of 1000 rpm. The experiments used 5% stearic acid in a 150 mL reaction volume with 0.4 g of catalyst and varied reaction times from 0 to 200 minutes. Catalyst particles had an average size of 175 μm. The effect of different stirring rates (500, 900, and 1000 rpm) on product distribution was analyzed at 300°C and 50 bars. The results showed no difference between 900 and 1000 rpm, indicating no external mass transfer limitations at these rates. However, at 500 rpm, limitations in H_2

transfer from the gas phase to the liquid and the catalyst surface were observed. Weisz-Prater values were also calculated at different temperatures, peaking at 3.0 for 325°C and 1.8 for 275°C, indicating a moderate influence of intraparticle mass transfer resistance on the reaction rate. For different feedstocks (e.g., $C_{18:1}$), both liquid-solid film and intraparticle diffusion had a stronger effect on mass transfer resistance. Additionally, at higher temperatures (325°C) and stirring rates (1000 rpm), the reaction favored DCO over HDO due to the limitations in H_2 transfer.

In conclusion, evaluations on mass transfer are needed for enhancing reaction efficiency and achieving selective production of desired products. The studies reviewed highlight the significant influence of operating conditions, such as stirring speed and temperature, along with catalyst design, in overcoming mass transfer limitations, particularly in complex reactions like HDO. Effectively managing mass transfer resistances, especially in gas-liquid-solid systems, can lead to higher yields, minimize undesired side reactions, and promote the desired reaction pathway.

1.6.6 CATALYST CHOICE

DO is an energy-intensive process, so employing catalysts is advantageous according to Green Chemistry principles (see Section 1.2), as it helps lower the energy requirements and reaction conditions can be milder. The development of catalysts with good chemical stability, high selectivity for alkanes in the diesel range, and high activity is crucial for the effectiveness of DO reactions. Typically, heterogeneous catalysts are employed in the green diesel production process via DO due to their ease of recovery and separation at the end of the process. Solid catalysts used in the DO process generally comprise an active phase and a catalytic support (see Table 7) [35]. Additionally, catalysts can be found as (i) monometallic, (ii) bimetallic and (iii) trimetallic, in supported or unsupported forms. The selection and combination of these components can significantly impact product distribution and feedstock conversion. Catalytic properties are largely determined by the choice of support and active phase, as well as the chemical interactions between the catalyst, reactants, and products [189]. Additionally,

factors such as regenerability, regeneration cost, and toxicity must also be considered when selecting a catalyst [189].

Table 7 Summary of principal supports, and active metals typically used for DO in the production of green diesel.

Catalysts			
Active phases		***Supports***	
Type	*References*	*Type*	*References*
Non-noble metals *(Ni, Mo, Zn, W, Co)*	[190-204]	Metal oxides *(Al_2O_3, TiO_2, ZrO_2)*	[159, 171, 181, 187, 190, 191, 193, 198, 200, 205-216]
Noble metals *(Pd, Pt, Rh, Ru, Os)*	[206, 211, 212, 214, 215, 217-225]	Carbon (A*ctive carbon, etc.)*	[226-230]
		Zeolites *(NaY, Beta, etc.)*	[129, 131, 133, 161, 181, 214, 225, 231-239]
		Mesoporous materials	[152, 233, 240, 241]
		Metal mixed oxides	[179, 190, 221, 242-244]

1.6.6.1 CATALYSTS ACTIVE PHASES

Metals typically form the active component of DO solid catalysts, which are generally classified into two categories: (i) noble metals and (ii) non-noble metals (see Table 7). Noble metals include Pt, Pd, Rh, Os, Ru, Ir, and Re, while non-noble metals typically used in DO catalysts are Ni, Mo, Cu, Co, Zn, V, and W.

Noble metals and vulcanized molybdenum are commonly used as active catalytic phases for producing green diesel [245]. However, their application is limited by the high cost of noble metals and environmental issues associated with sulfur compounds in vulcanized molybdenum [245]. Additionally, Pt/Pd-based catalysts demonstrate superior selectivity for DCO and DCO_2, and they consume less H_2 compared to those that use non-noble metals [216]. Meanwhile, Ru-based catalysts exhibit outstanding catalytic activity for HDO [246]. Although noble-metal-based catalysts exhibit excellent DO performance and high selectivity for diesel HCs, their industrial application potential is limited by their low abundance, high production costs,

and the susceptibility of certain types, like Pd-based catalysts, to rapid deactivation and poisoning [247].

For these reasons, significant advancements have been made in recent years in the development of sulfur free non-noble-metal-based catalysts (see Table 7). Among them, Ni-based catalysts have garnered significant interest primarily because of their low cost, lack of need for sulfur treatments, and relatively low reduction temperature of Ni oxides [248]. Despite the numerous advantages of Ni-based catalysts, their catalytic performance can be hindered by poor metal dispersion and agglomeration, leading to a reduced number of active sites [248, 249]. To address these issues, the performance of Ni-based catalysts for green diesel production can be enhanced by incorporating other metals, including Cu, Sn, Mo, and Zn [245]. For example, the addition of Cu improves the dispersion of Ni sites and increases Ni's electron density, boosting catalytic activity [245]. This results in a more effective Ni-Cu bimetallic catalyst, which lowers the binding energy of H_2 on Ni, promoting hydrogen dissociation and enhancing hydrogenation performance [208, 250]. Moreover, the addition of W enhances the physicochemical properties of the catalysts by increasing the specific surface area, improving Ni dispersion, and adjusting the catalyst's acidity [35].

Bimetallic catalysts based on MoS_2 are also employed, including $CoMoS_2$ and $NiMoS_2$ [35]. These catalysts exhibit high activity for the DO of TGs and model compounds but face high costs and serious challenges in terms of equipment, safety, and industrial scalability [251]. In fact, sulfide catalysts are prone to corrosion due to sulfidation, which transforms oxides into sulfides at the catalyst's active sites [176].

Sulfonated acid catalysts are also employed for the DO of FFAs and TGs. Although these catalysts are effective, they have a high propensity to generate HC components and contaminate the resulting green diesel with substantial sulfur content, which negatively impacts fuel quality [213]. An additional drawback of these catalysts is their loss of catalytic activity due to sulfur leaching [35].

Recent research has highlighted metal nitrides as promising candidates for green diesel production. Their metal-like properties arise from the electronegativity difference between metal and nitrogen atoms, which can create acid or base centers and redox centers for catalytic reactions [252, 253]. Supported early transition metal nitrides (such as Mo, W, and V nitrides on γ-Al_2O_3) and carbides (like NiMo and NiW carbides) have demonstrated DO activity comparable to noble metals [253]. These nitrides and carbides offer a potential alternative to traditional sulfide-based catalysts, which suffer from issues like sulfur leaching and high sulfur content in the final product [253].

1.6.6.2 CATALYSTS' SUPPORTS

The nature and textural properties of the catalysts support, including specific surface area, pore volume, pore diameter, and crystallite domain size, play a crucial role in determining the catalyst's properties and impacting the DO process. Effective catalytic support can significantly enhance DO reactions by improving the dispersion of active metal particles and increasing the number of available active sites [230]. For instance, the pores of the support must be large enough to allow TG molecules to reach the active metals and enable sufficient movement within the pores [254]. Since the reactions occur on the catalyst surface, a large surface area is essential [254]. The support could also facilitate the uniform distribution of the metal across this large surface area.

Catalytic supports are divided into five categories (see Table 7): (i) metal oxides, (ii) carbon-based supports, (iii) zeolites, (iv) mesoporous supports, and (v) mixed metal oxides. Commonly used DO catalyst supports include: Al_2O_3, ZnO-Al_2O_3, SiO_2, ZrO_2, zeolites, and carbon-based materials. Acidic supports, including metal oxides, zeolites, and Al-doped mesoporous silica, provide protic (Brønsted) and aprotic (Lewis) acid sites during the HDO process, which enhance the hydrogenolysis activity of the C-O bond [177]. However, the acid centers in supports can lead to significant coking issues by promoting the formation of condensation products, key precursors to coke [115]. Brønsted acid sites facilitate hydrogenation–dehydration–hydrogenation sequences that favor HDO pathways, while Lewis acid sites

drive indirect DCO reactions [177]. Al_2O_3-supported catalysts exhibit the highest acidity compared to other supports, following the order $Al_2O_3 > TiO_2 > ZrO_2 > CeO_2 > SiO_2$ [255]. However, the high acidity of Al_2O_3 leads to issues such as coke deposition, instability, and deactivation, reducing its effectiveness in catalytic DO for green diesel production [255]. The use of mixed metal oxides helps mitigate these problems, offering improved catalyst stability and activity, higher surface area, well-defined pores, enhanced reducibility, better metal dispersion, and stronger acid centers compared to pure oxides [255].

Historically, zeolites have been considered effective catalysts for green diesel production due to their high cracking capacity, distinctive porous structure, strong acidity, and excellent intrinsic stability [35]. There are around 40 natural zeolites and more than 150 synthetic zeolites available for DO reactions [137]. Among them, Y-zeolites are particularly significant thanks to their acidity, which is characterized by a high ratio of Brønsted and Lewis acid sites [137].

With regard to carbon-based supports, carbon's inertness in DO catalysis leads to significantly lower coking tendencies and minimize cracking reaction, compared to alumina and silica [256, 257]. Unlike these materials, carbon interacts weakly with the active phase, meaning the catalyst's behavior is mainly governed by the characteristics of the active phase itself [257]. This weak interaction also aids in the reduction of metallic precursors to their active forms and supports the formation of metal phases in multi-element catalysts [257]. Additionally, activated carbon, especially when derived from biomass, is increasingly promising due to its environmental benefits and low production costs [257, 258].

Mesoporous materials are currently favored for their high thermal stability, ease of surface modification, moderate pore size, large surface area, and inert characteristics [189]. Mesoporous silica-based materials like Santa Barbara Amorphous-15 (SBA-15), Santa Barbara Amorphous-16 (SBA-16), and Mobil Composition of Matter No. 41 (MCM-41) have become popular due to their moderate acidity, high specific surface area, and large pore diameters

[247]. These properties are crucial for processing the large and complex molecules present in TGs. These three materials provide a high specific surface area (between 600 and 1000 m^2/g), and feature a uniform pore size distribution (between 1.5 and 10 nm) [141].

In summary, selecting the appropriate catalytic support affects both the reaction pathway and the catalyst's selectivity. Specifically, it can alter the dispersion of active species, enhance interactions between the active phase and the support, and modify the distribution of acid sites regarding their strength and density.

1.7 AIM AND STRUCTURE OF THIS WORK

The present PhD thesis focuses on renewable energy, specifically on developing, characterizing, and testing new catalysts for the catalytic DO of vegetable oils to synthesize green diesel.

More in detail, three catalysts for DO of TGs were synthesized:

- two of these were sourced from the literature [259]. This part of the PhD thesis aims to repurpose Velasquez et al.'s catalysts, replicating their synthesis and unprecedently testing them for green diesel production through the DO process.

  Repurposing catalysts from other reaction pathways is intriguing. Velasquez et al. [259] developed two unsupported trimetallic catalysts, NiCoMo and ZnCoMo, for propane oxidative-dehydrogenation (ODH), an oxidation process, whereas DO is a reduction process [35]. Additionally, DO operates as a gas-liquid-solid reaction [35, 59], while ODH is a gas-solid process [259]. In addition, DO is scalable to industrial levels [35, 59], while ODH faces commercialization challenges due to high carbon oxide emissions [259]. Adapting these catalysts from ODH to DO presents significant challenges but opens up promising industrial possibility
- The third catalyst was developed based on a Green Chemistry concept proposed by two research groups at the University of L'Aquila: Prof. Katia Gallucci's group from the "Industrial Chemistry: Catalysis and

Green Engineering" laboratory (DIIIE), and Prof. Leucio Rossi's group from the "Green Chemistry" laboratory within the Department of Physical and Chemical Sciences. In fact, this catalyst is the subject of an Italian patent application filed on 08th November 2023, titled "*Catalizzatore solido a base di ossidi di nichel, molibdeno e alluminio, per la deossigenazione catalitica eterogenea di trigliceridi di origine biologica finalizzata alla produzione di idrocarburi, e relativo metodo di sintesi privo di solventi*" (Patent Application No. 102023000023556) [260]. The main goal of this original synthesis method was to simplify the catalyst production in the light of Green Chemistry and Green Engineering principles, eliminating solvents and lowering the number of synthesis steps.

Overall, the purpose of the study of these three catalysts is to demonstrate that it is possible to achieve good efficiency in the production of green diesel from vegetable oils using catalysts synthesized by faster and cheaper methods than conventional ones (as those listed in Section 1.6.6).

The details of the work done are described in the rest of this PhD thesis, as follows:

- **Chapter 2**: provides a comprehensive description of the experimental procedures employed for the synthesis and characterization of the catalysts used in the DO tests. It also covers the analytical techniques utilized for the characterization of the raw materials (i.e., rapeseed oil and WCO). Detailed information is presented on the equipment and methods used for conducting the DO tests, including the Design of Experiments (DoE) plans and the protocols followed for catalyst recycling tests. Furthermore, the chapter outlines the equipment and techniques applied for the characterization of reaction products and subsequent data analysis.
- **Chapter 3**: presents the characterization results for the NiCoMo, ZnCoMo, and Ni-Mo-Al catalysts. The successful synthesis of NiCoMo and ZnCoMo is verified and compared with the work of

Velasquez et al. [259]. Additionally, a full characterization is provided for the Ni-Mo-Al catalyst.

- **Chapter 4**: this chapter details the chemical characterization of rapeseed oil, WCO and sunflower oil (i.e., the fresh oil from which WCO is derived), which were utilized as feedstocks for the DO tests.
- **Chapter 5**: presents the results of DO tests conducted with the catalysts studied (i.e., NiCoMo, ZnCoMo and Ni-Mo-Al), providing a comprehensive analysis of their catalytic performance. The findings from experiments of 2^3 factorial design, as well as recycling tests, are discussed, highlighting the impact of various operating parameters on the final products. Additionally, the chapter includes the results of statistical analysis, focusing on the significance of different parameters on the responses. Furthermore, it covers the outcomes of the face-centered cubic experimental design, aimed at evaluating the influence of reactor stirring speed on DO performance, alongside the corresponding statistical analysis.
- **Chapter 6**: this chapter presents the results of post-test catalyst characterizations, examining whether the catalysts experienced any chemical or physical changes during the DO tests, and if these changes can be linked to a decline in catalyst performance.
- **Chapter 7**: presents the outcomes of preliminary tests conducted during the final part of the doctoral program. Specifically, it details the findings on the impact of stirring speed on DO performance for NiCoMo catalyst, as well as the results of preliminary DO tests carried out using WCO as feedstock.
- **Chapter 8**: provides a summary of the main results of this PhD thesis, highlighting both the successes and limitations of the study. Finally, it suggests possible future directions for the research.

2. MATERIALS AND METHODS

2.1 CATALYSTS SYNTHESIS

This section describes the synthesis methods employed for the three catalysts investigated in this PhD thesis. Two of these catalysts, NiCoMo and ZnCoMo, were adapted from the work of Velasquez et al. [259] and synthesized via conventional coprecipitation methods. The third catalyst, Ni-Mo-Al, was developed as part of this research through a solventless synthesis process, aligning with Green Chemistry principles (outlined in Section 1.2) and representing a novel approach in catalyst development.

2.1.1 NICOMO AND ZNCOMO CATALYST SYNTHESIS

The two catalysts adapted from the work of Velasquez et al. [259] are unsupported Nickel-Cobalt-Molybdenum (henceforth "NiCoMo") and Zinc-Cobalt-Molybdenum (henceforth "ZnCoMo") catalysts. The two catalysts, were originally thought and employed for the ODH of propane (for further details please refers to the Velasquez et al.'s work [259]), synthesized using the conventional coprecipitation method.

The catalysts were synthesized following the procedure outlined in the literature [259]. Milli-Q water was used for the synthesis of the catalysts. Two solutions were prepared. The first solution was made by dissolving 1.52 mmol of ammonium heptamolybdate tetrahydrate ($(NH_4)_6Mo_7O_{24}\cdot 4H_2O$, Alfa

Aesar, 99%) in 15 mL of hot water (80°C). The second solution was prepared by dissolving 9.00 mmol of cobalt nitrate hexahydrate ($Co(NO_3)_2 \cdot 6H_2O$, Sigma Aldrich, >98%) together with 1.00 mmol of the appropriate metal nitrate salt—either nickel nitrate hexahydrate ($Ni(NO_3)_2 \cdot 6H_2O$, Alfa Aesar, 98%) for NiCoMo or zinc nitrate hexahydrate ($Zn(NO_3)_2 \cdot 6H_2O$, Sigma Aldrich, >98%) for ZnCoMo—in 15 mL of water at room temperature (RT). The second solution was added to the first while stirring, followed by the addition of 1.4 mL of ammonium hydroxide (Sigma Aldrich, 28-30%$_{w/w}$). Additional ammonium hydroxide was added if necessary to adjust the pH to 8.5. The mixture was stirred at 80°C for 6 hours, then allowed to cool to RT. The resulting solid was filtered and washed with water until neutral, dried in an oven at 110°C overnight, and finally calcined at 400°C for 6 hours in static air with a heating rate of 10°C min^{-1}.

2.1.2 Solventless synthesis of Ni-Mo-Al catalyst

The third catalyst, developed as part of this PhD thesis and conceived within the framework of this doctoral research, is a Nickel-Molybdenum-Aluminum catalyst (henceforth Ni-Mo-Al) synthesized via solventless methods, aligning with the 12 principles of Green Chemistry and Green Engineering (outlined in Section 1.2), for DO of TGs into green diesel.

Before going into the details of the synthesis of the Ni-Mo-Al catalyst, it is important to outline the fundamental principles of Green Chemistry that guided the development of this catalyst. In this specific context, the following principles of Green Chemistry were particularly relevant: (i) waste prevention; (ii) atom economy; (iii) less hazardous chemical synthesis; (iv) safer solvents and auxiliaries; (v) design for energy efficiency; and (vi) reduce derivatives.

For these reasons, as this catalyst is novel in the literature, the synthesis method is the subject of patent application currently under review (Italian Patent application No. 102023000023556).

The Ni-Mo-Al catalyst was synthetized with solventless mechanical mixing of relative metal oxides in a ball-mill. The nickel, molybdenum, and aluminum oxides were produced through the calcination of their respective precursor salts: nickel nitrate hexahydrate ($Ni(NO_3)_2 \cdot 6H_2O$, Sigma-Aldrich, ≥97.0%), aluminum nitrate nonahydrate ($Al(NO_3)_3 \cdot 9H_2O$, Sigma-Aldrich, ≥98%), and ammonium heptamolybdate tetrahydrate ($(NH_4)_6Mo_7O_{24} \cdot 4H_2O$, Alfa-Aesar, >99%). The solvent-free synthesis aimed to create a catalyst with a nominal Ni/Al molar ratio of 0.667, while the Ni/Mo and Al/Mo molar ratios were set at 0.571 and 0.857, respectively. The first stage of synthesis involved the calcination of salts to obtain the corresponding oxides:

- ***Calcination of $Ni(NO_3)_2 \cdot 6H_2O$ to obtain NiO***: Nickel nitrate was calcined in a muffle furnace at 500°C for 12 hours, with an heating rate of 5°C min^{-1} [261]. The sample was then cooled to 120°C at 10°C min^{-1} and held at this temperature for 12 hours.
- ***Calcination of $Al(NO_3)_3 \cdot 9H_2O$ to obtain Al_2O_3***: Aluminum nitrate was calcined at 550°C for 12 hours, at an heating rate of 5°C min^{-1} [262]. The sample was similarly cooled to 120°C at a rate of 10°C min^{-1} and held there for 12 hours.
- ***Calcination of $(NH_4)_6Mo_7O_{24} \cdot 4H_2O$ to obtain MoO_3***: Ammonium heptamolybdate was calcined at 350°C for 12 hours, with an heating rate of 5°C min^{-1}[263]. The sample was then cooled to 120°C at 10°C min^{-1} and maintained at this temperature for 12 hours.

The formation of the desired oxides was confirmed through mass measurements of the solid products and analysis of the stoichiometries of the expected combustion reactions.

To produce the final catalyst, appropriate quantities of each calcined oxide were loaded into a ball mill (Planetary Monomill "PULVERISETTE 6" in Figure 7) with zirconia balls (50 balls of 10 mm diameter, 2.98 g each). The balls-to-powder mass ratio was equal to 8.3:1. The ball milling process was conducted at 300 rpm for 30 minutes, after which the final catalyst solid was recovered.



Figure 7 Planetary Monomill "PULVERISETTE 6" used for Ni-Mo-Al catalyst synthesis.

2.2 CATALYSTS CHARACTERIZATIONS

The synthesized catalysts (i.e., NiCoMo, ZnCoMo, and Ni-Mo-Al) were characterized using techniques such as:

- *Inductively Coupled Plasma-Mass Spectrometry (ICP-MS)* for the quantification of the metals in the catalysts.
- *CHNS elemental analysis* for the determination of C, H, N and S, e.g., organic deposits.
- *Fourier Transform Infrared Spectroscopy (FT-IR)* for the identification of the bands related to metal-oxygen bonding.
- *Laser diffractometry* to measure particle size distribution (PSD) and average diameter of catalyst particles.
- *X-Ray Diffraction (XRD)* for crystalline phase investigation.
- *N_2-Physisorption* for characterization and measurement of pores volume and surface properties of catalysts.
- *Scanning Electron Microscopy with Energy Dispersive X-ray Spectroscopy (SEM-EDS)* for local morphological, textural, and chemical analysis.
- *Transmission Electron Microscopy (TEM)* for nano-structural characteristics of catalysts.

- *Temperature Programmed Reduction (TPR)* to study sample reducibility.
- *H_2-Temperature Programmed Desorption (TPD-H_2)* to provide information on H_2 adsorption on the catalyst reduced surfaces.

Among the characterizations performed on the catalysts, some—such as XRD, N_2-Physisorption, TEM, TPR, and TPD-H_2—were conducted and related data were elaborated at the Institute of Chemistry and Processes for Energy, Environment, and Health (ICPEES) at University of Strasbourg. The other characterizations were conducted at the University of L'Aquila. More in detail, SEM-EDS analyses were performed at Microscopy Center; ICP-MS and FT-IR measurements at Department of Physical and Chemical Science; and CHNS analyses and laser diffractometry were performed at Department of Industrial and Information Engineering and Economics.

All characterizations were conducted on the catalysts in their calcined state (as-synthesized). For the Ni-Mo-Al catalyst, some characterizations were also performed on the individual oxides (i.e., NiO, MoO_3 and Al_2O_3) from which it derived. Additionally, some analyses were performed on post-reaction catalysts, including (i) the best-performing post-reaction catalyst, (ii) the worst-performing post-reaction catalyst, and (iii) the recycled post-test catalyst. These characterizations could help determine whether the catalysts experienced changes during the catalytic process and whether performance variations between reactions are attributable to the catalyst itself or to the reaction conditions.

2.2.1 Inductively Coupled Plasma-Mass Spectrometry (ICP-MS)

To assess the elemental composition of catalysts and determine the concentration of active metals, inductively coupled plasma-mass spectrometry (ICP-MS) is commonly used. This method helps quantify the actual metal content in catalysts. A typical ICP-MS setup includes six key components: sample introduction, nebulization, inductively coupled plasma

(ICP), an interface, a mass analyzer, and a detector [264]. The sample introduction system is typically an autosampler and a peristaltic pump to deliver the sample to a nebulizer, which converts the liquid into a fine aerosol [264]. The aerosol is then filtered in a spray chamber to remove larger droplets and smooth out pump pulses [264]. The nebulized sample is introduced into the ICP, which contains Argon plasma (i.e., a high-temperature, ionized gas of charged particles) [264]. Inside the plasma, the sample undergoes deprivation of solvent, vaporization, atomization, and ionization. The ionized sample is then guided by the Argon flow through an interface into a mass spectrometer, in which ions are separated based on their mass-to-charge ratios [264]. These ions are finally detected by an electron multiplier, which converts ion signals into electrical pulses for analysis by a computer system [264].

The ICP-MS analysis of the catalysts was conducted using a Thermo-Scientific iCAP-TQ equipped with a triple quadrupole MS detector (see Figure 8). Prior to the ICP-MS analysis, the catalysts were subjected to mineralization. Approximately 20 mg of each sample was placed in vials and processed in a microwave oven (SRC Microwave Digestion) with 15 mL of Aqua Regia. The microwave heating program for sample mineralization involved three steps: (i) the temperature gradually increased over 10 minutes until reaching 180°C, (ii) the temperature was held at 180°C for 40 minutes, and (iii) the system was cooled down. After mineralization, the samples were diluted with Milli-Q water, and 200 µL of nitric acid (Suprapure® nitric acid, 65%, Supelco) was added during the dilution process. Before analyzing the samples, a calibration curve was created using Ni, Co, Mo, Al and Zn mono-elemental standard solutions (Inorganic Ventures). For further details about calibration line construction, please refers to Addendum A.



Figure 8 iCAP-TQ and ICP-MS used for catalysts characterization.

2.2.2 CHNS ELEMENTAL ANALYSIS

CHNS elemental analysis enables the quantification of carbon (C), hydrogen (H), nitrogen (N), and sulfur (S) in both organic and inorganic samples, whether in solid form or as non-volatile liquids.

CHNS elemental analyses of catalysts were carried out using a Perkin Elmer CHNS ANALYZER 2400 SERIES II (in Figure 9). The samples were first dehumidified to prevent any water-derived hydrogen from interfering with the measurement of the hydrogen content present in the sample. After dehumidification, the sample was finely ground to achieve maximum homogenization and then weighed (approximately 2-3 mg). The sample was placed in a tin capsule, which was then dropped into a quartz tube preheated to 975°C. Helium continuously flowed through the quartz tube, and oxygen was introduced at the moment of sample injection.

As the sample decomposed in the quartz tube, the resulting gases first passed through the upper portion of the tube (i.e., the combustion zone), which contained EA-6000 (a reagent, N2410692, Perkin Elmer), and then through the lower portion (i.e., the reduction zone), which contained Copper Plus in wire form. The gas mixture exiting the quartz tube — composed of N_2, CO_2, H_2O, and SO_2 — was directed to a detection system that included a gas chromatograph (GC) with an oven, a chromatography column, and a thermal conductivity detector.

As the gases pass through the column and detector, a chromatogram was produced, with peaks corresponding to each component. The software

integrated these peaks and based on the sample's weight, calculated the percentages of carbon (C), hydrogen (H), nitrogen (N), and sulfur (S) present in the sample. Before analysis, the instrument was calibrated using standards with known C, H, N, and S percentages, which undergo the same preparation steps as the samples.



Figure 9 CHNS analyzer used for catalysts elemental analyses.

2.2.3 Fourier Transform Infrared Spectroscopy (FT-IR)

FT-IR measurements were performed using a PerkinElmer Spectrum instrument in ATR (Attenuated Total Reflection) mode (Figure 10). When infrared (IR) radiation interacts with a sample, it causes molecular vibrations, with each chemical bond undergoing a vibrational transition at a specific energy [265]. The number of vibrational modes of a molecule has depends on its bonds and atoms [265]. FT-IR spectrometers are highly sensitive and require minimal acquisition time. Instead of selecting wavelengths with a monochromator, these instruments use an interferometer to pass all IR photons through [265]. The interferometer splits the IR beam, introduces a path difference, and then recombines the beams, creating interference patterns [265]. These patterns form an interferogram, which is transformed into an IR spectrum using a Fourier transform [265]. In ATR mode, the IR beam is directed onto a high-refraction crystal (such as diamond), over which the

sample is placed [265]. ATR offers fast, reproducible analyses, but it requires direct contact between the sample and the crystal, which must have a significantly different refractive index from the sample [265].

To characterize the catalysts, they were placed in direct contact with the ATR crystal, which is made of diamond and the available area is 2x2 mm square. The IR spectrum was obtained by averaging 16 scans at a resolution of 2 cm^{-1}, covering the range from 4000 to 400 cm^{-1}.



Figure 10 PerkinElmer Spectrum instrument with ATR unit.

2.2.4 Laser diffractometry for determination of particle size distribution (PSD)

The PSD of catalysts were determined using the Malvern Mastersizer 2000 (in Figure 11), which employs laser diffraction for measurement. To analyze the solid samples, they were dispersed in distilled water (since the catalysts are insoluble in water) and placed in a baker. The particle retention index was set to 2.08, and the absorption index was set to 1. The device emitted a laser beam that passed through the sample. As the particles interacted with the laser, they diffracted the light at various angles based on their size: larger particles diffract light at smaller angles, and vice versa. A series of detectors arranged in a ring around the sample collect the diffracted light and measure its intensity at different angles. The data collected from these detectors were processed using Mie's mathematical model [266], which interprets the diffraction patterns to calculate the PSD. The instrument then generated a PSD graph, typically shown as a cumulative curve or frequency distribution.

The PSD allows for the calculation of several key parameters that provide insights into the characteristics of the sample. These include size percentiles such as *d(0,1)*, *d(0,5)*, and *d(0,9)*. The parameter *d(0,1)* represents the particle size below which 10% of the total particle population is found, while *d(0,5)*, known as the median size, indicates the particle size below which 50% of the particles are located [267]. Additionally, *d(0,9)* denotes the particle size below which 90% of the total population is found [267].

Another important parameter derived from the PSD is the Sauter mean diameter, represented as *d(3,2)*. The parameter *d(3,2)* reflects the volume-weighted mean diameter, which takes into account the volume of the particles, providing a more accurate representation of the average particle size in the sample [267].



Figure 11 Malvern Mastersizer 2000 for PSD measurements.

2.2.5 X-RAY DIFFRACTION (XRD)

XRD is a valuable technique for determining the crystalline structure of catalysts. This method relies on the interaction between X-ray waves and the atoms within a crystalline structure [268]. Specifically, it examines the interference between the X-ray beam directed at the sample and the X-rays that are diffracted by the sample [268]. The interference pattern produced is known as the diffraction pattern. By analyzing these patterns, one can identify the crystalline phases present, as the diffraction peaks provide information about them. The condition for constructive interference in this context is described by Bragg's law (Equation 2.1, Figure 12) [269].

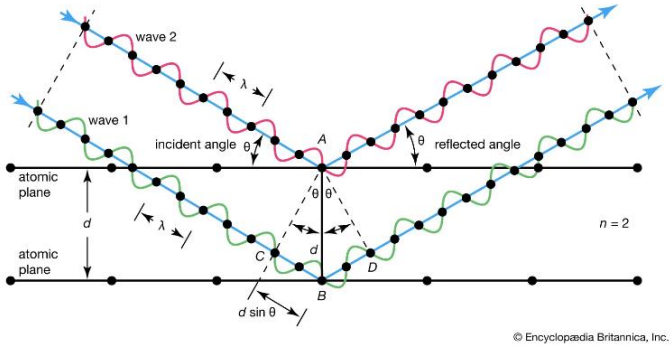


Figure 12 Bragg's law, taken from [270].

$$2 \cdot d \cdot sen\theta = n \cdot \lambda \qquad \textit{Equation 2.1}$$

where d is the interplanar distance, θ is the scattering angle, λ is the wavelength of the incident wave, and n is a positive integer number.

By physically varying the angle θ, Bragg's law is fulfilled for various distances in crystalline materials. This generates a diffractogram displaying peaks corresponding to the different crystalline phases in the sample. Each material has a distinctive diffractogram, which can be identified by comparing it with reference standards.

Catalysts XRD spectra were obtained using a BRUKER AXS D8 ADVANCE X-ray diffractometer, which uses CuKα1 radiation to detect crystalline phases in a Bragg-Brentano geometry (see Figure 13).

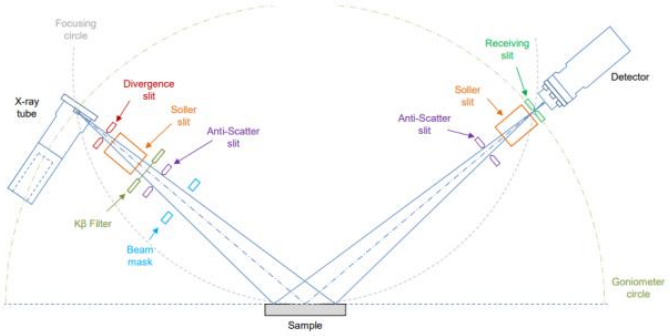


Figure 13 Bragg-Brentano geometry, taken from [271].

Diffractograms were recorded over a Bragg angle range of 20° to 90° for all samples, with a scanning step of 0.0158° and a sampling time of 1 second per step. Additionally, the average crystallite size (D) for all samples was determined. This parameter is related to the full width at half maximum

(FWHM) of an X-ray diffraction peak using the Debye-Scherrer formula (Equation 2.2).

$$D = \frac{k \cdot \lambda}{\beta \cdot cos\theta} \qquad \textit{Equation 2.2}$$

where k is the adimensional factor used for spherical particles (k = 0.9), λ is wavenumber of the electromagnetic beam (λKα(Cu)=1.5418 Å) and β is the FWHM of the diffraction peak in radian.

2.2.6 N_2-PHYSISORPTION

The textural properties of materials, including surface area, pore volume, and pore diameter, are typically evaluated using N_2-physisorption through BET (Brunauer-Emmett-Teller) and BJH (Barret-Joiner-Halenda) analysis.

BET analysis relies on the physisorption of inert gas, usually N_2 at its boiling point (-196°C). By measuring N_2 adsorption isotherms, which track how equilibrium adsorbate quantity changes with gas partial pressure, the quantity of adsorbed-N_2 corresponding to a monolayer of gas molecules that covers the material surface can be identified [272, 273]. Knowing the number of molecules in this monolayer and the area occupied by each allows for the calculation of the solid surface area [272, 273]. The BET method is based on four key assumptions: (i) the heat of adsorption for the first layer is constant, (ii) interactions between molecules within the same layer are negligible, (iii) each adsorbed molecule can form a new adsorption surface, and (iv) the heat of adsorption for all subsequent layers equals the heat of liquefaction [274, 275].

The BET isotherm is reported in Equation 2.3 [274]:

$$v = \frac{v_m \cdot c \cdot P}{(P_0 - P) \cdot \left[1 + (c - 1) \cdot \frac{P}{P_0}\right]} \qquad \textit{Equation 2.3}$$

Here, v represents the volume of gas adsorbed at pressure P and at a temperature where the vapor pressure of the adsorbate is P_0; c is the BET constant, and v_m is the volume of gas adsorbed when the adsorbent surface is fully covered by a complete monolayer of molecules.

The BET constant c is defined as in Equation 2.4 [274]:

$$c = \exp\left(\frac{E_m - E_L}{R \cdot T}\right) \qquad \textit{Equation 2.4}$$

Here, E_m refers to the heat of adsorption for the monolayer (N_2-solid interaction); E_L is the heat associated with the second and subsequent adsorbed layers, which is set equivalent to the heat of liquefaction or vaporization; R is the gas constant; and T is the temperature expressed in Kelvin.

The BET surface area can be calculated using the volume of monolayer adsorbed nitrogen, v_m, as in Equation 2.5 [276]:

$$S_{BET} = \frac{v_m \cdot N_A \cdot \sigma_m}{m} \qquad \textit{Equation 2.5}$$

where σ_m is the molecular cross-sectional area occupied by N_2 (equal to 0.162 nm^2); N_A is Avogadro's number; and m is the mass of the sample.

The BJH mesoporosity assessment can also be derived from the N_2-physisorption isotherm. The BJH method is founded on two key assumptions: (i) all pores are cylindrical in shape, and (ii) there are no interconnected pores [277]. Using these assumptions, the BJH method applies the Kelvin equation (Equation 2.6), which relates pore radius to the partial pressure responsible for nitrogen adsorption and desorption within the pores [277].

$$\ln\left(\frac{P}{P_0}\right) = -\frac{2 \cdot \gamma \cdot v_t}{r_k \cdot R \cdot T} \qquad \textit{Equation 2.6}$$

Here, γ represents the surface tension; v_t is the molar volume; T is the temperature at which the adsorption/desorption measurement is taken; and r_k is the Kelvin radius, which corresponds to the radius of the pore with the most probable volume [277].

Using the Kelvin equation (Equation 2.6), the relationship between vapor pressure and pore radius is established [277]. This allows for the calculation of the volume of liquid desorbed between two successive relative pressures. By integrating over all pore radii, the total pore volume (V_{BJH}) can be determined [277].

At this stage, assuming the pores are cylindrically shaped, the inner surface can be linked to the volume via geometric relationships. Furthermore, it is assumed that the adsorbent material has a uniform pore distribution, enabling a direct connection between surface area and pore volume [277]. This simplification permits the use of the total surface area and total pore volume to calculate the average diameter, by the Equation 2.7:

$$d_{BJH} = 4\frac{V_{BJH}}{S_{BET}} \qquad \textit{Equation 2.7}$$

Where V_{BJH} represents the sum of pore volumes of different sizes in the sample, calculated by the BJH method using N_2 isotherm data.

For the three catalysts of this work, N_2-physisorption measurements were carried out using a MICROMERITICS ASAP 2420 surface area and porosity analyzer (Figure 14). N_2 adsorption and desorption isotherms were recorded at the boiling point of nitrogen (-196°C), with calculations performed using the BET and BJH methods through the ASAP 2420 software (version 2.09). The samples consisted of 50-100 mg of powder, which underwent degassing under vacuum at 200°C for at least 8 hours prior to analysis. The measured parameters include the BET surface area (S_{BET}, Equation 2.5), BJH cumulative pore volumes (V_{BJH}, from Equation 2.6) and BJH average cylindrical pore diameter (d_{BJH}, Equation 2.7).



Figure 14 MICROMERITICS ASAP 2420 analyzer for N_2-physisorption measurements.

2.2.7 SCANNING ELECTRON MICROSCOPY AND ENERGY DISPERSIVE X-RAY SPECTROSCOPY (SEM-EDS)

SEM-EDS (Scanning Electron Microscopy with Energy-Dispersive X-ray Spectroscopy) is a powerful analytical technique that combines the imaging capabilities of scanning electron microscopy (SEM) with the elemental analysis capabilities of energy-dispersive X-ray spectroscopy (EDS) [278]. This combined approach allows for detailed examination of the local morphology and composition of a sample. SEM provides high-resolution images of the sample by scanning it with a focused beam of high-energy electrons [279]. The electrons interact with the atoms in the sample, producing various signals [279]. In a standard SEM, the electron beam is thermionically emitted from an electron gun equipped with a tungsten or lanthanum hexaboride cathode [279]. This beam, with energies ranging from 0.2 to 40 keV, is focused by one or two condenser lenses to a spot with a diameter between 0.4 nm and 5 nm. The focused electrons are then directed into the scanning system, where a deflection coil scans the surface [279]. The signals produced include: (i) secondary electrons, which are useful for visualizing surface morphology and creating images; (ii) backscattered electrons, which help in distinguishing compositional contrasts in multiphase samples; (iii) diffracted backscattered electrons, which provide information on crystal structures and material orientation; (iv) and characteristic X-rays, used for EDS elemental analysis, along with continuum X-rays [279]. To operate the SEM, a vacuum is required to minimize interactions between electrons and gas molecules [278, 279]. EDS analyzes the X-rays emitted from the sample when it is bombarded with electrons. Each element in the sample emits X-rays at characteristic energies, allowing for the identification and quantification of elements [278, 279]. The EDS detector collects these X-rays and measures their energy to produce an EDS spectrum. The spectrum displays peaks corresponding to specific elements. Additionally, topographical analysis is performed to provide qualitative maps showing the distribution of metals on the surfaces. Combining SEM and EDS offers a

detailed view of both the surface morphology and elemental composition of the sample.

SEM-EDS was utilized to examine the morphological and topological features of the catalysts. Observations were conducted using a Zeiss Gemini SEM 500 microscope, which is equipped with EDS for elemental analysis, specifically using the OXFORD AztecLive system with an Ultim Max 100 detector. The analysis was performed at a working voltage of approximately 15 keV, with an analytical working distance of 8.6 mm. The detector used for imaging was the Back Scatter Detector (BSD), and the measurements were carried out under high vacuum conditions.

2.2.8 TRANSMISSION ELECTRON MICROSCOPY (TEM)

Transmission Electron Microscopy (TEM) is an advanced imaging technique utilized to analyze the microstructure of nanoscale materials. TEM employs an electron beam to capture images of samples. To enable electrons to pass through, samples must be extremely thin (less than 100 nm) [280].

The analysis begins with the generation of an electron emission from a cathode, which is usually a tungsten filament or a field electron emitter [280]. The emitted electrons are then accelerated by a high voltage, usually ranging from 60 to 300 kV, and concentrated into a collimated beam [280]. This electron beam is directed through the sample, where it interacts with the material. During this interaction, some electrons are transmitted through the sample, while others are scattered or absorbed, depending on the sample's composition and structure [280]. Electrons that exit the sample are collected by a series of electromagnetic lenses, which focus the beam onto a detector to create an image [280].

TEM images were obtained using a JEOL 2100 LaB6 microscope, which operated at 200 kV. It featured a point resolution of 0.2 nm in parallel mode and 2-3 nm in Scanning Transmission Electron Microscopy (STEM) mode. To prepare the sample, approximately 5 mg of powder was dispersed in pure ethanol and sonicated for 5 minutes to create a suspension. Two or three drops of this catalyst suspension were then placed on a sample holder, which

consisted of a polymeric membrane supported by a copper grid. Once ethanol evaporated, the powder particles were evenly distributed on the membrane.

2.2.9 TEMPERATURE PROGRAMMED REDUCTION (TPR)

TPR is a technique used to study the reduction behavior of solid materials, e.g., metal oxides and catalysts. In TPR, a reducible material is subjected to a flow of a reducing gas, typically mixture of hydrogen and inert gas, while the temperature is gradually increases by a controlled program [281]. The rate of reduction is continuously monitored by analyzing the composition of the reducing gas at the outlet of the reactor. Typically, a stream of gases flows through a bed of solids contained within a quartz tube. The tube is designed with a high aspect ratio (length to diameter) to maximize the contact between the gas and solids, thereby minimizing radial and thermal gradients [282]. A thermocouple positioned within or close to the bed measures the temperature rise as an electrical furnace increases the temperature [282]. The concentration of the effluent gas is continuously monitored by either a thermal conductivity detector (TCD) or a mass spectrometer (MS), with changes in the signal indicating variations in the oxidation state of the sample [282]. The TPR profile, a plot of the amount of H_2 consumed versus temperature, reveals information about the different metal species present in the sample and their reduction characteristics [282]. The shape and position of peaks in the TPR profile can help determine the activation energy required for the reduction processes [282].

TPR experiments were conducted using a MICROMERITICS AUTOCHEM II 2920 chemisorption analyzer (Figure 15). A 100 mg catalyst sample was placed in a Flow-Thru "U"-shaped fused quartz tube with a 9 mm inner diameter and positioned between two quartz wool flocks to create a packed bed. This reaction cell was situated within a furnace regulated by an internal thermocouple. The TPR process began with heating at a rate of 10°C min^{-1} until reaching 1000°C, followed by a 30-minute dwell at 1000°C, all under a flow of 50 NmL/min of reducing gas (10% H_2 in Ar). A cold trap downstream captured the steam produced, while a TCD measured the consumption of H_2.

The resulting data, which were recorded as a function of temperature and time, were saved using AUTOCHEM II software version 4.02.



Figure 15 TPR/TPD-H_2 equipment used for catalysts characterization.

2.2.10 H_2-Temperature Programmed Desorption (TPD-H_2)

TPD-H_2 is a technique used to study the interaction between H_2 and catalyst surface. It provides valuable insights into how H_2 adsorbed onto the surface of the catalyst and at what temperatures they desorbed, helping to characterize the material surface properties [283]. The temperature at which H_2 is desorbed from the surface provides information about the strength of the hydrogen binding to different sites on the material [283]. This technique helps in understanding how a catalyst will perform in reactions involving hydrogen, such as DO processes.

The same equipment used for TPR (described in Section 2.2.9, Figure 15) was employed for TPD-H_2 experiments. The TPD-H_2 process began with a reduction step, with a flow of 50 NmL/min of reducing gas (10% H_2 in Ar) was fed to the packed bed. The sample was heated at a rate of 5°C min^{-1} up to 320°C, followed by a 4-hour dwell at 320°C. This reduction procedure was selected to closely match the in-situ pre-reduction performed in the batch reactor for the DO experimental tests (see Section 2.4). After the reduction, the TPD-H_2 cell was purged with Ar flow at 320°C for 90 minutes, continuing during the cooling phase until RT, to remove any H_2 presented in the cell and any weakly adsorbed (physiosorbed) H_2 on the sample surface. The next step

involved H_2 sorption, conducted at 50°C by injecting H_2 in pulses (30 times) to saturate the solid surface. The final step was the desorption phase, where H_2 was desorbed under an Ar flow of 50 NmL/min, with the temperature ramped up at 15°C min^{-1} to 500°C, followed by a 30-minute dwell at 500°C.

2.3 FEEDSTOCKS FOR DO TESTS

Two oil feedstocks were investigated in this PhD thesis:

- considering that all catalysts in this thesis were never tested before for DO, simple commercial rapeseed oil (Brand: VitaD'or) was chosen for the experimental tests of a first comparative experimental campaign (Section from 2.4.1 to 2.4.3).
- Afterwards, pursuing the effort of developing a more sustainable and eco-friendly DO process in line with the principles of Green Chemistry (outlined in Section 1.6.1 and Section 1.2), WCO was used as a feedstock for some experimental tests (Section 2.6.2). That WCO was sourced from a local fast food restaurant: it originated from high oleic sunflower oil (Brand: Sagra) used for frying at 180°C for 5 days. Before any potential use, the WCO was filtered through a vacuum funnel equipped with filter paper to remove any impurities.

Before performing the catalytic tests, the oils were characterized.

2.3.1 FEEDSTOCK CHARACTERIZATION

The oils composition (i.e., rapeseed oil and WCO) was determined by transesterification according to AOAC (Association of Official Agricultural Chemists) International guidelines (AOAC 969.33-1969(1997)) [284]. This derivatization technique converts the TGs into FAMEs, which are more volatile, allowing for easier and more efficient analysis through Gas Chromatography-Flame Ionization Detector (GC-FID). During the transesterification reaction, TGs are initially saponified to release FFA. The subsequent addition of a BF_3-methanol solution catalyzes the esterification, resulting in the formation of FAMEs, which are analyzed with a GC-FID.

In the transesterification process, 350 mg of sample reacts with 6 mL of a 0.5 M solution of NaOH (Lancaster, 97%) in anhydrous methanol (Sigma Aldrich, 99.8%) added to a 50 mL flask, connected to reflux condenser, and heats (at 150°C) under continuous stirring. The reaction is allowed to reflux for 10 minutes. Subsequently, 7 mL of BF_3 in methanol solution (Sigma-Aldrich, 10% of BF_3 in methanol) is added, and the mixture is boiled for 1 minute. Then, 5 mL of n-hexane (C_6H_{14}, Carlo Erba, 99%) is added and boiled for another 1 minute. Once the heating is stopped, allow the mixture to cool for a few minutes before adding a supersaturated NaCl solution until to the neck of the flask. This increases the ionic strength, promoting the separation of the organic phase. Finally, 1.1 mL of the organic phase is taken and placed in a vial containing anhydrous Na_2SO_4 (Carlo Erba, $\geq$ 99%) to remove any residual water.

After completing the transesterification of the two oils (i.e., rapeseed oil and WCO), the resulting transesterified samples were injected into the GC-FID. The analysis was performed using a Thermo Trace GC Ultra 7820 GC (Figure 16), equipped with a flame ionization detector (FID) and a Supelco® SP-2380 capillary column (30 m x 0.25 mm x 25 µm, stationary phase = Poly(90% biscyanopropyl/10% cyanopropylphenyl siloxane)). A 1.0 µL sample of the transesterified oil was manually injected into the GC-FID (using the sandwich method). The injector and FID were set to 250°C. An isothermal run was conducted at 180°C for 25 minutes, using hydrogen as the carrier gas (split 25 mL/min). FAMEs were identified by comparing retention times with a C_{14}-C_{22} standard reference (F.A.M.E. MIX, C_{14}-C_{22}, Supelco). In Figure B 1 of Addendum B was reported the chromatogram of FAME standard. The chromatographic peaks were manually integrated using Xcalibur software.



Figure 16 Thermo Trace GC-FID used for FAMEs identification in transesterified samples.

2.4 DEOXYGENATION TESTS

Catalytic DO tests were performed in a PARR® mini batch reactor (series 4590, equipped with magnetic drives and a 4848 Reactor Controller), having total reactor volume of 100 mL (in Figure 17). Before each test, the catalyst was activated through in-situ pre-reduction (4 hours at 320°C, with an initial H_2 partial pressure of 60 bar at RT), except for two reference tests: a *"blank test"* conducted without a catalyst and a *"no pre-red"* test (for each catalyst), which skipped the catalyst pre-reduction step.

For each test, 2 g of oil and solvent, with a mass ratio of solvent-to-oil of 10:1, were loaded to the reactor. After a careful screening carried out during PhD Giuseppe Di Vito Nolfi's doctoral research [172], n-hexane (C_6H_{14}, Carlo Erba, 99%) was selected as the solvent of DO tests due to its promising performance, in agreement also with literature commented in Sections 1.6.3 and 1.6.5. After the reactor was loaded with the catalyst and reagents (i.e., oil and n-hexane), it undergoes three N_2 purges to eliminate any residual air, followed by three H_2 purges to ensure complete removal of N_2. The reactor is then pressurized with H_2 to the desired level (i.e., 40 bar of H_2 at RT).



Figure 17 PARR® batch reactor used for DO tests.

Once the test conditions are established, the temperature is set, and the magnetic stirring is activated at the desired speed (ranging from 100 to 700 rpm). After setting all parameters, the reaction was conducted for the designated duration. The reaction time was measured starting from the moment the temperature reached the desired value, thus excluding the reactor heating time.

Once the reaction time has ended, the reactor is switched off and allowed to cool to RT. At the end of each test, the catalyst was filtered and washed with n-hexane, and occasionally with chloroform ($CHCl_3$ stabilized with ethanol, Carlo Erba, ≥ 99.9%). The reaction product was then recovered, separated from the solvents, and weighed.

2.4.1 2^3 FACTORIAL DESIGN OF EXPERIMENT

A first comparative experimental campaign based on DO on rapeseed oil was performed on the three catalysts investigated in this thesis.

An unreplicated 2^3 factorial design of experiment (DoE) with replicated center point was applied for each catalyst (i.e., NiCoMo, ZnCoMo and Ni-Mo-Al), to explore the effect of 3 experimental factors (parameters), each at two levels (high and low), and their interactions on the outcome of interest [285].

Rapeseed oil was chosen as feedstock for the tests. The three process parameters were: (i) temperature (*T*) at 280°C (level -1) and 320°C (level +1); (ii) catalyst-to-oil weight ratio (Υ) at 4%$_{w/w}$ (level -1) and 10% $_{w/w}$ (level +1); and (iii) time (*t*) at 2 h (level -1) and 6 h (level +1), measured starting by the moment when the reactor reached the desired temperature. The tests at center point were replicated three times at intermediate levels (i.e., level 0 at 300°C, 7%$_{w/w}$, 4 h). For this experimental campaign, the stirring speed was set constant to 200 rpm.

The experiments of factorial plan were performed in randomized order (as it can see in Table 8), to ensure that the results are more reliable by minimizing the impact of uncontrolled variables and enhancing the robustness of the conclusions [285]. Replicated measurements were conducted at the center point of the factorial plan, fundamental to estimating reproducibility, assessing linearity and improving the accuracy of the experimental design [285]. Replicates were used to estimate the error of the experimental measurements.

In addition to the adopted DoE, as mentioned in Section 2.4, two reference tests (i.e., "*blank*" and "*no pre-red.*" test) were conducted for each experimental campaign.

Test conditions were summarized in Table 8. The treatments in Table 8 were labeled using the standard 2^k factorial design notation: *"(1)"* refers to the treatment where all factors (A, B, C) are at their lower levels; *"abc"* represents the treatment where all factors are at their higher levels; *"a"* indicates A at its higher level while B and C are at their lower levels; *"ab"* shows A and B at their higher levels with C at its lower level, and so forth. The test procedure was carried out as outlined in Section 2.4.

Table 8 DO experimental conditions: all listed tests carried out at H_2 initial partial pressure of 40 bar, 200 rpm, with 2 g of rapeseed oil and 20 g of n-hexane.

	A=*T* [°C]	B=*Y* [$\%_{w/w}$]	C=*t* [h]	*treatment*
blank	320	0	6	
no-pre-red	320	10	2 h for NiCoMo and ZnCoMo 6 h for Ni-Mo-Al	
	-	-	-	(1)
	+	-	-	a
	-	+	-	b
	+	+	-	ab
	-	-	+	c
	+	-	+	ac
	-	+	+	bc
	+	+	+	abc
	0	0	0	central
	0	0	0	central
	0	0	0	central

2.4.2 RECYCLING TESTS

To assess the reusability of the catalysts, four consecutive DO runs were conducted using the same catalyst sample (referred to as Test_R*n*, where *n*=1, 2, 3, 4) under the conditions that yielded the best results in the 2^3 factorial design. After each reaction, the catalysts were filtered, washed with n-hexane, and dried under vacuum at 50°C overnight. Due to some catalyst loss during the recovery process, the quantities of oil and n-hexane were adjusted in the recycling tests to maintain constant the catalyst-to-oil weight ratio and n-hexane-to-oil weight ratios. The procedure for performing the recycling tests is the same as that described in Section 2.4, except for in-situ pre-reduction, which was performed only before Test_R1, and not between repeated cycles.

2.4.3 ASSESSING THE EFFECT OF STIRRING SPEED ON THE EFFICIENCY OF DO

In order to assess whether impeller stirring speed affects DO performances at tested conditions, a dedicated DoE was applied by changing stirring speed (ω) as a factor (i.e., 200-400-600 rpm); this was done only for Ni-Mo-Al catalyst, as it resulted the most sensitive catalyst to variations of working

point within the domain of chosen temperature, oil-to-catalyst ratio, and reaction time.

In this case, a Face-Centered Central Composite Design (FCCCD) was conducted (Figure 18). In this experimental design, the 2^3 design is expanded by adding the central point of the cube along with the central points of each face of the cube (as shown in Figure 18).

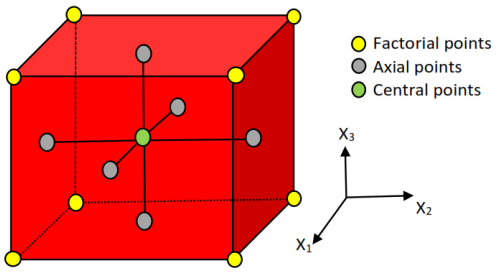


Figure 18 Graphical representation of FCCCD. Taken from [286].

For this experimental design, the varied parameters include: (i) T at 280°C (level -1), 300°C (level 0), and 320°C (level +1); (ii) Υ at 4%$_{w/w}$ (level -1), 7% $_{w/w}$ (level 0), and 10% $_{w/w}$ (level +1); and (iii) ω at 200 rpm (level -1), 400 rpm (level 0), and 600 rpm (level +1). Table 9 summarizes the FCCCD experiments.

Table 9 List of FCCCD experiments.

Test n°	***A=T [°C]***	***B=Υ [%$_{w/w}$]***	***D=ω [rpm]***
1	-1	-1	-1
2	-1	1	-1
3	1	-1	-1
4	1	1	-1
5	1	-1	1
6	-1	1	1
7	-1	-1	1
8	1	1	1
9	0	0	0
10	-1	0	0
11	0	-1	0
12	0	0	-1
13	1	0	0
14	0	1	0
15	0	0	1

Other operational parameters are maintained constant, including reaction time of 2 hours; solvent-to-oil mass ratio of 10:1; and amount of oil at 2 g. The procedure for performing the tests is the same as defined in Section 2.4.

2.5 CHARACTERIZATION OF THE REACTION PRODUCT AND DATA ANALYSIS

To assess the catalysts performances in DO experiments, the recovered reaction product underwent three types of analyses:

- Attenuated Total Reflection Fourier Transform Infrared Spectroscopy (ATR FT-IR).
- Gas Chromatography with Flame Ionization Detection (GC-FID).
- Gas Chromatography-Mass Spectrometry (GC-MS)

2.5.1 PRODUCT COMPOSITION ANALYSIS USING FT-IR IN ATR MODE

FT-IR is a fast and effective analytical technique for qualitatively evaluating the conversion degree of the TGs into alkanes in DO reactions. The operating principle and equipment used are the same as those described for the catalyst's characterization (refer to Section 2.2.3, Figure 10).

The reaction product was again directly applied to the ATR crystal (only few drops of the product). The IR spectrum was acquired by averaging 4 scans with a resolution of 2 cm^{-1}, in the range from 4000 to 400 cm^{-1}.

To better illustrate the usefulness of FT-IR, an exemplificative comparison was made between the IR spectrum of fresh rapeseed oil and the product of DO test obtained from its reaction with 100% of conversion of TGs into HCs (see Figure 19).

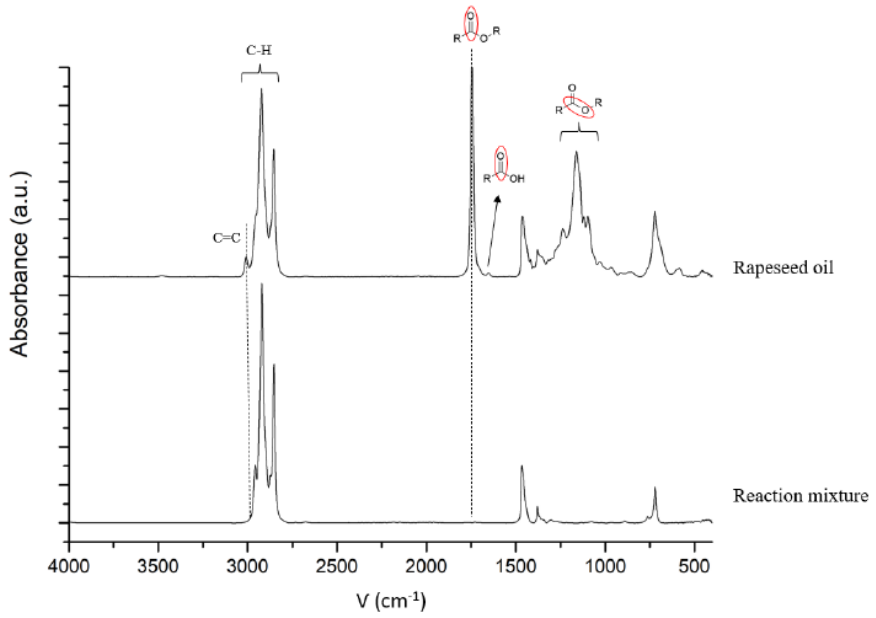


Figure 19 Comparison of IR spectra between rapeseed oil and reaction product, taken from [172].

The most notable difference between the spectra was observed in the band centered at 1745 cm^{-1}. This region (i.e., 1745-1700 cm^{-1}) represents the C=O stretching vibrations of TG esters (around 1745 cm^{-1}) and FFAs (around 1710 cm^{-1}) [287]. If the reaction mixture shows no signals in this area, it indicates complete conversion of TGs in HCs, because there are no bands related to the double bond C=O. Additionally, the region between 1350-900 cm^{-1}, which corresponds to C-O stretching vibrations [287], provides further evidence of the conversion degree. Other signals reflect C-H bond vibrations [287]. A slight change in the 2750-3150 cm^{-1} region indicates hydrogenation of double bonds in the TGs.

2.5.2 Product characterization: Gas Chromatography with Flame Ionization Detection (GC-FID)

The composition of the product obtained from the various DO catalytic tests was analyzed using GC-FID. Prior to the analysis, the reaction product was processed through transesterification, following the same procedure used for characterization of vegetable oils (see Section 2.3.1). A portion of the reaction

product was analyzed with the Thermo Trace GC-FID (the same used in Section 2.3.1).

Another product portion was analyzed with a different GC-FID, to carry out a semi-quantitative analysis of product composition and calculate relative percentage areas. 1.0 µL of the transesterified product (prepared as reported in Section 2.3.1) was automatically injected into an Agilent GC/7820A gas chromatograph (in Figure 20) equipped with a FID and an HP-5 capillary column (30 m x 0.32 mm x 0.25 µm, stationary phase: 5%-phenyl)-methylpolysiloxane). The chromatographic analysis lasted 35 minutes, beginning with an initial column temperature of 50°C held for 5 minutes. The temperature was then increased to 280°C at a rate of 10°C/min and maintained at 280°C for 7 minutes. H_2 was used as the carrier gas at a flow rate of 2.0 mL/min. The injector and FID were set to 250°C, with an inlet pressure of 0.4 bar. The chromatographic peaks corresponding to n-alkanes were identified by comparing them with a linear standard solution of C_7-C_{40} saturated alkanes (C_7-C_{40} Saturated Alkanes Standard, 1000 µg/mL for each component, Supelco). In Figure B 2 of Addendum B was reported the chromatogram of C_7-C_{40} saturated alkanes standard used for the identification of the reaction product.



Figure 20 Agilent GC/7820A gas chromatograph.

The semi-quantitative analysis of the reaction product was performed by manually integrating the peaks from the GC-FID chromatogram. The composition of the reaction product was then expressed as a percentage of the GC area (*A%*), assumed as a reliable estimation of the mass percentage.

After semiquantitative analysis, product composition was classified into the following groups: (i) n-alkanes C_8-C_{14}, (ii) n-alkanes C_{15}-C_{18}, (iii) n-alkanes C_{19}-C_{30}, (iv) branched HCs (BHC), (v) unsaturated HCs (UHC), (vi) FAME, and (vii) Others (which include compounds that could not be identified through GC-FID and GC-MS analyses).

2.5.3 Product characterization: Gas Chromatography Mass Spectrometry (GC-MS)

Chromatographic peaks that are not identified by GC-FID were identified using GC-MS analysis (GC model: Varian star 3400cx, MS model: Varian Saturn 2000, Figure 21). The GC is equipped with an HP-5 column (30 m × 0.25 μm × 0.25 mm, with a stationary phase of 5% phenyl-methyl polysiloxane). The chromatographic run lasts 35 minutes, starting with the column maintained at 50°C for 5 minutes, followed by a temperature increase of 10°C/min until reaching 280°C, where it is held for 7 minutes. Both the trap and injector temperatures are set at 250°C, and helium is used as the carrier gas at a split flow rate of 50 mL/min. N-alkanes are identified by comparison with a C_7-C_{40} standard (C_7-C_{40} Saturated Alkanes Standard, 1000 μg/mL for each component, Supelco), which is also used to calculate the Kovats retention index [288]. Unknown peaks were identified by matching the corresponding mass spectra with the NIST 2014 library and comparing the calculated Kovats retention index (RI, Equation 2.8) with the RI provided by the library.

$$RI = \left[\frac{tr_i - tr_z}{tr_z - tr_{z+1}} + z\right] \cdot 100 \qquad \textit{Equation 2.8}$$

Where: tr_i is the retention time of the unknown compound; tr_z is the retention time of the linear alkane eluting before the unknown peak; tr_{z+1} is the retention

time of the linear alkane eluting after the unknown peak; and z is the number of carbon atoms of the linear alkane eluting before the unknown peak.

For the same column, the Kovats RI remains independent of the operating conditions used in the chromatographic run and the physical properties of the column.

For the analysis, 20 μL of the transesterified sample was diluted in 1.3 mL of n-hexane; then 1 μL of this sample was injected into the GC-MS apparatus.



Figure 21 GC-MS. Varian star 3400cx (GC model), Varian Saturn 2000 (MS model).

An example illustrating how unknown compounds were identified using the reference library and RI can be found in Addendum B, Figure B 3.

2.5.4 EVALUATION OF DO PERFORMANCES

To consistently assess the DO performance across various tests, the following parameters, commonly used in the literature, were applied [173, 289-291]: (i) product yield ($Y_{product}$, Equation 2.9); (ii) conversion of TG (χ, Equation 2.10); (iii) diesel yield (Y_{diesel}, Equation 2.11); and (iv) catalyst selectivity ($S_{HDO/DCOx}$, Equation 2.12).

$$Y_{product} = \frac{m_{product}}{m_{oil}} \cdot 100 \qquad \text{Equation 2.9}$$

$$\chi = \left(1 - \frac{m_{product} \cdot \frac{A\%_{FAME}}{100}}{m_{oil}}\right) \cdot 100 \qquad \text{Equation 2.10}$$

$$Y_{diesel} = \frac{m_{product}}{m_{oil}} \cdot \sum_{i=15}^{18} A\%_{C_i} \quad \text{Equation 2.11}$$

$$S_{\frac{HDO}{DCOx}} = \frac{\left(A\%_{C_{16}} + A\%_{C_{18}}\right)}{\left(A\%_{C_{15}} + A\%_{C_{17}}\right)} \quad \text{Equation 2.12}$$

Alkanes from C_{15} to C_{18} were the primary focus within product compositions, as they are essential for green diesel production, whereas the presence of FAMEs indicated unreacted TGs.

Product yield ($Y_{product}$, Equation 2.9) is an index of how much liquid product has been recovered compared to the quantity of the starting oil. Low $Y_{product}$ values suggest that a significant portion of the starting oil has been converted into gaseous products, indicating that gas-phase reactions have occurred (see Section 1.5.2). Conversely, excessively high $Y_{product}$ values might indicate that the process has primarily involved hydrogenation rather than DO. If DO had occurred, the final mass product would have been lower due to the formation of gaseous by-products, as outlined in the reaction mechanisms (see Section 1.5). Therefore, an optimal $Y_{product}$ (between around 70-80%) should indicate a well-balanced process where DO reactions are maximized, promoting the formation of diesel HCs while minimizing excessive gas-phase reactions or over-hydrogenation. Achieving this balance is essential, as gas-phase reactions often lead to energy loss and undesired by-products, whereas over-hydrogenation can hinder the removal of oxygen-containing groups, reducing the overall effectiveness of DO [292].

Conversion (χ, Equation 2.10) reflects the efficiency of the DO process. It represents the percentage of the initial TGs that have been converted into HCs (i.e., C_8-C_{14} and/or C_{19}-C_{30} n-alkanes, C_{15}-C_{18} n-alkanes, BHC and UHC) or others compound except FAME. A 100% conversion indicates that all the starting TGs have been completely transformed into HCs or others compound. If the conversion is less than 100%, it means that a portion of the TGs remains unconverted. This unconverted fraction can still be present in the product as FFAs or TGs, but after the transesterification process, these remaining TGs or FFAs are converted into FAME for the analysis.

The diesel yield (Y_{diesel}, Equation 2.11) quantifies the proportion of diesel-like HCs (i.e., C_{15}-C_{18} HCs) in the final product. Essentially, this formula calculates the fraction of the initial oil that has become diesel HCs. High values indicate a greater proportion of diesel HCs in the final product. Conversely, lower values suggest that a smaller fraction of the final product consists of these HCs, which might indicate a less efficient conversion and lower yield of diesel-like components. In addition, the Y_{diesel} serves as a key indicator of the preference of the process towards producing diesel-range HCs. High Y_{diesel} values not only signify efficient conversion but also suggest that the process conditions are optimized to favor the formation of diesel-like HCs. On the other hand, lower Y_{diesel} values might point to side reactions, such as cracking or over-hydrogenation, leading to the formation of lighter or heavier HCs, which are less desirable in diesel fuel applications. Monitoring Y_{diesel} is crucial for ensuring that the process maximizes the production of high-quality, energy-dense diesel HCs while minimizing unwanted by-products.

Selectivity ($S_{HDO/DCOx}$, Equation 2.12) is defined as the ratio of the *A%* of C_{16}-C_{18} to that of C_{15}-C_{17} n-alkanes. This ratio indicates the catalyst's preference for the HDO pathway versus the decarbonylation-decarboxylation (DCO_x) pathway (for further details about reaction mechanism see Section 1.5.1.2). Selectivity value greater than 1 signifies a higher production of C_{16} and C_{18} n-alkanes, suggesting that the HDO pathway is favored (see Section 1.5.1.2). Conversely, selectivity less than 1 indicates a preference for the DCO_x reactions (see Section 1.5.1.2), resulting in a greater formation of C_{15} and C_{17} n-alkanes. At the end, if the selectivity equals 1, it implies that neither the HDO nor the DCO_x pathway is predominant. As discussed in the Section 1.5.1.2, HDO is preferable for achieving higher AE, whereas DCO_x pathways consume less H_2 but lead to carbon loss through the formation of CO_2 and CO (which are GHG), which ultimately results in lower AE. By favoring the HDO pathway, we can enhance the sustainability of the process by minimizing GHGEs. Consequently, monitoring and optimizing selectivity is essential for

developing catalysts that not only exhibit high performance but also meet environmental objectives.

2.5.4.1 ANALYSIS OF DATA FROM 2^3 EXPERIMENTAL DESIGNS

The analysis of data obtained from 2^3 experimental designs (see Section 2.4.1) were performed by the software CAT® (Chemometric Agile Tool) version 3.1.2. The design matrix of the full 2^3 DoE is reported in Table 8.

Multiple Linear Regression (MLR) was employed to analyze and interpret the results of the 2^3 full factorial design DoE. Regression analysis focuses on the relationship between a dependent variable, called the response variable (i.e., Product composition, $Y_{product}$, χ, Y_{diesel}, and $S_{HDO/DCOx}$), and one or more independent variables, called predictors (i.e., A, B and C in Table 8) [293].

In general, the MLR model characterizes the linear relationship between a single response variable and a set of predictor variables [294]. The MLR model is expressed as in Equation 2.13:

$$Y = \beta_0 + \sum_{n=1}^{k} \beta_n x_n + \sum \sum_{n<q} \beta_{nq} x_n x_q + \varepsilon \qquad \textit{Equation 2.13}$$

Where: Y is the dependent variable; x_n are the independent variables; β_0 is the intercept; β_n are the coefficients of the independent variables, β_{nq} = half of interaction effect between factors, and ε represents the error term.
For the 2^3 factorial plan of this work, the general MLR model is:

$$Y = \beta_0 + \beta_A x_A + \beta_B x_B + \beta_C x_C + \beta_{AB} x_A x_B + \beta_{AC} x_A x_C + \beta_{BC} x_B x_C \qquad \textit{Equation 2.14}$$

Where: x_A is the temperature; x_B is the catalyst-to-oil weight ratio; x_C is the reaction time; Y is the response variable (i.e., $A\%$ of product composition, $Y_{product}$, χ, Y_{diesel}, and $S_{HDO/DCOx}$); β_0 is the intercept of the regression line; β_A, β_B and β_C are the coefficients of the linear terms for the factors x_A, x_B and x_C; and β_{AB}, β_{AC} and β_{BC} are the two-way interaction coefficients, representing the combined effect of the factors $x_A x_B$, $x_A x_C$ and $x_B x_C$.

Replicates at the central point (i.e., From test_09 to test_11 of Table 8) were used to estimate the error of the experimental measurements (i.e., value of standard deviation) of each parameter analyzed (i.e., *A%* of product composition, $Y_{product}$, χ, Y_{diesel}, and $S_{HDO/DCOx}$).

The CAT® software performs MLR through the instruction "*Model Computation*", according to the Ordinary Least Squares (OLS) method: model coefficients that minimize the sum of squares errors (or residuals) were found [295]. Using the OLS method, the coefficients of the model (β's in Equation 2.14) were determined, together with their standard deviation and statistical significance. Remember that the lower the calculated P-value, the higher the "statistical significance" of the coefficient. The P-value is compared to a predefined significance level, typically set at 0.05 (or 5%). If the p-value is ≤ 0.05, the parameter is deemed statistically significant [296]. Conversely, if the P-value is > 0.05, the parameter is considered not significant, indicating that there is insufficient evidence to conclude that it has a real effect [296].
Regarding the fitting of the experimental data, the Explained Variance ("*Expl Var*" [297], Equation 2.15) was calculated and reported.

$$Expl.Var\ [\%] = R^2 \cdot 100 \qquad \textit{Equation 2.15}$$

where R^2 is the coefficient of determination. In other words, a high value of *Expl. Var* suggests that the model is very effective in representing the experimental data and explaining the observed variability [297].

To further evaluate the theoretical quality of the model's predictions, model validation was performed using the "*leave-one-out*" cross-validation method [298]. In this approach, each iteration involves using one observation as the test set and the remaining observations as the training set [299]. Consequently, the percentage of Explained Variance in Cross-Validation (henceforth "*CV Expl. Var*") was calculated to determine how well the model generalizes to unseen data [298]. *CV Expl. Var* was calculated similarly to *Expl. Var*, but using the results obtained from cross-validation data. *Expl. Var* calculated on a single dataset can be influenced by overfitting, where the

model may fit the training data too closely [300]. In contrast, *CV Expl. Var* helps address this issue by offering a more balanced evaluation, as it assesses the model performance across multiple subsets of data and is less susceptible to the peculiarities of any single dataset [300].

Additionally, it was calculated $SS_{pure\ quadratic}$, that is used to assess whether adding quadratic terms to the model significantly improves the explanation of the variability in the response compared to a model without quadratic terms [285]. In unreplicated 2^k factorial designs of DoE with n_C observations at the center point, the pure error mean square (MS_E) of a response *Y* can be estimated using the center observations y_{jC}, as indicated in Equation 2.16 [285]. The degrees of freedom for this estimation are n_{C-1}. Additionally, the pure quadratic curvature ($SS_{pure\ quadratic}$) of the response surface can be calculated using Equation 2.17, where $n_F=2^k$ represents the number of unreplicated factorial observations. The calculated MS_E and $SS_{pure\ quadratic}$ can be incorporated into the ANOVA of the unreplicated factorial observations. MS_E serves as the reference for all F-tests, while the ratio $SS_{pure\ quadratic}/MS_E$ provides the statistics for testing the pure quadratic curvature hypothesis (Equation 2.18) [285]. If the F-test fails to reject the null hypothesis H_0 (indicating no significant quadratic effect), the response *y* can be modeled using a first-order main effects model with interactions (Equation 2.13) [285]. Conversely, if H_0 is rejected, indicating a significant quadratic effect (H_1 is true), a second-order model must be employed (Equation 2.19), which requires a more complex DoE for regression of the coefficients β [285].

$$MS_E = \frac{\sum_{j=1}^{n_C}\left(y_{jC} - \bar{y}_C\right)^2}{n_C - 1} \qquad \textit{Equation 2.16}$$

$$SS_{pure\ quadratic} = \frac{n_F n_C (\bar{y}_F - \bar{y}_C)}{n_F + n_C} \qquad \textit{Equation 2.17}$$

$$H_0 : \sum_{n=1}^{k} \beta_{nn} = 0 \quad ; \quad H_1 : \sum_{n=1}^{k} \beta_{nn} \neq 0 \qquad \textit{Equation 2.18}$$

$$y = \beta_0 + \sum_{n=1}^{k} \beta_n x_n + \sum\sum_{n<q} \beta_{nq} x_n x_q + \sum_{n=1}^{k} \beta_{nn} x_n^2 + \varepsilon \qquad \textit{Equation 2.19}$$

Following the statistical analysis are produced (i) contour plots and (ii) surface response of each analyzed response. The contour plot is a two-dimensional representation useful for visualizing simple relationships, while the response surface provides a more detailed three-dimensional representation, allowing to explore interactions and complexities between variables in a more complete way. In summary, the contour plot is a two-dimensional representation of the response surface. Both provide complementary information on the relationships between independent variables and a dependent variable, but the contour plot provides a simpler and more direct view, The response surface allows a more detailed and complex representation of interactions.

2.5.4.2 Analysis of data from FCCCD

The data analysis from FCCCD (refer to Section 2.4.3) was conducted using the same software CAT® used for the analysis of 2^3 experimental design in Section 2.5.4.1. The full design matrix for this FCCCD is presented in Table 9.

In this case, the MLR model used was the one presented in Equation 2.19, which is given in its explicit form in Equation 2.20:

$$Y = \beta_0 + \beta_A x_A + \beta_B x_B + \beta_D x_D + \beta_{AB} x_A x_B + \beta_{AD} x_A x_D + \beta_{BD} x_B x_D + \beta_{AA} x_A^2 + \beta_{BB} x_B^2 + \beta_{DD} x_D^2 \qquad \textit{Equation 2.20}$$

Where: x_A is the temperature; x_B is the catalyst-to-oil weight ratio; x_D is the stirring speed; Y is the response variable (i.e., $A\%$ of product composition, $Y_{product}$, χ, Y_{diesel}, and $S_{HDO/DCOx}$); β_0 is the intercept of the regression line; β_A, β_B and β_D are the coefficients of the linear terms for the factors x_A, x_B and x_D; β_{AB}, β_{AD} and β_{BD} are the two-way interaction coefficients, representing the combined effect of the factors $x_A x_B$, $x_A x_D$ and $x_B x_D$; β_{AA}, β_{BB} and β_{DD} are the coefficients of the quadratic terms for the factors x^2_A, x^2_B and x^2_D.

To estimate the values of standard deviation, which is essential for determining the statistical significance of the factors (i.e., T, Υ, and ω) and their interactions, the standard deviation values for each parameter analyzed (i.e., *A%* of the product composition, $Y_{product}$, χ, Y_{diesel}, and $S_{HDO/DCOx}$) are based on measurements taken at the central point of the 2^3 DoE for the Ni-Mo-Al catalyst (see Section 2.4.1). The assumption of this method is that the standard deviation values obtained from the central point data provide a reliable estimation of the system's natural variability. This assumes that the central point measurements accurately reflect the experimental system's repeatability and precision, enabling a reliable assessment of the significance of the factors and their interactions.

As in the analysis of the 2^3 DoE, the *Exp. Var* (Equation 2.15) and the *CV Exp. Var* were also calculated. Additionally, contour plots and response surfaces are provided, as detailed in Section 2.5.4.1.

2.6 PRELIMINARY EXPERIMENTAL STUDIES-AWAITING COMPLETION

In the final phase of this doctoral program, additional experimental campaigns were conducted. These initial campaigns serve as a foundation for future studies, which will undoubtedly be carried out with clearly defined experimental campaigns.

These preliminary experimental tests focused on: (i) investigating the effect of stirring speed on the NiCoMo catalyst (see Section 2.6.1), and (ii) exploring the use of WCO as a raw material for DO production (see Section 2.6.2).

2.6.1 PRELIMINARY MIXING TESTS ON NICOMO CATALYST

Preliminary tests were conducted to determine whether the reactor's rotation speed (RS) (ranging from 200 to 700 rpm) could influence the DO yield and

the composition of the obtained product for NiCoMo catalyst. A total of 6 preliminary tests were carried out.

In this case, only the RS was varied (i.e., 200, 300, 400, 500, 600 and 700 rpm). All the other parameters were maintained constant: temperature at 280°C, H_2 partial pressure at 40 bar at RT, reaction time of 2 hours; solvent-to-oil mass ratio of 10:1; catalyst-to-oil weight ratio at 4%$_{w/w}$; and amount of rapeseed oil at 2 g. The testing procedure followed the same method outlined in Section 2.4, while the product and data analysis followed the approach outlined in Section 2.5.

2.6.2 DO TESTS WITH WCO

As mentioned in Section 2.3, tests were carried out on the three catalysts (i.e., NiCoMo, ZnCoMo, and Ni-Mo-Al) using WCO as the feedstock. These tests represented a preliminary exploration of the usability of catalysts with more prohibitive feedstock.

For each catalyst, two experiments with WCO as feedstock were conducted at temperatures of 280°C and 320°C, while maintaining constant parameters: (i) reaction time (i.e., 2 h), (ii) stirring speed (i.e., 200 rpm), (iii) catalyst-to-oil weight ratio (i.e., 10 %$_{w/w}$), (iv) mass of WCO (i.e., 2 g), and (v) solvent-to-oil weight ratio (i.e., 10:1). Also in this case, the procedure for performing the tests was the same as that described in Section 2.4. The product and data analysis followed the approach outlined in Section 2.5.

These preliminary tests were conducted to determine whether the catalysts would exhibit the same or similar performance with WCO as they did with fresh rapeseed oil. Additionally, the experiments aimed to assess whether waste could be effectively used to produce green diesel in a sustainable way, in agreement with Principles of Green Chemistry (see Section 1.2).

3. RESULTS OF AS-SYNTHESIZED CATALYSTS CHARACTERIZATIONS

The three catalysts discussed in this PhD thesis, i.e., NiCoMo, ZnCoMo, and Ni-Mo-Al (see Section 2.1), were characterized using the techniques outlined in Section 2.2. Characterizations of the NiCoMo and ZnCoMo catalysts were conducted to verify the success of replicating Velasquez et al. [259]'s coprecipitation method, and to compare the results with those obtained by their study. Additional characterizations were performed to gain deeper insights into the properties, structure, and functionality of these two catalysts.

For the Ni-Mo-Al catalyst, synthesized using an innovative solventless method currently under review for patent application (as mentioned in Section 2.1.2), all characterizations yielded valuable insights into its structure and functionality.

Therefore, this Chapter discusses the characterizations results of the as-synthetize NiCoMo and ZnCoMo, and Ni-Mo-Al catalysts individually.

3.1 NiCoMo and ZnCoMo catalyst characterization results

In this section, the results of all characterizations (see Section 2.2 for further details about characterization techniques) of NiCoMo and ZnCoMo catalysts are presented and compared to Velasquez et. al. [259]'s ones.

3.1.1 ICP-MS results

Table 10 shows the ICP-MS results of as-synthesized NiCoMo and ZnCoMo catalysts, with reference to the nominal values calculated based on the initial moles of metal introduced during the synthesis process (see Section 2.1.1).

Table 10 Results of NiCoMo and ZnCoMo analysis by ICP-MS in terms of elemental molar ratios.

	Ni/Mo (mol/mol)	***Ni/Co (mol/mol)***	***Co/Mo (mol/mol)***
Nominal	0.09	0.11	0.85
As-synthesized NiCoMo	0.08	0.08	1.03
	Zn/Mo (mol/mol)	***Zn/Co (mol/mol)***	***Co/Mo (mol/mol)***
Nominal	0.09	0.11	0.85
As-synthesized ZnCoMo	0.13	0.11	1.26

Since Velasquez et al. [259] did not conduct this analysis, the results were only compared with the nominal values (see Table 10). The Table 10 indicates that the molar ratios of the catalyst metals differed reasonably from the expected nominal values, with a relative slight excess of Co on Mo. Furthermore, the ZnCoMo catalyst exhibited a more pronounced excess of Co relative to Mo when compared to the NiCoMo catalyst.

Overall, these findings (see Table 10) indicate that the syntheses were successful, resulting in catalysts with compositions that, although slightly different from the nominal values, remain close to the intended design.

3.1.2 FT-IR results

Figure 22 reports the FT-IR ATR spectra of NiCoMo and ZnCoMo.

The spectra of the NiCoMo and ZnCoMo catalysts in Figure 22 qualitatively correspond to those presented in "Figure S1(b)" of Velasquez et al. [259].

Similar bands were observed in the range of 950-750 cm^{-1}, attributed to the symmetric and asymmetric stretching of O-Mo-O [259], and in the range of 700-400 cm^{-1}, corresponding to the stretching vibrations of Co/Ni/Zn-O-Mo [259]. In contrast to the findings of Velasquez et al. [259], no peaks were detected in the 4000-1000 cm^{-1} range (i.e., characteristic zones for organic components) in the current samples, as they were analyzed in their calcined state. The absence of these peaks may imply that the organic precursor of the salt (see Section 2.1.1 for details about reactants), used during the syntheses, were effectively removed during the calcination process, leading to a oxide structure in the final catalyst.

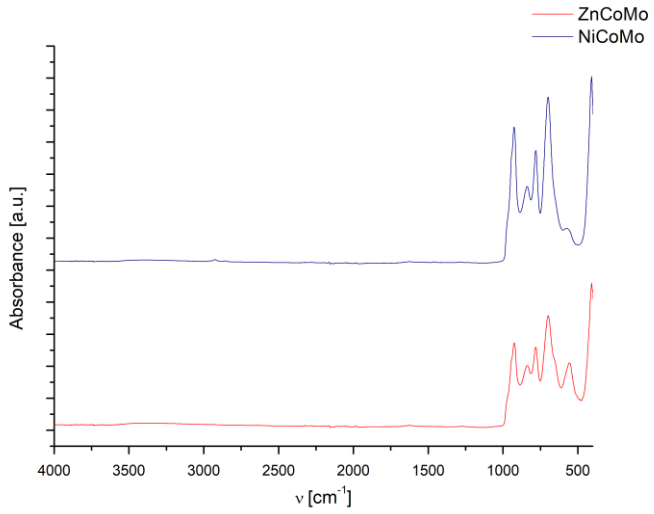
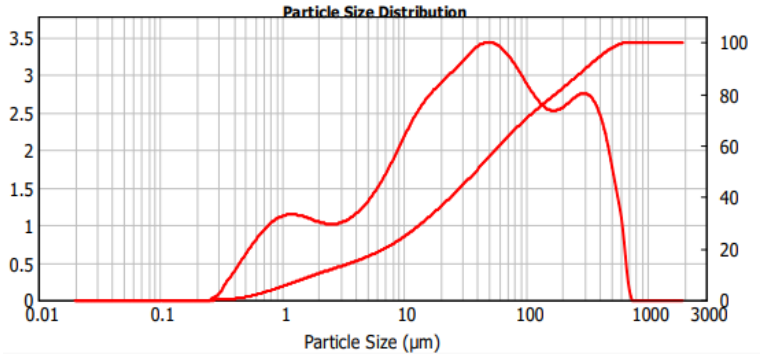


Figure 22 FT-IR results of NiCoMo and ZnCoMo catalyst.

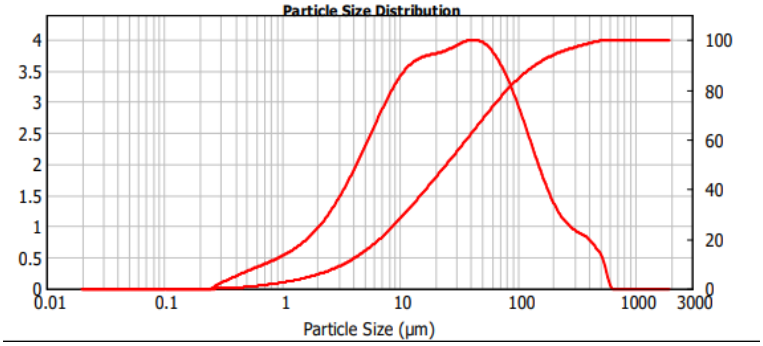
3.1.3 PSD MEASUREMENTS

The PSDs of NiCoMo and ZnCoMo catalysts are presented in Figure 23 (a) and Figure 23 (b), respectively.

The PSD of NiCoMo is multimodal, with bells between about 0.3-2.5 µm, 3-150 µm and 150-700 µm (Figure 23 (a)). The PSD of ZnCoMo is closer to unimodal features (Figure 23 (b)), with one approximate bell extended in the range between 0.3 and 600 µm (even though minor shoulders corresponding to the multimodality of Figure 23 (a) can be found). The 10^{th} (*d(0,1)*), 50^{th} (*d(0,5)*) and 90^{th} (*d(0,9)*) percentiles of the cumulative PSDs and the average particle diameter *d(3,2)* of NiCoMo and ZnCoMo were reported in Table 11.



(**a**)



(**b**)

Figure 23 Average and cumulative PSD of (a) NiCoMo and (b) ZnCoMo catalysts

For NiCoMo, about 10% of the particles have a size less than approximately 2 µm (*d(0,1)* in Table 11). In contrast, for ZnCoMo, this value is larger (i.e., 3 µm, Table 11), indicating that a higher proportion of particles are found in the larger sizes at the lower end of the PSD compared to NiCoMo.

Table 11 Statistical parameters of PSD of NiCoMo and ZnCoMo.

	NiCoMo	***ZnCoMo***
d(0,1) [µm]	2	3
d(0,5) [µm]	39	25
d(0,9) [µm]	313	142
d(3,2) [µm]	6	7

The median particle size (50th percentile) for NiCoMo is significantly larger (39 µm, Table 11), compared to ZnCoMo (25 µm, Table 11). This means that NiCoMo has a larger central particle size than ZnCoMo. The 90th percentile

indicates that a greater proportion of particles in NiCoMo are significantly larger (i.e., 313 µm in Table 11) than ZnCoMo (i.e., 142 µm in Table 11). Therefore, the size distribution for NiCoMo is broader (see Table 11), characterized by a prevalence of larger particles, particularly in the upper size range. In contrast, ZnCoMo exhibits a more concentrated distribution, featuring relatively smaller average and median particle sizes.

The Sauter mean diameter (*d(3,2)* in Table 11) is higher for ZnCoMo (i.e., 7 µm) compared to NiCoMo (i.e., 6 µm).These values in the order of 10^0 µm should mitigate the dominancy of intraparticle transport phenomena on the overall rate [301].

3.1.4 XRD SPECTRA OF NICOMO AND ZNCOMO

Figure 24 reports the XRD outcomes of NiCoMo and ZnCoMo catalysts, acquired and analyzed by ICPEES (University of Strasbourg).

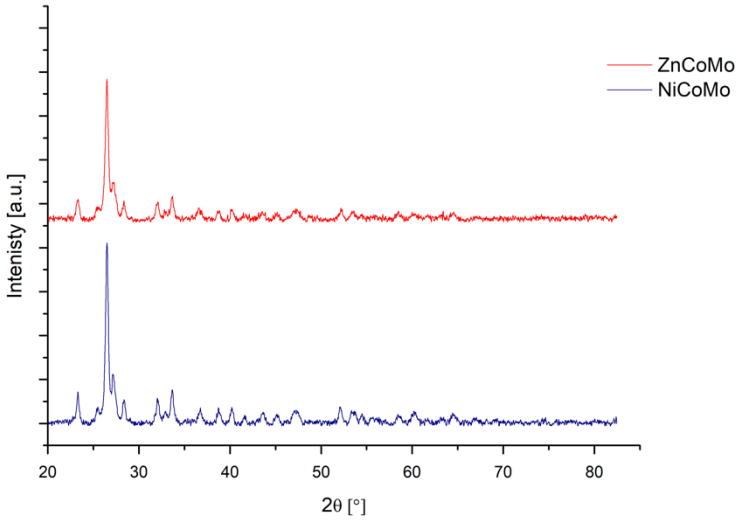


Figure 24 XRD patterns of NiCoMo and ZnCoMo catalysts.

These patterns (in Figure 24) revealed identical structures with high crystallinity for both samples (between 20 and 40°), with no peaks detected beyond 65°, consistent with the findings of "Figure 2b" of Velasquez et al. [259]. The similarities in crystal structures to those reported in the original synthesis paper [259] further supported the consistency of the catalyst

syntheses. Unfortunately, on the XRD pattern of NiCoMo and ZnCoMo (Figure 24) the main ray is not well separated; therefore, any determination of the crystallite particle size was evaluated as misleading.

3.1.5 RESULTS OF PORE ANALYSES

The results of N_2-physisorption isotherms of NiCoMo and ZnCoMo are reported in Figure 25 and Figure 26, respectively, acquired and analyzed by ICPEES (University of Strasbourg).

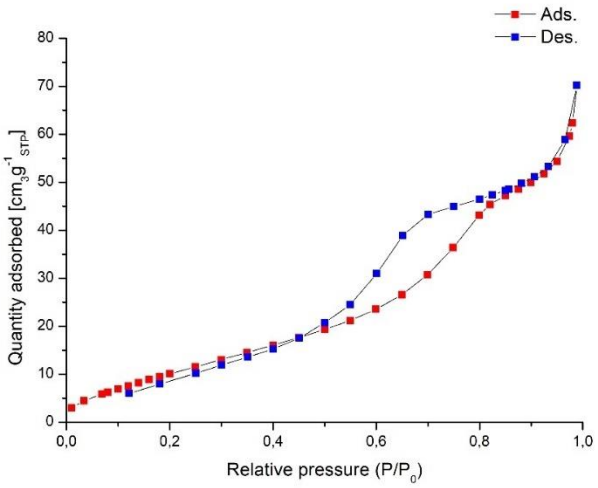


Figure 25 N_2-physisorption isotherm of NiCoMo catalyst.

The N_2-physisorption isotherm of NiCoMo, shown in Figure 25, indicated the catalyst's slightly porous nature. The isotherm corresponds to an IUPAC Type IV(a) isotherm [302] (characteristic of mesoporous materials) due to the presence of hysteresis (Figure 25). Additionally, the terminal asymptotic region at high relative pressure aligned with IUPAC Type II isotherms, typically associated with macroporous or nonporous adsorbents [302]. The shape of the hysteresis loop in Figure 25 could be attributed to IUPAC Type H_2(b), which is commonly observed in materials with complex pore structures that exhibit mesoporosity [302], that may improve the accessibility of reactants to active sites, promoting diffusion and adsorption, which is critical in reactions involving larger molecules [303, 304]. The combination of Type IV(a) and Type II isotherms suggested the presence of both mesopores and macropores, which can significantly impact catalyst performance by

providing a hierarchical pore structure that enhances surface area, mass transport, and the accessibility of active sites [305].

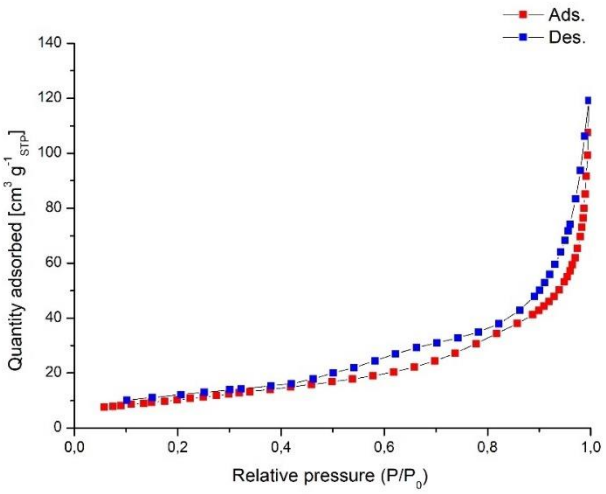


Figure 26 N_2-physisorption isotherm of ZnCoMo catalyst.

The N_2-physisorption isotherm of the ZnCoMo catalyst, shown in Figure 26, exhibited characteristics of both Type IV(a) (hysteresis) and Type II (asymptotic behavior at high relative pressure) isotherms [302], with the Type II features being more pronounced compared to Figure 25. This suggests that ZnCoMo is also a slightly porous material.

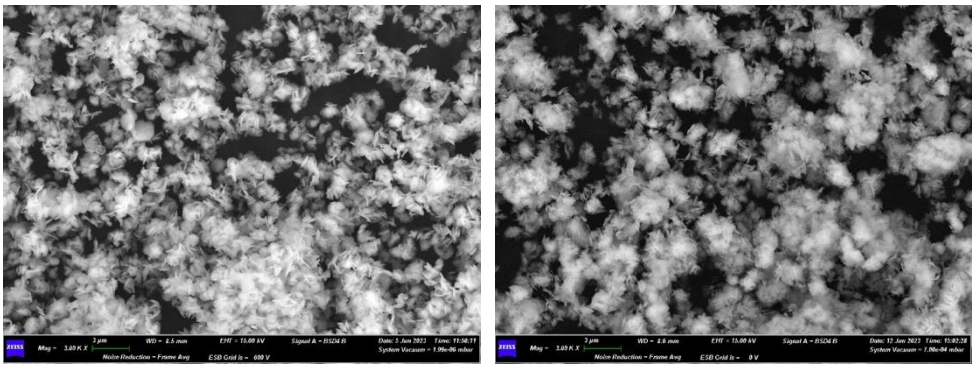
The S_{BET} (Equation 2.5, Section 2.2.6), V_{BJH}, and d_{BJH} (Equation 2.7, Section 2.2.6) values in Table 12 of NiCoMo and ZnCoMo supported the qualitative analysis of the isotherm shapes presented in Figure 25 and Figure 26, quantifying characteristics indicative of slightly porous materials. The textural properties of both NiCoMo and ZnCoMo were comparable. Furthermore, it is important to highlight that the S_{BET} (values for the current NiCoMo and ZnCoMo in Table 12) were consistent with those reported by Velasquez et al., which were 32 m²/g and 27 m²/g, respectively [259].

Table 12 S_{BET}, V_{BJH}, and d_{BJH} of NiCoMo and ZnCoMo.

Sample	S_{BET} (m^2/g)	V_{BJH} (cm^3/g)	d_{BJH} (nm)
NiCoMo	45	0.09	6
ZnCoMo	39	0.11	5

3.1.6 NiCoMo and ZnCoMo SEM-EDS

The results of SEM analyses of NiCoMo and ZnCoMo are reported in Figure 27 (a) and Figure 27 (b), respectively.



(**a**) (**b**)

Figure 27 SEM micrographs at 3000x magnification of as-synthesized catalysts: (a) NiCoMo and (b) ZnCoMo.

The morphological arrangement of NiCoMo and ZnCoMo included lamellar shapes (Figure 27 (a) and (b)): this morphology, as proposed by Velasquez et al. [259], could indicated a layered or structured composition. Additionally, it was observed that morphology is uniform, with the lamellar structure being evenly distributed. A high-magnification images of SEM analysis, reported in Figure C 1 in Addendum C, detailed the morphology of the catalysts.

In addition, the two EDS analyses, in Figure 28 (a) for NiCoMo and Figure 28 (b) for ZnCoMo, highlighted that in both catalysts the three component metals are uniformly distributed, .which aligns well with the primary objectives of coprecipitation.

The detailed SEM-EDS spectra of the two catalysts are presented in Figure C 2 and Figure C 3 of Addendum C.

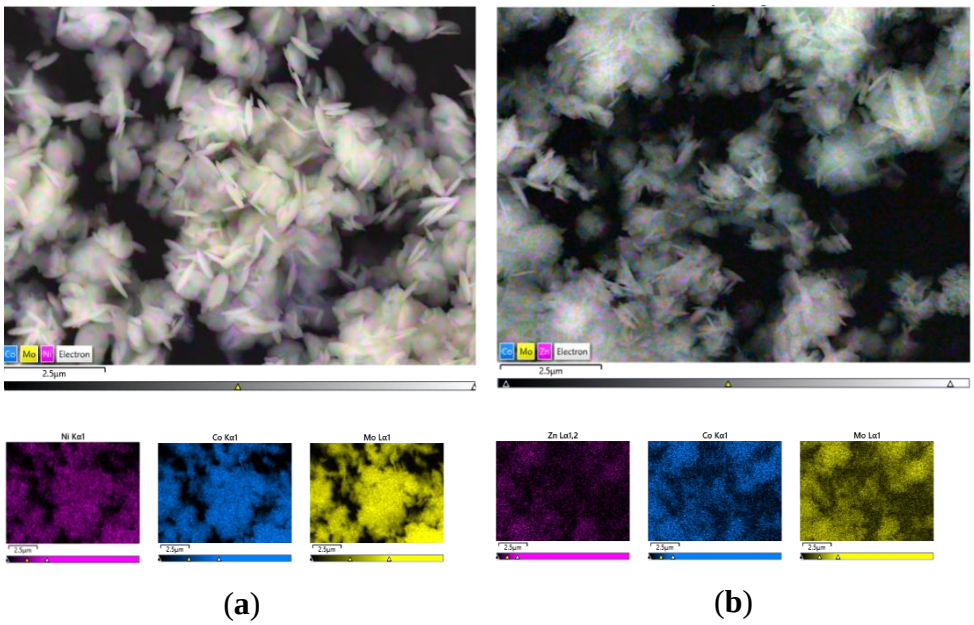


Figure 28 SEM-EDS analyses with elemental maps of as-synthesized catalysts: (a) NiCoMo (Ni = magenta; Co = blue; Mo = yellow) and (b) ZnCoMo (Zn = magenta; Co = blue; Mo = yellow).

3.1.7 TPR Results

TPR profiles, acquired and analyzed by ICPEES (University of Strasbourg), of NiCoMo and ZnCoMo catalysts are presented in Figure 29.

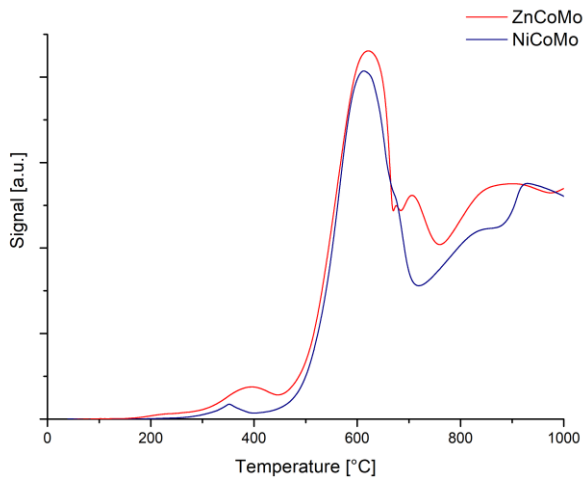


Figure 29 TPR profiles of NiCoMo and ZnCoMo catalysts.

The profiles for both catalysts are comparable and align with the literature [259]. Four peaks were identified at the following temperatures: (i) 350-400°C and (ii) 630°C for both samples; (iii) 700°C specifically for ZnCoMo;

and (iv) 850-900°C for both samples. The reduction temperatures reported by Velasquez et al. [259] are lower, likely due to variations in the TPR analysis conditions (30 mL min^{-1} and 10°C min^{-1} in [259] compare to 50 mL min^{-1} and 10°C min^{-1} in this case) or differences in the particle size of their catalyst (which was not specified).

Peak (i) might be attributed to the reduction of Ni^{2+} strongly interacting with the support [239], or to the reduction of Co^{3+} to Co^{2+} [141]. Since ZnO is not reducible under the studied conditions, it may facilitate the reduction of Co^{3+} [306]. Peak (ii) was likely related to the reduction of the β-$CoMoO_4$ phase, resulting in an equimolar mixture of $Co_2Mo_3O_8$ and Co_2MoO_4 [307]. Meanwhile, peaks (iii) and (iv) could correspond to the reduction of the metals occurring at higher temperatures [307].

3.1.8 TPD-H_2 Results

Figure 30 illustrates the preparative TPR profiles for the NiCoMo and ZnCoMo samples before TPD-H_2, obtained at 320°C for 4 hours, acquired and analyzed by ICPEES (University of Strasbourg).

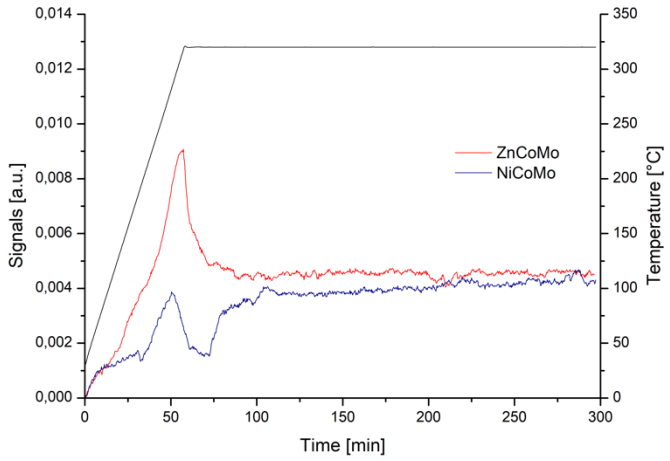


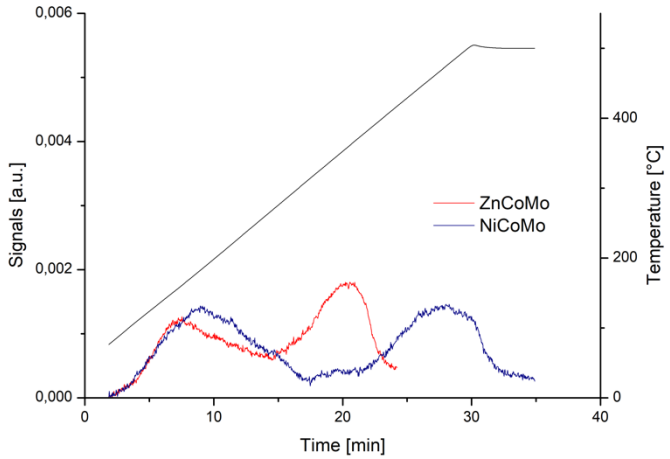
Figure 30 Time profiles of TPR preparative procedure (i.e., 320 °C, 4 h) for NiCoMo and ZnCoMo before TPD-H_2.

It's important to note that the preparative TPR (in Figure 30) of the samples conducted prior to TPD-H_2 was designed to closely mimic the actual in-situ pre-reduction performed before each experimental DO test (i.e., 4 hours at

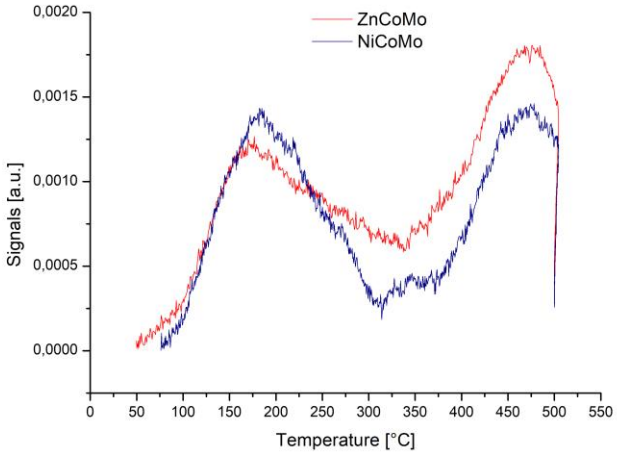
320°C, for further details refers to Section 2.4). While the 320°C for 4 hours did not fully reduce the metal oxides in these samples, as indicated by the TPR results shown in Figure 29, it appeared sufficient to partially reduce Ni^{2+} and Co^{3+}, which were previously identified in TPR around 350-400°C (Figure 29). Thus, this preparatory step facilitated the initial activation of the catalysts for the experimental tests.

Additionally, the TPD-H_2 preparative reduction was carried out at atmospheric pressure with 10% vol H_2, whereas the actual in-situ pre-reduction prior to each experimental DO run was conducted at an initial H_2 partial pressure of 60 bar at RT (see Section 2.4). The H_2 consumption for the reduction of NiCoMo under the conditions outlined in Figure 30 was measured at 1.20 mmol H_2/g, compared to 0.0728 mmol H_2/g for the peak family (i) in the TPR conditions (Figure 29). For ZnCoMo, the H_2 consumption in these conditions was 2.05 mmol H_2/g, in contrast to 0.50 mmol H_2/g for the peak family (i) in the TPR conditions (Figure 29). These values suggest that the preparative reduction step effectively facilitated the reduction of Ni^{2+} and Co^{3+}, as well as the mixed CoMo-oxide phase.

The TPD-H_2 profiles for the NiCoMo and ZnCoMo samples are shown in Figure 31 (a, b).



(**a**)



(**b**)

Figure 31 Results of TPD-H_2: (a) time profiles of TPD-H_2 for NiCoMo and ZnCoMo; (b) temperatures profiles of TPD-H_2 for NiCoMo and ZnCoMo.

The H_2 desorption appeared to be linked to two distinct active sites, as evidenced by two desorption steps: the first peak occurs around 175°C (Figure 31 (a, b)), followed by a second peak around 475°C (Figure 31 (a, b)). These desorption peaks suggested the presence of two different chemical bonds with the metal surface of each catalyst, indicating varying metal environments.

The quantities of desorbed H_2 during these steps are quantified in Table 13 for both catalysts. The amounts of H_2 released during the first peak (175°C) and the second peak (475°C) were quite similar for both catalysts. This strong resemblance in desorption temperatures and amounts of desorbed H_2 suggests that the pre-reduced NiCoMo and ZnCoMo exhibit comparable exposed metallic surfaces and metal environments.

Table 13 H_2 desorption during TPD-H_2 of NiCoMo and ZnCoMo samples.

Sample	***First peak*** (175°C) ($mmol_{H2}/g$)	***Second peak*** (475°C) ($mmol_{H2}/g$)	***Total*** ($mmol_{H2}/g$)
NiCoMo	0.010	0.009	0.019
ZnCoMo	0.008	0.009	0.017

3.2 Ni-Mo-Al catalyst characterization results

This section presented the characterization results for the Ni-Mo-Al catalyst, synthesized using the solventless method outlined in Section 2.1.2.

3.2.1 Ni-Mo-Al ICP-MS results

Table 14 displayed the ICP-MS results for the Ni-Mo-Al catalyst. These results demonstrated a good alignment between the nominal and actual molar ratios, indicating that the synthesis method effectively produced a catalyst with the intended composition. The as-synthesized Ni/Al molar ratio (see Table 14) was slightly increased (of 6%) compared to the nominal value. This variation suggests a relative excess of nickel in the final product. Conversely, the Ni/Mo ratio (i.e., 0.535) is lower than the nominal value (of 0.571), indicating a decrease of approximately 6.3 %. This deviation implied that the molybdenum content in the final catalyst might have been somewhat reduced. Additionally, the decrease in the Al/Mo ratio (see Table 14) could indicate that there was an increase in the molybdenum content, as just stated.
The slight variations observed in the as-synthesized ratios suggest that the synthesis process was successful overall, only with minor deviations.

Table 14 ICP-MS results of Ni-Mo-Al catalyst in as-synthetize form.

	Ni/Al (mol/mol)	***Ni/Mo (mol/mol)***	***Al/Mo (mol/mol)***
Nominal	0.667	0.571	0.857
As-synthesized Ni-Mo-Al	0.708	0.535	0.756

3.2.2 FT-IR spectrum of Ni-Mo-Al

The FT-IR ATR results for the Ni-Mo-Al catalyst and the individual oxides, derived from the calcination of their respective salts (refer to Section 2.1.2), were presented in Figure 32.

The FT-IR spectra (Figure 32) revealed that Al_2O_3 and NiO single oxides showed no signals within the selected wavelength range (i.e., from 4000 to 400 cm^{-1}). In contrast, MoO_3 exhibited signals in the range of 1100-400 cm^{-1}. Specifically, peaks between 800 and 700 cm^{-1} were associated with Mo-O-

Mo interactions, while the region between 500 and 600 cm^{-1} corresponds to Mo-O bonding [308]. Additionally, the vibrational bands at 990 cm^{-1} and 870 cm^{-1} were attributed to the stretching vibrations of Mo=O [308]. The peaks at 605 cm^{-1} and 489 cm^{-1} indicated the stretching vibrations of Mo-O-Mo and the vibrations of oxygen atoms coordinated to three molybdenum atoms, respectively [308].

Given these observations and considering the composition of the Ni-Mo-Al catalyst (see Table 14 in Section 3.2.1), which was predominantly composed of MoO_3, its FT-IR signal closely resembled that of MoO_3, albeit with different intensities.

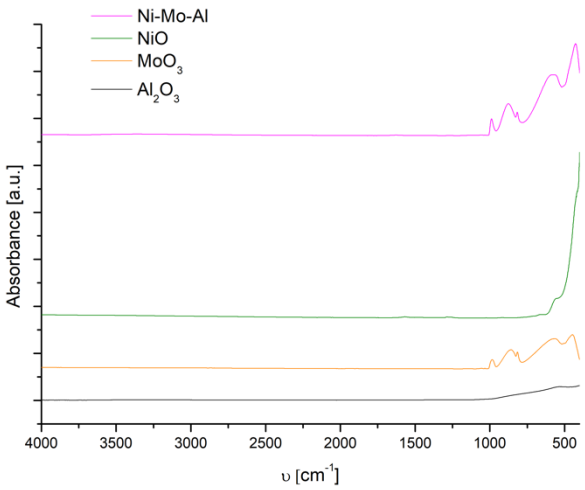


Figure 32 FT-IR spectra of Ni-Mo-Al catalyst and single oxides (NiO, MoO_3 and Al_2O_3).

3.2.3 PSD OF NI-MO-AL CATALYST

The results of the PSD measurements for the Ni-Mo-Al catalyst, presented as both a cumulative curve and an average curve, were shown in Figure 33.

As illustrated in Figure 33, the PSD was bimodal, featuring peaks within two distinct ranges: (i) between 0.3 and 3 µm (with a maximum around 0.8 to 0.9 µm) and (ii) between 3 and 600 µm (peaking at approximately 10 µm).

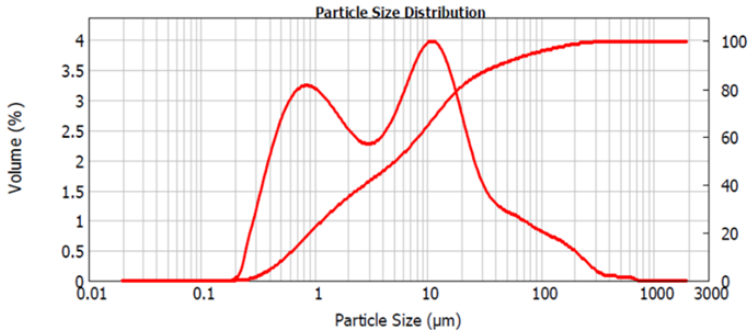


Figure 33 Average and cumulative PSD of Ni-Mo-Al catalyst.

Most of the sample population was concentrated in the range of 0.3 to 50 µm. This information is further detailed in Table 15, which presents the 10th percentile (*d(0.1)*), 50th percentile (*d(0.5)*), and 90th percentile (*d(0.9)*) of the cumulative PSD.

Table 15 Statistical parameters of PSD of Ni-Mo-Al catalyst.

	Ni-Mo-Al
d(0,1) [µm]	0.5
d(0,5) [µm]	5
d(0,9) [µm]	43
d(3,2) [µm]	2

The particle size of the Ni-Mo-Al catalyst was relatively small (refer to the average particle diameter *d(3,2)* in Table 15), which was consistent with the ball milling process used. This small size enabled the neglect of any mass transfer resistance due to intraparticle diffusion [309].

3.2.4 Ni-Mo-Al XRD results

Figure 34 compared the XRD patterns of single oxides (NiO, MoO_3 and Al_2O_3) and Ni-Mo-Al catalyst, all acquired and analyzed by ICPEES (University of Strasbourg).

The XRD analysis of the single oxides (Figure 34) confirmed that NiO and MoO_3 (specifically, molybdite) were successfully obtained at the specified calcination temperatures (refer to Section 2.1.2). However, the structure of Al_2O_3 could not be identified due to its lack of crystallinity.

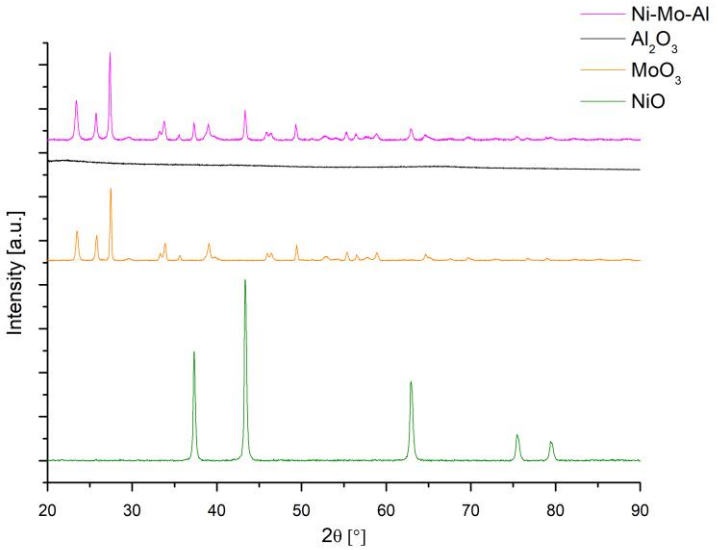


Figure 34 XRD pattern of Ni-Mo-Al catalyst and single oxides (Al_2O_3, MoO_3, and NiO).

The XRD pattern of the Ni-Mo-Al catalyst (Figure 34) revealed the presence of both NiO and MoO_3 phases, but did not indicate the presence of any other phases, including those based on aluminum. However, ICP-MS analysis confirmed the presence of aluminum in the Ni-Mo-Al catalyst (see Table 14 in Section 3.2.1). Therefore, it was reasonable to conclude that the ball milling process resulted in significant physical mixing without inducing chemical reactions between the milled oxides. The XRD results showed that NiO and MoO_3 were separately identified in the catalyst, while aluminum kept its amorphous Al_2O_3 nature.

Table 16 presented the values of average crystallite particle sizes (*D*, Equation 2.2 in Section 2.2.5). Notably, a significant increase in the *D* of NiO crystals, approximately 30%, was observed following the ball milling operation.

Table 16 Crystalline particle size (D, expressed in nm) of NiO and MoO_3 in single and Ni-Mo-Al catalyst.

Sample/Phase	***NiO [nm]***	***MoO_3 [nm]***
NiO single oxide	33	-
MoO_3 single oxide	-	47
Ni-Mo-Al catalyst	41	46

3.2.5 Results of pore analysis of Ni-Mo-Al

Figure 35 shows the N_2-physisorption isotherm of Ni-Mo-Al catalyst, acquired and analyzed by ICPEES (University of Strasbourg).

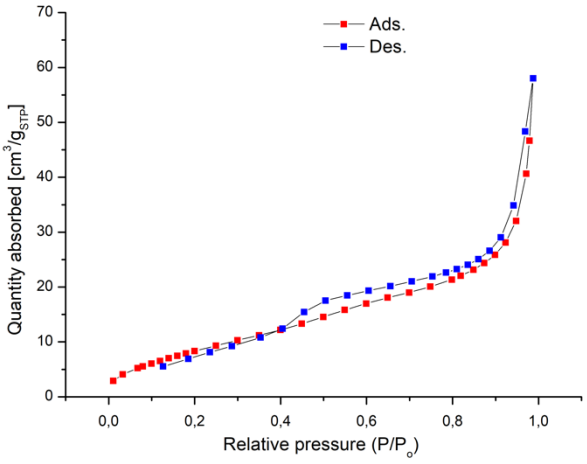


Figure 35 N_2-physisorption isotherm of Ni-Mo-Al catalyst.

The isotherm for the Ni-Mo-Al catalyst in Figure 35 indicated a low porosity linked to small pore sizes. Additionally, the sharpness of the curve suggested potential particle coalescence, which aligned with the concept of a physical mixing of very finely milled materials. The isotherm exhibited characteristics of Type IV(a) (hysteresis) and Type II (vertical asymptote at high relative pressure) according to IUPAC standard isotherms [302]. Specifically, Type IV(a) isotherm with hysteresis is indicative of mesoporous adsorbents with cylindrical pores wider than approximately 4 nm, while Type II behavior is typical of multilayer adsorption on non-porous or macroporous adsorbents [302]. Similar characteristics were found for NiCoMo and ZnCoMo catalysts (see Section 3.1.5).

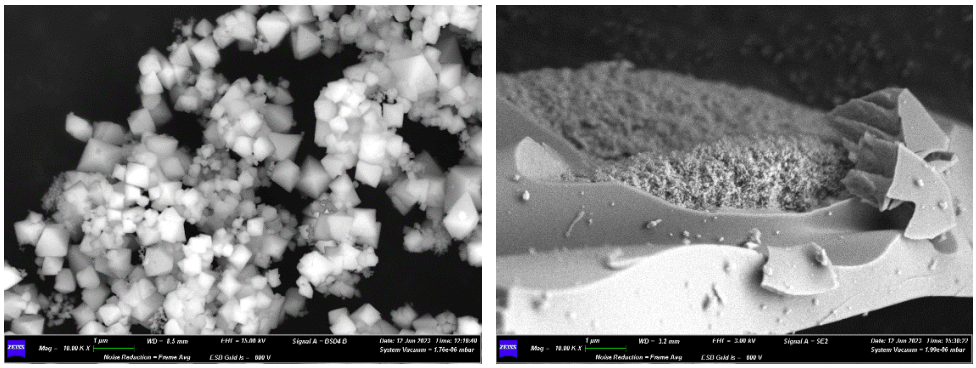
The Ni-Mo-Al catalyst exhibited a specific surface area (S_{BET}, Equation 2.5) of 35 m²/g, a BJH pore volume (V_{BJH}) of 0.06 cm³/g, and a BJH pore diameter (d_{BJH}, Equation 2.7) of 4 nm. These values were slightly lower compared to the two previously evaluated catalysts (see Section 3.1.5). The obtained measurements reinforced the findings of low porosity and small pore sizes in

the Ni-Mo-Al sample, aligning with the qualitative analysis of the isotherm shapes in comparison to IUPAC standards [302].

3.2.6 Results of SEM-EDS analysis for Ni-Mo-Al

Figure 36 gathers SEM analyzes of catalyst and single metals oxide obtained by following the procedure in Section 2.1.2: (i) NiO (Figure 36 (a)); (ii) Al_2O_3 Figure 36 (b)); (iii) MoO_3 (Figure 36 (c)); and (iv) Ni-Mo-Al catalyst (Figure 36 from (d) to (f)).

For NiO, heterogeneously distributed octahedral shapes were observed (Figure 36 (a)), consistent with the findings of Estellé et al. [310], who obtained similar NiO structures through the calcination of nickel nitrates. A detailed view of the NiO octahedral structure at high magnification is presented in Figure C 4 (a) of Addendum C. The Al_2O_3 in Figure 36 (b) has an irregular morphology and reported a detail of an Al_2O_3 flake. A low magnification figure is shown in Figure C 4 (b) of Addendum C. The Al_2O_3 particles had variable size and might appear as agglomerates or granules of various shapes (Figure C 4 (b) of Addendum C), as also underlined by Mohammed et al. [311] in their work. For MoO_3, a lamellar morphology was observed (Figure 36 (c)), consistent with the findings of Yang et al.[312], who reports similar structures resulting from the decomposition of ammonium molybdate at 350°C. A higher magnification image is reported in Figure C 4 (c) of Addendum C, and highlighted the morphology of MoO_3.



(**a**) (**b**)

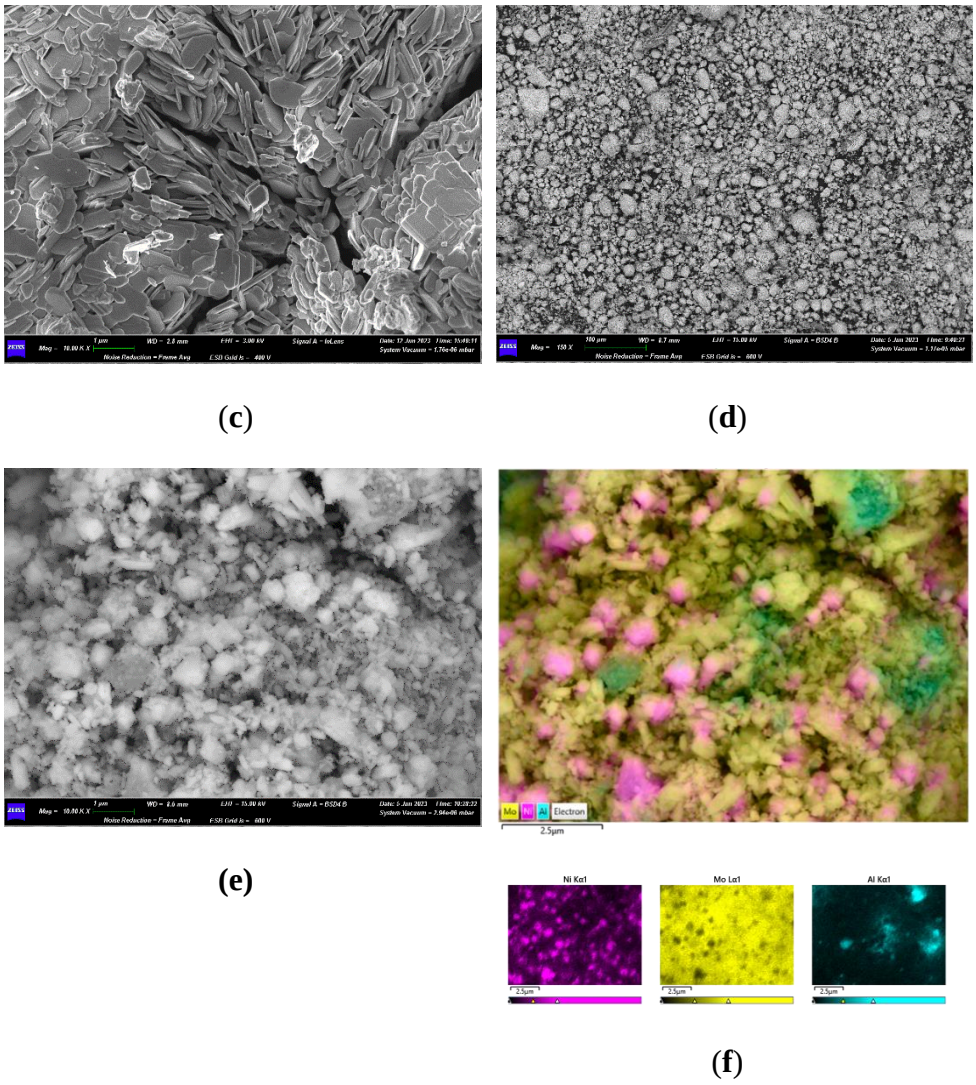


Figure 36 SEM analysis of: (a) calcined NiO at 10kx magnification; (b) calcined Al_2O_3 at 10kx magnification; (c) calcined MoO_3 at 10kx magnification; (d) as-synthesized Ni-Mo-Al catalyst at 150x magnification; (e) as-synthesized Ni-Mo-Al catalyst at 10kx magnification; and (f) SEM-EDS analysis at 10kx magnification.

Figure 36 (d) presents a low magnification overview of the Ni-Mo-Al catalyst. The image revealed that the particles predominantly exhibited an irregular spherical geometry, with variable dimensions; some particles were notably small, others were relatively coarse. In Figure C 4 of Addendum C, a low-magnification SEM image of Ni-Mo-Al is presented, illustrating the dimensions of several particles (in particular, the largest particles were considered), which align with the measurements obtained from PSD analysis. The high-magnification image in Figure 36 (e) confirmed the irregular morphology and the presence of particles with varying sizes, while also highlighting the seemingly porous surface of particles (also visible in Figure

C 4 Figure C 4 SEM images of: (i) NiO at 20kx magnification; (b) Al2O3 at 150x magnification; (c) MoO3 at 20kx magnification; (d) Ni-Mo-Al catalyst at 500x magnification.of Addendum C).

Regarding elemental distribution, EDS analysis in Figure 36 (f) revealed that the catalyst particles were aggregates of Mo and Ni with Al inclusions. This was qualitatively consistent with the relative abundances of elements measured in the bulk Ni-Mo-Al catalyst via ICP-MS (see Section 3.2.1). As a result, it could be assumed that the catalyst composition was uniform, despite the lack of detected chemical interactions between the oxide components, as indicated by XRD (Section 3.2.4).

SEM-EDS spectra of Ni-Mo-Al catalysts are provided in Figure C 5 of Addendum C.

3.2.7 Ni-Mo-Al TPR Results

TPR profiles of Ni-Mo-Al catalyst and oxides (i.e., NiO and MoO_3) are reported in Figure 37, all acquired and analyzed by ICPEES (University of Strasbourg).

Al_2O_3 did not undergo reduction under the TPR (see Section 2.2.9 for TPR details) or DO test conditions (see Section 2.4) used in this study; therefore, it was not analyzed separately by TPR.

From Figure 37, it appeared that NiO sample was reduced in a very large temperature zone (i.e., between 310 and 900°C), probably due to the presence of various NiO particle sizes (underlined in the SEM-EDS analysis, see Figure 36 (f) in Section 3.2.6). At relatively low temperatures, 270–500°C, the reduction curve exhibited a sigmoidal shape. This suggested that complete reduction of NiO to Ni did not occur, as observed by Manukyan et al. [313]. They [313] reported also that the low temperature reduction forms a complex polycrystalline Ni/NiO porous structure with characteristic pore sizes on the order of 100 nm. Complete reduction of NiO to Ni is achieved at high temperatures (i.e., 900-1000°C), as shown in Figure 37.

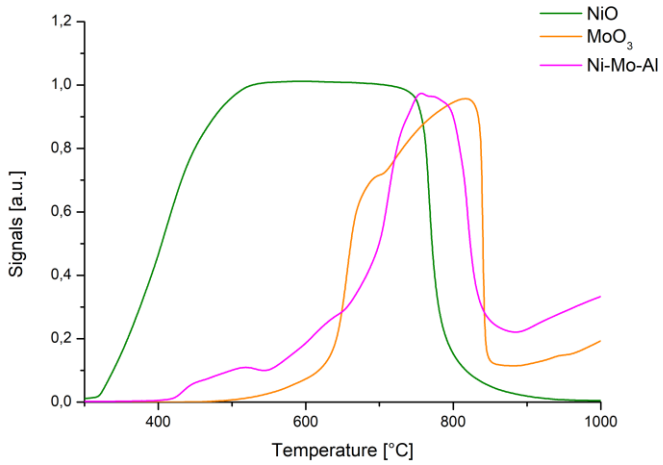


Figure 37 TPR profiles of NiO, MoO_3 and Ni-Mo-Al catalyst samples.

The reduction observed at higher temperature in Figure 37 could be due to higher particle sizes and associated diffusion limitations of H_2, determining slower reduction kinetics compared to heating rate.

MoO_3 sample was reduced at higher temperatures and in a narrower zone (between 500 and 850°C, Figure 37). A very complete study of MoO_3 reduction reports a reduction zone between 330 and 730°C for the same heating rate (10°C min^{-1}) [314].

The Ni-Mo-Al catalyst (see Figure 37) began reduction at a lower temperature (around 400°C) than MoO_3 and has a slightly larger reduction peak (between 400 and less than 900°C), indicating the influence of different oxides in the Ni-Mo-Al catalyst.

3.2.8 Results of TPD-H_2 analysis

Figure 38 shows the preparative TPR profiles of Ni-Mo-Al sample before TPD-H_2, all acquired and analyzed by ICPEES (University of Strasbourg): the temperature (i.e., 320°C) and the dwell duration (i.e., 4 h) chosen for this step were the same used for the in-situ pre-reduction performed before each experimental DO test (for further details refers to Section 2.4). As indicated by the TPR results shown in Figure 37, the preparative TPR conditions were not sufficient for the complete reduction of metal oxides.

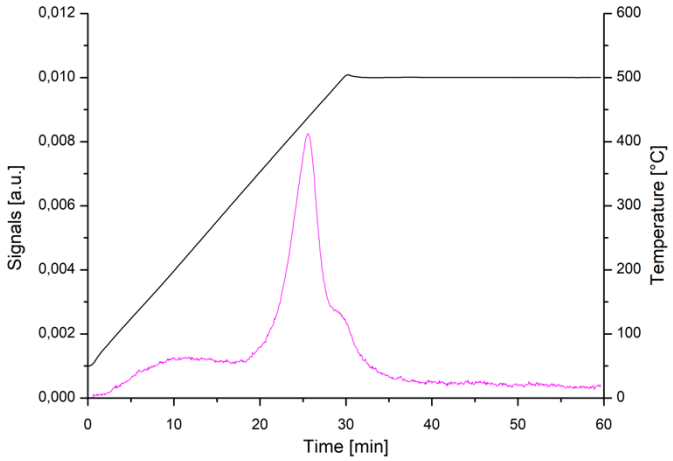
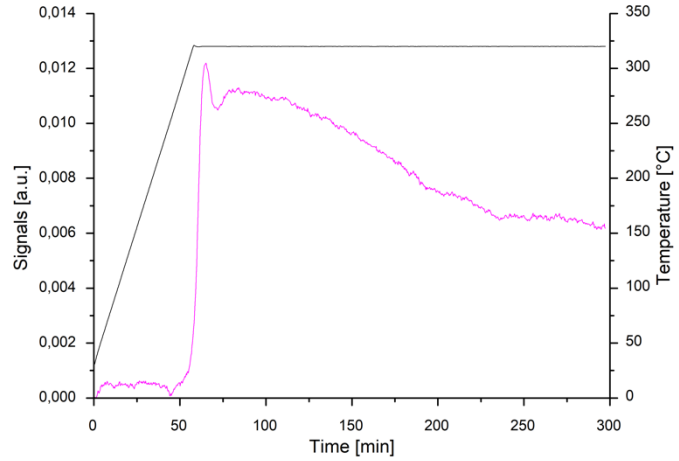


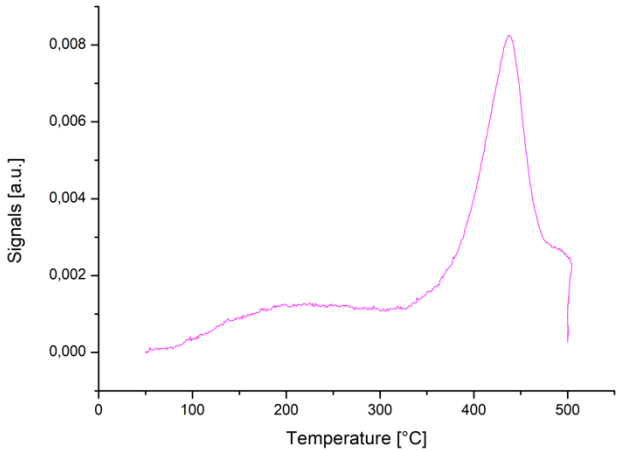
Figure 38 TPR profile of Ni-Mo-Al sample as a preparative step before TPD-H_2 (i.e., 320°C, 4 h).

In addition, as mentioned in Section 3.1.8 for the NiCoMo and ZnCoMo catalysts, the preparative TPD-H_2 reduction was carried out at atmospheric pressure with 10 % vol of H_2, while the actual in situ prereduction before each experimental DO run was conducted at an initial partial pressure of H_2 of 60 bar at RT (see Section 2.4). The H_2 consumption for the reduction in Figure 39 (a) was 3.87 $mmol_{H2}/g$ against the 10.76 $mmol_{H2}/g$ for the full TPR in Figure 37, i.e., 36 % of the full TPR: only 36 % of the required reduction was achieved.

The incomplete reduction of the Ni-Mo-Al catalyst might undermine its performance, as unreduced metal oxides might not participate effectively in catalysis. This limitation could hinder the catalyst's effectiveness in DO reactions. Furthermore, a comparison of H_2 consumption during TPD-H_2 (i.e., 3.87 $mmol_{H_2}/g$) and full TPR (i.e., 10.76 $mmol_{H_2}/g$) suggested that the reduction conditions used were not optimal. However, the catalyst in-situ pre-reduction conditions (see Section 2.4) were constrained by the operational limits of the reactor used for the tests. Since these parameters could not be adjusted, the only feasible conditions were the ones that were implemented. In summary, while incomplete reduction might diminish the catalyst's effectiveness and impact its stability and selectivity during reactions, the only available conditions were those that have been employed.



(**a**)



(**b**)

Figure 39 Results of Ni-Mo-Al TPD-H_2: (a) time profiles of TPD-H_2; (b) temperatures profiles of TPD-H_2.

The TPD-H_2 profile of Ni-Mo-Al sample is reported in Figure 39 (b). The desorption took place in several steps: (i) a first small peak was around 200°C, corresponds to approximately 0.04 $mmol_{H2}$/g of released H_2; (ii) a second higher peak around 440°C with a shoulder just before 500°C corresponding to around 0.18 $mmol_{H2}$/g of H_2 desorbed.

Ameen et al. [315], for NiMo-based catalyst, reports similar TPR peak, between 400-500°C, which are those related to the reduction of NiO and MoO_3.

Zhang et al. [316], for the modified NiO-MoO_3 catalyst with different ratios of Al_2O_3, find a broad and weak peak at low temperature (~242°C), which is attributed to the reduction of free NiO on the catalytic surface.

Instead, Ma et al. [317] find, through Gaussian fitting of the H_2-TPD results of the Ni-based catalysts with different supports, a multi-peak profile. At lower temperatures (<400°C), these peaks are likely attributed to the desorption of weakly chemisorbed H_2 on the surface, facilitated by highly dispersed Ni and a high defect density that may act as traps during hydrogen diffusion [317]. In contrast, the peaks at higher temperatures (>400°C) for Ni/Al_2O_3 may result from the strong chemisorption of H_2 on the catalyst surface. Additionally, they could be related to the desorption of hydrogen that is strongly bonded to the catalyst substrate or trapped hydrogen, which could enhance the H_2 storage capacity [318].

In conclusion, the H_2 desorption profile of the Ni-Mo-Al sample in Figure 39 (b) highlighted the presence of both weakly and strongly adsorbed hydrogen species. Low-temperature peak (200°C) has been associated with weakly adsorbed hydrogen on free or heavily dispersed NiO/MoO_3, while higher-temperature peak (440°C, with a shoulder before 500°C) was associated with stronger hydrogen-catalyst interactions, likely due to the desorption of hydrogen chemisorbed more strongly on the Ni-Mo-Al surface. These results are consistent with the observations of literature references [315], [316], and [317].

3.3 CONCLUSIONS

In this chapter, we examined the characterizations of the as-synthesized catalysts, NiCoMo and ZnCoMo, alongside Ni-Mo-Al. A comprehensive assessment was conducted using various analytical techniques to ensure successful synthesis and to understand the structural and functional properties of these catalysts.

As NiCoMo and ZnCoMo catalysts, the successful replication of the coprecipitation method established by Velasquez et al. [259] was confirmed through ICP-MS analysis, revealing that the elemental molar ratios of the catalysts were close to the nominal values, with slight variations indicating successful synthesis. FT-IR spectroscopy showed that the catalysts retained similar spectral characteristics to those reported in the literature [259], suggesting the effective removal of organic precursors during calcination. The XRD patterns confirmed high crystallinity and consistent structures between the synthesized catalysts and those from Velasquez et al. [259].

PSD measurements revealed a multimodal distribution for NiCoMo, indicating a broader range of particle sizes, while ZnCoMo exhibited a more unimodal distribution with generally smaller average and median particle sizes. This information is critical for understanding the potential impact on catalytic activity and performance.

The N_2-physisorption analysis highlighted the mesoporous nature of both catalysts, with quantified BET surface areas indicating slightly porous characteristics. The presence of hierarchical pore structures in both catalysts could enhance mass transport and accessibility of active sites.

SEM analyses confirmed the uniform distribution of metals in both catalysts, consistent with the coprecipitation objectives. The lamellar morphology observed may contribute to improved catalytic properties.

TPR results indicated the presence of multiple reduction peaks, with significant insights into the reduction temperatures of metal oxides, while TPD-H_2 analyses provided a clear understanding of the hydrogen desorption behavior, revealing the presence of distinct active sites for both catalysts.

Overall, the findings affirm the successful synthesis and characterization of NiCoMo and ZnCoMo catalysts, compared to those synthesized by Velasquez et al. [259].

The characterization of the Ni-Mo-Al catalyst synthesized through a solventless method provided comprehensive insights into its structural and compositional properties.

The ICP-MS results indicated a good alignment between the nominal and actual molar ratios of the catalyst's components. Specifically, the Ni/Al ratio

was slightly higher than expected, suggesting an excess of nickel, while the Ni/Mo ratio was lower than nominal, indicating a potential reduction in molybdenum content.

The FT-IR analysis demonstrated that the as-synthesized Ni-Mo-Al catalyst exhibited spectral characteristics similar to those of MoO_3, indicating the presence of this oxide phase, while the other oxides (NiO and Al_2O_3) did not produce significant signals in the analyzed range. This suggests that the catalyst's properties are predominantly governed by molybdenum oxide interactions.

The PSD results revealed a bimodal distribution with a majority of particle sizes concentrated between 0.3 and 50 μm. The small average particle size also suggests minimal mass transfer resistance, which is beneficial for catalytic applications.

The XRD patterns confirmed the successful formation of NiO and MoO_3, while the amorphous Al_2O_3 was present but not distinctly identifiable. The significant increase in crystallite size for NiO post-ball milling suggests structural changes that may affect catalytic behavior.

The N_2-physisorption results indicated low porosity and small pore sizes for the Ni-Mo-Al catalyst, confirming the presence of mesoporous features. The specific surface area and pore volume measurements were relatively low, reinforcing the notion of a compact structure formed through physical mixing.

The SEM-EDS findings illustrated that the catalyst particles had irregular spherical morphologies with a heterogeneous distribution of elements. This supports the notion of uniform composition across the catalyst despite the lack of chemical interactions among the individual metal oxides, as shown by the XRD analysis.

The TPR results highlighted that NiO underwent reduction over a broad temperature range, indicating varying particle sizes, while MoO_3 exhibited narrower reduction characteristics at higher temperatures. The Ni-Mo-Al catalyst began reduction at lower temperatures, suggesting enhanced catalytic interactions due to the combination of oxides. The TPD-H_2 analysis revealed both weakly and strongly adsorbed hydrogen species on the catalyst surface. The presence of desorption peaks at different temperatures indicates diverse

interaction strengths, which could significantly influence catalytic performance in reactions involving hydrogen.

4. RESULTS OF FEEDSTOCKS CHARACTERIZATION

This section presents the results of the oils characterizations detailed in Section 2.3. Specifically, the fatty acid composition of rapeseed oil and WCO was analyzed.

4.1 RAPESEED OIL CHARACTERIZATION

Table 17 presents the fatty acid composition of the rapeseed oil (see Section 2.3) used as a feedstock of several DO experimental tests of this study (see Section 2.4), expressed as the *A%* of the chromatography peaks (refer to Section 2.3.1 for further details about the characterization method).

Table 17 Composition of commercial rapeseed oil in terms of A% of chromatographic peaks. $C_{n:m}$ is a fatty acid with n carbon atoms and m double bonds.

Fatty Acid	**Composition**	***A%***
Myristic acid	$C_{14:0}$	0.0
Palmitic acid	$C_{16:0}$	4.9
Stearic acid	$C_{18:0}$	1.7
Oleic acid	$C_{18:1}$	64.5
Linoleic acid	$C_{18:2}$	19.5
Linolenic acid	$C_{18:3}$	7.3
Arachidonic acid	$C_{20:0}$	0.6
Cis-9-Eicosenoic acid	$C_{20:1}$	1.2
Behenic acid	$C_{22:0}$	0.0
Erucic acid	$C_{22:1}$	0.3

The fresh rapeseed oil primarily consisted of fatty acids containing 16 and 18 carbon atoms (see Table 17), with minor traces of fatty acids ranging from 20 to 22 carbon atoms. More in detail, rapeseed oil contained predominantly oleic acid ($C_{18:1}$), linoleic acid ($C_{18:2}$), and linolenic acid ($C_{18:3}$), with palmitic acid ($C_{16:0}$) and stearic acid ($C_{18:0}$) present in smaller amounts. It was thus inferred that rapeseed oil had a high content of monounsaturated and polyunsaturated fatty acids, while it had a low percentage of saturated fatty acids. The high oleic acid ($C_{18:1}$) content gave rapeseed oil good oxidative stability, making it particularly suitable for industrial processes, such as green diesel production [319].

4.2 WCO CHARACTERIZATION

Table 18 presented the fatty acids composition of WCO and its source, high oleic sunflower oil, from which the WCO is derived (see Section 2.3 for further details).

Table 18 WCO and high oleic sunflower oil fatty acid compositions, in terms of A% of chromatographic peaks. $C_{n:m}$ is a fatty acid with n carbon atoms and m double bonds.

Fatty Acid	**Composition**	***A% WCO***	***A% Sunflower oil***
Myristic acid	$C_{14:0}$	0.1	0.1
Palmitic acid	$C_{16:0}$	7.2	4.7
Stearic acid	$C_{18:0}$	4.1	2.7
Oleic acid	$C_{18:1}$	79.5	85.5
Linoleic acid	$C_{18:2}$	7.0	5.9
Linolenic acid	$C_{18:3}$	0.4	0.2
Arachidic acid	$C_{20:0}$	0.5	0.2
Cis-9-Eicosenoic acid	$C_{20:1}$	0.0	0.0
Behenic acid	$C_{22:0}$	1.3	0.8
Erucic acid	$C_{22:1}$	0.0	0.0

Oleic acid ($C_{18:1}$), palmitic acid ($C_{16:0}$), linoleic acid ($C_{18:}1$) and stearic acid ($C_{18:0}$) were the predominant fatty acids in both oils. However, palmitic acid and stearic acid were found in higher concentrations in WCO, with levels of 7.2% and 4.1%, respectively, compared to sunflower oil, which contained 4.7% and 2.7%. This indicated that WCO might have had a higher saturated fat content than sunflower oil. This occurs because the high temperatures achieved during cooking can lead to the degradation of unsaturated fatty acids

and the formation of saturated fatty ones [320]. Additionally, prolonged use of oil in frying can result in the transformation of unsaturated fatty acids into more stable, often saturated compounds [321]. Moreover, the fatty acid profile in the oil can be influenced by the composition of the foods being cooked [322].

However, overall, the two oils exhibited similar characteristics and did not show significant differences in their fatty acid distribution.

5. RESULTS OF DO TESTS

This section presents the results of the catalytic DO tests (as described in Section 2.4) conducted on three catalysts: NiCoMo, ZnCoMo, and Ni-Mo-Al. First, an overview of the general findings is provided, followed by a detailed statistical analysis of the data (see Section 2.5.4.1). Next, the results from the recycling tests are discussed, and finally, the analysis of the FCCCD for Ni-Mo-Al catalyst is presented (Section 2.4.3). In all sets of experiments, product composition and key DO performance metrics were used to assess the results, including: $Y_{product}$ (Equation 2.9, Section 2.5.4), χ (Equation 2.10, Section 2.5.4), Y_{diesel} (Equation 2.11, Section 2.5.4), and $S_{HDO/DCOx}$ (Equation 2.12, Section 2.5.4).

5.1 DO TEST RESULTS FOR NICOMO AND ZNCOMO CATALYSTS

The experimental campaign for the DO of NiCoMo and ZnCoMo catalysts was divided into two parts: (i) a factor screening and process characterization using an unreplicated 2^3 factorial design with three center-point replications (as outlined in Table 8 in Section 2.5.4.1); and (ii) recycling tests conducted under optimal conditions for performance at a shorter duration (i.e., 320°C, 10%$_{w/w}$ catalyst-to-oil ratio, 2 hours).

5.1.1 RESULTS OF 2^3 FACTORIAL DESIGN EXPERIMENTS

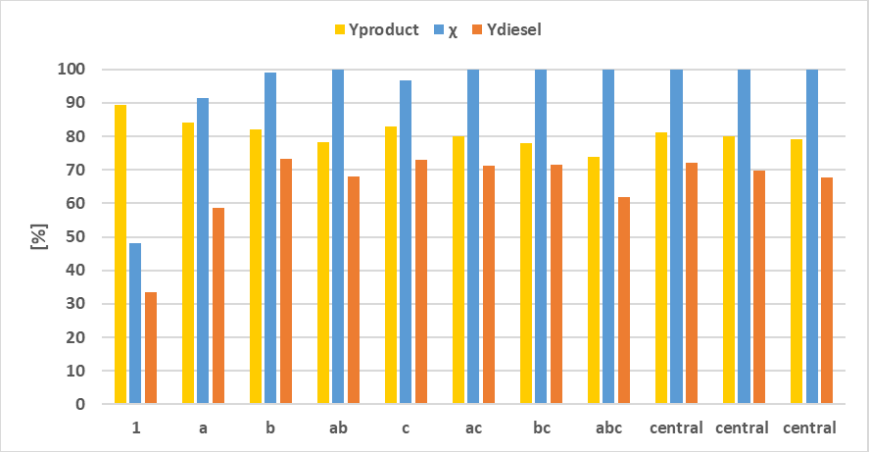
The results of the DO tests, conducted according to the experimental design outlined in Section 2.4.1, are summarized in Table 19 for both NiCoMo and ZnCoMo catalysts. These results include product composition and DO performance parameters: $Y_{product}$ (Equation 2.9, Section 2.5.4), χ (Equation 2.10, Section 2.5.4), Y_{diesel} (Equation 2.11, Section 2.5.4), and $S_{HDO/DCOx}$ (Equation 2.12, Section 2.5.4). The "Test" numbers in Table 19 indicates the order in which the factorial tests were executed.

5.1.1.1 QUALITATIVE ANALYSIS

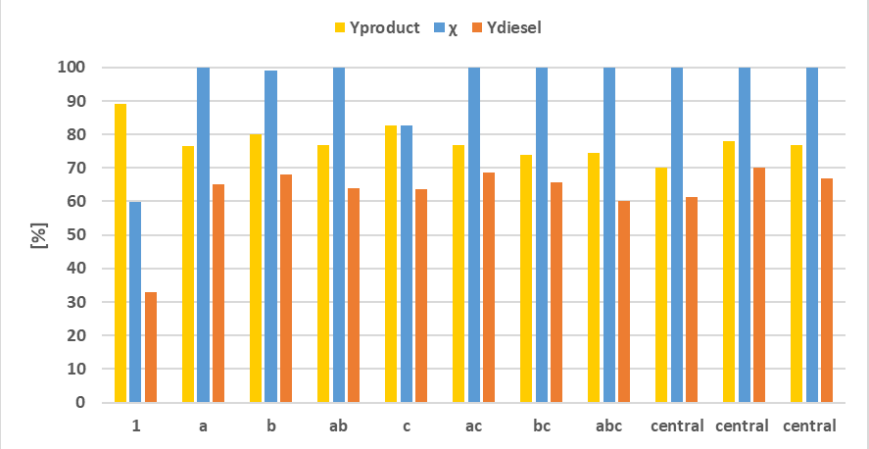
Several general comments emerged from a qualitative analysis of data in Table 19.

In the "*blank*" test (320°C, 6 hours, no catalyst), no conversion of TGs into n-alkanes (i.e., C_8-C_{14}, C_{19}-C_{30}), C_{15}-C_{18}, BHC, or UHC was observed (Table 19) for each catalyst. This indicated that pressurized H_2 and temperature alone are insufficient to initiate DO processes. Consequently, it underscored the necessity of an appropriate catalyst to facilitate the conversion of TGs into n-alkanes for DO pathways under the conditions studied. Therefore, all subsequent discussions have been attributed to the effects of catalytic activity.

The "*no-pre-red*" tests, conducted with NiCoMo and ZnCoMo, led to some transformations indicative of DO, with formation of n-alkanes including C_{15} to C_{18} (Table 19). However, the performance of these tests was less effective compared to those under similar conditions with pre-reduced catalysts (treatment *"ab"*, Table 19), highlighting the importance of a pre-reduction step for both catalysts. This effect, explored through TPR in Section 3.1.7 and TPD-H_2 in Section 3.1.8, emphasized the role of pre-reduction in enhancing catalyst activity. Nevertheless, the unreduced NiCoMo and ZnCoMo ("no-pre-red", Table 19) displayed partial activity, showing some resilience in the DO process. ZnCoMo, in particular, demonstrated more promising results, yielding a higher overall fraction of n-alkanes and slightly better DO performance metrics compared to NiCoMo (Table 19).



(**a**)



(**b**)

Figure 40 $Y_{product}$, χ, and Y_{diesel} of DO test for (a) NiCoMo and (b) ZnCoMo catalyst. Values are taken from Table 19.

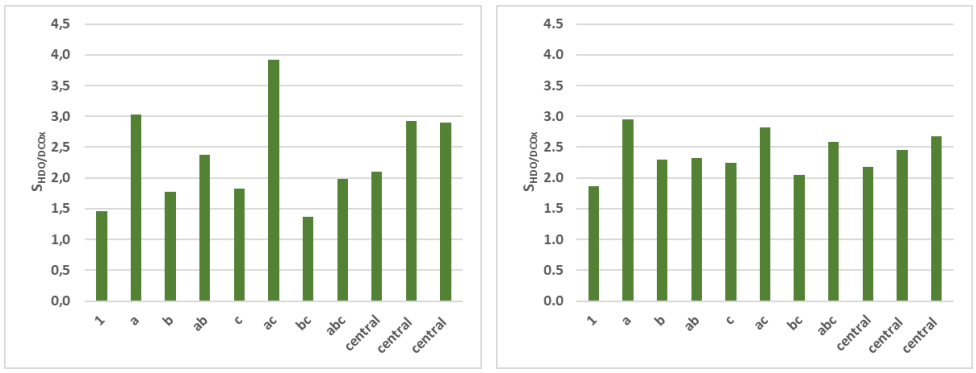
In the tests conducted across the two experimental designs (see Section 2.4.1), the $Y_{product}$ (Equation 2.9, Section 2.5.4) values consistently ranged from 70% to 90% (see Table 19 and Figure 40). This range suggested that a non-negligible mass loss of the initial mass of oil occurred when attempting DO, primarily as volatile products. The highest $Y_{product}$ values were observed at lower conversion levels (see Table 19 and Figure 40). This occurred because when the conversion was less than 100%, not all TGs were fully transformed into n-alkanes. Incomplete conversion could lead to the formation of additional by-products (see Scheme 4, Scheme 5, Scheme 6 and Scheme 7 in

Section 1.5). In contrast, when the conversion is complete, TGs are entirely converted into n-alkanes, and only gaseous by-products are produced (see the reaction mechanism in Section 1.5), leading to a lower $Y_{product}$.

The χ values for both catalysts were generally very high, often reaching 100%, indicating strong activity under the experimental conditions studied (Table 19 and Figure 40). The only exception was treatment *"(1)"*, where χ values were notably lower, at 48.0% for NiCoMo and 59.8 % for ZnCoMo (see Figure 40), which corresponded to higher fractions of FAMEs (Table 19). The superior χ observed for ZnCoMo under these more challenging conditions (treatment *"(1)"*, Table 19 and Figure 40) might be attributed to its higher intrinsic activity compared to NiCoMo.

In terms of Y_{diesel} (Equation 2.11), a key parameter for the aim of this PhD thesis, the values ranged from 58.8% to 73.2% for NiCoMo and from 60.1% to 70.0% for ZnCoMo (Figure 40), excluding treatment *"(1)"*, where both catalysts yielded around 33% (Table 19), indicating that the DO performance of both NiCoMo and ZnCoMo was satisfactory across the experimental conditions, except for treatment *"(1)"* (i.e., 280°C, 4 $\%_{w/w}$, 2 h). The strong Y_{diesel} performance could be attributed to the high fractions of diesel-range n-alkanes (C_{15}-C_{18}) produced (Table 19).

The $S_{HDO/DCOx}$ (Equation 2.12) values for both NiCoMo and ZnCoMo consistently exceeded 1 (Table 19 and Figure 41), indicating a strong selectivity for the HDO pathway (see definition of $S_{HDO/DCOx}$ in Section 2.5.4) across all investigated experimental conditions. This similarity in selectivity aligns with the comparable interactions between H_2 and the exposed metallic surfaces of the catalysts, as suggested by the TPD-H_2 results (Section 3.1.8, Figure 31 (b), Table 13). As outlined in Section 1.5.1.2, HDO is preferred for achieving higher AE, as it avoids carbon loss by producing water rather than CO_2 and CO. While DCO_x pathways (Section 1.5.1.2) use less hydrogen, they result in carbon loss and lower AE. Favoring the HDO pathway enhances process sustainability by reducing GHGEs.



(**a**) (**b**)

Figure 41 $S_{HDO/DCOx}$ of DO tests for (a) NiCoMo and (b) ZnCoMo catalyst. Values are taken from Table 19.

Regarding product composition (Table 19): (i) the frequent presence of BHC should not be viewed negatively, as BHC contribute positively to the cold properties of green diesel by lowering its freezing point (as underlined in Section 1.4.3); (ii) the absence (or trace amounts) of UHC is a desirable outcome, as UHC reduce the oxidative stability of green diesel and promote polymerization [90].

Overall, both catalysts demonstrated very good performance across nearly all tested conditions. However, the conditions that yielded the best DO performance—achieving high values of χ and Y_{diesel} while minimizing reaction time and temperature, in order to respect the principles of Green Chemistry and Green Engineering—were the conditions of treatment *"ab"* (i.e., 320°C, 10%$_{w/w}$ of catalyst-to-oil, 2 h) and conditions of treatment *"b"* (i.e., 280°C, 10% $_{w/w}$ of catalyst-to-oil, 2 h) for the NiCoMo catalyst.
For the ZnCoMo catalyst, the optimal reaction conditions, for maximizing χ and Y_{diesel} and minimizing time and temperature, were also associated with the *"ab"* and *"b"* treatments.

5.1.1.2 Statistical analysis for NiCoMo and ZnCoMo

For a quantitative and objective analysis of the experimental data, the effects of the investigated factors (A = T, B = Y, C = t, as shown in Table 8) were statistically evaluated through the calculation of coefficients of the model (as described in Section 2.5.4.1). In summary, in ANOVA, the factors represent

the independent variables whose influence on the dependent variable is to be estimated, while the coefficients provide an estimate of the magnitude of that influence [285]. Explained variance and cross-validation explained variance were also calculated (see Section 2.5.4.1 for further details). Additionally, an investigation was carried out on the significance of the pure quadratic terms in the empirical response models/response surfaces (Equation 2.14, Equation 2.18, and Equation 2.19).

Table 20 presents the results of this statistical evaluation in two key areas: (i) coefficients of factors and their interactions (see Equation 2.14) for the product composition and performance parameters, including $Y_{product}$ (Equation 2.9), χ (Equation 2.10), Y_{diesel} (Equation 2.11), and $S_{HDO/DCOx}$ (Equation 2.12); and (ii) significance of the coefficients, indicating the statistical relevance of the factors.

In certain cases, such as for $A\%_{FAME}$ and χ (Equation 2.10), it was not possible to calculate significance because the experimental error variance could not be estimated from the center points due to the lack of variability in the data (see Table 19).

For NiCoMo, the $Y_{product}$ (Equation 2.9) was significantly affected by the main effects of temperature (A=*T*, see the significance * in Table 20), catalyst-to-oil weight ratio (B=Υ, see the significance * in Table 20), and reaction time (C=*t*, see the significance * in Table 20), with all showing negative effects. Similarly, for ZnCoMo, the main effects of *T* (A), Υ (B), and *t* (C) on $Y_{product}$ were also negative, although neither the main coefficients nor the interaction coefficients were statistically significant (Table 20). These negative main effects align with findings from the literature [210], which indicate that as catalytic DO increases, driven by higher temperature, catalyst-to-oil ratio, and reaction time, greater quantities of volatile HCs are formed (e.g., propane from glycerol and light HCs from cracking), leading to a reduction in $Y_{product}$. Conversely, lower temperature and shorter reaction times suppress cracking, resulting in a higher $Y_{product}$ [210]. The same results were obtained from qualitative analysis in Section 5.1.1.1.

The significance of the response variable χ (Equation 2.10) could not be determined due to the lack of variability in the replicated central points (all of these are equal, see Table 19). Nonetheless, the coefficients of χ model were calculated, and interestingly, they showed the same trend for both catalysts (see Table 20). The main effects of coefficients of T (A), Υ (B), and t (C) were all positive, which is reasonable; however, all binary interactions had negative effects. This observation aligns with the sparsity-of-effects principle [285], which suggests that a few main effects (and possibly some low-order interactions) are more likely to have a significant impact.

For NiCoMo, the Y_{diesel} (Equation 2.11) was not significantly influenced by temperature (T, A), while the main effects of catalyst-to-oil ratio (Υ, B) and reaction time (t, C) were both significant and positive (Table 20), indicating that Y_{diesel} increased as either Υ or t was raised, consistent with findings for commercial catalysts in the literature [180, 323]. All binary interactions for NiCoMo were significant, with negative effects on Y_{diesel} (Table 20).
For ZnCoMo, only the binary interactions between Υ and T (AB), as well as Υ and t (BC), were weakly significant, also with negative effects (Table 20). Overall, the negative effects of these binary interactions on Y_{diesel} suggested that a combined increase in the investigated factors may promote secondary reactions. This interpretation is partially supported by some significant positive effects of binary interactions on the fractions of non-alkane components in the products, such as the positive coefficient of BC on the "*others*" fraction for NiCoMo, or the positive coefficients of AC and BC on "*UHC*" for ZnCoMo (Table 20).

The $S_{HDO/DCOx}$ (Equation 2.12) was influenced only by temperature (T, A), showing a positive effect, although with weak significance (Table 20).

The fraction of diesel n-alkanes in the product ($A\%_{Ci}$, where $15 \leq i \leq 18$, Table 20) was significantly affected by all main factors and interactions of T (A), Υ (B), and t (C) for both NiCoMo and ZnCoMo. Notably, the signs of these coefficients were the same for both catalysts (Table 20), suggesting similar behavior in DO reactions, as shown in surface responses in Figure 42.

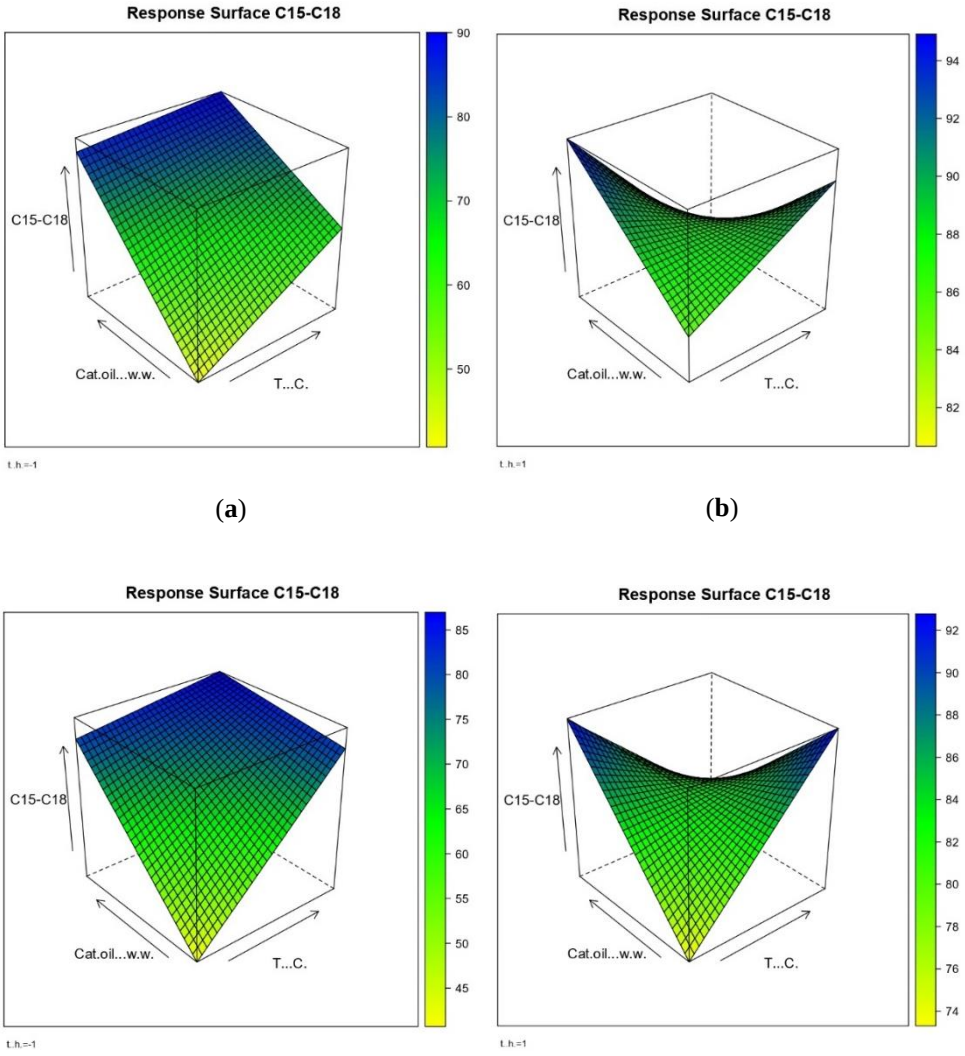


Figure 42 Surface responses of $A\%_{Ci}$ (with $15 \leq i \leq 18$) for NiCoMo at (a) t=-1, (b) t=1 and ZnCoMo at (c) t=-1 and (d) t=1.

This observation aligns with similarities noted from TPD-H_2 profiles (Section 3.1.8, Figure 31 (b), Table 13). The main coefficients on $A\%_{Ci}$ ($15 \leq i \leq 18$) were all positive (Table 20), meaning that increasing T (A), Υ (B), and t (C) led to a higher diesel fraction in the product. All binary interactions (AB, BC, and AC) had negative effects (Table 20), likely due to processes such as cracking and isomerization occurring when the factors are simultaneously high [180, 323]. This observation is consistent with the earlier discussion on the combined effects of these factors on Y_{diesel}.

Regarding the good fit of the data with the proposed model (see Section 2.5.4.1, Equation 2.14) and the estimated coefficients (see Table 20), it was evident that for the NiCoMo catalyst, the model provides a good fit for $A\%_{Ci}$ ($19 \leq i \leq 30$), $A\%_{UHC}$, $Y_{product}$, and $S_{HDO/DCOx}$, because the values of *Expl. Var* are greater than 95% (high value of *Exp. Var* means that the model is able to explain a large part of the dependent variable's variability, while a low value indicates that the model is not able to represent data well). However, for other compositions and parameters of Table 20, the model did not fit the data as well (low values of *Expl. Var*) While the model appeared to accurately capture the experimental data for some cases, this does not hold true when considering the *CV Exp. Var* (high value indicates that the model is robust and does not fit only training data, but also on new data sets). Only for $A\%_{UHC}$ (Table 20) the model did not only fit well with experimental data, but also with new data sets, as the *CV Expl. Var* is 99.9%.

For the ZnCoMo catalyst, the model provided a good match for $A\%_{Ci}$ ($8 \leq i \leq 14$), $A\%_{UHC}$, and $Y_{product}$, with *Expl. Var* was above 95%. Although the model for these parameters fitted well with existing experimental data, the *CV Expl. Var* values were lower than *Expl. Var*, this means that the actual predictive ability of the model was lower than that suggested by the performance on the training set. However, for other compositions and parameters in Table 20, the model did not fit well the data (low values of *Expl. Var*), and no values of *CV Expl. Var* were taken.

For both catalysts, the pure quadratic terms (in Table 20) in the hypothetical response surface were significant only for the fraction of diesel n-alkanes ($A\%_{Ci}$, where $15 \leq i \leq 18$), which is the primary product of interest for DO, as well as for some secondary product fractions. In fact, the response surfaces in Figure 42 (b) and (c) show the presence of curve surface, suggesting a non-linear relationship between the variables and the response ($A\%_{Ci}$, where $15 \leq i \leq 18$). This indicates that a first-order model is insufficient to adequately describe the composition data; instead, a second-order model would provide a better fit. For this reason, it is advisable for future studies to employ a DoE approach that supports second-order model regressions (Equation 2.19).

Table 19 Experimental results of unreplicated 2^3 factorial DoE with 3 replicated central points (with treatments classified for ANOVA) and supplementary "blank" and "no-pre-red" tests.

NiCoMo test	**A**	**B**	**C**	**treatment**	$A\%_{Ci}$ **8≤*i*≤14**	$A\%_{Ci}$ **15≤*i*≤18**	$A\%_{Ci}$ **19≤*i*≤30**	$A\%_{BHC}$	$A\%_{UHC}$	$A\%_{Others}$	$A\%_{FAME}$	$Y_{product}$	χ	Y_{diesel}	$S_{HDO/DCOx}$
	[°C]	**[%w/w]**	**[h]**		**[%]**	**[%]**	**[%]**	**[%]**	**[%]**	**[%]**	**[%]**	**[wt%]**	**[wt%]**	**[wt%]**	**[-]**
blank	320	0	6		0.00	0.00	0.00	0.00	0.00	14.15	85.85	85.07	26.97	0.00	-
no-pre-red	320	10	2		3.77	37.20	3.55	0.00	3.38	14.07	38.12	86.93	66.87	32.34	2.1
Test_04	-	-	-	(1)	0.00	37.48	1.95	0.00	1.15	1.19	58.23	89.24	48.03	33.45	1.5
Test_02	+	-	-	a	3.14	69.87	1.80	6.89	1.69	6.31	10.30	84.09	91.34	58.75	3.0
Test_06	-	+	-	b	4.94	89.18	3.92	0.35	0.00	0.39	1.22	82.04	99.00	73.16	1.8
Test_03	+	+	-	ab	4.38	86.77	3.04	4.67	0.28	0.86	0.00	78.39	100.00	68.01	2.4
Test_08	-	-	+	c	3.74	87.96	3.37	0.37	0.00	0.56	4.00	82.99	96.68	73.00	1.8
Test_07	+	-	+	ac	3.63	89.08	3.23	2.99	0.24	0.83	0.00	79.95	100.00	71.22	3.9
Test_05	-	+	+	bc	4.70	91.67	3.29	0.34	0.00	0.00	0.00	77.96	100.00	71.47	1.4
Test_01	+	+	+	abc	3.02	83.90	2.87	5.62	0.00	4.59	0.00	73.81	100.00	61.92	2.0
Test_09	0	0	0	central	5.00	88.54	4.42	1.34	0.00	0.70	0.00	81.28	100.00	71.97	2.1
Test_10	0	0	0	central	4.72	87.05	4.30	3.63	0.00	0.30	0.00	80.05	100.00	69.68	2.9
Test_11	0	0	0	central	4.01	85.73	3.46	6.39	0.41	0.00	0.00	78.97	100.00	67.70	2.9
ZnCoMo test	**A**	**B**	**C**	**treatment**	$A\%_{Ci}$ **8≤*i*≤14**	$A\%_{Ci}$ **15≤*i*≤18**	$A\%_{Ci}$ **19≤*i*≤30**	$A\%_{BHC}$	$A\%_{UHC}$	$A\%_{Others}$	$A\%_{FAME}$	$Y_{product}$	χ	Y_{diesel}	$S_{HDO/DCOx}$
	[°C]	**[%w/w]**	**[h]**		**[%]**	**[%]**	**[%]**	**[%]**	**[%]**	**[%]**	**[%]**	**[wt%]**	**[wt%]**	**[wt%]**	**[-]**
blank	320	0	6		0.00	0.00	0.00	0.00	0.00	14.15	85.85	85.07	26.97	0.00	-
no-pre-red	320	10	2		3.74	38.61	9.78	0.00	10.99	0.00	36.88	88.60	67.33	34.20	2.9
Test_04	-	-	-	(1)	3.39	37.07	3.61	0.00	2.17	8.63	45.13	89.01	59.83	32.99	1.9
Test_02	+	-	-	a	5.36	85.04	3.88	4.27	1.45	0.00	0.00	76.59	100.00	65.13	2.9
Test_06	-	+	-	b	6.35	84.76	4.52	1.80	1.51	0.00	1.06	80.16	99.15	67.95	2.3
Test_03	+	+	-	ab	6.94	83.30	3.74	5.69	0.33	0.00	0.00	76.81	100.00	63.98	2.3
Test_08	-	-	+	c	1.82	76.94	2.54	0.83	0.00	0.00	17.87	82.77	82.77	63.68	2.2
Test_07	+	-	+	ac	5.66	89.14	2.99	2.21	0.00	0.00	0.00	76.82	100.00	68.48	2.8
Test_05	-	+	+	bc	6.00	88.99	3.78	1.23	0.00	0.00	0.00	73.79	100.00	65.66	2.1
Test_01	+	+	+	abc	7.59	80.88	4.40	5.25	0.00	1.88	0.00	74.35	100.00	60.13	2.6
Test_09	0	0	0	central	6.24	87.36	3.70	2.51	0.19	0.00	0.00	70.10	100.00	61.24	2.2
Test_10	0	0	0	central	5.08	89.62	3.62	1.68	0.00	0.00	0.00	78.06	100.00	69.96	2.5
Test_11	0	0	0	central	4.60	87.19	3.19	2.62	0.00	2.40	0.00	76.80	100.00	66.96	2.7

*Table 20 Regression coefficients, explained variance and explained variance in cross validation of main factors and interactions from experimental data of unreplicated 2^3 factorial DoE with 3 replicated central points and their significance (see Section 2.5.4.1); Significance P-value intervals: 0 < *** ≤ 0.001 < ** ≤ 0.01 < * ≤ 0.05 < . < 0.1 < no < 1. "N.v" means that the CV Expl. Var has negative value (no fitting).*

NiCoMo	$A\%_{Ci}$ **8≤*i*≤14**		$A\%_{Ci}$ **15≤*i*≤18**		$A\%_{Ci}$ **19≤*i*≤30**		$A\%_{BHC}$		$A\%_{UHC}$		$A\%_{Others}$		$A\%_{FAME}$		$Y_{product}$		χ		Y_{diesel}		$S_{HDO/DCOx}$	
	[%]		**[%]**		**[%]**		**[%]**		**[%]**		**[%]**		**[%]**		**[wt%]**		**[wt%]**		**[wt%]**		**[-]**	
β_0	3.45	-	79.49	-	2.93	-	2.65	-	0.42	-	1.84	-	9.22	-	81.06	-	91.88		63.87		2.22	-
β_A	0.09	no	2.91	*	-0.19	no	2.39	no	0.13	no	1.31	**	-6.64	n.d.	-2.00	*	5.95	n.d.	1.10	no	0.61	.
β_B	0.82	*	8.40	**	0.35	no	0.09	no	-0.35	.	-0.36	.	-8.91	n.d.	-3.01	*	7.87	n.d.	4.77	*	-0.34	no
β_{AB}	-0.66	.	-5.46	**	-0.13	no	0.01	no	-0.06	no	-0.05	no	6.34	n.d.	0.05	no	-5.70	n.d.	-4.78	*	-0.31	no
β_C	0.33	no	8.66	**	0.26	no	-0.32	no	-0.36	*	-0.38	no	-8.22	n.d.	-2.38	*	7.29	n.d.	5.53	*	0.05	no
β_{AC}	-0.56	.	-4.58	*	0.06	no	-0.41	no	-0.07	no	-0.1	no	5.64	n.d.	0.20	no	-5.12	n.d.	-3.94	*	0.07	no
β_{BC}	-0.73	.	-8.76	**	-0.46	no	0.056	no	0.29	.	1.18	*	7.91	n.d.	0.22	no	-7.04	n.d.	-7.48	*	-0.26	no
Expl. Var.	76.83		74.79		95.16		55.55		99.99		no		43.69		96.06		41.16		64.11		95.83	
CV Expl. Var	n.v		n.v		61.24		n.v		99.90		n.v		n.v		68.49		n.v		n.v		66.64	
Pure quadratic		.		*		.		no		no		*		n.d.		no		n.d.		.		no
ZnCoMo	$A\%_{Ci}$ **8≤*i*≤14**		$A\%_{Ci}$ **15≤*i*≤18**		$A\%_{Ci}$ **19≤*i*≤30**		$A\%_{BHC}$		$A\%_{UHC}$		$A\%_{Others}$		$A\%_{FAME}$		$Y_{product}$		χ		Y_{diesel}		$S_{HDO/DCOx}$	
	[%]		**[%]**		**[%]**		**[%]**		**[%]**		**[%]**		**[%]**		**[wt%]**		**[wt%]**		**[wt%]**		**[-]**	
β_0	5.39	-	78.26	-	3.68	-	2.66	-	0.68	-	1.32	-	8.00	-	78.79	-	92.72	-	61.00	-	2.39	-
β_A	0.99	.	6.32	**	0.07	no	1.69	*	-0.24	*	-0.85	no	-8.00	n.d.	-2.65	no	7.28	n.d.	3.43	no	0.28	.
β_B	1.33	*	6.22	**	0.42	*	0.83	*	-0.22	*	-0.85	no	-7.74	n.d.	-2.51	no	7.07	n.d.	3.43	no	-0.08	no
β_{AB}	-0.45	no	-8.72	**	-0.11	no	0.28	no	-0.05	no	1.32	no	7.74	n.d.	1.95	no	-7.07	n.d.	-5.81	.	-0.14	no
β_C	-0.12	no	5.72	**	-0.25	no	-0.28	no	-0.68	**	-0.85	no	-3.54	n.d.	-1.86	no	2.97	n.d.	3.49	no	0.03	no
β_{AC}	0.36	no	-5.30	**	0.19	no	-0.34	no	0.24	*	1.32	no	3.54	n.d.	1.30	no	-2.97	n.d.	-3.61	no	0.00	no
β_{BC}	0.20	no	-5.27	**	0.23	no	0.03	no	0.22	*	1.32	no	3.28	n.d.	-0.35	no	-2.76	n.d.	-5.02	.	-0.03	no
Expl. Var. [%]	97.44	-	63.85		57.88		74.98		96.62		37.86		67.43		96.81		71.29		38.42		8.35	
CV Expl. Var [%]	79.52	-	n.v		n.v		n.v		72.94		n.v		n.v		74.45		n.v		n.v		n.v	
Pure quadratic		no		**		no		no		*		no		n.d.		no		n.d.		no		no

5.1.2 RESULTS OF NICOMO AND ZNCOMO RECYCLING TEST

For both catalysts, the treatment conditions labeled "*ab*" in Table 19 (i.e., 320°C, 10%$_{w/w}$ catalyst-to-oil ratio, 2 hours) were chosen for the recycling tests (see Section 2.4.2 for further details about the procedure of tests). These conditions provided optimal results in terms of product composition, conversion, and diesel yield, while minimizing the reaction time (see Table 19). A total of four cycles were conducted. Table 21 reports the results of NiCoMo and ZnCoMo recycling tests.

The overall $Y_{product}$ remained relatively consistent throughout the four cycles, showing a slight upward trend, ranging between 75-80% (Table 21 and Figure 43).

The two catalysts achieved a 100% of χ across all DO cycles (as shown in Figure 43). This result was further supported by the absence of bands in the IR spectra between 1745-1700 cm^{-1} and 1350-900 cm^{-1}, which are characteristic of C=O and C-O stretching, in Figure 44 (a) for NiCoMo reaction products and Figure 44 (b) for ZnCoMo reaction products. This is a noteworthy result, as it highlights the catalysts' effectiveness and stability in achieving complete TGs conversion without significant loss of catalytic activity, throughout 4 cycles.

The Y_{diesel} for both catalysts also exhibited a gradual increase (see Figure 43), with NiCoMo rising from 66.6% to 72.2%, and ZnCoMo increasing from 64.1% to 74.4% (values in Table 21).

Regarding $S_{HDO/DCOx}$, this parameter ranged between 1.7 and 2.2 for NiCoMo and between 2.5 and 3.1 for ZnCoMo (see Table 21), again emphasizing the preference to the HDO pathway over DCO and DCO_2, as obtained from the results of the 2^3 experimental campaigns in Section 5.1.1.

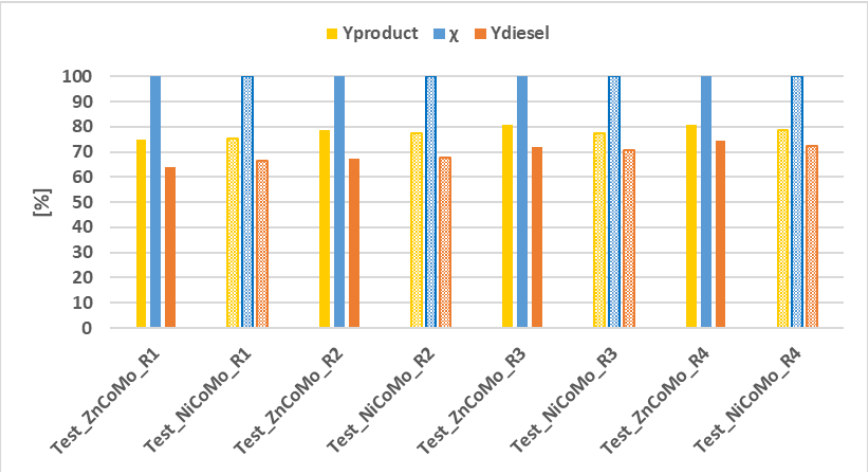
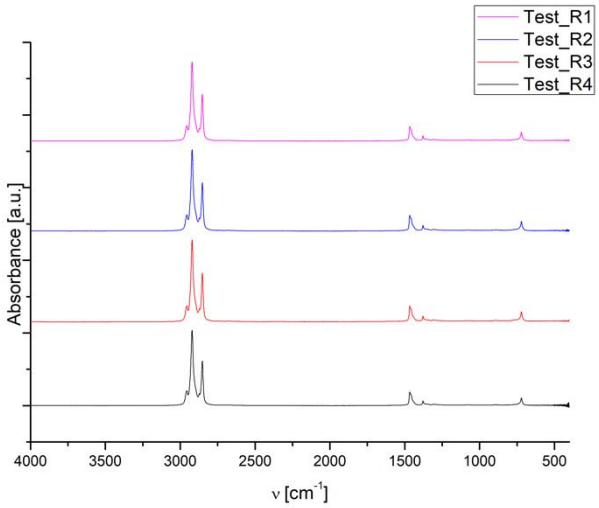


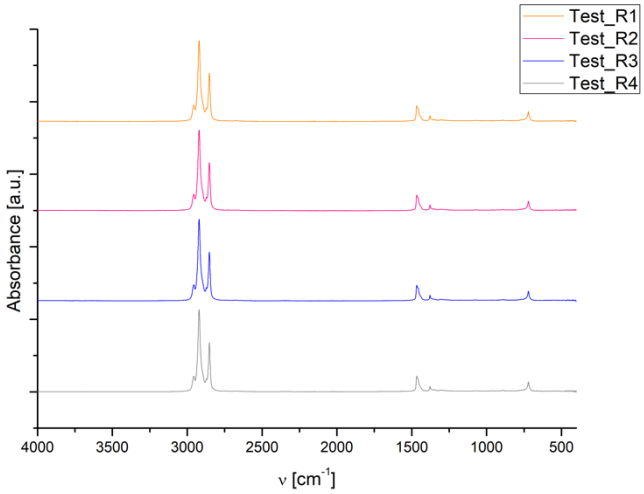
Figure 43 Comparison of $Y_{product}$, χ, Y_{diesel} of recycling test for NiCoMo and ZnCoMo catalyst. Values are taken from Table 21.

With regard to product composition (see Table 21), both catalysts showed similar trends: (i) the $A\%_{Ci}$ ($8 \leq i \leq 14$) decreased from cycle R1 to R4, with a more pronounced reduction for ZnCoMo; (ii) the $A\%_{Ci}$ ($19 \leq i \leq 30$) and $A\%_{BHC}$ remained relatively stable throughout the cycles; (iii) the $A\%_{Ci}$ ($15 \leq i \leq 18$) increased from R1 to R4, rising by 4% for NiCoMo and by 7.6% for ZnCoMo; (iv) all other potential reaction by-products were absent (as indicated by the null values of $A\%_{UHC}$, $A\%_{Others}$, and $A\%_{FAME}$ in Table 21). The decrease in the $A\%_{Ci}$ ($8 \leq i \leq 14$) and the increase in the $A\%_{Ci}$ ($15 \leq i \leq 18$) suggested a shift toward the production of longer-chain n-alkanes over successive cycles. This trend may indicate a reduced catalytic activity for cracking reactions (see Section 1.5.1.3), which, in this case, was beneficial as it promotes an increase in the diesel n-alkanes fraction with each cycle.

Overall, NiCoMo and ZnCoMo demonstrated outstanding performance and stability across all four DO cycles. This is particularly noteworthy given that no pre-reduction was carried out before cycles 2, 3, and 4 (as indicated in Section 2.4.2), indicating that the catalysts maintained their effectiveness during repeated use without needing to restore the initial conditions.



(**a**)



(**b**)

Figure 44 FT-IR spectra of recycling tests reaction product of (a) NiCoMo and (b) ZnCoMo catalyst.

Table 21 Results of recycling tests (320°C, 10 $\%_{w/w}$ catalyst-to-oil, 2 h) with (a) NiCoMo; (b) ZnCoMo, in terms of product composition (A%), $Y_{product}$ (Equation 2.9), χ (Equation 2.10), Y_{diesel} (Equation 2.11), and $S_{HDO/DCOx}$ (Equation 2.12). Test_Ni/Zn_CoMo_Rr is the r^{th} DO cycle on the same catalyst sample.

NiCoMo	$A\%_{Ci}$ $8 \leq i \leq 14$	$A\%_{Ci}$ $15 \leq i \leq 18$	$A\%_{Ci}$ $19 \leq i \leq 30$	$A\%_{BHC}$	$A\%_{UHC}$	$A\%_{Others}$	$A\%_{FAME}$	$Y_{product}$	χ	Y_{diesel}	$S_{HDO/DCOx}$
	[%]	**[%]**	**[%]**	**[%]**	**[%]**	**[%]**	**[%]**	**[wt%]**	**[wt%]**	**[wt%]**	**[-]**
Test_NiCoMo_R1	5.42	88.38	3.58	2.62	0.00	0.00	0.00	75.33	100.00	66.58	2.1
Test_NiCoMo_R2	5.15	87.73	3.52	3.60	0.00	0.00	0.00	77.20	100.00	67.73	1.9
Test_NiCoMo_R3	3.83	90.93	3.44	1.80	0.00	0.00	0.00	77.57	100.00	70.53	1.7
Test_NiCoMo_R4	2.75	91.85	3.31	2.09	0.00	0.00	0.00	78.57	100.00	72.16	2.2
ZnCoMo	$A\%_{Ci}$ $8 \leq i \leq 14$	$A\%_{Ci}$ $15 \leq i \leq 18$	$A\%_{Ci}$ $19 \leq i \leq 30$	$A\%_{BHC}$	$A\%_{UHC}$	$A\%_{Others}$	$A\%_{FAME}$	$Y_{product}$	χ	Y_{diesel}	$S_{HDO/DCOx}$
	[%]	**[%]**	**[%]**	**[%]**	**[%]**	**[%]**	**[%]**	**[wt%]**	**[wt%]**	**[wt%]**	**[-]**
Test_ZnCoMo_R1	7.41	85.62	4.47	2.50	0.00	0.00	0.00	74.81	100.00	64.05	2.5
Test_ZnCoMo_R2	5.18	85.56	3.51	5.75	0.00	0.00	0.00	78.53	100.00	67.19	2.7
Test_ZnCoMo_R3	3.25	88.77	3.43	4.56	0.00	0.00	0.00	80.91	100.00	71.82	3.1
Test_ZnCoMo_R4	1.98	92.11	3.29	2.62	0.00	0.00	0.00	80.80	100.00	74.43	2.9

5.2 Ni-Mo-Al DO test results

The experimental campaign for DO of the Ni-Mo-Al catalyst was conducted in three phases: (i) a factor screening and process characterization utilizing an unreplicated 2^3 factorial design with three center-point replicates (as detailed in Table 8 of Section 2.4.1); (ii) recycling tests performed under optimal conditions (specifically, 320°C, 10 $\%_{w/w}$ catalyst-to-oil ratio, and 6 hours, Section 2.4.2); and (iii) an experimental campaign using a FCCCD (as detailed in 2.4.3, Table 9) to evaluate the impact of stirring speed on DO performances.

This section presents the findings from the three experimental test campaigns.

5.2.1 Results of the Ni-Mo-Al 2^3 experimental campaign

The results of the DO tests, conducted according to the experimental design outlined in Section 2.4.1, are summarized in Table 22. These results include product composition and DO performance parameters: $Y_{product}$ (Equation 2.9, Section 2.5.4), χ (Equation 2.10, Section 2.5.4), Y_{diesel} (Equation 2.11, Section 2.5.4), and $S_{HDO/DCOx}$ (Equation 2.12, Section 2.5.4). The "Test" numbers in Table 22 indicates the order in which the factorial tests were executed.

5.2.1.1 Qualitative results

This section provides a qualitative analysis of the data presented in Table 22, highlighting general comments.

The observations related to the "*blank*" test (320°C, 6 hours, no catalyst) were consistent with those presented in Section 5.1.1.1 for NiCoMo and ZnCoMo catalyst, as the *"blank"* test served as a common reference for all three catalysts. Since this test highlighted the necessity of using a catalyst for the conversion of TGs into n-alkanes (see Section 5.1.1.1), all subsequent discussions focused on the effects of catalytic activity.

The *"no pre-red."* test yielded impressive results (see Table 22), especially considering that the catalyst was not activated through pre-reduction step

prior to the test (see Section 2.4 for further details). In fact, the performance of this test was comparable to that of other tests (e.g., *Test_01*, Table 22), which required a pre-reduction step. This may be explained by the hypotheses that under the tested conditions, the catalyst may have undergone some form of self-reduction during the reaction and the heating phase. While the no-pre-reduced Ni-Mo-Al catalyst demonstrated good performance, the results shown in Table 22 for *Test_01* (which was conducted under the same conditions as the *"no pre-red."* test) suggested that the pre-reduction step enhances the catalyst's ability to reduce itself more effectively, leading to significantly improved performance. However, as indicated by TPR (Figure 37) and TPD-H_2 (Figure 39) analyses, the catalyst did not achieve complete reduction under the conditions applied for pre-reduction step.

The $Y_{product}$ (Equation 2.9) ranged from 70% to 90% (see Table 22 and Figure 45), indicating a substantial loss of initial oil mass, primarily as volatile by-products. Also in this case, as well as for NiCoMo and ZnCoMo catalysts (Section 5.1.1.1), the highest $Y_{product}$ values were noted at lower conversion values (see Figure 45) because, when conversion was incomplete, not all TGs were fully converted to n-alkanes. This incomplete conversion can result in the formation of by-products (refer to the reaction mechanism in Section 1.5).

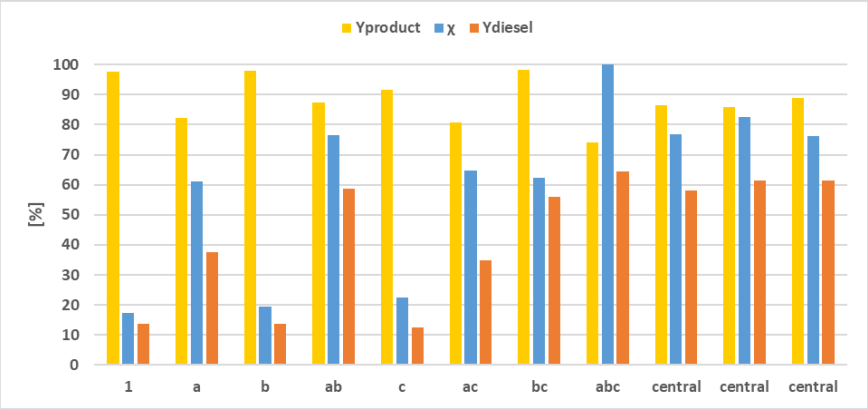


Figure 45 $Y_{product}$, χ, Y_{diesel} of DO tests for Ni-Mo-Al catalyst. Values are taken from Table 22.

The χ (Equation 2.10) values covered a broad range, from 17% to 100% (see Table 22 and Figure 45). Full conversion (100%) was achieved only at all higher levels of reaction conditions (i.e., 320°C, 10%$_{w/w}$ catalyst-to-oil ratio,

and 6 hours). The remaining tests fell into two categories: (i) χ between 62-82%, and (ii) χ between 17-22% (see Figure 45). Although these χ values may not seem ideal, the literature [35, 59] indicates that good conversion values are often above 65%, even though the desired outcome is the complete conversion of TGs into n-alkanes. Notably, from Figure 45, an increase in temperature significantly enhanced the χ values.

The Y_{diesel} values (Equation 2.11) ranged from 12% to 65%, with most falling between 55% and 65%, which aligns with literature values for the most part [35, 59]. Low Y_{diesel} values corresponded to low χ (see Figure 45), highlighting the incomplete conversion of TGs into n-alkanes, particularly in the C_{15}-C_{18} range (the target n-alkanes). Additionally, low Y_{diesel} and low χ values were associated with a high *A%* of FAME (see Table 22), indicating that TGs were not fully converted, even into by-products.

Overall, the $S_{HDO/DCOx}$ (Equation 2.12) ranged from 0.5 to 1.2 (Table 22 and Figure 46). In most cases, $S_{HDO/DCOx}$ was below 1, indicating that the catalyst favored the DCO and DCO_2 pathways (see Section 1.5.1.2 for further details) under the given test conditions. $S_{HDO/DCOx}$ values slightly above 1 were observed only at the central points of the experimental plan (see Figure 46).

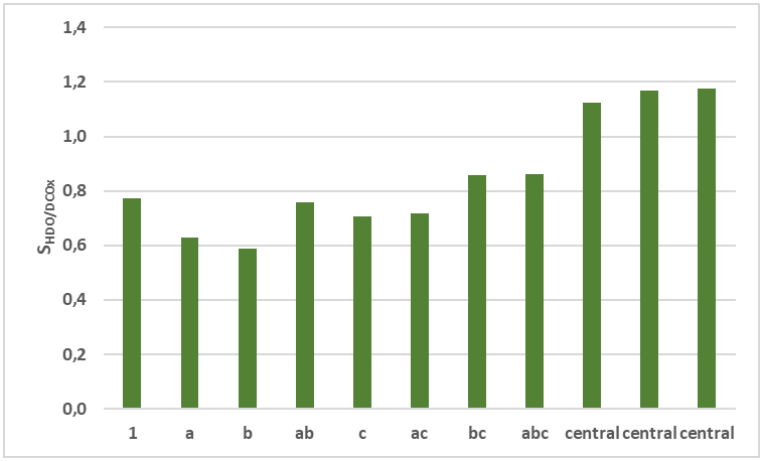


Figure 46 $S_{HDO/DCOx}$ for 2^3 experimental DO tests for Ni-Mo-Al catalyst. Data are taken from Table 22.

With regard to product composition (Table 22): (i) the absence or traces (<5%) of UHC, C_8-C_{14}, and C_{19}-C_{30} suggested that both cracking and polymerization reactions were minimized under these reaction conditions

(see Section 1.5.1.3); (ii) the lack of BHC, which was only present in *Test_01*, is undesirable since BHCs enhance the cold properties of green diesel by lowering its freezing point (as noted in Section 1.4.3); (iii) the high percentages of FAME (ranging from 20% to 80%) indicated the inefficiency of the DO process, under corresponding reaction conditions, in fully converting TGs into n-alkanes.

The Ni-Mo-Al catalyst exhibited superior performance in terms of χ, Y_{diesel}, and diesel HC composition in the product at the highest reaction conditions tested—320°C, 10%$_{w/w}$ of catalyst-to-oil ratio, and 6 hours. Even at the midpoint conditions (i.e., 300°C, 7%$_{w/w}$ of catalyst-to-oil ratio, and 4 hours) of the experimental design (see Table 8), the catalyst exhibited strong DO performance, achieving Y_{diesel} values (ranging from 58.2% to 61.5%) comparable to those attained under the most severe reaction conditions (i.e., 320°C, 10%$_{w/w}$ of catalyst-to-oil ratio, and 6 hours).

5.2.1.2 STATISTICAL ANALYSIS

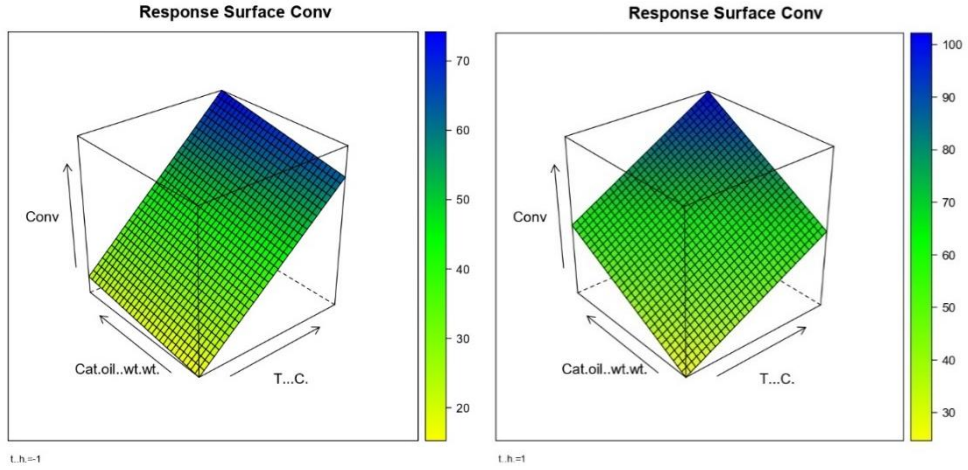
As with the two catalysts, NiCoMo and ZnCoMo (Section 5.1.1.2), a quantitative objective analysis of the experimental data was performed by statistically estimating the effects of the investigated factors (A = T, B = Υ, C = t, as shown in Table 8), through the calculation of the model coefficients, *Exp. Var* and *CV Exp. Var*, and significance of the pure quadratic terms as detailed in Section 2.4.1.

Table 23 presents the results of this statistical evaluation in two key areas: (i) coefficients of factors and their interactions (see Equation 2.14) for the product composition and performance parameters ($Y_{product}$ in Equation 2.9, χ in Equation 2.10, Y_{diesel} in Equation 2.11, and $S_{HDO/DCOx}$ in Equation 2.12); and (ii) significance of the coefficients, indicating the statistical relevance of the factors.

Only for $A\%_{BHC}$, it was not possible to calculate significance because the experimental error variance could not be estimated from the center points due to the lack of variability in the data (see Table 22).

The $Y_{product}$ (Equation 2.9) was significantly influenced by the main effects of temperature (A = *T*, see coefficient significance in Table 23) and reaction time (C = *t*, see coefficient significance in Table 23), both of which exhibited negative effects. These negative impacts align with literature findings [210], and results from NiCoMo and ZnCoMo catalysts (Section 5.1.1.2), which suggest that as higher temperature and longer reaction times are exerted, more volatile n-alkanes are produced, leading to a decrease in $Y_{product}$. Conversely, lower temperatures and shorter reaction times suppress cracking, resulting in an increase in $Y_{product}$ [210]. Similar results were observed in the qualitative analysis (Section 5.2.1.1).

χ (Equation 2.10) was found to be significantly influenced by the three main factors (A=*T*, B=Υ, and C=*t*), as well as by the interaction between Υ and *t*. All these factors had a positive effect (see Table 23 and response surfaces in Figure 47), meaning that an increase in any of them led to a corresponding increase in χ, while a decrease in the factors resulted in a reduction in χ [35, 59, 172, 324].



(**a**) (**b**)

Figure 47 Surface responses of χ for Ni-Mo-Al DO tests at (a) t=-1 and (b) t=1. Regression coefficients are taken from Table 23.

Y_{diesel} (Equation 2.11) was significantly influenced by all the main factors (A=*T*, B=Υ, and C=*t*), as well as by the interactions between Υ-*t*, and *T*-*t* (see Table 23). Notably, the effects were positive, except for the interaction between *T*-*t* (coefficient β_{AC} negative in Table 23). This indicated that as the

three main factors and the Υ-*t* increased, Y_{diesel} also increased, consistent with literature findings [180, 323]. However, when *T*-*t* increased simultaneously, Y_{diesel} decreased, likely due to an increase in secondary reactions such as cracking or polymerization (as explained in Section 1.5.1.3). This interpretation is partially supported by significant positive effects of AC interaction showed a positive coefficient for the "others" fraction and the C_8-C_{14} fraction, along with a negative coefficient for the C_{15}-C_{18} fraction, which is closely related to Y_{diesel} (see Table 23).

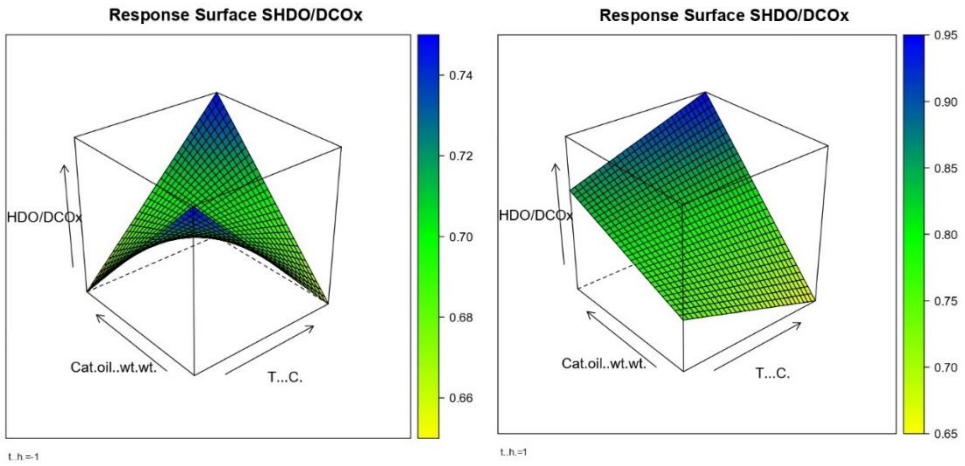
The $S_{HDO/DCOx}$ (Equation 2.12) was influenced by Υ and *t*, and by the interactions between *T*-*t* and *t*-Υ with positive effects observed.

Regarding *A%:*
(i) $A\%_{Ci}$ ($8 \leq i \leq 14$) showed that all factors (A=*T*, B=Υ, and C=*t*) and their interactions were found to be weakly significant with a positive effect;
(ii) $A\%_{Ci}$ ($15 \leq i \leq 18$) revealed that all factors and their interactions were positively significant, except for the *T*-*t* interaction (coefficient AC in Table 23), which had a negative effect (similar to the observations for Y_{diesel});
(iii) $A\%_{FAME}$ was significantly and negatively affected by the three main factors (A=*T*, B=Υ, and C=*t*) as well as the interaction between Υ-*t*. An increase in these parameters resulted in a decrease in the composition of FAME in the product, indicating an increase in the conversion of fatty acids to n-alkanes.

Regarding the adequacy of the data to the proposed model (see Section 2.5.4.1) and the estimated coefficients (see Table 23), a good fit was observed for $A\%_{Ci}$, $A\%_{FAME}$, $A\%_{Others}$, and χ, with *Exp. Var* values exceeding 92%. However, the model is not suitable for validating external data, as the *CV Exp. Var* appeared to be unacceptably low. This discrepancy between *Exp. Var* and *CV Exp. Var* often suggests overfitting, where the model closely captures the noise and specific patterns of the training dataset.

The pure quadratic terms (as shown in Table 23) in the hypothetical response surface were significant for $A\%_{Ci}$ ($15 \leq i \leq 18$), $A\%_{FAME}$, $A\%_{Others}$, χ, Y_{diesel}, and $S_{HDO/DCOx}$ (e.g., see the presence of curve surfaces in the response surfaces of $S_{HDO/DCOx}$ in Figure 48, that indicated non-linear relationship between the

variables and the response)—responses that are critical for DO performance evaluation. This suggests that a first-order model is inadequate for accurately describing the data. In contrast, a second-order model (Equation 2.19) would offer a better fit.



(**a**) (**b**)

Figure 48 Surface responses of $S_{HDO/DCOx}$ for Ni-Mo-Al DO tests at (a) t=-1 and (b) t=1. Regression coefficients are taken from Table 23.

Table 22 Experimental results of unreplicated 2^3 factorial DoE with 3 replicated central points (with treatments classified for ANOVA) of Ni-Mo-Al catalyst, and supplementary "blank" and "no-pre-red" tests.

	A	**B**	**C**	**treatment**	$A\%_{Ci}$ $8 \leq i \leq 14$	$A\%_{Ci}$ $15 \leq i \leq 18$	$A\%_{Ci}$ $19 \leq i \leq 30$	$A\%_{BHC}$	$A\%_{UHC}$	$A\%_{Others}$	$A\%_{FAME}$	$Y_{product}$	χ	Y_{diesel}	$S_{HDO/DCOx}$
	[°C]	**[%w/w]**	**[h]**		**[%]**	**[%]**	**[%]**	**[%]**	**[%]**	**[%]**	**[%]**	**[wt%]**	**[wt%]**	**[wt%]**	**[-]**
blank	320	0	6		0.00	0.00	0.00	0.00	0.00	14.15	85.85	85.07	26.97	0.00	-
no-pre-red	320	10	6		4.22	71.22	3.32	1.44	0.40	1.40	18.00	77.43	86.04	55.15	0.5
Test_07	-	-	-	(1)	0.00	13.96	0.00	0.00	0.00	1.36	84.68	97.57	17.38	13.62	0.8
Test_06	+	-	-	a	1.34	45.89	1.29	0.00	0.27	3.99	47.22	82.10	61.23	37.68	0.6
Test_05	-	+	-	b	0.00	13.97	0.64	0.00	0.00	3.17	82.22	97.89	19.52	13.68	0.6
Test_03	+	+	-	ab	1.74	67.10	2.07	0.00	1.66	0.34	27.09	87.29	76.35	58.58	0.8
Test_08	-	-	+	c	0.00	13.70	0.37	0.00	0.00	1.23	84.70	91.52	22.48	12.54	0.7
Test_02	+	-	+	ac	2.33	43.17	2.40	0.00	3.06	5.20	43.84	80.60	64.66	34.80	0.7
Test_04	-	+	+	bc	0.00	56.89	1.66	0.00	0.00	2.96	38.49	98.19	62.21	55.68	0.9
Test_01	+	+	+	abc	3.39	86.88	2.83	6.63	0.00	0.27	0.00	74.14	100	64.41	0.9
Test_09	0	0	0	central	0.34	67.41	4.52	0.00	0.00	0.96	26.77	86.36	76.88	58.22	1.1
Test_10	0	0	0	central	2.09	71.50	3.10	0.00	2.02	0.97	20.31	85.96	82.54	61.46	1.2
Test_11	0	0	0	central	0.00	68.91	1.56	0.00	1.57	1.15	26.81	88.93	76.16	61.28	1.2

*Table 23 Regression coefficients, explained variance and explained variance in cross validation of main factors and interactions from experimental data of unreplicated 2^3 factorial DoE for Ni-Mo-Al catalyst with 3 replicated central points and their significance (see Section 2.5.4.1); Significance P-value intervals: 0 < *** ≤ 0.001 < ** ≤ 0.01 < * ≤ 0.05 < . < 0.1 < no < 1. "N.v" means that CV Expl. Var has negative value (no fitting).*

Ni-Mo-Al	***A%Ci*** **8≤*i*≤14**		***A%Ci*** **15≤*i*≤18**		***A%Ci*** **19≤*i*≤30**		***A%BHC***		***A%UHC***		***A%Others***		***A%FAME***		***Yproduct***		***χ***		***Ydiesel***		***SHDO/DCOx***	
	[%]		**[%]**		**[%]**		**[%]**		**[%]**		**[%]**		**[%]**		**[wt%]**		**[wt%]**		**[wt%]**		**[-]**	
β_0	1.10	-	42.70	-	1.41	-	0.83	n.d	0.62	-	2.31	-	51.03	-	88.02	-	52.98	-	36.40	-	0.75	-
β_A	1.10	.	18.07	**	0.74	no	0.83	n.d	0.62	no	0.13	.	-21.49	**	-6.99	*	22.58	**	12.47	**	0.00	n.d
β_B	0.18	.	13.52	**	0.39	no	0.83	n.d	-0.21	no	-0.63	**	-14.08	**	1.36	no	11.54	*	11.74	**	0.05	*
β_{AB}	0.18	.	2.72	.	-0.09	no	0.83	n.d	-0.21	no	-1.52	***	-1.91	no	-1.68	no	1.07	no	0.89	no	0.05	*
β_C	0.33	.	7.47	**	0.41	no	0.83	n.d	0.14	no	0.10	no	-9.27	*	-3.20	.	9.36	*	5.51	*	0.05	*
β_{AC}	0.33	.	-3.20	*	0.06	no	0.83	n.d	0.14	no	0.19	*	1.66	no	-0.47	no	-2.60	no	-4.77	*	0.00	n.d
β_{BC}	0.08	.	8.21	**	0.04	no	0.83	n.d	-0.56	no	-0.17	*	-8.43	*	-0.02	no	7.23	*	6.50	**	0.05	*
Expl. Var.	96.84		92.87		87.8		none		none		94.49		94.71		18.81		95.85		68.00		none	
CV Expl. Var.	74.73		42.99		2.39		n.v		n.v		55.92		57.66		n.v		66.81		n.v		n.v	
Pure quadratic		no		***		no		n.d		no		***		**		no		**		***		***

Table 24 Results of Ni-Mo-Al recycling tests (320°C, 10 $\%_{w/w}$ catalyst-to-oil, 6 h) in terms of product composition (A%), $Y_{product}$ (Equation 2.9), χ (Equation 2.10), Y_{diesel} (Equation 2.11), and $S_{HDO/DCOx}$ (Equation 2.12). Test_Rr is the r^{th} DO cycle on the same catalyst sample.

Ni-Mo-Al	***A%Ci*** **8≤*i*≤14**	***A%Ci*** **15≤*i*≤18**	***A%Ci*** **19≤*i*≤30**	***A%BHC***	***A%UHC***	***A%Others***	***A%FAME***	***Yproduct***	***χ***	***Ydiesel***	***SHDO/DCOx***
	[%]	**[%]**	**[%]**	**[%]**	**[%]**	**[%]**	**[%]**	**[wt%]**	**[wt%]**	**[wt%]**	**[-]**
Test_R1	3.44	91.39	3.07	2.10	0.00	0.00	0.00	77.75	100.00	71.06	1.0
Test_R2	0.32	72.10	2.17	0.00	1.04	1.37	23.00	86.37	80.14	62.28	1.1
Test_R3	0.98	35.17	1.05	0.00	3.87	0.00	58.93	85.94	49.36	30.22	0.9
Test_R4	1.53	17.30	1.31	0.85	11.30	0.76	66.95	76.02	49.10	13.20	0.8

5.2.2 Results of recycling tests

For Ni-Mo-Al catalyst, the treatment conditions labeled *"abc"* in Table 22 (i.e., 320°C, 10%$_{w/w}$ of catalyst-to-oil, and 6 hours) were selected (refer to Section 2.4.2 for more details on the test procedure), because these conditions produced the best results in term of product composition, χ, and Y_{diesel}. A total of four cycles were performed. Table 24 reports the results of recycling tests. The $Y_{product}$ (Equation 2.9) was around 76-86%, outlining no real trend (see Table 24 and Figure 49).

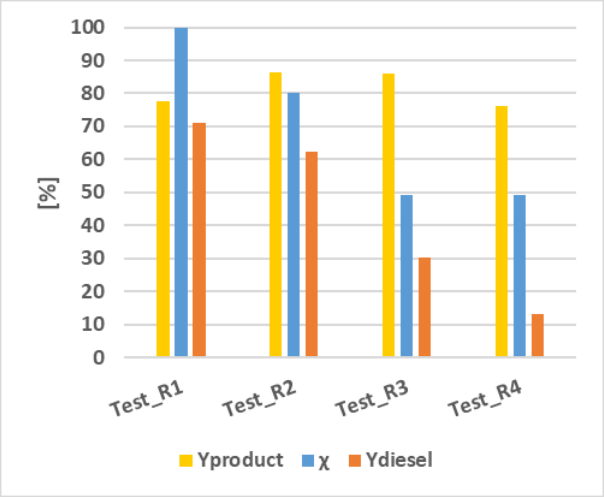


Figure 49 Results of Ni-Mo-Al recycling tests, in terms of $Y_{product}$, χ, and Y_{diesel}. Data are taken from Table 24.

The χ (Equation 2.10) values decreased from 100% to 49% (see Table 24). From *Test_R1* to *Test_R2*, the χ dropped from 100% to 80%, reaching 49% by *Test_R3*, where it remains stable in the 4th reaction cycle (see Figure 49). This suggested a reduction in catalytic activity of DO, as evidenced by the decreased composition of diesel n-alkanes in the product (i.e., $A\%_{Ci}$ with $15 \leq i \leq 18$ in Table 24) and the corresponding increase in FAME ($A\%_{FAME}$). These results were also confirmed by FT-IR spectra in Figure 51: an increase of the signals related to the presence of FFAs (i.e., at 1710 cm^{-1}) and TG esters (i.e., at 1745 cm^{-1}) could be observed as the number of cycles increases.

Since χ is an indicator of how much of the initial TGs have been transformed into n-alkanes or other by-products (see Section 2.5.4, Equation 2.10), it is also influenced by the composition of non n-alkanes (i.e., UHC, BHC and

Others in Table 24). In fact, it was observed that as n-alkanes decreased, the proportion of non n-alkanes (especially $A\%_{UHC}$) increased, leading the χ to reach a plateau at 3rd cycle of reaction (see Figure 49), because the decrease in diesel n-alkanes was balanced by the increase in by-products.

Consequently, the Y_{diesel} (Equation 2.11) exhibited a declining trend, dropping from 71% to 13% by the end of the recycling test (see Figure 49). Similar to the χ, a reduction in catalytic activity toward diesel n-alkanes production was observed (see $A\%_{Ci}$ with $15 \leq i \leq 18$ in Table 24). However, while the χ stabilized by the 3rd reaction cycle, the Y_{diesel} continued to decrease (see Figure 49). This can be attributed to the fact that the Y_{diesel} is closely linked to the $A\%_{Ci}$ with $15 \leq i \leq 18$, which has progressively diminished over time.

The $S_{HDO/DCOx}$ (Equation 2.12) fluctuated between 1.1 and 0.8 (see trend in Figure 50), indicating a slight selectivity toward HDO in *Test_R2* (see Table 24), before shifting back to favor DCO and DCO_2 in the subsequent tests.

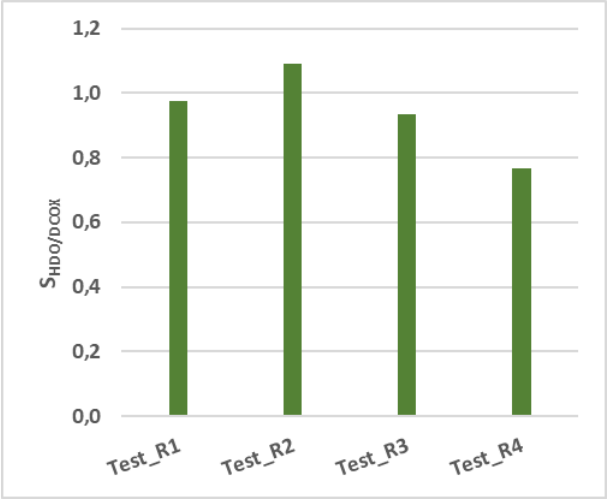


Figure 50 $S_{HDO/DCOx}$ for Ni-Mo-Al recycling tests.

As the number of successive cycles increased (from *Test_R1* to *Test_R4* in Table 24), the following trends were observed: (i) the overall fraction of n-alkanes decreased (i.e., $A\%_{Ci}$ with $8 \leq i \leq 14$, $A\%_{Ci}$ with $15 \leq i \leq 18$ and $A\%_{Ci}$ with $19 \leq i \leq 30$) while the FAME fraction increased (i.e., $A\%_{FAME}$); (ii) the $A\%_{UHC}$ rose significantly from 0% to 11.3%; (iii) $A\%_{BHC}$ significantly decreased, nearly disappearing for central tests; (iv) only traces of $A\%_{Others}$ were detected.

In summary, the recycling tests showed a marked decline in catalytic performance over successive cycles, as indicated by the reduction in χ and Y_{diesel}, along with a shift in product composition from n-alkanes to FAME and other by-products. This highlighted the decline in catalyst efficiency for producing diesel-range n-alkanes in cycles following the first, likely due to the deactivation of the catalyst's active sites, since no pre-reduction step was performed in the cycles after the first (as explained in Section 2.4.2).

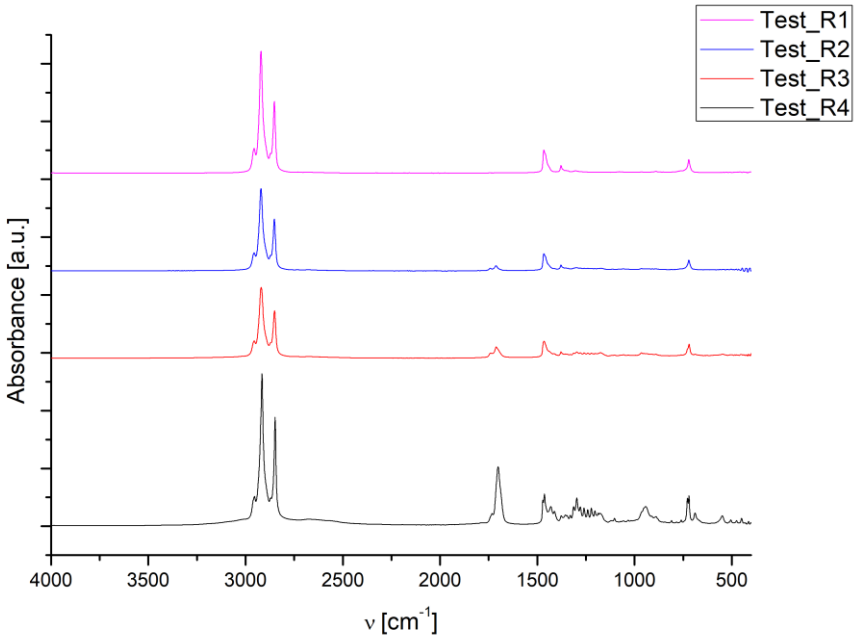


Figure 51 FT-IR spectra of reaction products from recycling tests of Ni-Mo-Al catalyst.

5.2.3 Impact of Stirring Speed on DO Efficiency

The results of the DO tests conducted on the Ni-Mo-Al catalyst, which involved varying the reactor's stirring speed and were performed according to the FCCCD experimental design described in Section 2.4.3, are summarized in Table 25. This summary includes product composition as well as DO performance parameters such as $Y_{product}$ (Equation 2.9, Section 2.4.3), χ (Equation 2.10, Section 2.4.3), Y_{diesel} (Equation 2.11, Section 2.4.3), and $S_{HDO/DCOx}$ (Equation 2.12, Section 2.4.3).

5.2.3.1 GENERAL COMMENTS

General comments emerged from the FCCCD data analysis from Table 25.

The overall $Y_{product}$ (Equation 2.9) ranged from 77.40% to 97.89%. Similar to previous DoEs (see Section 5.1.1 and Section 5.2.1), high $Y_{product}$ values were achieved at lower χ values (Equation 2.10), and vice versa (as discussed in Section 2.5.4).

χ values (Equation 2.10) ranged from 17.38% to 91.78% (see Table 25), with the lowest value observed under the mildest conditions (i.e., 280°C, 4%$_{w/w}$ catalyst-to-oil ratio, 200 rpm) and the highest under the most severe conditions tested (i.e., 320°C, 10%$_{w/w}$ catalyst-to-oil ratio, 600 rpm). Complete conversion of TGs was not achieved in any of the tests (see Table 25), as indicated by the presence of FAMEs, which were never null (see $A\%_{FAME}$ in Table 25).

Regarding Y_{diesel} (Equation 2.11), the values ranged from 7.86% to 64.43%. Among the tests performed, only 4 (Test_04, Test_08, Test_13, and Test_14 in Table 25) reported Y_{diesel} values comparable to those typically found in the literature [35, 59].

$S_{HDO/DCOx}$ (Equation 2.12) ranged from 0.4 to 1.1. Notably, in most tests, selectivity was below 1, indicating a preference for the DCO_x pathways (see Section 1.5.1.2). In Test_08 in Table 25 (i.e., 320°C, 10% $_{w/w}$ catalyst-to-oil ratio, 600 rpm), the $S_{HDO/DCOx}$ value was 1, meaning neither HDO nor DCO_x was favored. Conversely, in Test_13 of Table 25, selectivity reached 1.1, indicating a little preference for the HDO pathways over DCO_x.

Regarding the product composition:
(i) $A\%_{Ci}$ (with $8 \leq i \leq 14$): the C_8-C_{14} compounds were generally very low or absent on most tests, except for Test_08 (e.g., 2.61%) and Test_13 in Table 25 (e.g., 2.49%). This means that under the conditions investigated, the cracking reactions were minimized (see Section 1.5.1.3);
(ii) $A\%_{Ci}$ (with $15 \leq i \leq 18$) increased significantly under more severe conditions, with a peak of 80.16% in Test_08 (i.e., 320°C, 10% $_{w/w}$ catalyst-to-oil, 600 rpm);

(iii) long-chain compounds ($A\%_{Ci}$ with $19 \leq i \leq 30$, in Table 25) were present in very low or negligible amounts across all tests;
(iv) by-products, like *BHC* and *UHC*, were detected only in traces in some of the tests:
(v) $A\%_{Others}$: these values were generally low, with a maximum of 11.53% in Test_07 (i.e., 280°C, 10%$_{w/w}$ catalyst-to-oil and 600 rpm) and 4.63% in Test_10 of Table 25 (i.e., 280°C, 7%$_{w/w}$ catalyst-to-oil and 400 rpm);
(vi) the presence of FAME ($A\%_{FAME}$ in Table 25) fluctuated significantly, from a minimum of 10.23% under severe conditions (i.e., 320°C, 10%$_{w/w}$ catalyst-to-oil, 600 rpm) to a maximum of 88.07% (i.e., 280°C, 4%$_{w/w}$ catalyst-to-oil, 600 rpm). This indicated that TGs conversion was incomplete in all tests, as χ values never reached 100%.

To gain a more comprehensive understanding of the effects of the three investigated variables (i.e., T, Υ and ω, in Table 25) and their interactions on the DO performances, a statistical analysis of the data was conducted, as described in Section 2.5.4.2.

5.2.3.2 STATISTICAL CONSIDERATIONS

For a quantitative and objective analysis of the experimental data, the effects of the investigated factors (A = T, B = Υ, D = ω, as shown in Table 9) were statistically assessed by calculating the model coefficients, as described in Section 2.4.3.

Table 26 presents the results of statistical evaluation divided in two key areas: (i) coefficients of factors and their interactions (see Equation 2.20) for the product composition and performance parameters, including $Y_{product}$ (Equation 2.9), χ (Equation 2.10), Y_{diesel} (Equation 2.11), and $S_{HDO/DCOx}$ (Equation 2.12); and (ii) significance of the coefficients, indicating the statistical relevance of the factors.

The significance of the factors and their interactions was determined using the variance of the experimental error calculated from central points of the Ni-Mo-Al full factorial 2^3 design (see Table 19 in Section 5.2), based on the assumption that this variance provides a reliable estimate of the system's natural variability, as discussed in Section 2.5.4.2.

For $A\%_{BHC}$, however, it was not possible to calculate significance because the experimental error variance could not be estimated from the central points due to a lack of data variability (see Table 19).

The $Y_{product}$ (Equation 2.9) was significantly affected by the main effects of temperature (A = T, see significance in Table 26) and stirring speed (D = ω, see significance in Table 26), both showing negative effects. These negative impacts align with findings from the literature [210], which suggest that as catalytic DO increases—driven by high temperatures—more volatile HCs (e.g., glycerol propane and light cracking HCs) are produced, leading to a reduction in $Y_{product}$. As regards the ω, the increase in stirring speed improves the contact between reagents and catalyst, thus increasing the efficiency of the reaction [309], and consequently the conversion of TGs into n-alkanes. In contrast, lower T and ω inhibit cracking and reduce the interaction between reagents and catalysts, resulting in an increase in $Y_{product}$.

The statistical analysis on χ (Equation 2.10) revealed significant effects for the three main factors (T, Υ, and ω), all of which were positively correlated with χ (see Table 26). As these factors increase, χ also increases. An increase in T favors endothermic reactions, and since the DO process is an overall endothermic, sees it benefits from higher temperatures, as detailed in Section 1.6.2. Additionally, as the catalyst amount increases, the available active surface area for reactant adsorption also grows, enhancing χ. Regarding ω it was pointed out that ω speeds improve the interaction between reactants and the catalyst, leading to more efficient reactions [309]. The interaction between the Υ-ω was also significantly positive. This makes sense because increasing both the catalyst amount and stirring speed enhances the contact between reactants and the catalyst, further improving χ.

A weak but significantly negative effect was found for the quadratic term of Υ (see β_{BB} coefficient in Table 26) indicating that the relationship between Υ and χ follows a downward-pointing parabola [325]. Initially, increasing Υ leads to higher χ, but after reaching a certain maximum, further increases in Υ result in a decline in χ. An excessive increase in Υ can result in a decrease in χ. An overabundance of catalyst can cause agglomeration or reduce the

available space between catalyst particles, hindering the diffusion of reactants to active surfaces [301]. Moreover, too much catalyst may promote undesirable side reactions that compete with the main reaction, further reducing the overall efficiency of the process [301].

The Y_{diesel} (Equation 2.11) was significantly influenced by T, Υ, ω, and the interactions between T-Υ, and Υ-ω, with all regression coefficients being positive (see Table 26). This is consistent with the literature, as an increase in these parameters promotes the reactions leading to the formation of diesel-range n-alkanes (C_{15}-C_{18}) in the product [180, 323], as confirmed by the similar trend in $A\%_{Ci}$ (with $15 \leq i \leq 18$). However, the quadratic term for T (see β_{AA} in Table 26) was also statistically significant, but with a negative coefficient. This indicates a concave response curve, meaning that an excessive increase in T leads to a reduction in Y_{diesel}. The reason is that overly high T promotes secondary cracking reactions (see Section 1.5.1.3), which in turn decrease the Y_{diesel}.

$S_{HDO/DCOx}$ (Equation 2.12) was significantly influenced by all linear and quadratic factors, as well as their interactions (see Table 26), with some of these having a positive effect, while others a negative impact.

The $A\%_{Ci}$ (with $15 \leq i \leq 18$) was found to be statistically influenced by the three main factors (T, Υ, ω) and the interaction between Υ and ω in a positive manner, while the quadratic term Υ^2 had a negative influence. In this case, an increase in the parameters T, Υ and ω leads to a higher percentage of C_{15}-C_{18} in the product. Additionally, a simultaneous increase in Υ and ω enhances the contact between the reactants and the catalyst, making the reaction more efficient. The negative coefficient for Υ^2 in Table 26 indicated that a significant increase in this factor results in a substantial decrease in $A\%_{Ci}$ (with $15 \leq i \leq 18$). This phenomenon mirrors the behavior observed for χ, where an excessive increase in Υ could lead to a decrease in χ due to factors such as saturation, limited diffusion, and side reactions.

The $A\%_{FAME}$ was found to be statistically influenced by T, Υ, and ω, as well as by the interaction between Υ and ω in a negative manner (as shown by the sign of the coefficients in Table 26). In contrast, the quadratic term Υ^2 has a

positive influence on $A\%_{FAME}$. Notably, the behavior of $A\%_{FAME}$ is exactly the opposite of that observed for $A\%_{Ci}$ (with $15 \leq i \leq 18$). Indeed, an increase in the $A\%_{FAME}$ corresponds to a decrease in the $A\%_{Ci}$ (with $15 \leq i \leq 18$), as the DO reaction is not completed, and the formation of n-alkanes (C_{15}-C_{18}) are disfavored. This phenomenon is explained by the reaction mechanisms discussed in Section 1.5.

As the process parameters increase, there is an increase in $A\%_{Ci}$ (with $15 \leq i \leq 18$) and a decrease in $A\%_{FAME}$, because the reaction conditions become more favorable for the DO of TGs into n-alkanes, leading to an increase in $A\%_{Ci}$ (with $15 \leq i \leq 18$) and a decrease in $A\%_{FAME}$, as detailed in Section 1.5.

$A\%_{Ci}$ (with $8 \leq i \leq 14$) was statistically influenced solely by T, with positive coefficient (see Table 26). Indeed, an increase in T favors cracking reactions that lead to the formation of lighter compounds (as described in Section 1.5.1.3).

$A\%_{UHC}$ was statistically influenced by both T and T^2 positively. This is because the saturation of n-alkenes to form n-alkanes is typically exothermic reaction [326]. Thus, an increase in T tends to hinder the saturation reaction, resulting in a higher content of UHC.

Regarding the by-products labeled as "*Others*" in Table 26, all factors and their interactions were found to be statistically significant, except for T^2, with both positive and negative effects.

Regarding the good fit of the data with the proposed model (see Section 2.5.4.2, Equation 2.20) and the estimated coefficients (see Table 26), none of the models demonstrated an excellent fit for the data; however, the model proposed for certain responses (i.e., $A\%_{Ci}$ with $15 \leq i \leq 18$, $A\%_{FAME}$, χ and Y_{diesel}) appeared to have a reasonably good value for *Expl. Var* (around or more than 80%). On the other hand, the models suggested for the responses in Table 26 did not exhibit a good fit for the external data, as indicated by *CV Expl. Var* values, which assumed not good value, pointing out the inadequacy of the proposed model for other data external to those in the experimental plan by emphasizing a probable overfitting problem.

Table 25 Experimental results of unreplicated FCCCD of Ni-Mo-Al catalyst.

	T	Υ	ω	$A\%_{Ci}$ $8 \leq i \leq 14$	$A\%_{Ci}$ $15 \leq i \leq 18$	$A\%_{Ci}$ $19 \leq i \leq 30$	$A\%_{BHC}$	$A\%_{UHC}$	$A\%_{Others}$	$A\%_{FAME}$	$Y_{product}$	χ	Y_{diesel}	$S_{HDO/DCOx}$
	[°C]	**[%w/w]**	**[rpm]**	**[%]**	**[%]**	**[%]**	**[%]**	**[%]**	**[%]**	**[%]**	**[wt%]**	**[wt%]**	**[wt%]**	**[-]**
Test_01	-1	-1	-1	0.00	13.96	0.00	0.00	0.00	1.36	84.68	97.57	17.38	13.62	0.8
Test_02	-1	1	-1	0.00	13.97	0.64	0.00	0.00	3.17	82.22	97.89	19.52	13.68	0.6
Test_03	1	-1	-1	1.34	45.89	1.29	0.00	0.27	3.99	47.22	82.10	61.23	37.68	0.6
Test_04	1	1	-1	1.74	67.10	2.07	0.00	1.66	0.34	27.09	87.29	76.35	58.58	0.8
Test_05	1	-1	1	0.63	54.17	1.58	0.00	3.00	1.34	39.28	82.54	67.58	44.71	0.8
Test_06	-1	1	1	0.00	8.82	1.06	0.00	0.46	1.59	88.07	89.11	21.53	7.86	0.4
Test_07	-1	-1	1	0.00	29.69	0.56	0.00	0.00	11.53	58.22	89.06	48.15	26.44	0.4
Test_08	1	1	1	2.61	80.16	2.12	1.10	2.10	1.68	10.23	80.37	91.78	64.43	1.0
Test_09	0	0	0	0.37	35.09	2.57	0.00	0.92	2.25	58.80	91.27	46.33	30.02	0.7
Test_10	-1	0	0	0.00	20.74	0.40	0.00	0.38	4.63	73.85	92.36	31.79	19.15	0.5
Test_11	0	-1	0	0.00	23.45	0.45	0.00	0.00	1.89	74.21	91.71	31.94	21.51	0.6
Test_12	0	0	-1	0.00	39.10	0.00	0.00	0.00	4.57	56.33	87.89	50.49	34.37	0.7
Test_13	1	0	0	2.49	76.74	2.70	0.48	3.62	0.00	13.97	77.40	89.19	59.40	1.1
Test_14	0	1	0	1.88	66.70	2.60	0.00	0.00	1.25	27.57	87.81	75.79	58.56	0.8
Test_15	0	0	1	0.40	54.84	2.04	0.00	0.00	2.88	39.84	85.59	65.90	46.94	0.7

*Table 26 Regression coefficients, explained variance and explained variance in cross validation of main factors and interactions from experimental data of unreplicated FCCCD for Ni-Mo-Al catalyst and their significance (see Section 2.4.3). Significance P-value intervals: 0 < *** ≤ 0.001 < ** ≤ 0.01 < * ≤ 0.05 < . < 0.1 < no < 1. "N.v" means that CV Expl. Var has negative value (no fitting).*

Ni-Mo-Al	$A\%_{Ci}$ **8≤*i*≤14**		$A\%_{Ci}$ **15≤*i*≤18**		$A\%_{Ci}$ **19≤*i*≤30**		$A\%_{BHC}$		$A\%_{UHC}$		$A\%_{Others}$		$A\%_{FAME}$		$Y_{product}$		χ		Y_{diesel}		$S_{HDO/DCOx}$	
	[%]		**[%]**		**[%]**		**[%]**		**[%]**		**[%]**		**[%]**		**[wt%]**		**[wt%]**		**[wt%]**		**[-]**	
β_0	0.67	-	46.25	-	1.79	-	0.04	-	0.64	-	2.24	-	48.37	-	87.93	-	56.80	-	40.03	-	0.75	-
β_A	0.88	*	23.69	***	0.71	no	0.16	n.d	0.98	*	-1.49	***	-24.93	***	-5.63	***	24.78	***	18.41	***	0.16	***
β_B	0.43	no	11.13	***	0.36	no	0.11	n.d	0.01	no	0.78	***	-12.81	***	-0.06	no	11.19	***	9.63	***	0.04	**
β_C	0.06	no	4.77	***	0.34	no	0.11	n.d	0.36	no	0.56	***	-6.19	***	-2.61	*	7.00	***	3.25	**	-0.02	.
β_{AB}	0.30	no	3.29	**	0.15	no	0.14	n.d	0.12	no	-1.89	***	-2.11	no	0.34	no	1.32	no	2.75	**	0.08	***
β_{AC}	0.02	no	1.35	no	-0.08	no	0.14	n.d	0.34	no	-1.24	***	-0.52	no	1.35	no	-1.38	no	0.74	no	0.13	***
β_{BC}	0.20	no	3.21	**	-0.17	no	0.14	n.d	-0.34	no	1.52	***	-4.54	*	-0.97	no	4.20	*	2.17	*	0.03	.
β_{AA}	0.50	no	-0.30	no	-0.04	no	0.19	n.d	1.43	.	0.07	no	-1.85	no	-2.21	no	1.07	no	-2.77	*	0.05	.
β_{BB}	0.19	no	-3.96	*	-0.07	no	-0.05	n.d	-0.58	no	-0.67	***	5.13	.	2.67	no	-5.55	*	-2.01	no	-0.06	*
β_{CC}	-0.55	no	-2.07	no	-0.57	no	-0.05	n.d	-0.58	no	1.48	***	2.33	no	-0.35	no	-1.22	no	-1.39	no	-0.06	*
Expl. Var.	68.74		80.41		16.75		49.36		74.10		69.91		83.22		73.80		83.49		79.30		65.37	
CV Expl. Var.	n.v		47.53		n.v		n.v		n.v		n.v		52.23		21.01		55.34		34.01		n.v	

5.3 FINAL REMARKS

NiCoMo and ZnCoMo catalysts were successfully repurposed from propane ODH to DO for green diesel production, with satisfying performances in the whole domain of tested conditions. Specifically, from a general analysis of results of the 2^3 experimental designs, for the two catalysts NiCoMo and ZnCoMo, the reaction conditions that resulted in maximizing DO parameters and minimizing reaction conditions were: temperature of 320°C, $10\%_{w/w}$ of catalyst-to-oil ratio, and 2 hours of reaction time, although the two catalysts performed well under almost all reaction conditions tested.

The applied DoEs aimed to screen factors and conduct a preliminary characterization of the process for repurposing NiCoMo and ZnCoMo catalysts in the DO for green diesel production. The results indicated that a pre-reduction step is critical for maximizing the activity of both catalysts.

For both catalysts, the pure quadratic terms in the hypothetical response surface were significant solely for the fraction of diesel n-alkanes ($A\%_{Ci}$ where $15 \leq i \leq 18$), which is the primary product of interest in the DO process, as well as for certain secondary product fractions. Furthermore, all main effects and interactions involving temperature (T), catalyst-to-oil ratio (Υ), and reaction time (t) had a highly significant impact on $A\%_{Ci}$ with $15 \leq i \leq 18$ for both NiCoMo and ZnCoMo. Conversely, several responses did not exhibit significant influences from the main effects, even though the catalysts demonstrated high-quality performance across most experimental conditions. The interactions between various factors were noted, suggesting that complex relationships exist that influence the outcome of the DO process.

While the proposed statistical models captured much of the variability in the data for certain response variables, a second-order regression model may provide better predictive ability. Future studies should consider employing DoE methodologies that facilitate such advanced modeling.

The preference for the HDO pathway over DCO_x aligns with sustainability goals, as it minimizes carbon loss and promotes the efficient use of hydrogen. This aspect is critical in advancing the green fuel agenda and reducing GHGE associated with traditional fuel production processes.

The catalysts exhibited encouraging performance stability over recycling tests, keeping complete conversions of TGs and high Y_{diesel} up to four successive DO cycles. ZnCoMo could be slightly more promising than NiCoMo because it showed hints of higher catalytic activity and elemental stability in cyclic usage.

The Ni-Mo-Al catalyst demonstrated significant catalytic activity even without a pre-reduction step, suggesting self-reduction under reaction conditions. In this case, the reaction conditions that maximized DO performances, in terms of χ, Y_{diesel}, and product composition, were the most severe: temperature of 320°C, 10%$_{w/w}$ of catalyst-to-oil ratio, and 6 hours of reaction time.

Statistical evaluations demonstrated that $Y_{product}$, χ, and Y_{diesel} were significantly influenced by the main factors of T, Υ, and t, as well as their interactions. Interaction effects highlighted the complexity of the DO process, with certain conditions leading to counterintuitive outcomes, such as decreased Y_{diesel} when both T and t were increased simultaneously.

The established models showed a good fit for several performance parameters, although the potential for overfitting was evident due to discrepancies between *Exp. Var* and *CV Expl. Var*. The significance of pure quadratic terms for key responses suggests that a second-order model may be necessary for more accurately representing the data.

The recycling tests demonstrated a marked decline in the catalytic performance of the Ni-Mo-Al catalyst, as indicated by the reduction in χ and Y_{diesel}, along with a shift in product composition from n-alkanes to FAME and other by-products. Although χ stabilized by the third cycle, Y_{diesel} continued to decrease. As the number of cycles increased, the overall fraction of n-alkanes decreased, while the FAME fraction increased.

The analysis of the FCCCD data presents several insights into the performance of the catalytic DO process.

The statistical evaluation confirmed the significance of temperature (T), catalyst-to-oil ratio (Υ), and stirring speed (ω) on key performance

parameters. Specifically, χ is positively correlated with all three factors, indicating that higher T, Υ, and ω lead to improve this parameter.

The analysis highlighted a complex relationship where increasing Υ initially improves performance but can lead to diminishing returns due to factors like saturation and limited diffusion. Significant interactions between Υ and ω were also noted, further enhanced.

While the proposed model provided reasonable explanatory power for several responses, issues with external validity were identified, suggesting potential overfitting. The variability in responses indicated that while the model captured significant trends, it might not generalize well beyond the tested conditions.

6. CATALYSTS CHARACTERIZATIONS POST TEST

This section presents the results of the characterizations conducted on the post-test catalyst samples. Specifically, the analyses focused on the catalysts that exhibited the best performance, those recovered after recycling, and the catalysts that underperformed in the post-test evaluations. The aim is to assess whether any structural or compositional changes occurred during these tests and to explore if the observed loss of catalytic activity in some cases may be linked to these changes.

The following characterizations were conducted for this purpose: (i) ***ICP-MS*** to assess potential compositional variations; (ii) ***elemental CHNS analysis*** to determine the possible presence of C deposit on the catalyst surface; (iii) ***XRD*** to detect any changes in the crystallinity of the catalyst. (iv) ***SEM*** to examine any catalyst morphological changes; and (v) ***TEM*** analysis to assess changes in the microstructure, morphology, and crystallinity of the catalyst.

6.1 NiCoMo and ZnCoMo post tests

The analyzed samples of the two catalysts, NiCoMo and ZnCoMo, were: (i) catalyst post treatment "*(1)"*, which resulted in the poorest DO performance (refer to the Table 19); (ii) samples post treatment *"ab"* that yielded the best

performance (refer to the Table 19); and (iii) post-recycling "*Test_R4"* (see Table 21), whose reaction conditions correspond to the *"ab"* treatment.

6.1.1 ICP-MS RESULTS

ICP-MS results of NiCoMo and ZnCoMo catalyst post-test are reported in Table 27.

For NiCoMo, a comparison of the elemental molar ratios in the as-synthesized state and those after one-run tests (treatments *(1)* and *"ab"*, conditions in Table 8) revealed no significant changes (see Table 27). However, the results after the recycling tests (*Test_R4* in Table 27) indicated a relative loss of Mo, as the Co/Mo ratio after *Test_R4* was higher than in the as-synthesized state. Additionally, the Ni/Mo and Ni/Co ratios after *Test_R4* were lower than those in the as-synthesized state (Table 27). This suggests that Ni was likely decreased as well.

Table 27 Results of NiCoMo and ZnCoMo analysis by ICP-MS in terms of elemental molar ratios; conditions of treatments (1) and "ab" are in Table 8.

NiCoMo	***Ni/Mo (mol/mol)***	***Ni/Co (mol/mol)***	***Co/Mo (mol/mol)***
As-synthesized	0.08	0.08	1.03
NiCoMo post-treatment (1)	0.10	0.11	0.94
NiCoMo post-treatment ab	0.10	0.11	0.95
NiCoMo post Test_R4	0.05	0.07	1.37
ZnCoMo	***Zn/Mo (mol/mol)***	***Zn/Co (mol/mol)***	***Co/Mo (mol/mol)***
As-synthesized	0.13	0.11	1.26
ZnCoMo post-treatment (1)	0.12	0.11	1.06
ZnCoMo post-treatment ab	0.10	0.09	1.10
ZnCoMo post Test_R4	0.11	0.09	1.27

In contrast, ZnCoMo showed no significant trends in elemental ratios (Table 27), indicating a potentially greater stability than NiCoMo, especially during cyclic use (as underlined in Table 21).

6.1.2 CHNS RESULTS FOR NICOMO AND ZNCOMO

The results of the CHNS analysis on the various samples are reported in Table 28.

For the NiCoMo catalyst, the carbon content increased from 0.38% in the as-synthesized catalyst to approximately 5% after treatment *(1)*, and to 1.5-1.8% after recycling tests (*Test_R4* in Table 28) and treatment "*ab*". This rise may be attributed to carbon deposition or HCs and polymer fouling on the catalyst surface [35, 59], particularly for treatment *(1)*, which resulted in worst DO performance, as shown in Table 19. The poorer performance in treatment *(1)* can be attributed to carbon deposits forming on the catalyst's surface, which could negatively impact its effectiveness. No significant trends were observed for H, N, or S.

Table 28 Results of CHNS analysis of NiCoMo and ZnCoMo samples: (i) as-synthesized; (ii) post treatment (1); (iii) post treatment "ab"; (iv) post recycling test. Conditions of treatments (1) and "ab" are in Table 8.

NiCoMo	***C [%]***	***H [%]***	***N [%]***	***S [%]***
As-synthesized	0.38	0.15	0.92	0.05
NiCoMo post-treatment (1)	4.99	0.24	0.00	0.00
NiCoMo post-treatment ab	1.87	0.12	0.00	0.00
NiCoMo post Test_R4	1.64	0.09	0.00	0.00
ZnCoMo	***C [%]***	***H [%]***	***N [%]***	***S [%]***
As-synthesized	0.26	0.00	1.75	0.00
ZnCoMo post-treatment (1)	5.03	0.19	0.00	0.00
ZnCoMo post-treatment ab	1.39	0.06	0.00	0.00
ZnCoMo post Test_R4	1.61	0.00	0.00	0.00

For the ZnCoMo catalyst, like NiCoMo, there was an observed increase in carbon content, rising from 0.26% in the as-synthesized catalyst to approximately 5% after treatment *(1)*, and then to around 1.4-1.6% after treatment *ab* and recycling test, respectively. The same observations regarding carbon content in the post-test catalysts for NiCoMo are also applicable to ZnCoMo.

6.1.3 NiCoMo and ZnCoMo XRD post tests

Figure 52 and Figure 53 report the results of XRD analyses of NiCoMo and ZnCoMo post tests.

As shown in Figure 52, the "as-synthesized" NiCoMo catalyst had a crystalline structure (as also underlined in Section 3.1.4, Figure 24), while the post-treatment samples showed an amorphous structures, indicating that the reaction conditions caused a loss of catalyst crystallinity.

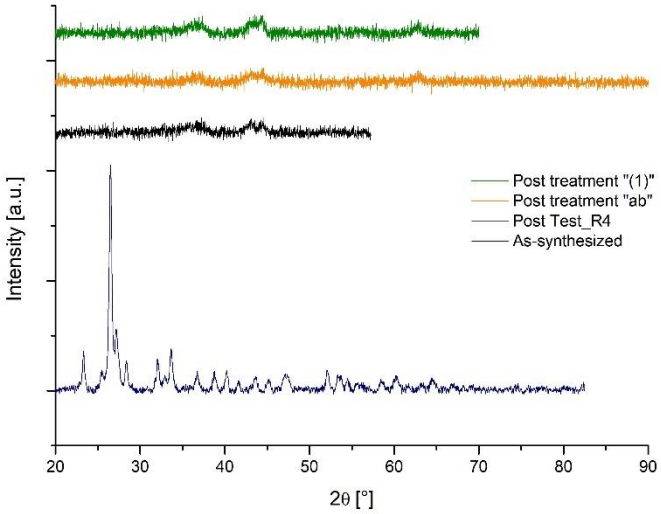


Figure 52 XRD of NiCoMo catalyst post test with reference to as-synthesized form: (i) NiCoMo post treatment (1); (ii) NiCoMo post treatment "ab"; and (iii) catalyst post recycling test (Test_R4). Experimental conditions of tests are reported in Table 8.

The same behavior of the NiCoMo catalyst was found for the ZnCoMo catalyst, as can be seen from Figure 53. Also in this case, a loss of crystallinity was observed for post-test catalysts.

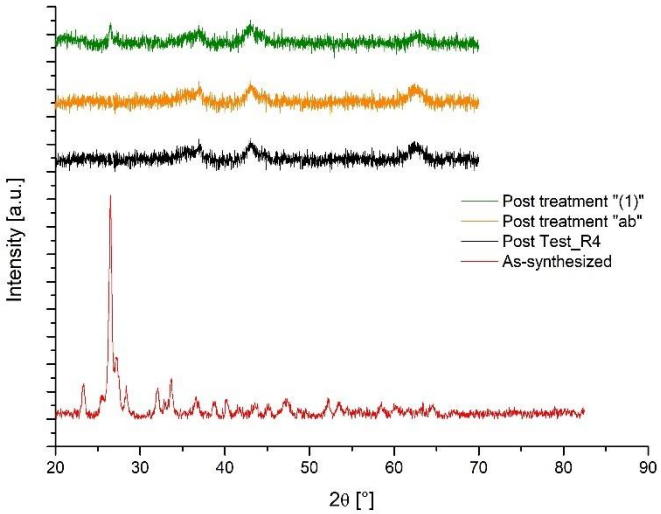


Figure 53 XRD of ZnCoMo catalyst post test with reference to as-synthesized form: (i) ZnCoMo post treatment (1); (ii) ZnCoMo post treatment "ab"; and (iii) catalyst post recycling test (Test_R4). Experimental conditions of tests are reported in Table 8.

Although the catalysts appeared to have lost crystallinity during the tests, their performance remained consistently high, as evidenced by the test results in Table 19 and Table 21. This loss of crystallinity was also observed in the catalyst post recycling tests (see Figure 52 and Figure 53), yet the catalysts maintained stable catalytic activity throughout (see Figure 43), demonstrating their durability and effectiveness despite structural changes.

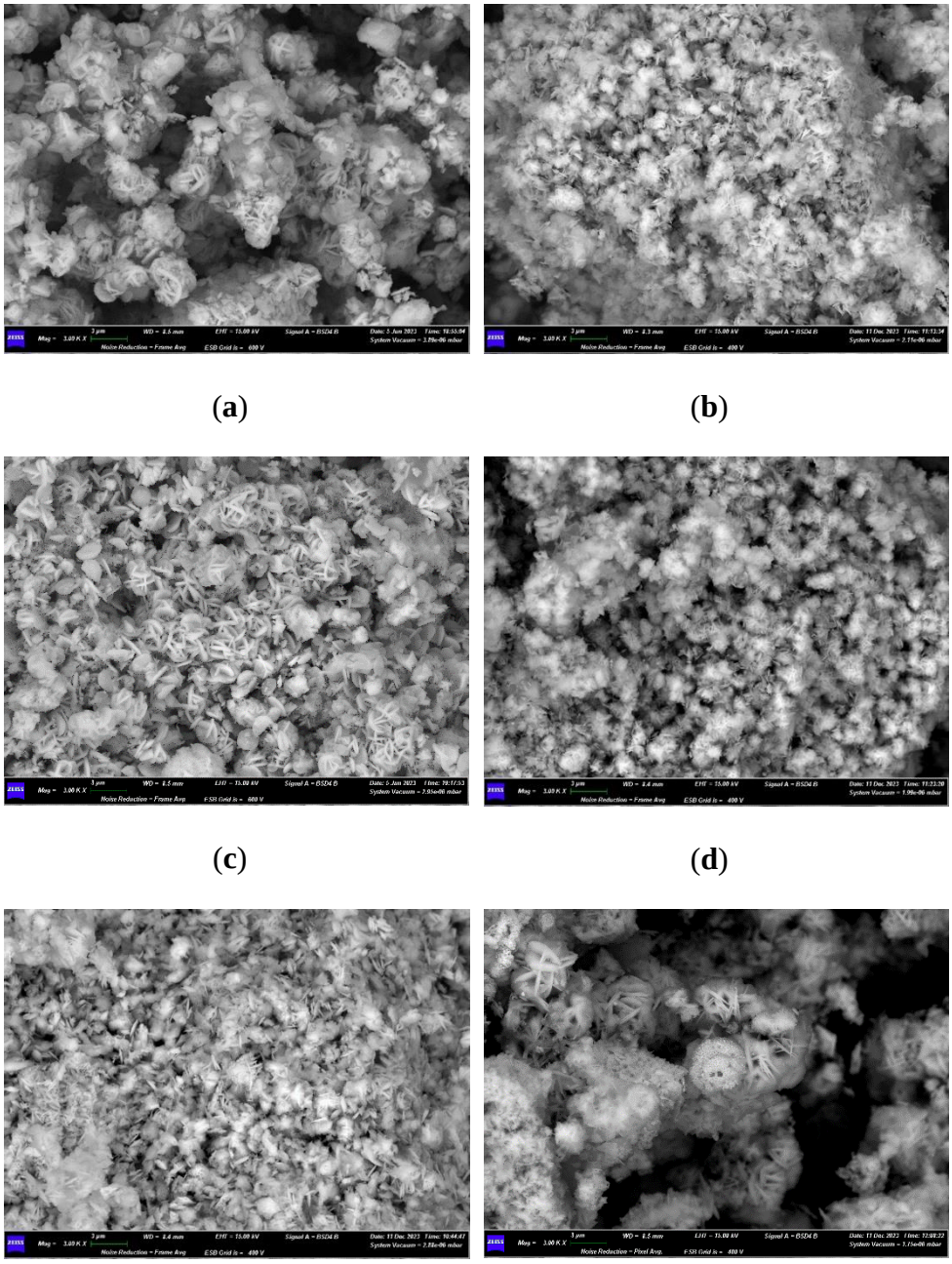
Amorphous catalysts are often more performers in the catalytic reactions due to their less ordered structure, which typically results in a higher surface area compared to crystalline catalysts [327]. This disordered structure exposes more active sites to the reactants, increasing the availability of catalytic sites for DO [328].

Furthermore, amorphous catalysts demonstrate greater resistance to deactivation and better adaptability to varying reaction conditions. These characteristics enable them to maintain strong performance (as shown in Table 19 and Table 21), even after losing crystallinity.

6.1.4 SEM POST TESTS

Figure 54 (a) and Figure 54 (b) present SEM micrographs of NiCoMo and ZnCoMo, respectively, following a one-run test after treatment "*ab*". The SEM images revealed that the catalysts exhibited a flaky morphology,

retaining some remnants of the original lamellar structure (compare to Figure 27 (a) and (b) with Figure 54 (a) and (b)). Therefore, there were no significant morphological differences between the two catalysts after treatment "*ab*".



(**a**) (**b**)

(**c**) (**d**)

(**e**) (**f**)

Figure 54 SEM micrographs at 3kx magnification of post-test NiCoMo and ZnCoMo: (a) NiCoMo after treatment "ab"; (b) ZnCoMo after treatment "ab"; (c) NiCoMo after treatment (1); (d) ZnCoMo after treatment (1); (e) NiCoMo after Test_R4; (f) ZnCoMo after Test_R4.

Figure 54 (c) and Figure 54 (d) display SEM micrographs of NiCoMo and ZnCoMo after treatment *(1)*, which was associated with lower DO performance (see Table 19). In this case, the micrographs also indicated that the catalysts developed a flaky morphology, with some residual lamellar structure.

Figure 54 (e) and Figure 54 (f) show the NiCoMo and ZnCoMo catalysts after the recycling test (*Test_R4*). The morphology of both catalysts remained flaky, although the lamellar remnants from the original as-synthesized state (Figure 27 (a) and (b)) were less pronounced.

Overall, SEM observations did not reveal significant structural or morphological differences among the various samples, despite their markedly different process performances.

6.2 CHARACTERIZATION OF NI-MO-AL POST TESTS

The analyzed Ni-Mo-Al catalyst samples post test were: (i) catalyst post treatment *"(1)"*, which resulted in the poorest DO performance (refer to Table 22); (ii) samples after treatment *"abc"*, which produced the best performance (refer to Table 22); and (iii) post-recycling samples from "*Test_R4*" (see Table 24), where the reaction conditions matched those of the "*abc*" treatment.

6.2.1 NI-MO-AL ICP-MS POST TESTS

ICP-MS results of Ni-Mo-Al post test samples are summarized in Table 29. The catalyst from treatment *(1)*, which delivered the poorest DO performance (refer to Table 22), was not analyzed due to insufficient sample availability. Ni-Mo-Al post treatment "*abc*" and post *Test_R4*, along with the fresh catalyst, together represented a progression in the catalyst's cyclic reuse.

Table 29 ICP-MS results of Ni-Mo-Al catalyst in terms of elemental molar ratios; conditions of treatments (1) and "abc" are in Table 8.

Ni-Mo-Al	***Ni/Al (mol/mol)***	***Ni/Mo (mol/mol)***	***Al/Mo (mol/mol)***
As-synthesized	0.708	0.535	0.756
Ni-Mo-Al post-treatment abc	0.684	0.544	0.795
Ni-Mo-Al post Test_R4	0.686	0.532	0.776

The ratios of Ni/Al, Ni/Mo, and Al/Mo in Table 29 remained largely unchanged, indicating that the relative amounts of metals stayed consistent throughout the repeated use of the Ni-Mo-Al catalyst. This stability suggests that the observed decline in catalytic activity, as discussed in Section 5.2, cannot be attributed to metal leaching or loss from the catalyst.

6.2.2 CHNS RESULTS FOR NI-MO-AL

Table 30 presents the results of the CHNS analyses for the Ni-Mo-Al samples. The carbon content increased from 0.38% in the fresh catalyst, to 0.90% after treatment "*abc*", and to approximately 3.7-4% after treatment *(1)* and *Test_R4*. This rise could be attributed to carbon deposition or fouling from HCs or polymers on the catalyst surface [35, 59], as seen for NiCoMo and ZnCoMo in Section 6.1.2. These carbon deposits might have been partially deactivated the catalyst, causing it to lose its catalytic performance, as shown by the results in Table 22 (see treatment *(1)*) and Table 24 for recycling test (*Test_R4*). No significant trends were observed for H, N, or S.

Table 30 Results of CHNS analysis of Ni-Mo-Al samples: (i) as-synthesized; (ii) post treatment (1); (ii) post treatment "abc"; (iv) post recycling test. Conditions of treatments (1) and "abc" are in Table 8.

NiCoMo	***C [%]***	***H [%]***	***N [%]***	***S [%]***
As-synthesized	0.38	0.15	0.92	0.05
Ni-Mo-Al post-treatment (1)	3.72	0.14	0.0	0.0
Ni-Mo-Al post-treatment abc	0.90	0.57	0.0	0.05
Ni-Mo-Al post Test_R4	3.95	0.15	0.0	0.0

6.2.3 XRD OF NI-MO-AL POST TESTS

The XRD results of Ni-Mo-Al catalyst post test are reported in Figure 55. The catalyst from treatment *(1)*, which delivered the poorest DO performance (refer to Table 22), was not analyzed due to insufficient sample availability.

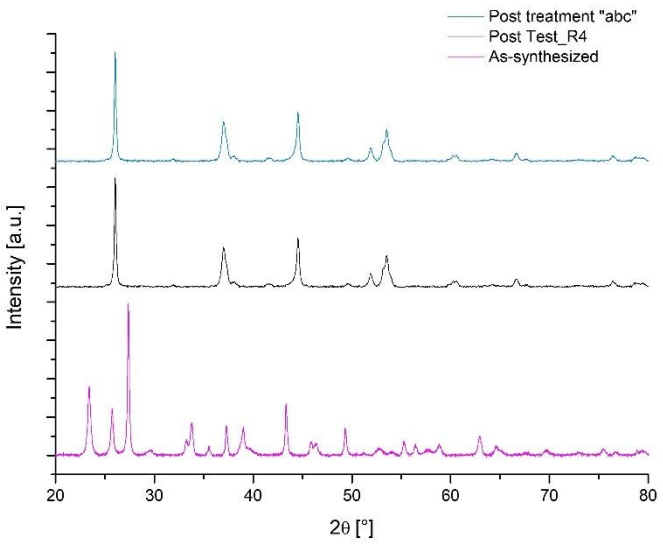


Figure 55 XRD results of Ni-Mo-Al catalyst post tests with reference to as-synthesized form: (i) catalyst post treatment "abc"; (ii) catalyst post Test_R4.

As shown in Figure 55, the as-synthesized sample exhibited a well-defined crystalline structure, as previously discussed in Section 3.2.4. The post *Test_R4* and treatment "*abc*" samples displayed a slight reduction in peak intensity, suggesting a possible decrease in crystallinity; however, the crystal structure remained clearly identifiable in both samples.

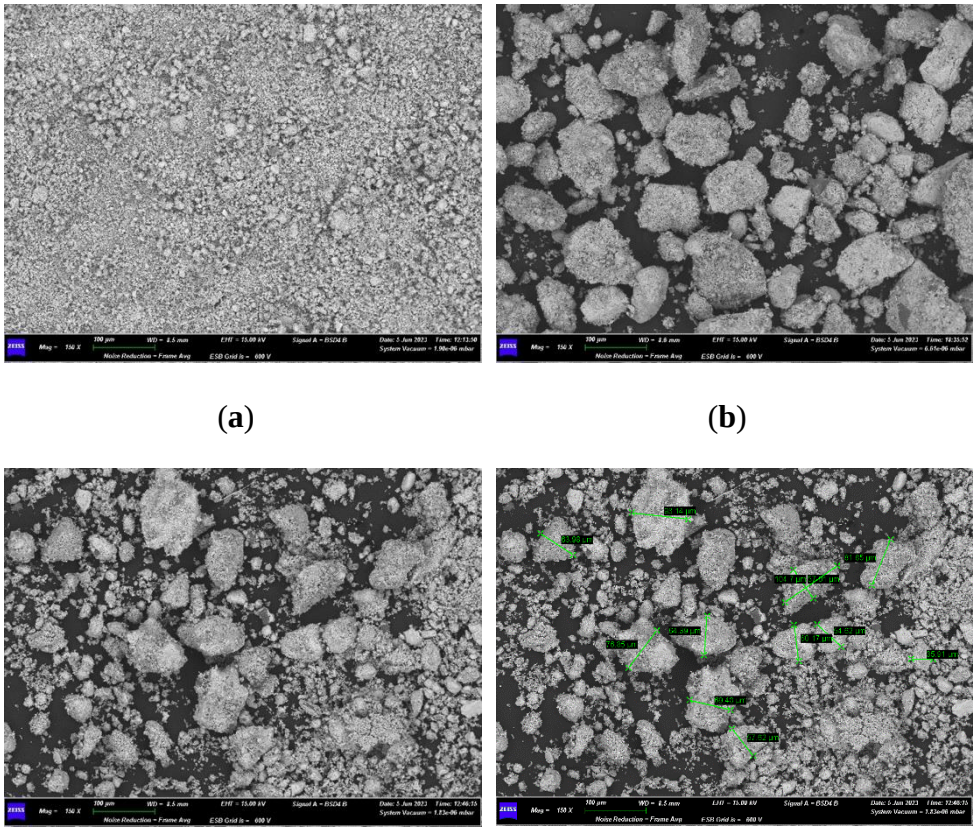
6.2.4 SEM OF NI-MO-AL POST TESTS

SEM post tests were reported in Figure 56.

The Ni-Mo-Al catalyst post treatment "*abc*" (i.e., 320°C, 10%$_{w/w}$ of catalyst-to-oil ratio, 6 h), in Figure 56 (a), exhibited a finer morphology compared to the as-synthesized catalyst (Figure 36 (d)).

After treatment *(1)*, the particle sizes of the Ni-Mo-Al catalyst (see Figure 56 (b)) were larger than those of both the fresh catalyst (Figure 36 (d)) and the catalyst after treatment *"abc"* (Figure 56 (a)).

Ni-Mo-Al post recycling tests (*Test_R4*, in Figure 56 (c) and (d)) developed a larger particle size (compare Figure 56 (d) with Figure C 4 in Addendum C) compared to its as-synthesized form (Figure 36 (d)) and after treatment "*abc*" (Figure 56 (a)). A comparison between Figure 56 (d) and Figure C 4 in Addendum C revealed that the particle size had doubled or tripled (~54-100 μm) relative to the size of the catalyst in its original state (~11-30 μm).



(**a**) (**b**)

(**c**) (**d**)

Figure 56 SEM micrographs of Ni-Mo-Al after DO test at 150x magnification: (a) Ni-Mo-Al post treatment "abc"; (b) Ni-Mo-Al post treatment (1); (c) Ni-Mo-Al post Test_R4; (d) Ni-Mo-Al post Test_R4 with measurements of diameter.

SEM results indicate that recycling or repeated use caused notable morphological changes, likely due to agglomeration, compromising the catalyst's long-term reusability and effectiveness. In fact, recycling tests showed a decline in DO performance as the number of catalytic reuse cycles increased (see Table 24 in Section 5.2.2). While the finer morphology after the *"abc"* treatment (*"abc"* treatment was conducted under the same reaction conditions as the 1st cycle of recycling tests) may enhance initial performance

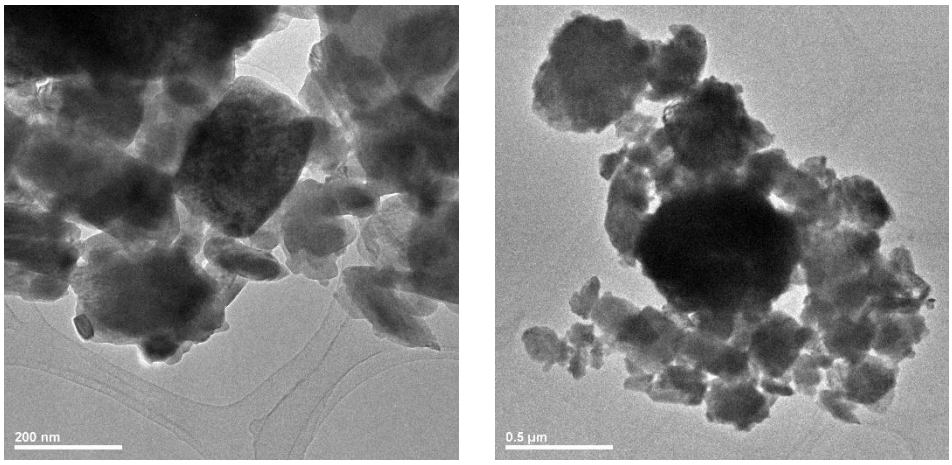
(see Table 22), further treatments and recycling lead to particle agglomeration, potentially reducing catalytic efficiency.

Wu et al. [329] and Wang et al. [228] observe that the decline in catalyst activity for DO to produce green diesel during recycling tests may be attributed to an increase in catalyst size, which in turn resulted in reduced surface area and pore volume.

So, the Ni-Mo-Al catalyst showed some modifications in terms of physical structure (i.e. aggregation of particles, Figure 56), that could negatively impact catalytic efficiency (see Table 22 and Table 24) without altering the metal composition and crystalline structure (see ICP-MS results in Table 29 and XRD in Figure 55).

6.2.5 RESULTS OF TEM ANALYSIS

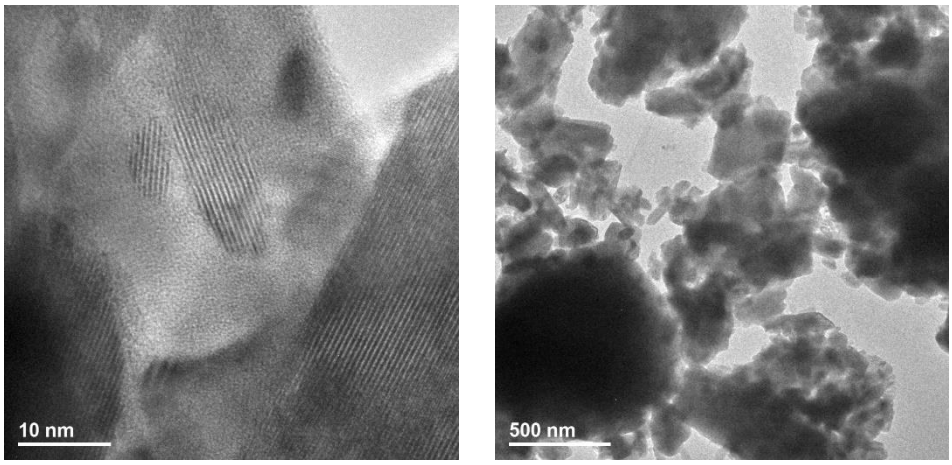
In Figure 57, the TEM micrographs (collected and analyzed at ICPEES of University of Strasbourg) of the as-synthesized Ni-Mo-Al catalyst are presented. However, a heterogeneous structure was evident, characterized by a mixture of multiple phases (as corroborated by XRD and SEM in Figure 34 and Figure 36). The Ni-Mo-Al catalyst exhibited an aggregated morphology, as shown in Figure 57, confirmed by SEM analysis in Figure 36.



(**a**) (**b**)

Figure 57 TEM micrographs of as-synthesized Ni-Mo-Al catalyst: (a) at 200 nm; (b) 0.5 µm.

Figure 58 displayed the TEM images of the catalyst following a TPR which simulates the in-situ pre-reduction conducted for catalyst activation before the DO tests (as detailed in Section 2.4). It was observed that although the catalyst consists of an aggregate of different phases (Figure 58 (b)), it had gained a certain degree of crystallinity after TPR (Figure 58 (a)). This suggested that TPR, which served as the in-situ pre-reduction before the DO test, may have enhanced the crystallinity of the catalyst.

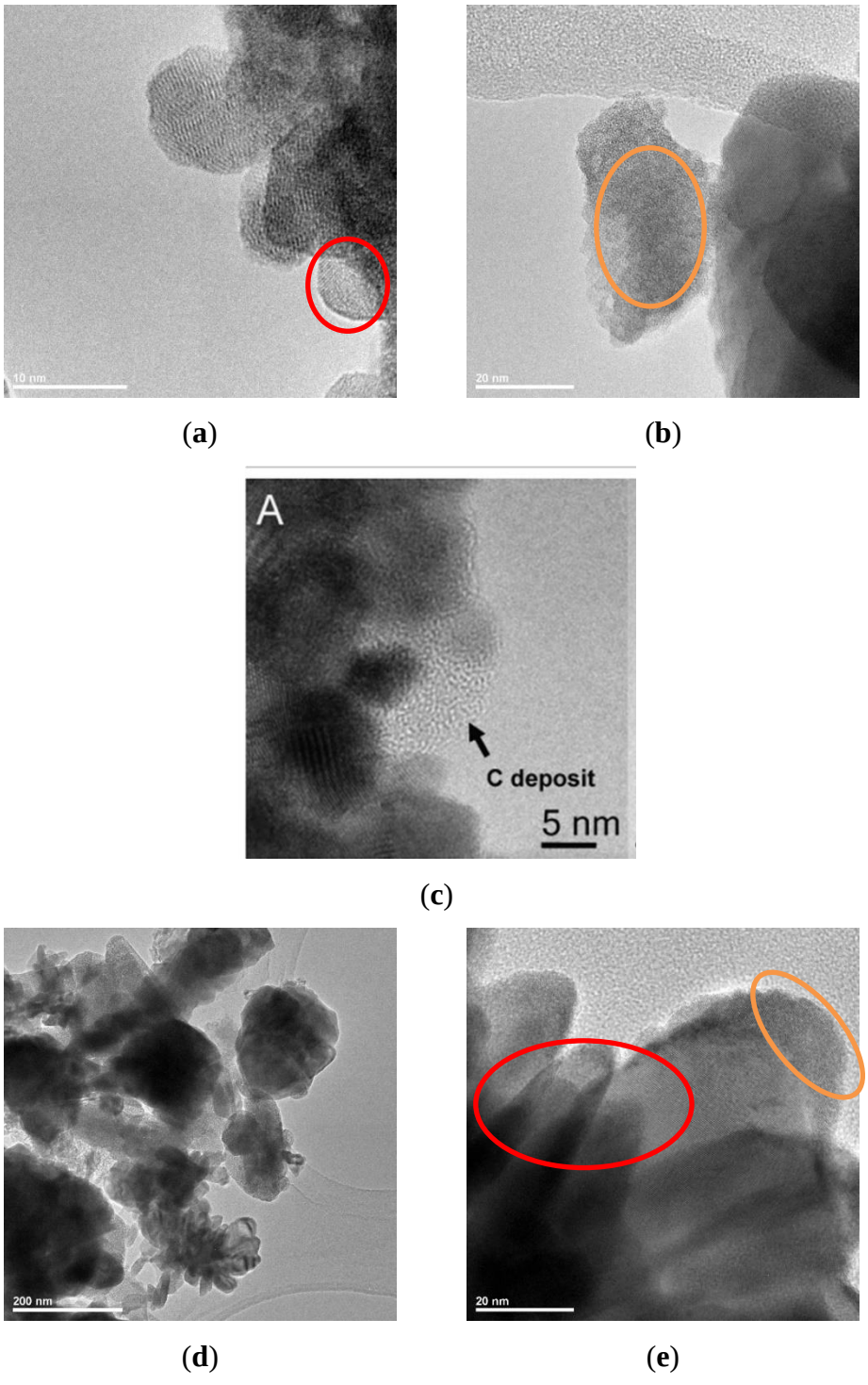


(**a**) (**b**)

Figure 58 TEM micrographs of Ni-Mo-Al post TPR: (a) at 10 nm; (b) at 500nm.

Figure 59 presented the TEM images of the post-treatment catalysts. Specifically, the two micrographs of the Ni-Mo-Al catalyst post treatment "*abc*" (Table 22), in Figure 59 (a) and (b), revealed that while some crystallinity of the material persisted (red circle in Figure 59 (a)), as also underlined in XRD analyses in Figure 55, it was accompanied by a new morphology likely associated to a C-deposit-like structure (compare Figure 59 (c) taken from literature [327], with orange circle in Figure 59 (b)). In fact, the CHNS analysis in Table 30 indicated an increase in C percentage in the post-test samples.

Figure 59 (d) showed the heterogeneous and aggregated morphology of the post *Test_R4* catalyst, while Figure 59 (e) showed some degree of catalyst crystallinity, as detailed in Figure 60 and as also underlined in XRD analyses in Figure 55, even after *Test_R4* superimposed on the same morphology attributable to C-deposits from the comparison with the literature [327].



(**a**) (**b**)

(**c**)

(**d**) (**e**)

Figure 59 TEM micrographs of post DO tests: (a) post treatment "abc" (320°C, 10% catalyst-to-oil, 6 h) at 10nm; (b) post treatment "abc" (320°C, 10% catalyst-to-oil, 6 h) at 20 nm; (c) C-deposit taken from [327]; (d) post Test_R4 (320°C, 10% catalyst-to-oil, 6 h) at 10 nm; (e) post Test_R4 (320°C, 10% catalyst-to-oil, 6 h) at 20 nm.

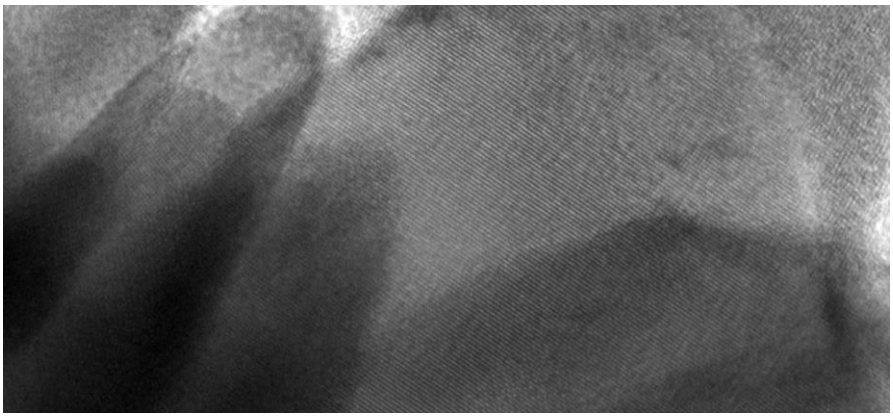


Figure 60 Detail of TEM image post Test_R4 circled in red in Figure 59 (d).

A plausible hypothesis was that these carbon deposits might have also aggregated the catalyst, as also noted by post-test SEMs in Figure 56, and caused partial catalyst deactivation confirmed by a decrease in catalytic performance (as reported in Table 21 and Table 23).

6.3 FINAL REMARKS

Both NiCoMo and ZnCoMo catalysts exhibited minimal structural changes (as observed in SEM, Figure 54) and loss in crystallinity (based on XRD, Figure 52 and Figure 53) in the post-test samples. Despite these changes, both catalysts maintained strong performances (see Table 19 and Table 21), highlighting their robustness and adaptability. However, carbon deposit (CHNS analysis, Table 28) and the loss of active components (ICP results, Table 27), particularly in the case of the NiCoMo catalyst, are factors that need to be addressed to ensure long-term efficiency.

The Ni-Mo-Al catalyst demonstrated consistent elemental stability in terms of metal composition, as evidenced by the ICP-MS results (Table 29), and maintained a crystalline structure, as shown in XRD analysis (Figure 55), even after recycling tests. However, structural changes such as particle aggregation (observed in SEM micrographs, Figure 56) and carbon deposition (indicated by CHNS analysis, Table 30, and supported by TEM images in Figure 59) emerged as significant factors affecting its catalytic performance over time. The carbon deposits, likely formed during the reaction, not only contributed to partial catalyst deactivation but also played

a role in the observed agglomeration, reducing the surface area and, consequently, the catalyst's overall efficiency.

Despite retaining some crystallinity, the catalyst's morphology evolved through each cycle, which negatively impacted long-term reusability and performance, as indicated by the decrease in DO efficiency after recycling tests (Figure 49). Thus, while the Ni-Mo-Al catalyst showed robustness in maintaining its structural integrity and elemental ratios, the accumulation of carbon deposits and agglomeration will require strategies to enhance the catalyst's long-term effectiveness.

7. RESULTS OF ADDITIONAL PRELIMINARY INVESTIGATIONS

At the conclusion of the PhD program, a series of preliminary tests were conducted to open new possible research lines, including: (i) preliminary study on the variation of stirring speed in DO tests for NiCoMo catalyst; (ii) DO tests with WCO as alternative feedstock to rapeseed oil. These initial investigations served not only as a basis for future experimental campaigns, but also provided critical insights into the behavior of the three catalysts under different feedstock conditions.

This chapter therefore discusses the methodologies employed, the results obtained, and the implications of these preliminary tests.

7.1 PRELIMINARY TEST RESULTS ON THE INFLUENCE OF STIRRING SPEED ON DO PERFORMANCE FOR NICOMO

Preliminary tests were performed to evaluate whether the reactor's stirring speed, varying from 200 to 700 rpm, influenced the general DO performance and product composition for the NiCoMo catalyst. A total of six tests were conducted. For further details on the testing procedure, refer to Section 2.6.1. The test conditions for treatment *(1)* (i.e., 280°C, 4%$_{w/w}$ of catalyst-to-oil ratio and 2 h, in Table 19) were chosen because they were based on one of the tests that yielded the worst results, allowing for a better assessment of any differences in the DO performances due to fluid dynamic/mass transfer – related variations

Some general observations were given from Table 31:
(i) as the stirring speed increased from 200 rpm to 700 rpm, χ (Equation 2.10) steadily raised, reaching a maximum value of 88.57% at 600 rpm. The increasing in χ was also confirmed by FT-IR spectra of reaction product in Figure 61, in which the bands related to C=O of FFAs and TG esters (i.e., at 1745-1710 cm^{-1}) decreased as the rpm increase, as for the bands at 1350-900 cm^{-1} related to stretching of C-O (for further details about FT-IR refers to Section 2.5.1). However, at 700 rpm, χ decreased slightly to 85.39%, indicating that further increases in stirring speed may not be advantageous;
(ii) Y_{diesel} (Equation 2.11) also increased with stirring speed, peaking at 77.96% at 600 rpm before declining slightly at 700 rpm (i.e., 68.69%);
(iii) $S_{HDO/DCOx}$ (Equation 2.12) did not show significant trends, with values ranging between 1.5% and 2.1%;
(iv) $A\%_{Ci}$ (with $15 \leq i \leq 18$): the content of these compounds rose as rpm increased, hitting a maximum of 83.32% at 600 rpm;
(v) the FAME content was highest at lower stirring speeds (58.23% at 200 rpm), but it decreased significantly at higher speeds (as confirmed by FT-IR spectra in Figure 61), dropping to 13.05% at 500 rpm and 13.28% at 600 rpm;

(vi) by-products such as "*BHC*," "*UHC*," and "*Others*" appeared in small quantities and showed little variation with no significant trends.

In conclusion, 200 rpm produced not fully favorable results, while 600 rpm appeared to be the optimal stirring speed at 280°C and 4%$_{w/w}$ cat-to-oil, delivering the highest χ value (i.e., 88.57%, see Table 31), the greatest Y_{diesel} (i.e., 77.96%, Table 31), and the best product composition (highest value of $A\%_{Ci}$ with $15 \leq i \leq 18$, and low value of $A\%_{FAME}$, Table 31).

Increasing the agitation speed up to 600 rpm significantly enhances the DO performance, as higher agitation improves contact between the catalyst and reactants, thereby boosting the reaction [309]. However, further increasing the speed to 700 rpm does not offer additional benefits and may even slightly decrease the process efficiency. This occurs because at excessively high speeds, increased agitation may create negative effects, such as excessive turbulence, or physical issues with the catalyst itself, resulting in decreased process efficiency [301]. Future DoEs for NiCoMo and ZnCoMo catalysts should include the stirring speed as a factor.

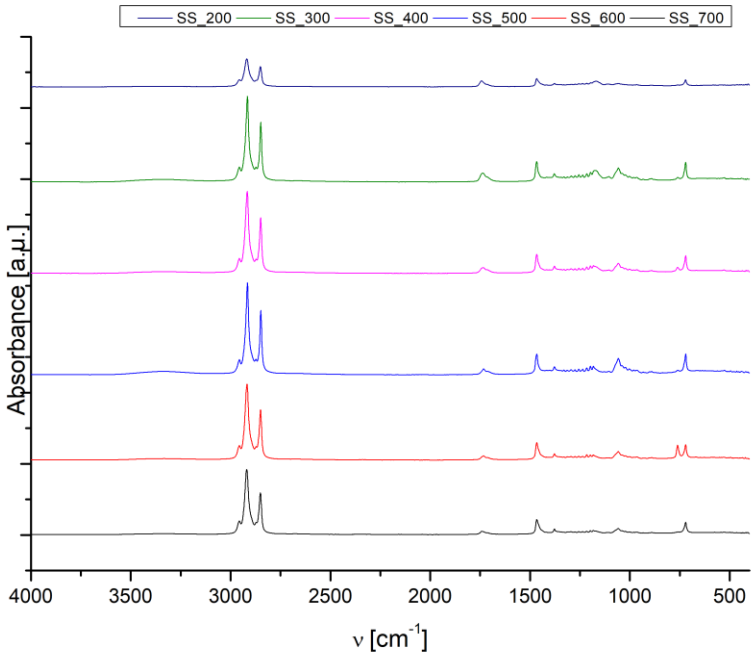


Figure 61 FT-IR spectra of reaction product from tests at 200, 300, 400, 500, 600 and 700 rpm for NiCoMo catalyst.

7.2 Results of DO tests on WCO

The results of the tests conducted on WCO are presented in two formats: (i) the overall results of the DO tests, and (ii) a comparison with the results obtained from tests on fresh rapeseed oil under the same conditions (see Sections 5.1.1 and 5.2.1). Experimental conditions and details on the execution of the tests are given in Section 2.6.2.

7.2.1 Overall results of WCO experiments

The preliminary FT-IR analysis results (in Figure 62) of the reaction products revealed the absence of bands between 1745-1700 cm^{-1} (i.e., C=O bond vibrations of TG esters and FFAs, see Section 2.5.1) for *Test_01* and *Test_03* in Figure 62, indicating complete conversion of TGs to n-alkanes. In contrast, *Test_02* and *Test_04* in Figure 62 displayed a weakly signal corresponding to bands around 1745-1700 cm^{-1} and 1350-900 cm^{-1} (associated with C-O vibrations), indicating that almost complete conversion has been achieved. In *Test_05* of Figure 62, both C=O and C-O vibration bands were clearly visible, indicating incomplete conversion.

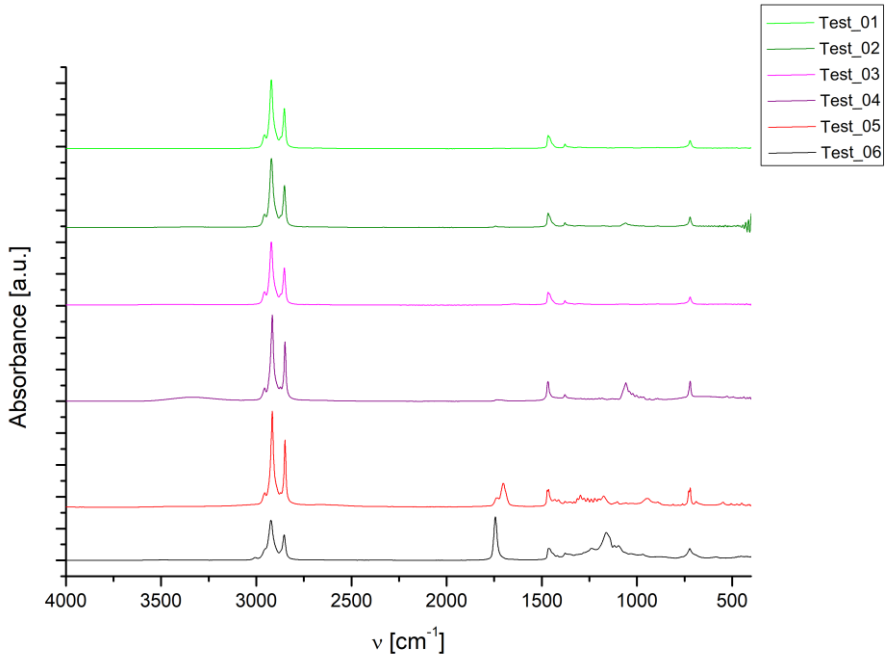


Figure 62 FT-IR spectra of product of DO test on WCO.

The overall results of preliminary tests on WCO are reported in Table 32.

The two catalysts, NiCoMo and ZnCoMo, exhibited similar trends with excellent results. Specifically, the $Y_{product}$ (Equation 2.9) ranged from 73% to 80% for both catalysts (see Table 32). The χ (Equation 2.10) ranges were 99% to 97% for NiCoMo and 100% to 95% for ZnCoMo, while the Y_{diesel} (Equation 2.11) ranged from 65% to 70% for NiCoMo and 64% to 69% for ZnCoMo.

For both catalysts, the $A\%_{BHC}$ decreased, dropping from 2.44% for NiCoMo and 2.91% for ZnCoMo at 320°C, to 0.00% at 280°C. This indicated that isomerization reactions (see Section 1.5.1.3) appear to be inhibited at 280°C when using WCO.
Overall, both catalysts demonstrated good DO performances, although NiCoMo showed slightly superior results in terms of Y_{diesel} and product composition ($A\%$) compared to ZnCoMo (see results in Table 32).

The Ni-Mo-Al catalyst demonstrated the worst performance compared to the other two catalysts. Table 32 indicated a notable decline in DO performance during tests at 280°C compared to those at 320°C, with both χ (Equation 2.10) and Y_{diesel} (Equation 2.11) decreasing significantly as the temperature decreased. $S_{HDO/DCOx}$ (Equation 2.12) also decreased, but the catalyst remained preferentially selective towards DCO_x pathways (see Section 1.5.1.2).

Regarding product composition: (i) the $A\%_{Ci}$ (with $15 \leq i \leq 18$ and with $19 \leq i \leq 30$) and $A\%_{UHC}$ decreased with the reduction in temperature; (ii) the $A\%_{FAME}$ increased significantly from 49% (at 320°C) to 84% (at 280°C).

In conclusion, the preliminary tests on WCO provided valuable insights into the performance of the various catalysts studied. Both NiCoMo and ZnCoMo exhibited comparable trends with good results. Conversely, the Ni-Mo-Al catalyst demonstrated lower overall performance compared to the other catalysts, particularly at 280°C, where a significant decline in DO performance was observed.

Overall, these results highlighted that the utilization of WCO as a feedstock for its conversion into green diesel through DO is highly promising, particularly for the NiCoMo and ZnCoMo catalysts, which demonstrated

excellent performances (see Table 32). This suggests that WCO not only serves as an effective raw material but also offers a sustainable approach to produce green diesel (in line with Green Chemistry principles, as underlined in Sections 1.2 and 1.6.1).

7.2.2 Performance Comparison: WCO vs. Rapeseed Oil

The results of the DO tests of WCO were compared with the similar tests (i.e., treatment "*ab*" and treatment "*b*", in Table 19 for NiCoMo and ZnCoMo and in Table 22 for Ni-Mo-Al catalyst) conducted using rapeseed oil, to determine whether there were significant differences in the performance of the two oils. The comparison of tests conducted with WCO and those carried out with rapeseed oil (referred to as RO_type of catalyst) is presented in Figure 63. Figure 63 (a) and Figure 63 (b) presents the comparison of the DO test conducted at 320°C (i.e., *Test_01*, *Test_03*, and *Test_05* of Table 32, and treatment "*ab*" of Table 19 and Table 22), while Figure 63 (c) and Figure 63 (d) at 280°C (i.e., *Test_02*, *Test_04*, and *Test_06* of Table 32, and treatment "*b*" of Table 19 and Table 22).

For the two catalysts, NiCoMo and ZnCoMo, at 320°C, there were no significant differences between the tests conducted with WCO and those with rapeseed oil. In the WCO tests, only a slight increase in $A\%_{Ci}$ (with $15 \leq i \leq 18$) and a decrease in $A\%_{BHC}$ (Figure 63 (a)) were observed. No notable differences were found in the DO parameters, such as $Y_{product}$ (Equation 2.9), χ (Equation 2.10), and Y_{diesel} (Equation 2.11), as shown in Figure 63 (b). No relevant differences were noted for $S_{HDO/DCOx}$ (compare values of Table 19 and Table 22 with those of Table 32).

For the Ni-Mo-Al catalyst, several differences were observed at 320°C: (i) in WCO test, there was a lower $A\%_{Ci}$ (with $15 \leq i \leq 18$) and a higher FAME content compared to test with rapeseed oil (see Figure 63 (a)); (ii) the χ was lower in WCO test (e.g., 61.81%, Table 32) compared to rapeseed oil test (e.g., 76.35%, Table 22); and (iii) the Y_{diesel} was also lower in WCO test (e.g., 34.82%, Table 32) than in rapeseed oil test (e.g., 58.58%, Table 22). Overall,

at 320°C, the test with rapeseed oil produced better results than those of WCO.

The results at 280°C (Figure 63 (c) and (d)) for NiCoMo and ZnCoMo indicated that the performance between WCO and rapeseed oil was not significantly different. However, two minor differences were noted: (i) the WCO tests produced more by-products (i.e., UHCs, Other and FAMEs) than tests with rapeseed oil; (ii) no BHCs were detected in the WCO tests, whereas traces were found in the rapeseed oil tests (compare values of Table 19 and Table 22 with those of Table 32); and (iii) the χ in WCO tests was slightly lower than in rapeseed oil tests, though it still maintained very high values (Figure 63 (d)).

For Ni-Mo-Al at 280°C (Figure 63 (c) and (d)), the only minor differences observed were: (i) a slight increase in $A\%_{FAME}$ in the WCO test (Figure 63 (c)); (ii) a lower $Y_{product}$ (Figure 63 (d)); and (iii) a marginally higher χ value (Figure 63 (d)).

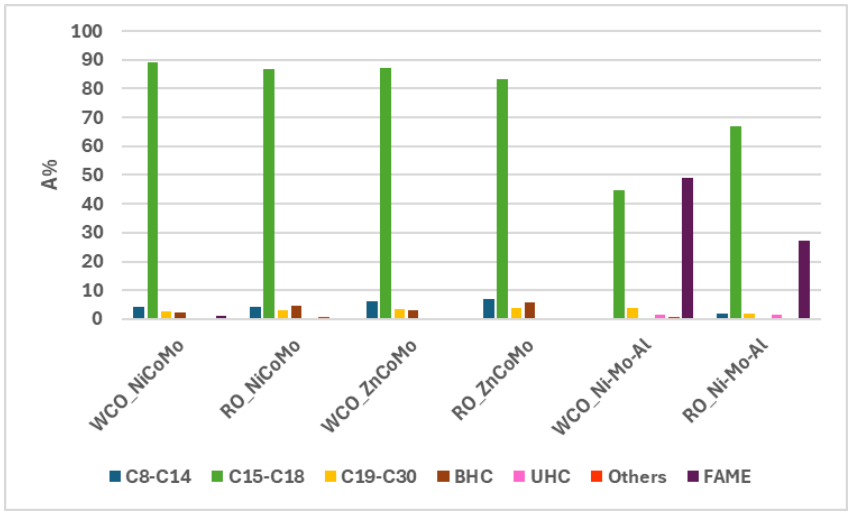
Overall, the comparison showed that WCO is a viable feedstock for green diesel production via DO, particularly with NiCoMo and ZnCoMo catalysts, where performance remained consistent with that of rapeseed oil. However, for the Ni-Mo-Al catalyst, rapeseed oil tends to perform better, especially at 320°C. These results align with the expectation based on the similar fatty acid profiles of the two oils (see Section 4. , suggesting that WCO can effectively serve as an alternative feedstock for green diesel production.

Table 31 Results of tests varying the reactor stirring speed (SS), conducted at 280°C, 4 $\%_{w/w}$ catalyst-to-oil and 2 h, in terms of product composition (A%), $Y_{product}$ (Equation 2.9), χ (Equation 2.10), Y_{diesel} (Equation 2.11), and $S_{HDO/DCOx}$ (Equation 2.12).

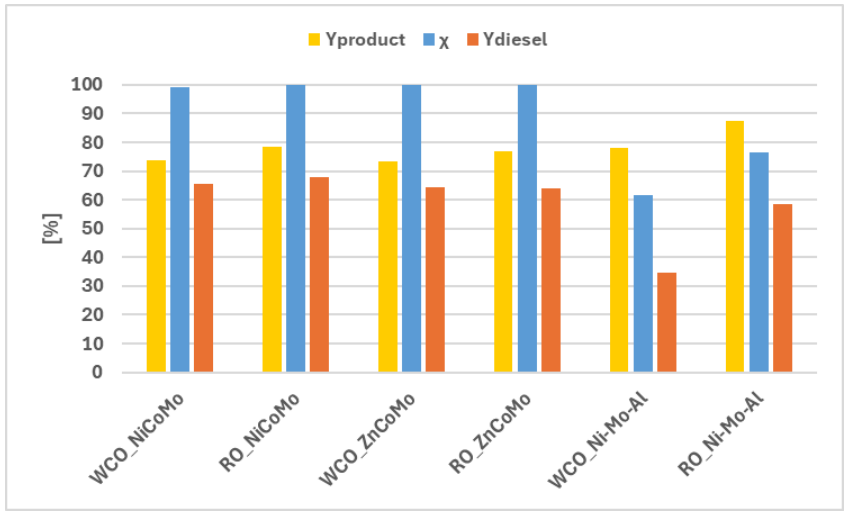
	RS	**$A\%_{Ci}$ $8\leq i\leq 14$**	**$A\%_{Ci}$ $15\leq i\leq 18$**	**$A\%_{Ci}$ $19\leq i\leq 30$**	**$A\%_{BHC}$**	**$A\%_{UHC}$**	**$A\%_{Others}$**	**$A\%_{FAME}$**	**$Y_{product}$**	**χ**	**Y_{diesel}**	**$S_{HDO/DCOx}$**
	[rpm]	**[%]**	**[%]**	**[%]**	**[%]**	**[%]**	**[%]**	**[%]**	**[wt%]**	**[wt%]**	**[wt%]**	**[-]**
SS_200	200	0.00	37.47	1.94	0.00	1.17	1.19	58.23	89.24	48.03	33.45	1.5
SS_300	300	4.50	78.22	2.65	0.00	0.00	0.00	14.63	86.34	87.37	67.53	1.7
SS_400	400	1.81	74.59	1.89	0.00	3.73	0.87	17.11	86.30	85.23	64.37	1.9
SS_500	500	4.02	76.31	2.83	0.56	2.85	0.38	13.05	90.30	88.21	68.91	2.1
SS_600	600	0.58	83.32	2.82	0.00	0.00	0.00	13.28	93.57	87.57	77.96	2.1
SS_700	700	2.25	77.58	2.51	0.00	0.00	1.16	16.50	88.54	85.39	68.69	1.8

Table 32 Results of preliminary DO tests on WCO (280°C/320°C, 10 $\%_{w/w}$ catalyst-to-oil, 2 h and 200 rpm) in terms of product composition (A%), $Y_{product}$ (Equation 2.9), χ (Equation 2.10), Y_{diesel} (Equation 2.11), and $S_{HDO/DCOx}$ (Equation 2.12).

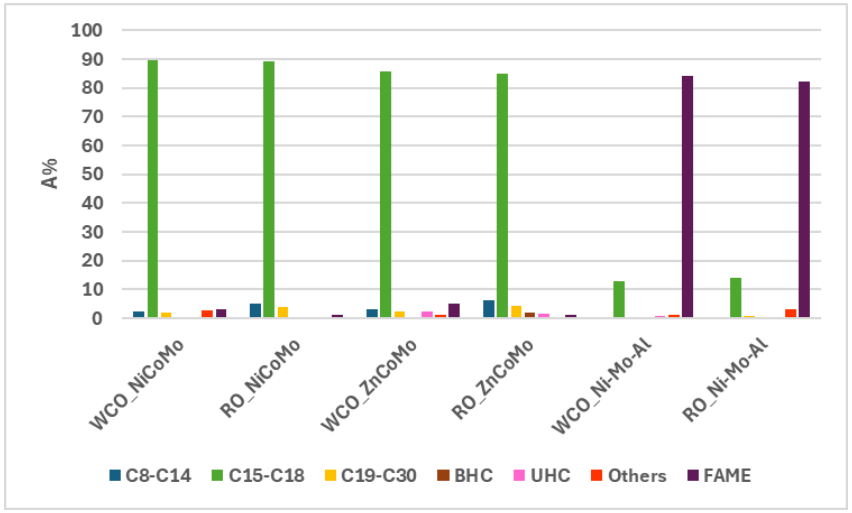
Catalyst		**T**	**$A\%_{Ci}$ $8\leq i\leq 14$**	**$A\%_{Ci}$ $15\leq i\leq 18$**	**$A\%_{Ci}$ $19\leq i\leq 30$**	**$A\%_{BHC}$**	**$A\%_{UHC}$**	**$A\%_{Others}$**	**$A\%_{FAME}$**	**$Y_{product}$**	**χ**	**Y_{diesel}**	**$S_{HDO/DCOx}$**
		[°C}	**[%]**	**[%]**	**[%]**	**[%]**	**[%]**	**[%]**	**[%]**	**[wt%]**	**[wt%]**	**[wt%]**	**[-]**
NiCoMo	*Test_01*	320	4.14	88.97	2.52	2.44	0.44	0.30	1.19	73.72	99.12	65.59	2.5
	Test_02	280	2.39	89.44	1.89	0.00	0.39	2.62	3.27	78.94	97.42	70.60	1.6
ZnCoMo	*Test_03*	320	6.15	87.31	3.26	2.91	0.37	0.00	0.00	73.51	100.00	64.18	2.8
	Test_04	280	3.28	85.65	2.48	0.00	2.34	1.23	5.02	80.33	95.97	68.81	2.0
Ni-Mo-Al	*Test_05*	320	0.00	44.70	3.89	0.00	1.65	0.73	49.03	77.89	61.81	34.82	0.7
	Test_06	280	0.00	12.98	0.61	0.40	0.78	1.05	84.18	91.65	22.84	11.90	0.4



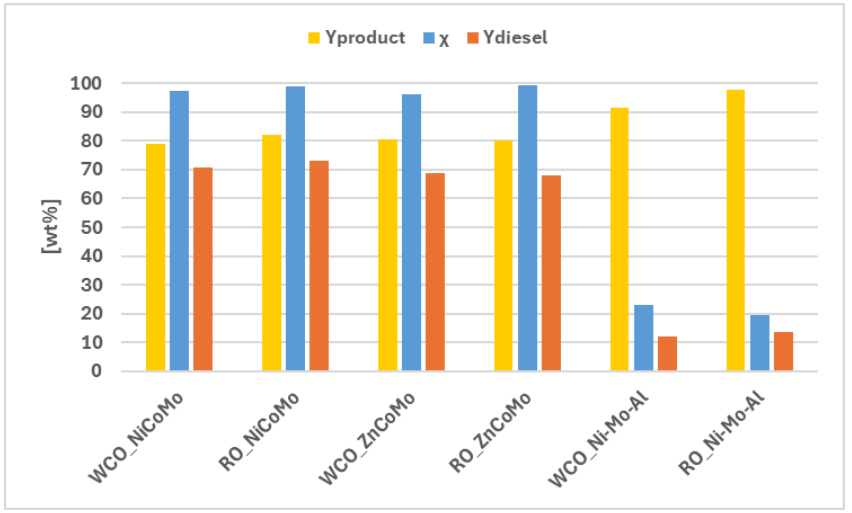
(**a**)



(**b**)



(**c**)



(**d**)

*Figure 63 Comparison between DO test of WCO and Rapeseed Oil, in terms of product composition at 320°C (a) and 280°C (c), and DO performance parameters (i.e., Y_{diesel}, χ and $Y_{product}$) at 320°C (b) and 280°C (c). *WCO and RO indicate tests performed with WCO and rapeseed oil at the same conditions.*

8. GENERAL CONCLUSIONS AND FUTURE OUTLOOKS

This chapter summarizes the key findings of the study on NiCoMo, ZnCoMo, and Ni-Mo-Al catalysts, examining their performance in DO process for green diesel production and highlighting both their catalytic effectiveness and structural properties.

- ***Synthesis and Characterization***:

  NiCoMo and ZnCoMo catalysts synthesized via coprecipitation demonstrated high crystallinity, mesoporosity, and uniform metal distribution. ICP-MS confirmed nominal elemental ratios, and FT-IR, XRD and N_2-Physisorption confirmed structural consistency with previous literature, ensuring synthesis success.

  The characterization of the Ni-Mo-Al catalyst synthesized by a solventless method revealed a structure dominated by molybdenum oxide (MoO_3) with contributions from NiO and Al_2O_3, as shown by FT-IR analysis. ICP-MS confirmed elemental alignment with expected ratios, though with slightly higher Ni and lower Mo than nominal values. XRD and SEM-EDS confirmed a mix of crystalline NiO and MoO_3, with irregular particle morphology and uniform elemental distribution. Low porosity and compact mesoporous structure, evidenced by N_2-physisorption, align with the physical mixing process,

while TPR and TPD-H_2 analyses revealed varied reduction temperatures and diverse hydrogen adsorption strengths, suggesting adaptable catalytic behavior.

- ***Catalytic Performance in DO process***:

  NiCoMo and ZnCoMo Catalysts originally used for propane oxidative dehydrogenation (ODH), were successfully repurposed for the DO process, yielding favorable performances across all tested conditions. Statistical modeling highlighted the importance of temperature, catalyst-to-oil ratio, and reaction time on diesel-range n-alkane yields. A pre-reduction step was essential for maximizing activity. ZnCoMo shows slightly superior activity and stability than NiCoMo, making them promising for green diesel production.

  Ni-Mo-Al catalyst demonstrated notable catalytic activity without a pre-reduction step, indicating possible self-reduction under reaction conditions. DO performances were significantly influenced by main factors and interactions.

- ***Statistical Analysis:***

  The statistical models deriving from 2^3 factorial experimental campaigns effectively captured key performance trends but suggested, in some cases, the need for a second-order regression model to improve predictive power and mitigate overfitting risks. The significant quadratic terms in key responses underscore the complex relationships between process variables.

- ***Recycling and Stability***:

  NiCoMo and ZnCoMo exhibited minimal structural changes (as observed in SEM and XRD) over multiple recycling cycles, retaining high catalytic activity with stable diesel yields. Carbon deposition and active component loss were observed in NiCoMo, which may limit its long-term efficiency and need addressing for extended use.

  Ni-Mo-Al demonstrated consistent elemental stability yet showed reduced efficiency over cycles, attributed to particle aggregation and carbon accumulation. The carbon deposits observed on the catalyst surface through TEM analysis hindered its reusability, as their

presence may lead to a reduction in the catalyst's surface area, consequently affecting DO performance. Structural integrity was generally maintained, but morphological changes may have negatively impacted long-term catalytic efficacy.

- ***Effects of stirring speed on catalytic DO performances***:

  Analysis of FCCCD of Ni-Mo-Al catalyst revealed that temperature (T), catalyst-to-oil ratio (Υ), and stirring speed (ω) significantly affected DO performance. Although the models were effective within tested ranges, variability in responses suggested limitations in external validity.

In conclusion, the three catalysts—NiCoMo, ZnCoMo, and Ni-Mo-Al—demonstrate potential for DO in green diesel production, albeit with some differences in effectiveness and long-term stability.

NiCoMo and ZnCoMo showed promising performance and stability across multiple cycles, maintaining complete TG conversions and high diesel yields for up to four DO cycles. A pre-reduction step proved to be essential to maximize catalytic activity, with reaction conditions (i.e., temperature, catalyst-to-oil ratio, and time) significantly impacting the yield of diesel alkanes. Of the two, ZnCoMo appears slightly more favorable in terms of activity and stability, suggesting an edge for cyclical applications.

The ***Ni-Mo-Al*** catalyst exhibited substantial catalytic activity even without pre-reduction, but its stability decreased over successive cycles, with declining diesel yields and increased formation of FFA and unreacted TGs and other by-products. The complex effects of reaction conditions indicate a need for further optimization, and issues like deactivation from carbon deposits and structural aggregation make Ni-Mo-Al less durable than the other two catalysts for intensive cyclic use.

In summary, NiCoMo and ZnCoMo emerge as more robust options for DO and are better suited for repeated industrial processes, while Ni-Mo-Al may require enhancements to improve its long-term stability.

The research conducted in this PhD thesis provides insights into the performance and structural characteristics of NiCoMo, ZnCoMo and Ni-Mo-

Al catalysts in DO reactions. Several avenues for further exploration and application emerge:

(1) In-depth studies with the execution of tailored experimental plans are necessary to evaluate the effect of stirring speed on the performance of NiCoMo and ZnCoMo catalysts. These investigations will help elucidate how variations in rotation speed influence catalytic activity, selectivity, and overall reaction performances.

(2) *Factorial plan for DO of WCO*: Development and implementation of an ad hoc experimental plan for the DO of WCO, potentially utilizing a Face-Centered Cubic Central Composite Design (FCCCD), in order to obtain complete information about the influence of process parameters.

(3) *Optimization of Catalyst Formulation*: future studies could focus on optimizing the composition and synthesis parameters of Ni-Mo-Al catalysts to enhance their activity and selectivity. Investigating different ratios of nickel, molybdenum, and aluminum, as well as exploring the addition of other metal or non-metal promoters, may lead to the development of more effective catalysts

(4) *Exploration of Alternative Feedstocks*: while this thesis primarily examines specific feedstocks, the applicability of the developed catalysts could be tested with a wider range of feedstocks, including those derived from agricultural waste or non-food biomass. This could contribute to more sustainable and economically viable processes for biofuel production.

(5) *Use of green hydrogen*: One future objective is to utilize a renewable energy source for hydrogen production, specifically by generating hydrogen through water electrolysis from solar power to create an E-Green Diesel.

(6) *Scaling Up from Lab to Pilot Scale, from batch to continuous*: the transition from laboratory-scale experiments to pilot-scale systems is critical. It will be important to conduct feasibility studies that evaluate the scalability of the catalysts under continuous operation. These studies should address reactor size, flow rates, and operational

parameters to ensure that the performance observed in lab settings can be replicated in larger systems. Future work should focus on the design and engineering aspects of continuous plants.

(7) *Environmental and Economic Impact Studies*: Finally, a comprehensive evaluation of the environmental and economic impacts of implementing these catalytic processes in green diesel production is essential. Future research could assess life-cycle analyses to ensure that the advancements in catalyst technology align with sustainability goals.

In conclusion, the results of this thesis open several pathways for future research that could contribute to the advancement of catalyst technology and the optimization of green diesel production processes.

ADDENDUM A

This addendum presents the procedure for running the ICP-MS calibration line.

For the calibration curve construction in ICP-MS analysis (as mentioned in Section 2.2.1), a series of five solutions containing the metals Ni, Co, Mo, Zn, and Al were prepared.

First, a stock solution was created in a 100 mL flask by adding: (i) 100 µL of single-element standards for each metal (i.e., Ni, Co, Mo, Zn, and Al); (ii) 200 µL of HNO_3 (Supelco, Suprapure® Nitric Acid 69%); and (iii) Milli-Q water to bring the solution to volume.

From the stock solution, five working solutions with varying metal concentrations were prepared:

- solution at 1 ppm;
- solution at 500 ppb;
- solution at 200 ppb;
- solution at 100 ppb;
- solution at 50 ppb.

These solutions were subsequently automatically injected into the ICP-MS for the calibration curve construction.

ADDENDUM B

This addendum presents the chromatograms from the GC-FID and GC-MS injected standards, which are essential for identification of compound in reaction product, and consequently for data analysis.

Figure B 1 reports the chromatogram of C_{14}-C_{22} FAME MIX standard used for FAME identification through Thermo Trace GC-FID analysis (described in Section 2.3.1).

Figure B 2 reports the chromatogram of C_7-C_{40} standard used for n-alkanes identification through Agilent GC/7820A GC-FID (see Section 2.5.2).

Figure B 3 illustrates an example of identification of unknown peak through RI (Retention Index) and comparison with the NIST library through GC-MS analysis (see Section 2.5.3 for further details).

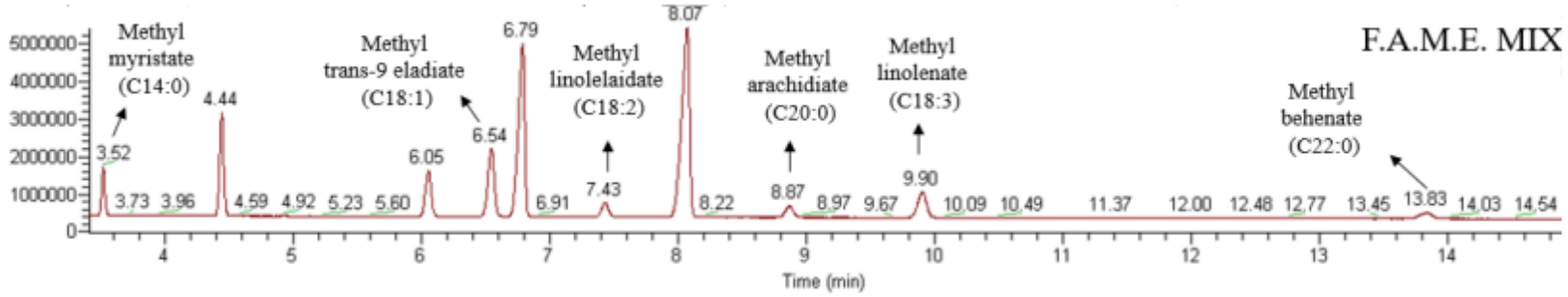


Figure B 1 C_{14}-C_{22} FAME MIX standard injected into Thermo Trace GC-FID.

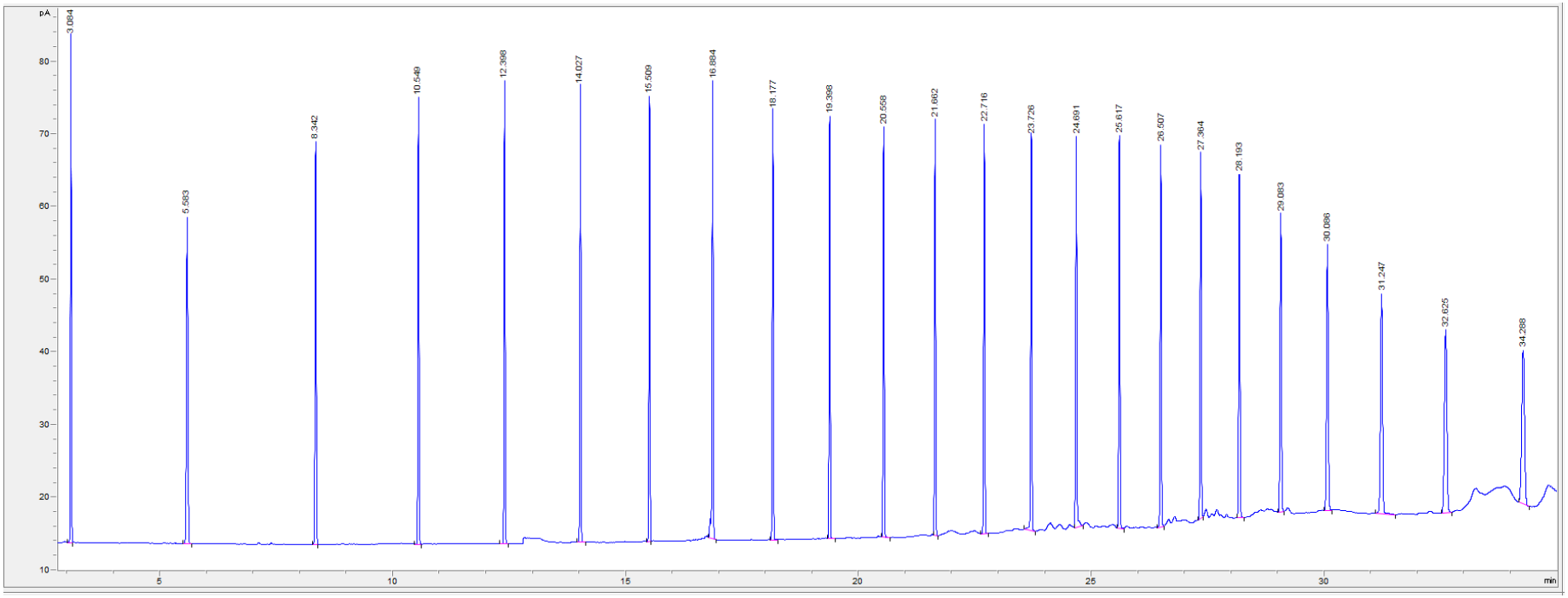


Figure B 2 C_7-C_{40} n-alkanes reference standard used for Agilent GC-FID.

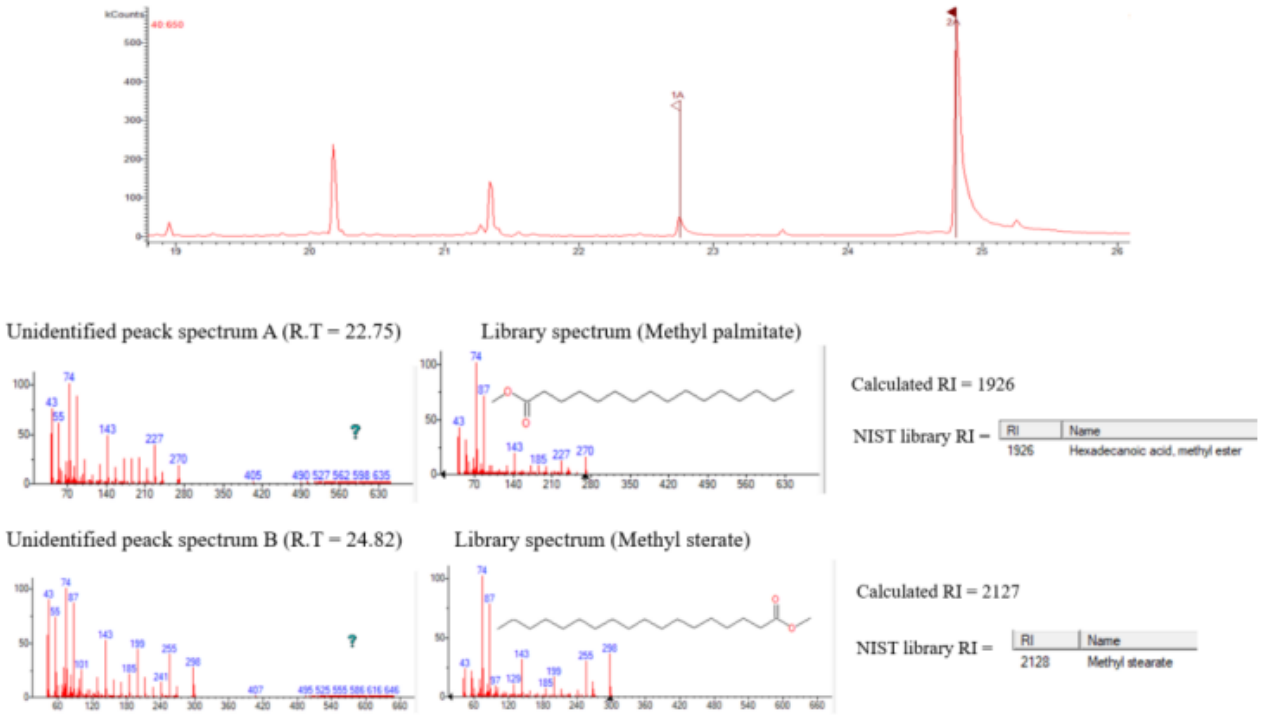
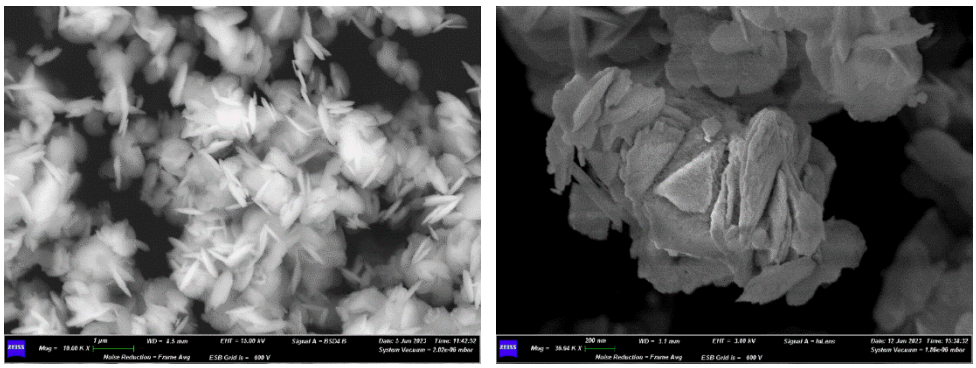


Figure B 3 Example of GC-MS analysis of two unidentified peaks.

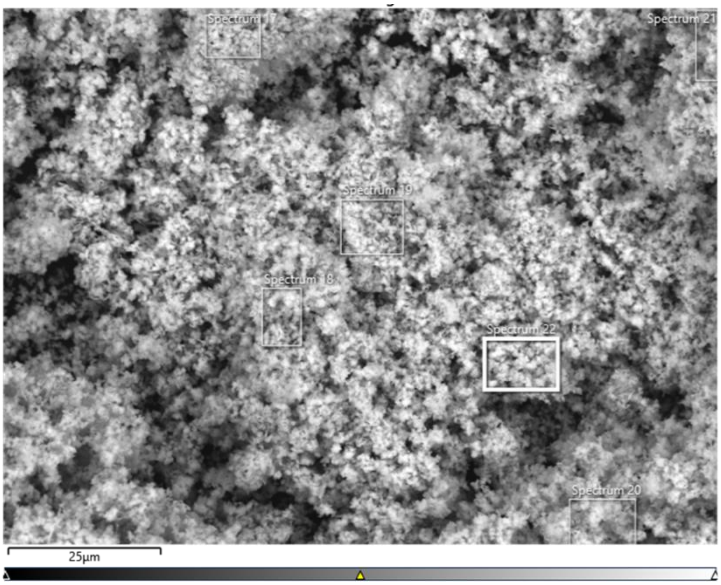
ADDENDUM C

Further results about catalysts characterization are provided in this Addendum.

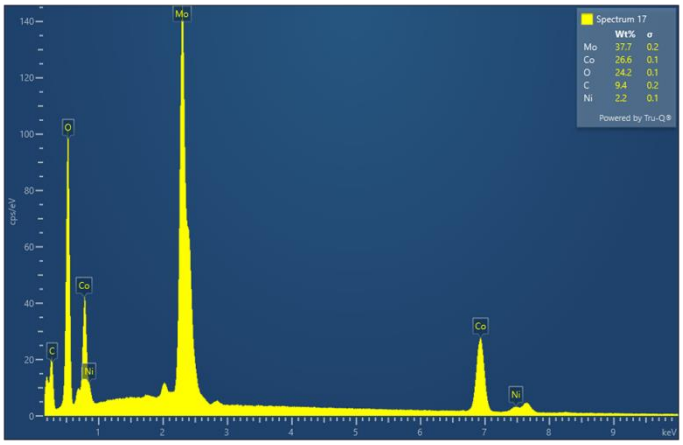


(**a**) (**b**)

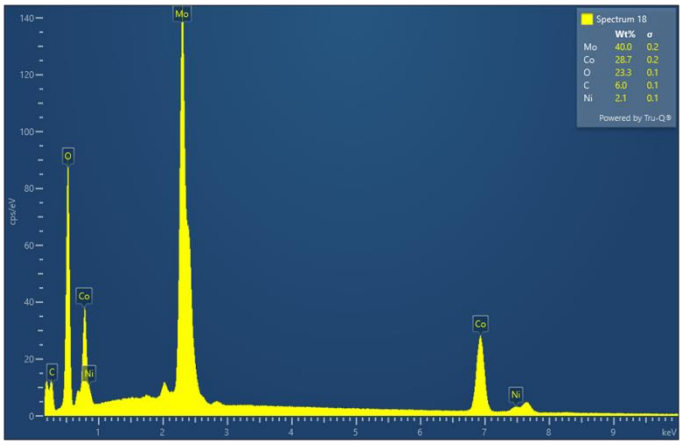
Figure C 1 High-magnification SEM micrograph illustrating the lamellar structure of the catalysts: (a) NiCoMo at 10kx magnification; and (b) ZnCoMo at 36.94kx magnification.


Spectrum 17
Spectrum 21
Spectrum 19
Spectrum 18
Spectrum 22
Spectrum 20
25µm

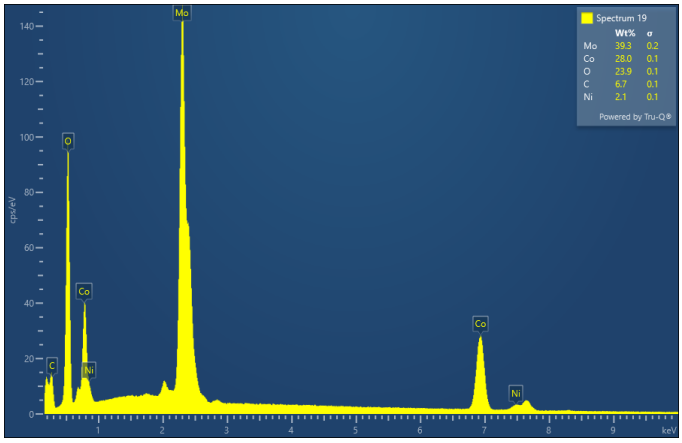
(**a**)


Spectrum 17
Wt% σ
Mo 37.7 0.2
Co 26.6 0.1
O 24.2 0.1
C 9.4 0.2
Ni 2.2 0.1
Powered by Tru-Q®
Mo
O
Co
C
Ni
Co
Ni
cps/eV
keV

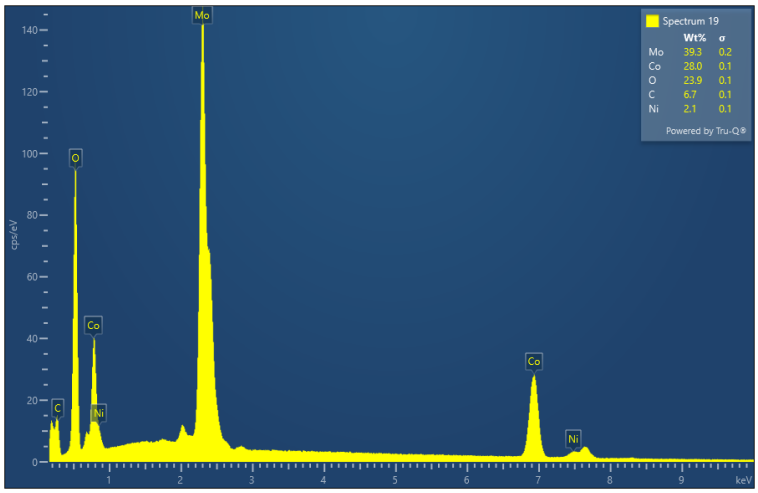
(**b**)


Spectrum 18
Wt% σ
Mo 40.0 0.2
Co 28.7 0.2
O 23.3 0.1
C 6.0 0.1
Ni 2.1 0.1
Powered by Tru-Q®
Mo
O
Co
C
Ni
Co
Ni
cps/eV
keV

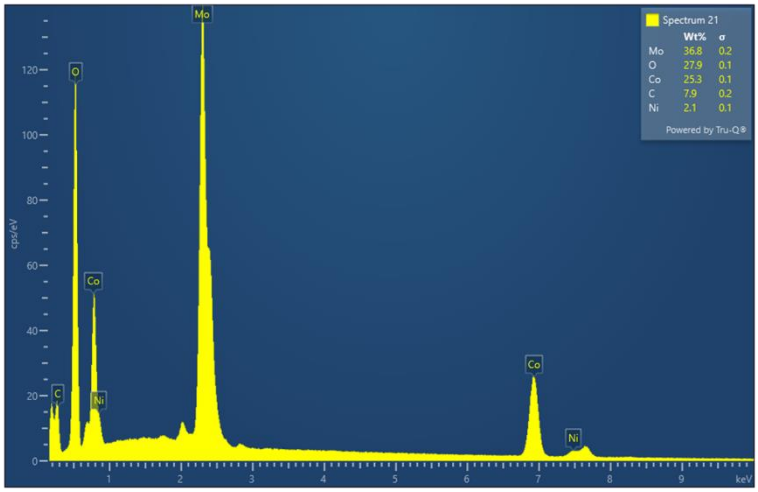
(**c**)



(**d**)

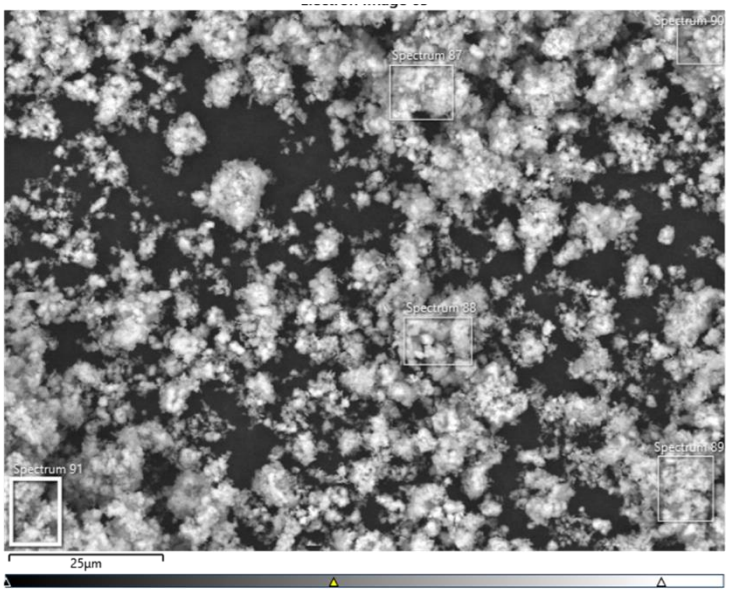


(**e**)

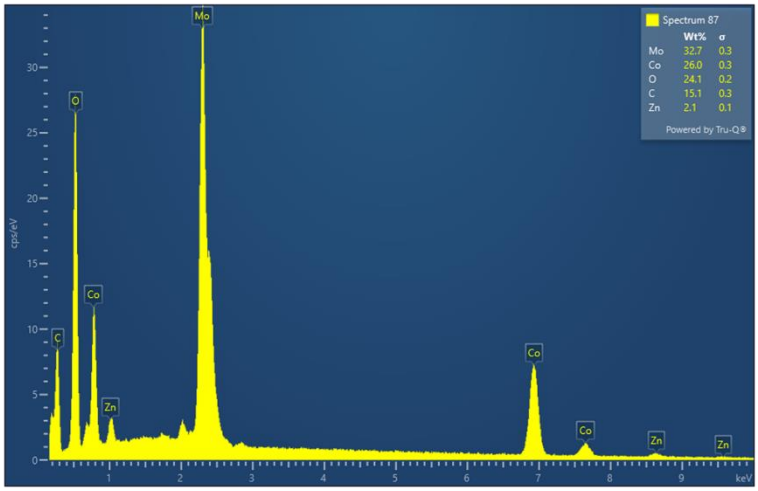


(**f**)

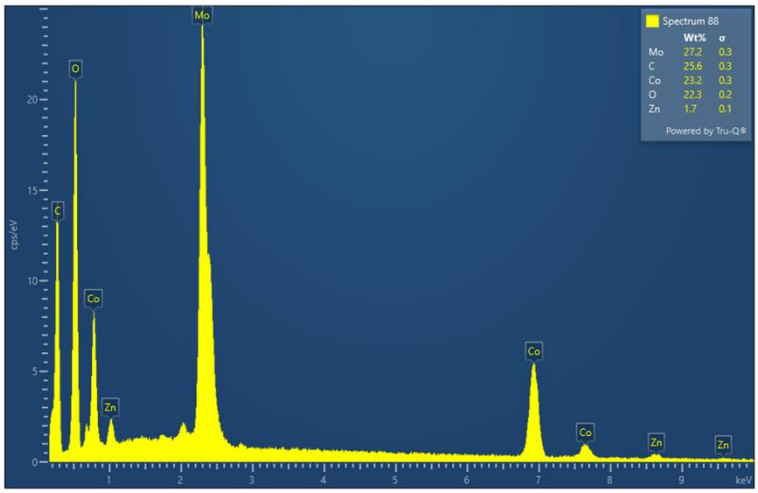
Figure C 2 EDS spectra of NiCoMo catalysts: (a) the SEM image at 1kx magnification, (b) Spectrum 17, (c) Spectrum 18, (d) Spectrum 19, (e) Spectrum 20, (f) Spectrum 21.


Spectrum 99
Spectrum 87
Spectrum 88
Spectrum 89
Spectrum 91
25µm

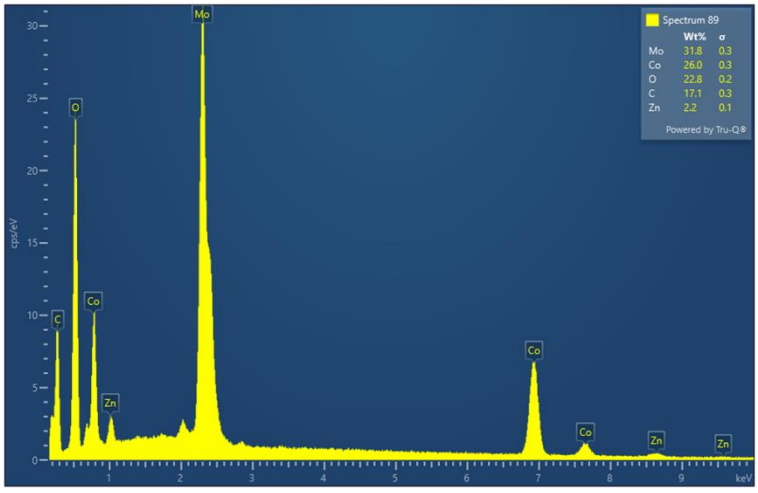
(**a**)


Spectrum 87
Wt% σ
Mo 32.7 0.3
Co 26.0 0.3
O 24.1 0.2
C 15.1 0.3
Zn 2.1 0.1
Powered by Tru-Q®
Mo
O
Co
C
Zn
Co
Co
Zn
Zn
cps/eV
keV

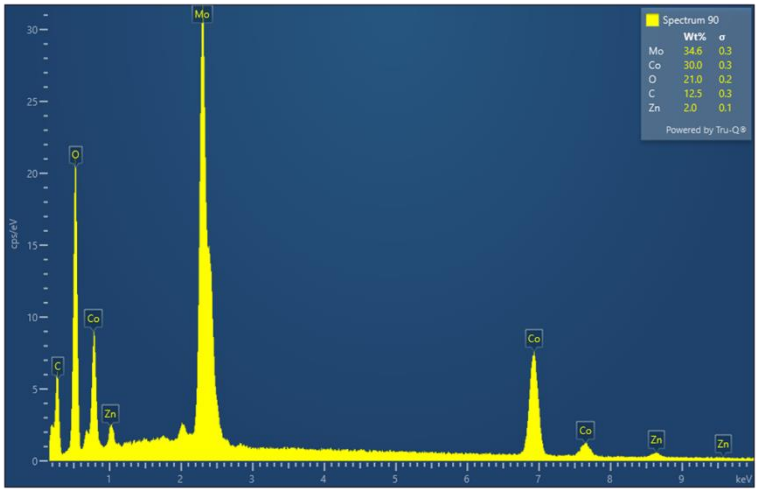
(**b**)


Spectrum 88
Wt% σ
Mo 27.2 0.3
C 25.6 0.3
Co 23.2 0.3
O 22.3 0.2
Zn 1.7 0.1
Powered by Tru-Q®
Mo
O
C
Co
Zn
Co
Co
Zn
Zn
cps/eV
keV

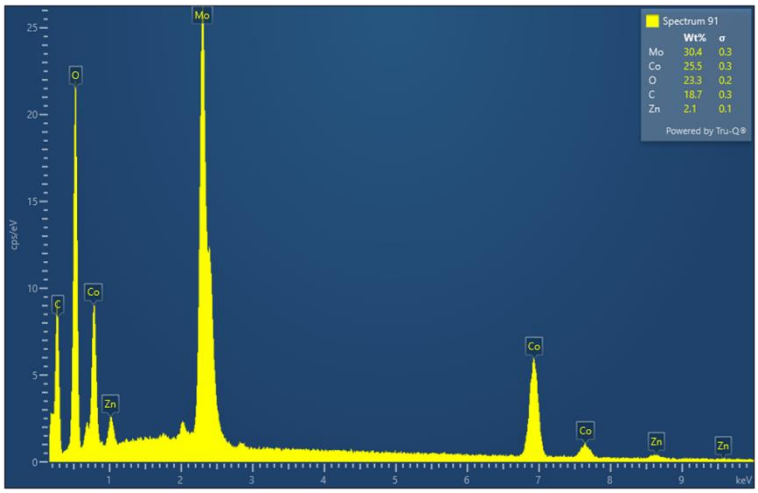
(**c**)



(**d**)

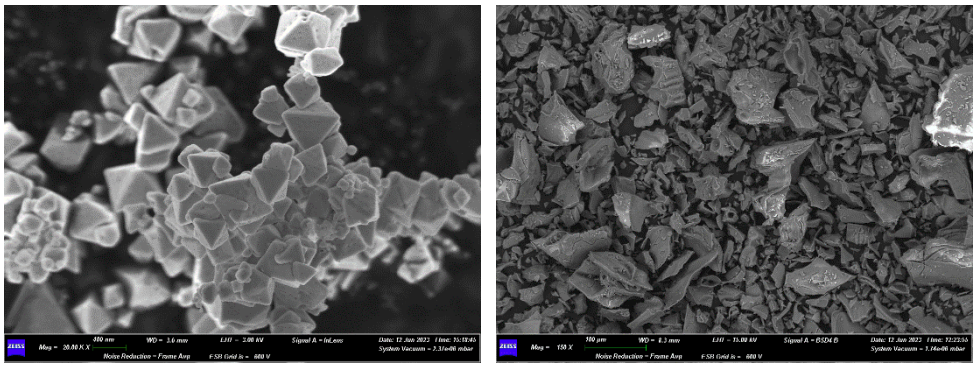


(**e**)

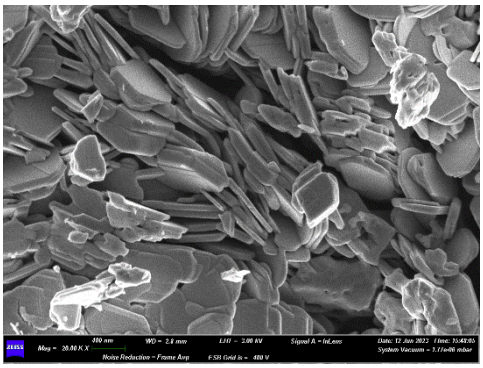


(**f**)

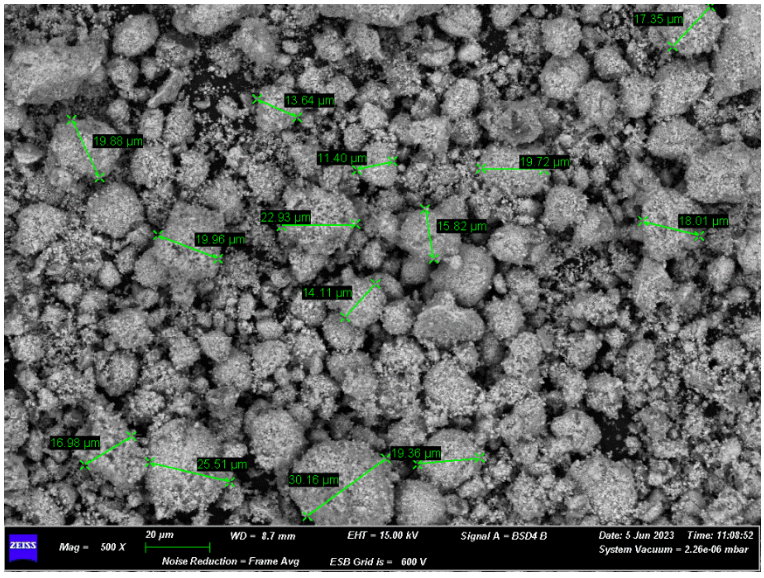
Figure C 3 EDS spectra of ZnCoMo catalysts (a) the SEM image at 1kx magnification, (b) Spectrum 87, (c) Spectrum 88, (d) Spectrum 89, (e) Spectrum 90, (f) Spectrum 91.



(**a**) (**b**)

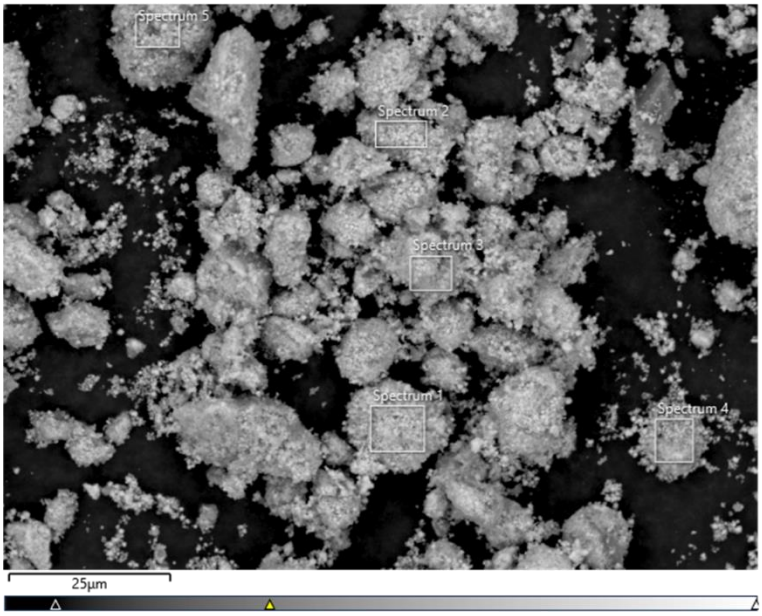


(**c**)

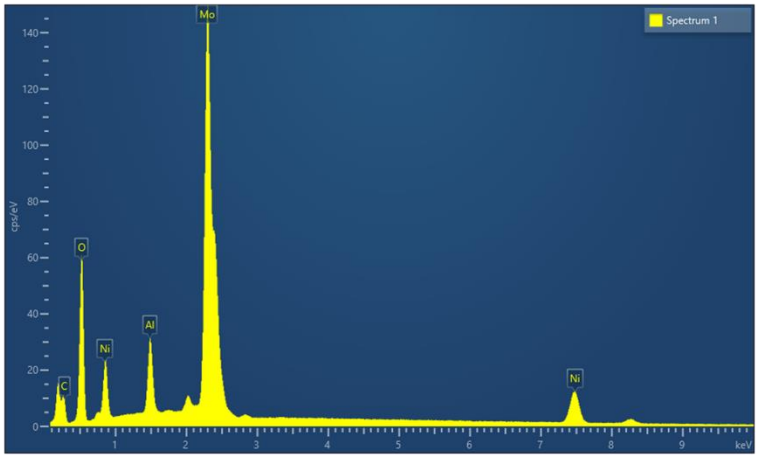


(**d**)

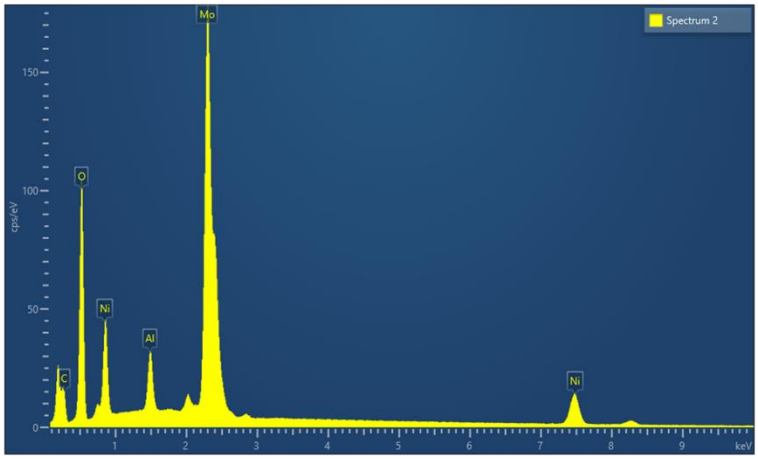
Figure C 4 SEM images of: (i) NiO at 20kx magnification; (b) Al_2O_3 at 150x magnification; (c) MoO_3 at 20kx magnification; (d) Ni-Mo-Al catalyst at 500x magnification.


Spectrum 5
Spectrum 2
Spectrum 3
Spectrum 1
Spectrum 4
25µm

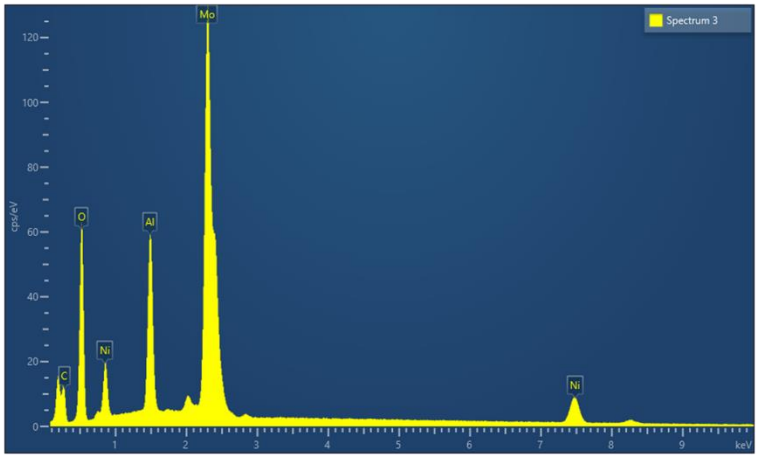
(**a**)


Spectrum 1
Mo
O
Ni
Al
C
Ni
cps/eV
keV

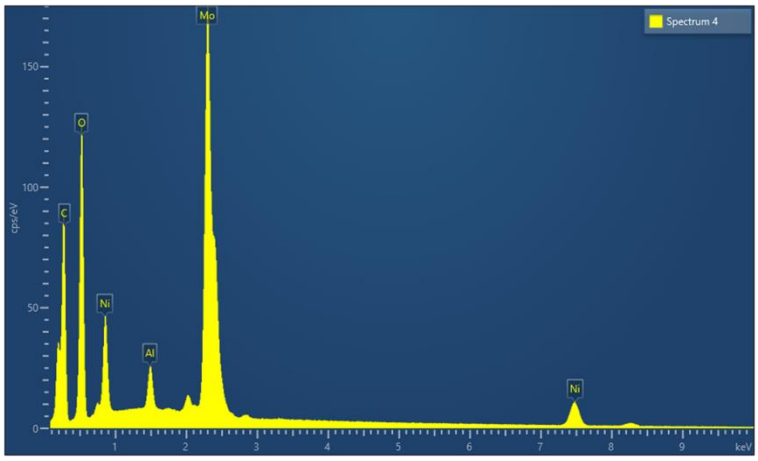
(**b**)


Spectrum 2
Mo
O
Ni
Al
C
Ni
cps/eV
keV

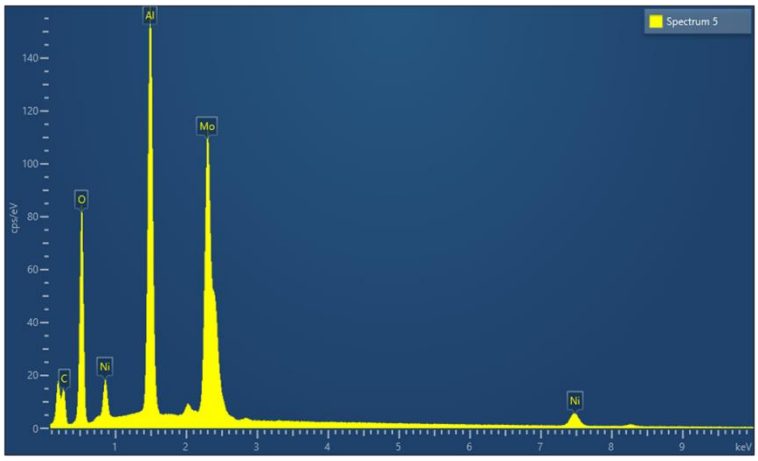
(**c**)



(**d**)



(**e**)

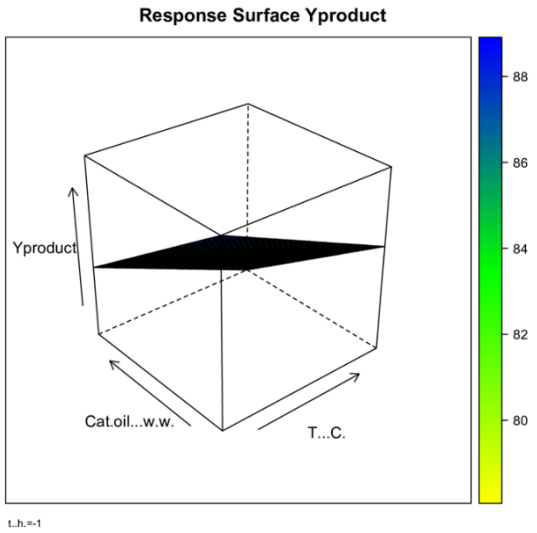


(**f**)

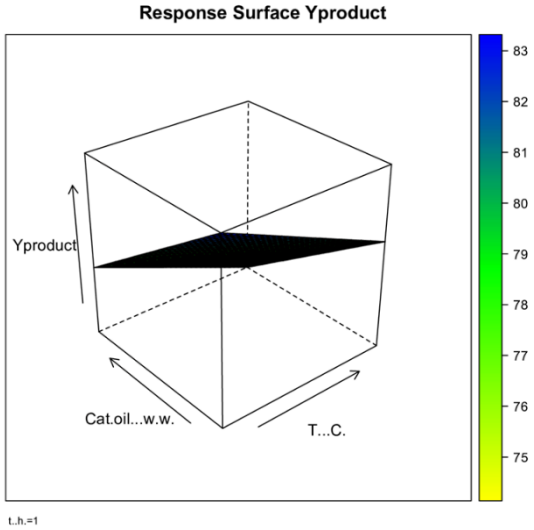
Figure C 5 EDS spectra of Ni-Mo-Al catalysts: (a) the SEM image at 1kx magnification, (b) Spectrum 1, (c) Spectrum 2, (d) Spectrum 3, (e) Spectrum 4, (f) Spectrum 5.

ADDENDUM D

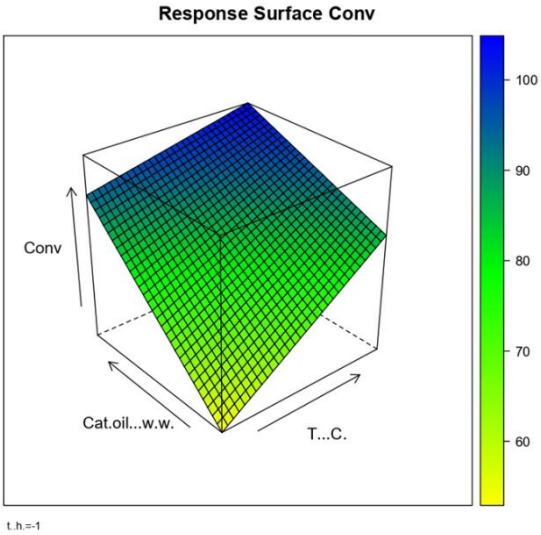
This addendum includes the response surfaces and contour plots generated from the response model equations corresponding to the experimental designs presented in Section 5.


Response Surface Yproduct
Yproduct
Cat.oil...w.w.
T...C.
t..h.=-1
88
86
84
82
80

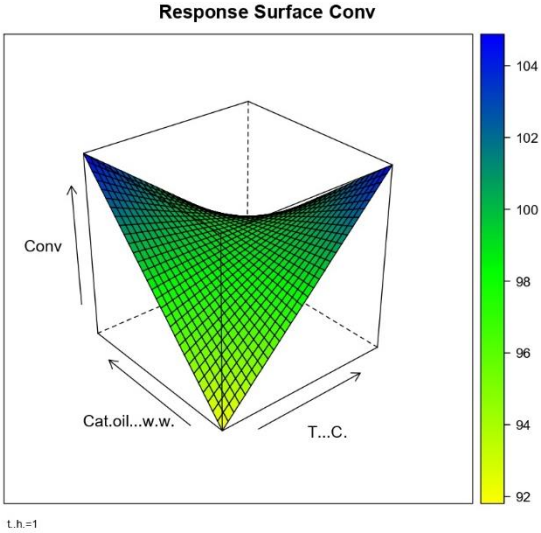
(**a**)


Response Surface Yproduct
Yproduct
Cat.oil...w.w.
T...C.
t..h.=1
83
82
81
80
79
78
77
76
75

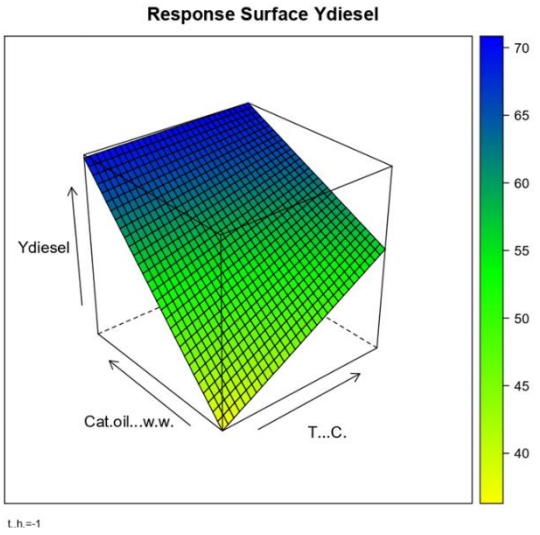
(**b**)


Response Surface Conv
Conv
Cat.oil...w.w.
T...C.
t..h.=-1
100
90
80
70
60

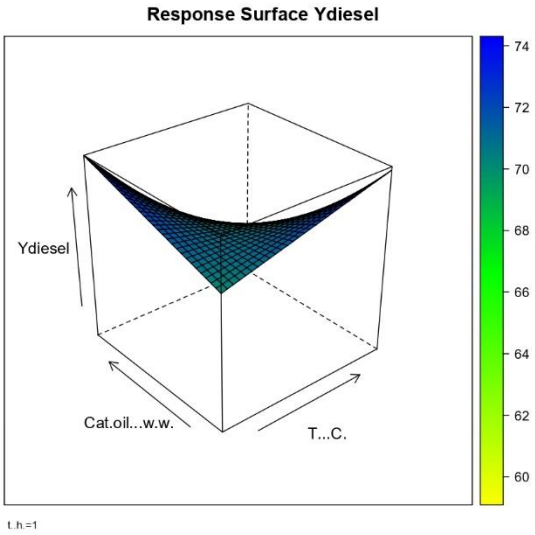
(**c**)


Response Surface Conv
Conv
Cat.oil...w.w.
T...C.
t..h.=1
104
102
100
98
96
94
92

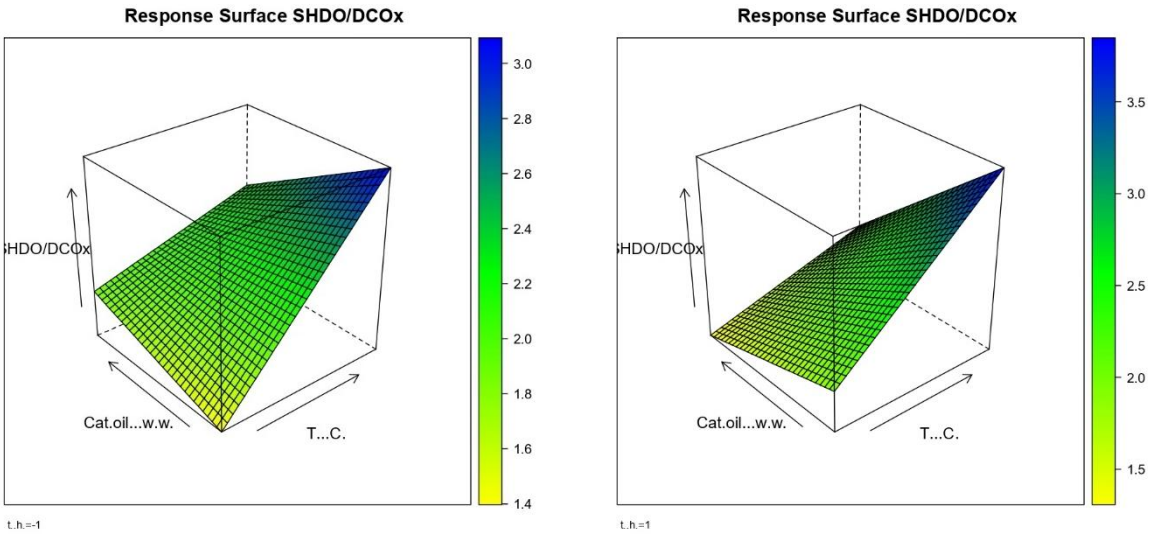
(**d**)


Response Surface Ydiesel
Ydiesel
Cat.oil...w.w.
T...C.
t..h.=-1
70
65
60
55
50
45
40

(**e**)

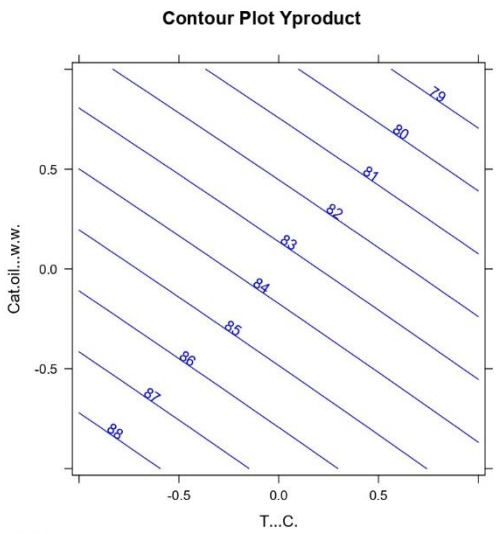

Response Surface Ydiesel
Ydiesel
Cat.oil...w.w.
T...C.
t..h.=1
74
72
70
68
66
64
62
60

(**f**)

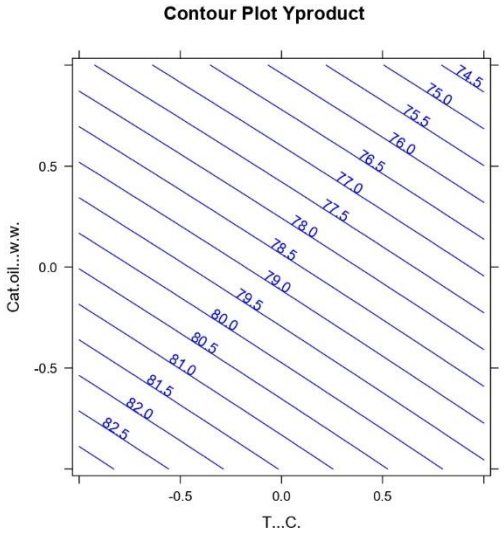


(**g**) (**h**)

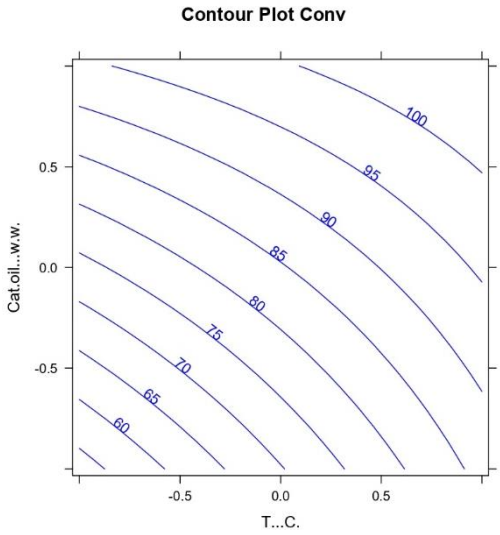
Figure D 1 Response surface of DO process parameters for NiCoMo catalyst derived from the regression model of 2^3 experimental DoE, with coefficients in Table 20, at t=±1: (a) $Y_{product}$ (Equation 2.9) at t=-1; (b) $Y_{product}$ (Equation 2.9) at t=1; (c) χ (Equation 2.10) at t=-1; (d) χ (Equation 2.10) at t=1; (e) Y_{diesel} (Equation 2.11) at t=-1; (f) Y_{diesel} (Equation 2.11) at t=1; (g) $S_{HDO/DCOx}$ (Equation 2.12) at t=-1; (e) $S_{HDO/DCOx}$ (Equation 2.12) at t=1.


Contour Plot Yproduct
Cat.oil...w.w.
T...C.
79
80
81
82
83
84
85
86
87
88

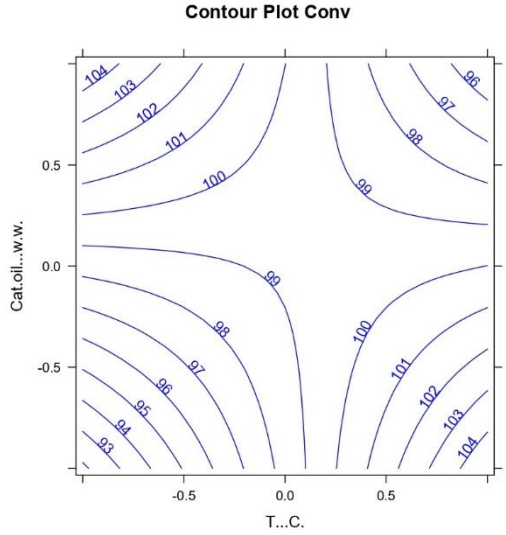
(**a**)


Contour Plot Yproduct
Cat.oil...w.w.
T...C.
74.5
75.0
75.5
76.0
76.5
77.0
77.5
78.0
78.5
79.0
79.5
80.0
80.5
81.0
81.5
82.0
82.5

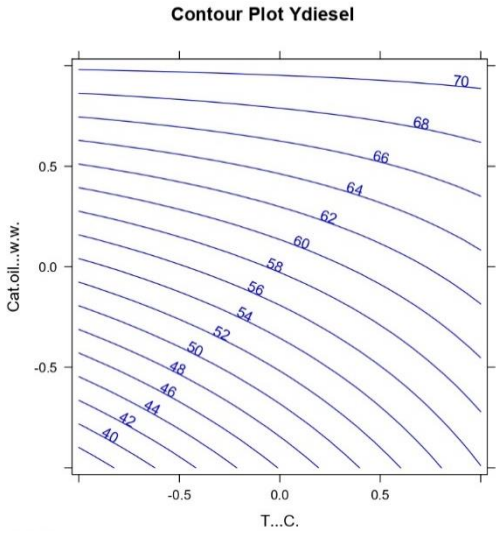
(**b**)


Contour Plot Conv
Cat.oil...w.w.
T...C.
100
95
90
85
80
75
70
65
60

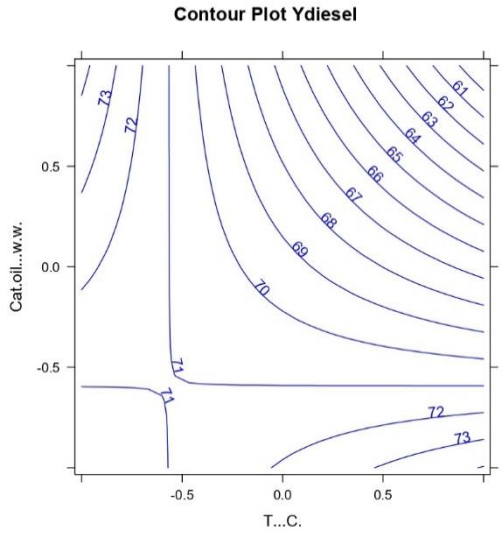
(**c**)


Contour Plot Conv
Cat.oil...w.w.
T...C.
104
103
102
101
100
99
98
97
96
95
94
93

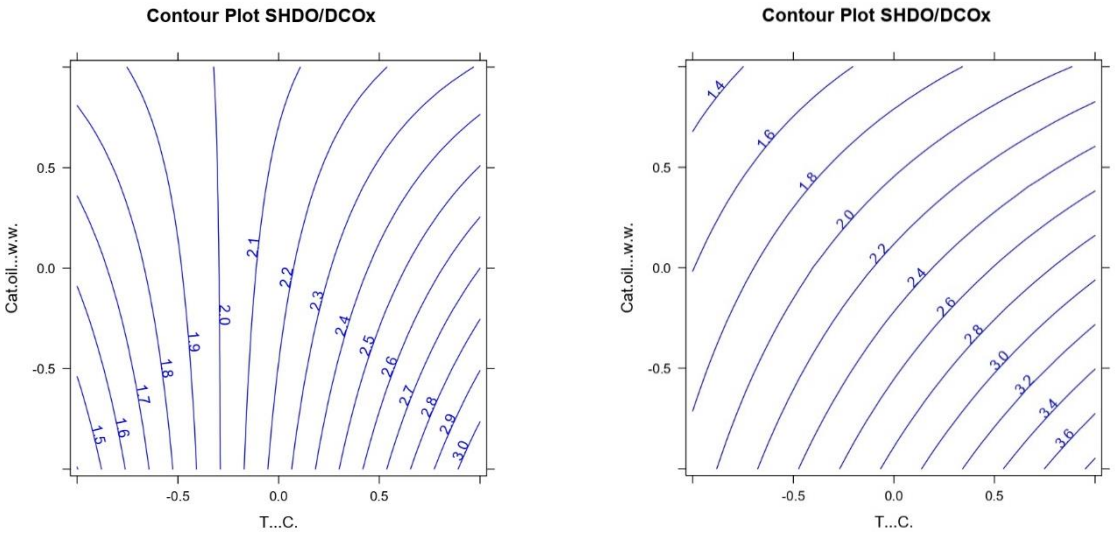
(**d**)


Contour Plot Ydiesel
Cat.oil...w.w.
T...C.
70
68
66
64
62
60
58
56
54
52
50
48
46
44
42
40

(**e**)

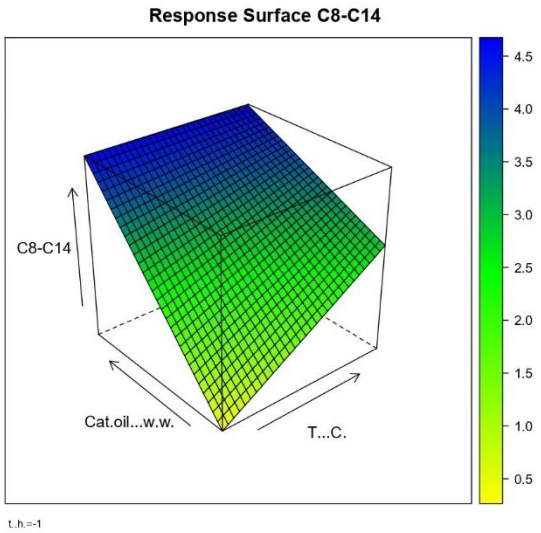

Contour Plot Ydiesel
Cat.oil...w.w.
T...C.
73
72
71
70
69
68
67
66
65
64
63
62
61

(**f**)

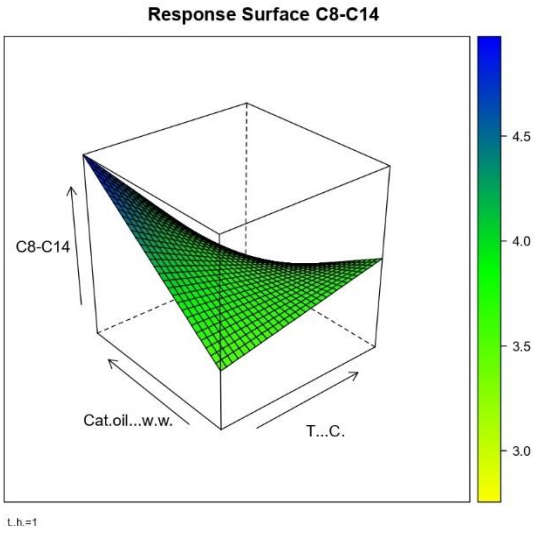


(**g**) (**h**)

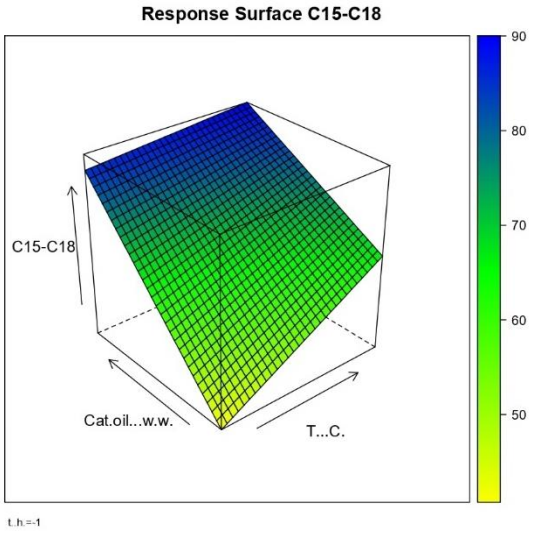
Figure D 2 Contour plots of DO process parameters for NiCoMo catalyst derived from the regression model of 2^3 experimental DoE, with coefficients in Table 20, at t=±1: (a) $Y_{product}$ (Equation 2.9) at t=-1; (b) $Y_{product}$ (Equation 2.9) at t=1; (c) χ (Equation 2.10) at t=-1; (d) χ (Equation 2.10) at t=1; (e) Y_{diesel} (Equation 2.11) at t=-1; (f) Y_{diesel} (Equation 2.11) at t=1; (g) $S_{HDO/DCOx}$ (Equation 2.12) at t=-1; (e) $S_{HDO/DCOx}$ (Equation 2.12) at t=1.


Response Surface C8-C14
C8-C14
Cat.oil...w.w.
T...C.
4.5
4.0
3.5
3.0
2.5
2.0
1.5
1.0
0.5
t.h.=-1

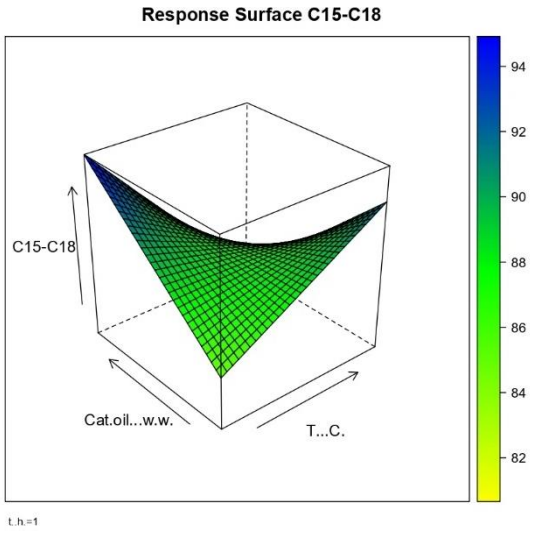
(**a**)


Response Surface C8-C14
C8-C14
Cat.oil...w.w.
T...C.
4.5
4.0
3.5
3.0
t.h.=1

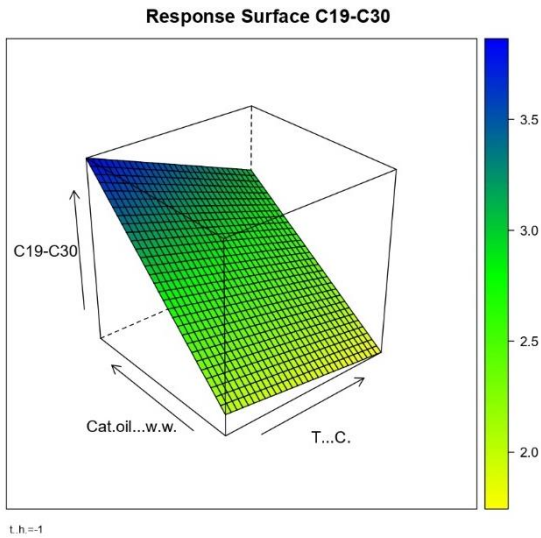
(**b**)


Response Surface C15-C18
C15-C18
Cat.oil...w.w.
T...C.
90
80
70
60
50
t.h.=-1

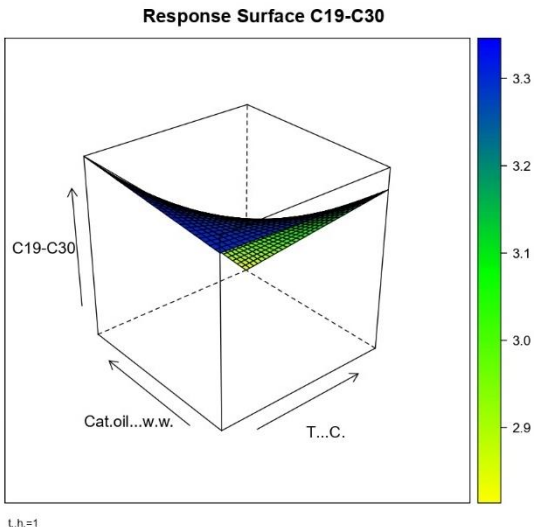
(**c**)


Response Surface C15-C18
C15-C18
Cat.oil...w.w.
T...C.
94
92
90
88
86
84
82
t.h.=1

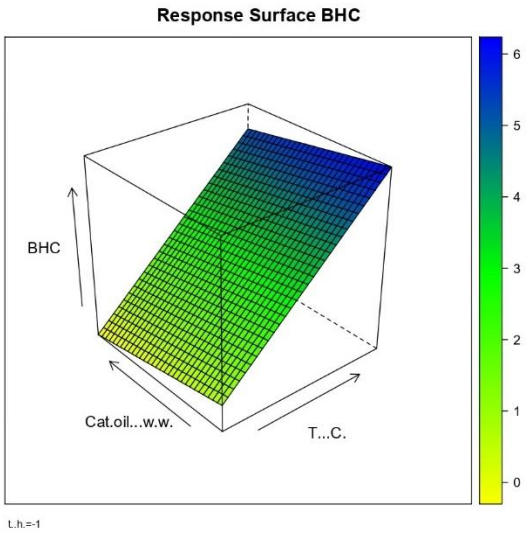
(**d**)


Response Surface C19-C30
C19-C30
Cat.oil...w.w.
T...C.
3.5
3.0
2.5
2.0
t.h.=-1

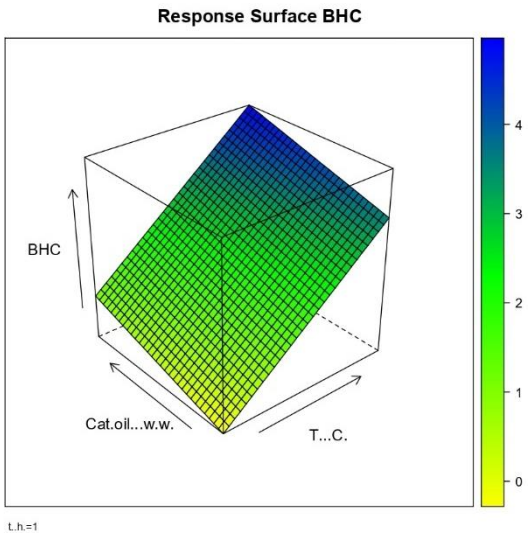
(**e**)


Response Surface C19-C30
C19-C30
Cat.oil...w.w.
T...C.
3.3
3.2
3.1
3.0
2.9
t.h.=1

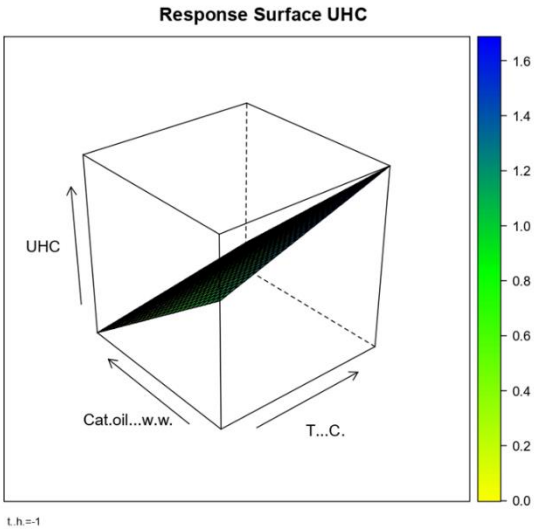
(**f**)


Response Surface BHC
BHC
Cat.oil...w.w.
T...C.
t.h.=-1
6
5
4
3
2
1
0

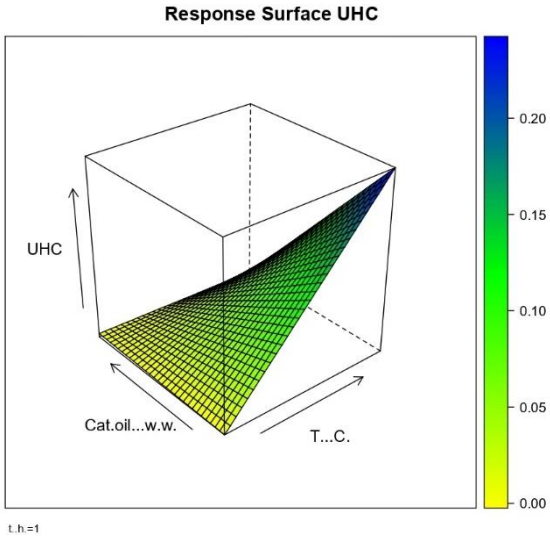
(g)


Response Surface BHC
BHC
Cat.oil...w.w.
T...C.
t.h.=1
4
3
2
1
0

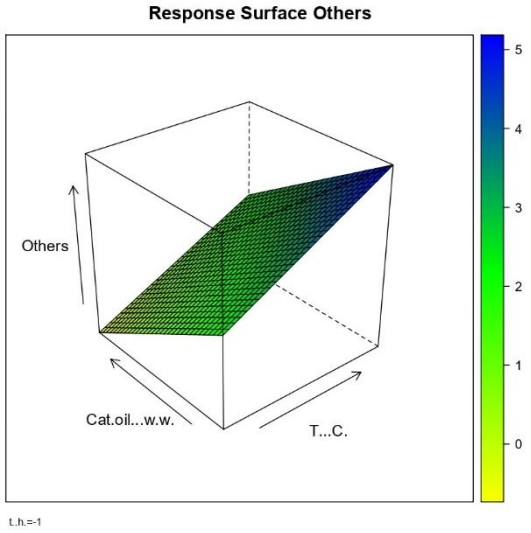
(h)


Response Surface UHC
UHC
Cat.oil...w.w.
T...C.
t.h.=-1
1.6
1.4
1.2
1.0
0.8
0.6
0.4
0.2
0.0

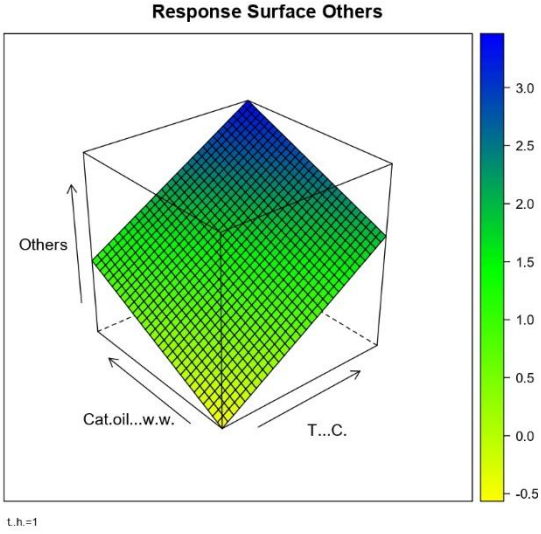
(i)


Response Surface UHC
UHC
Cat.oil...w.w.
T...C.
t.h.=1
0.20
0.15
0.10
0.05
0.00

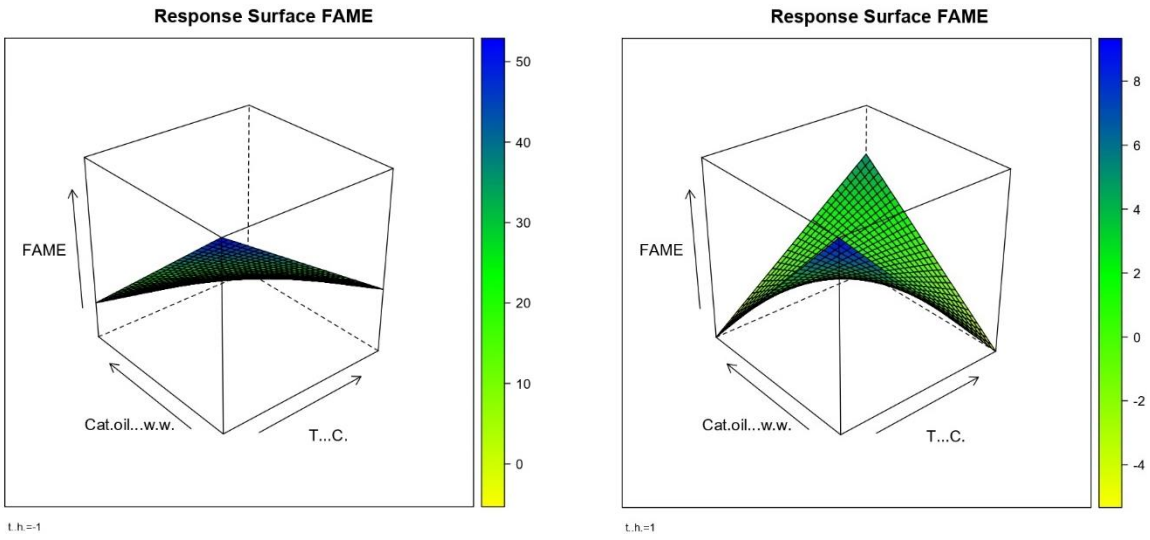
(l)


Response Surface Others
Others
Cat.oil...w.w.
T...C.
t.h.=-1
5
4
3
2
1
0

(m)

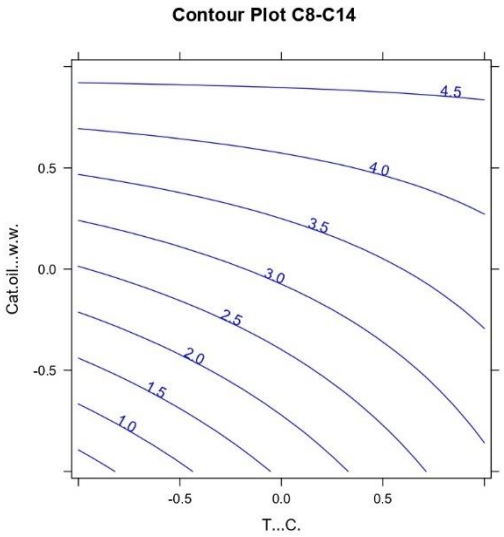

Response Surface Others
Others
Cat.oil...w.w.
T...C.
t.h.=1
3.0
2.5
2.0
1.5
1.0
0.5
0.0
-0.5

(n)

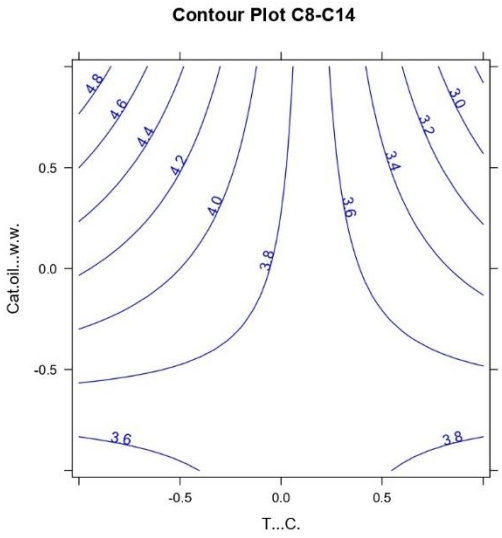


(**p**) (**q**)

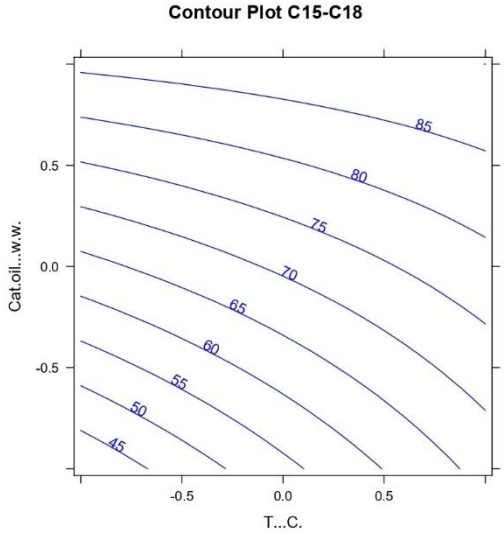
Figure D 3 Response surface of DO product composition for NiCoMo catalyst derived from the regression model of 2^3 experimental DoE, with coefficients in Table 20, at t=±1: (a) $A\%_{Ci}$ (with $C_8 \leq i \leq C_{14}$) at t=-1; (b) $A\%_{Ci}$ (with $C_8 \leq i \leq C_{14}$) at t=1; (c) $A\%_{Ci}$ (with $C_{15} \leq i \leq C_{18}$) at t=-1; (d) $A\%_{Ci}$ (with $C_{15} \leq i \leq C_{18}$) t=1; (e) $A\%_{Ci}$ (with $C_{19} \leq i \leq C_{30}$) at t=-1; (f) $A\%_{Ci}$ (with $C_{19} \leq i \leq C_{30}$) at t=1; (g) $A\%_{BHC}$ at t=-1; (h) $A\%_{BHC}$ at t=1; (i) $A\%_{UHC}$ at t=-1; (l) $A\%_{UHC}$ at t=1; (m) $A\%_{Others}$ at t=-1; (n) $A\%_{Others}$ at t=1; (p) $A\%_{FAME}$ at t=-1; (q) $A\%_{FAME}$ at t=1.


Contour Plot C8-C14
Cat.oil...w.w.
T...C.
4.5
4.0
3.5
3.0
2.5
2.0
1.5
1.0

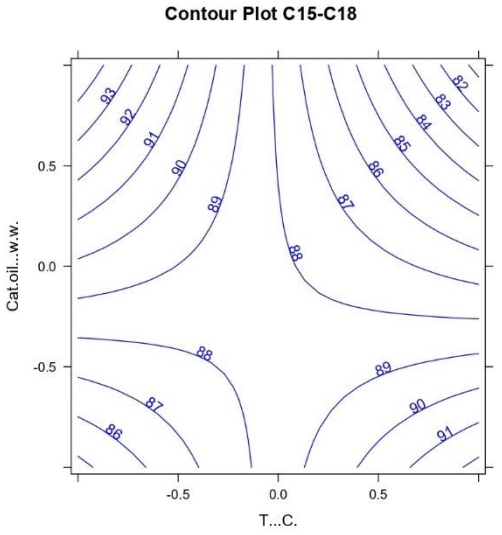
(**a**)


Contour Plot C8-C14
Cat.oil...w.w.
T...C.
4.8
4.6
4.4
4.2
4.0
3.8
3.6
3.4
3.2
3.0

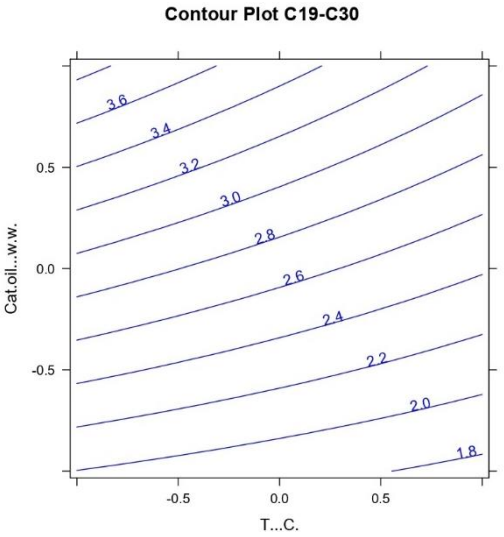
(**b**)


Contour Plot C15-C18
Cat.oil...w.w.
T...C.
85
80
75
70
65
60
55
50
45

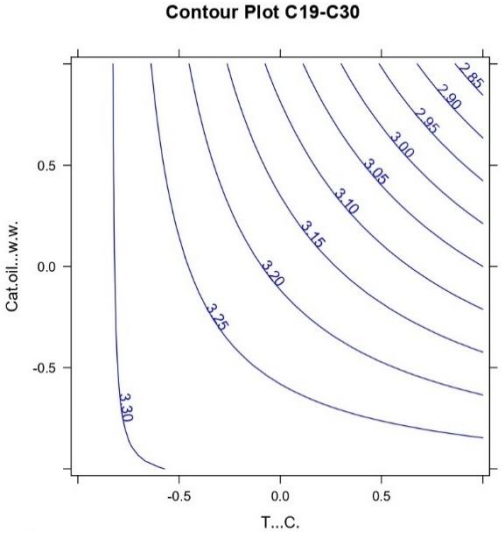
(**c**)


Contour Plot C15-C18
Cat.oil...w.w.
T...C.
93
92
91
90
89
88
87
86
85
84
83
82

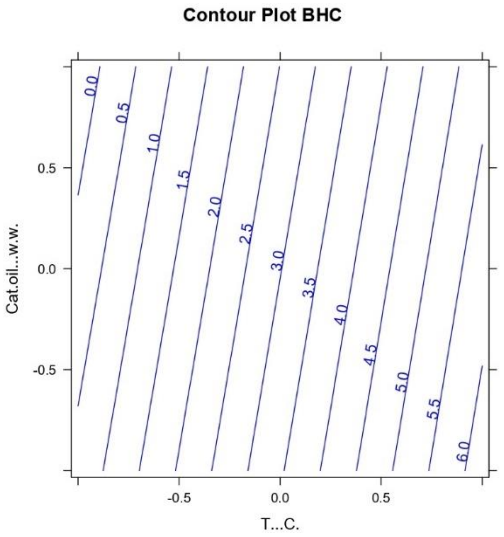
(**d**)


Contour Plot C19-C30
Cat.oil...w.w.
T...C.
3.6
3.4
3.2
3.0
2.8
2.6
2.4
2.2
2.0
1.8

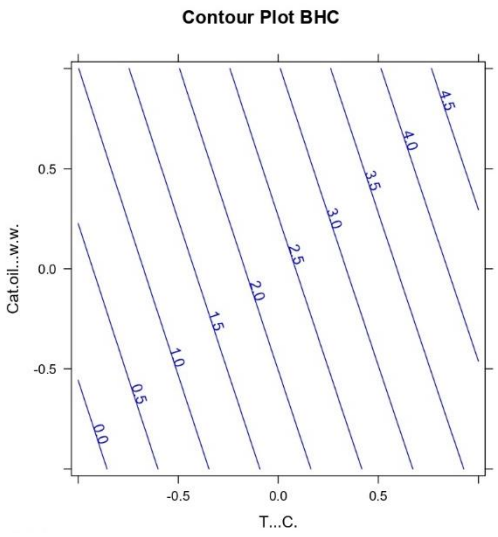
(**e**)


Contour Plot C19-C30
Cat.oil...w.w.
T...C.
2.85
2.90
2.95
3.00
3.05
3.10
3.15
3.20
3.25
3.30

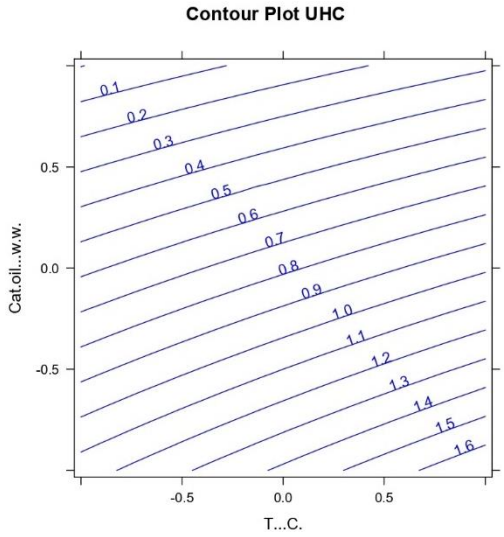
(**f**)


Contour Plot BHC
Cat.oil...w.w.
T...C.
0.0
0.5
1.0
1.5
2.0
2.5
3.0
3.5
4.0
4.5
5.0
5.5
6.0

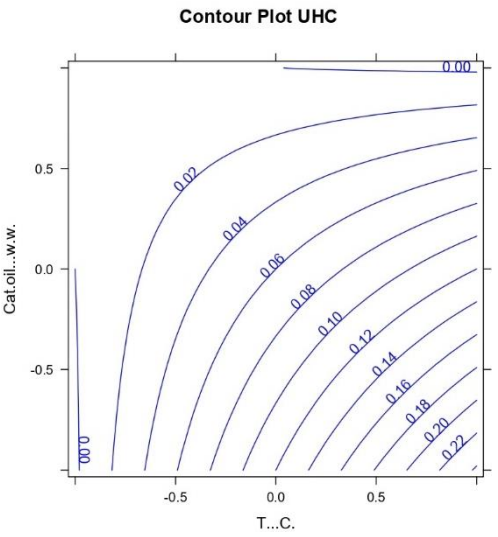
(**g**)


Contour Plot BHC
Cat.oil...w.w.
T...C.
0.0
0.5
1.0
1.5
2.0
2.5
3.0
3.5
4.0
4.5

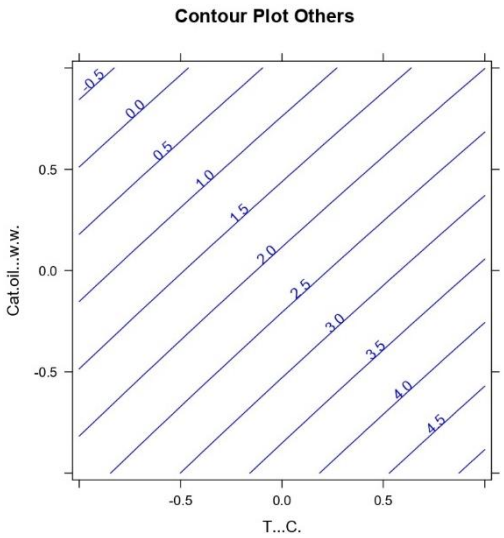
(**h**)


Contour Plot UHC
Cat.oil...w.w.
T...C.
0.1
0.2
0.3
0.4
0.5
0.6
0.7
0.8
0.9
1.0
1.1
1.2
1.3
1.4
1.5
1.6

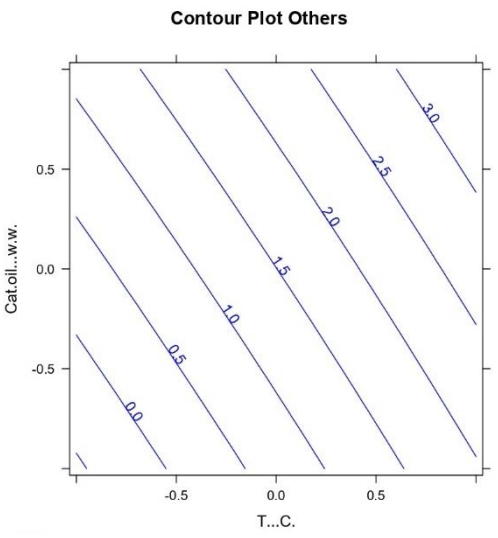
(**i**)


Contour Plot UHC
Cat.oil...w.w.
T...C.
0.00
0.02
0.04
0.06
0.08
0.10
0.12
0.14
0.16
0.18
0.20
0.22

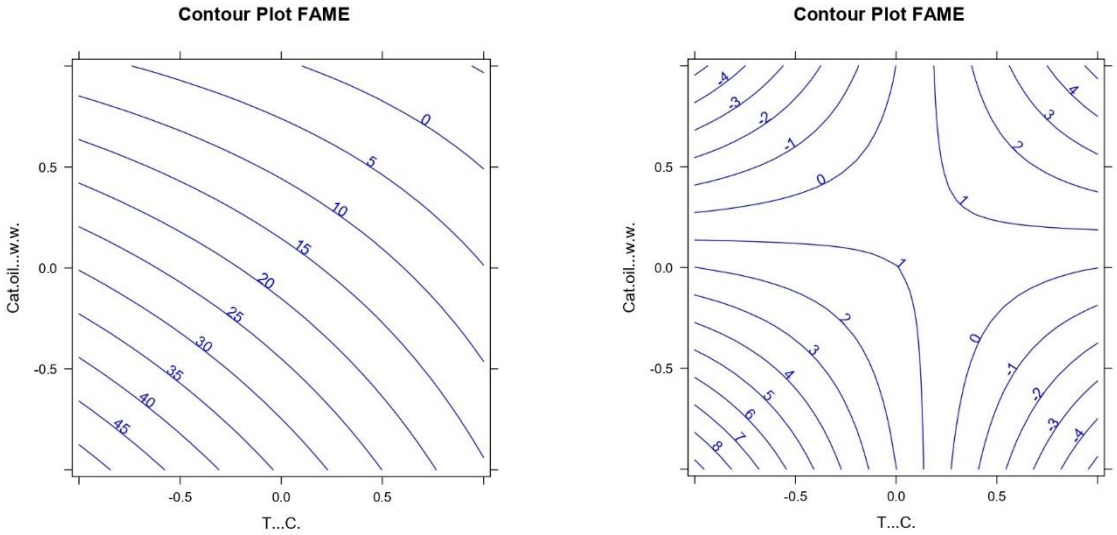
(**l**)


Contour Plot Others
Cat.oil...w.w.
T...C.
-0.5
0.0
0.5
1.0
1.5
2.0
2.5
3.0
3.5
4.0
4.5

(**m**)

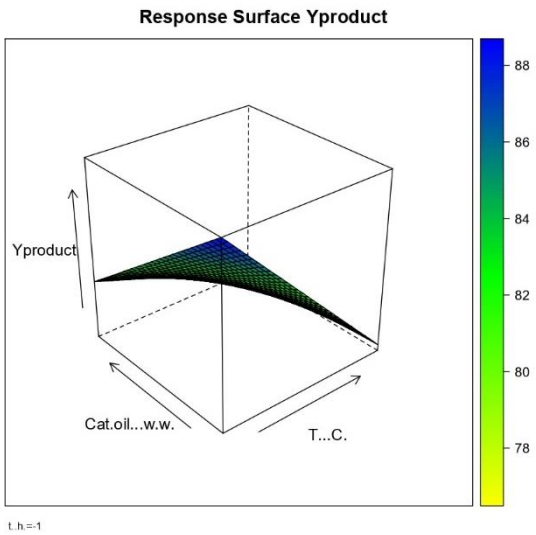

Contour Plot Others
Cat.oil...w.w.
T...C.
0.0
0.5
1.0
1.5
2.0
2.5
3.0

(**n**)

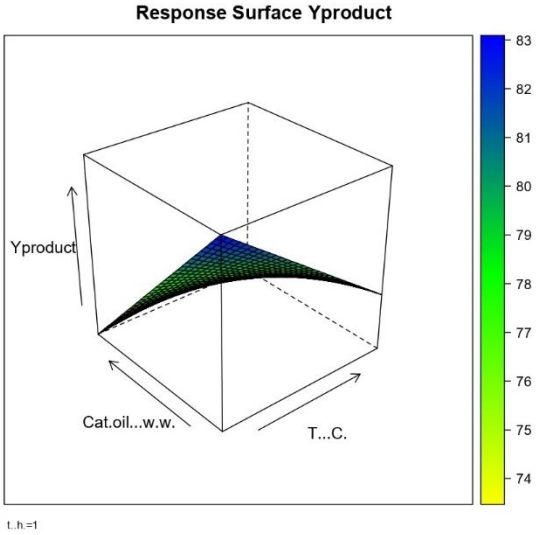


(**p**) (**q**)

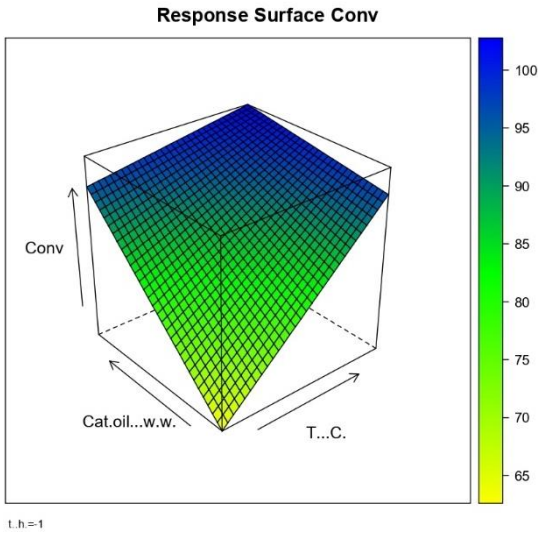
Figure D 4 Contour plots of DO product composition for NiCoMo catalyst derived from the regression model of 2^3 experimental DoE, with coefficients in Table 20, at t=±1: (a) $A\%_{Ci}$ (with $C_8 \leq i \leq C_{14}$) at t=-1; (b) $A\%_{Ci}$ (with $C_8 \leq i \leq C_{14}$) at t=1; (c) $A\%_{Ci}$ (with $C_{15} \leq i \leq C_{18}$) at t=-1; (d) $A\%_{Ci}$ (with $C_{15} \leq i \leq C_{18}$) at t=1; (e) $A\%_{Ci}$ (with $C_{19} \leq i \leq C_{30}$) at t=-1; (f) $A\%_{Ci}$ (with $C_{19} \leq i \leq C_{30}$) at t=1; (g) $A\%_{BHC}$ at t=-1; (h) $A\%_{BHC}$ at t=1; (i) $A\%_{UHC}$ at t=-1; (l) $A\%_{UHC}$ at t=1; (m) $A\%_{Others}$ at t=-1; (n) $A\%_{Others}$ at t=1; (p) $A\%_{FAME}$ at t=-1; (q) $A\%_{FAME}$ at t=1.


Response Surface Yproduct
Yproduct
Cat.oil...w.w.
T...C.
88
86
84
82
80
78
t..h.=-1

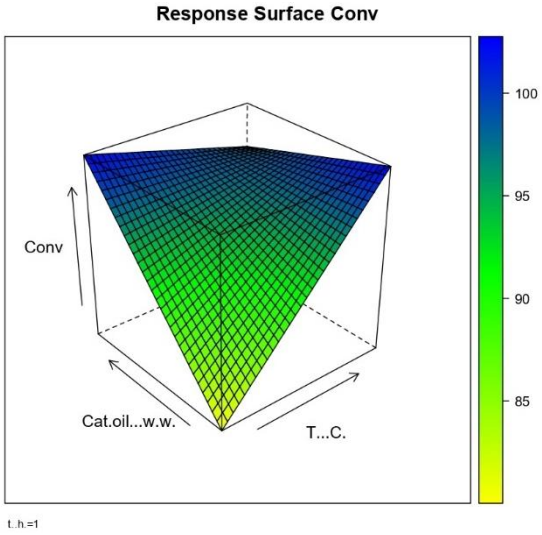
(**a**)


Response Surface Yproduct
Yproduct
Cat.oil...w.w.
T...C.
83
82
81
80
79
78
77
76
75
74
t..h.=1

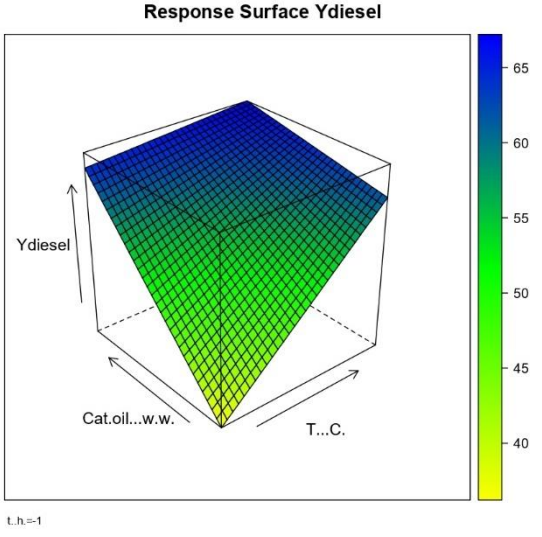
(**b**)


Response Surface Conv
Conv
Cat.oil...w.w.
T...C.
100
95
90
85
80
75
70
65
t..h.=-1

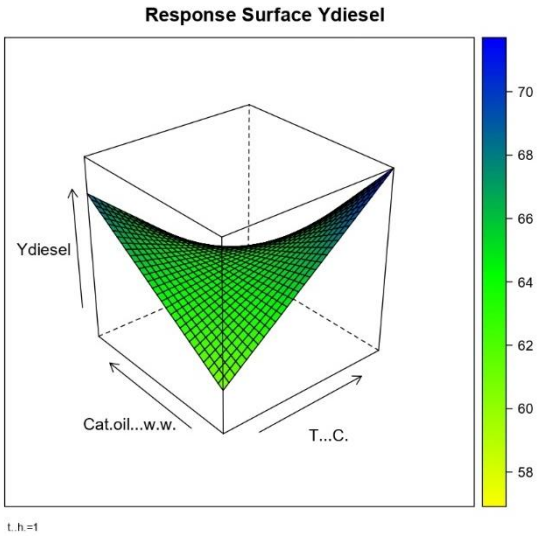
(**c**)


Response Surface Conv
Conv
Cat.oil...w.w.
T...C.
100
95
90
85
t..h.=1

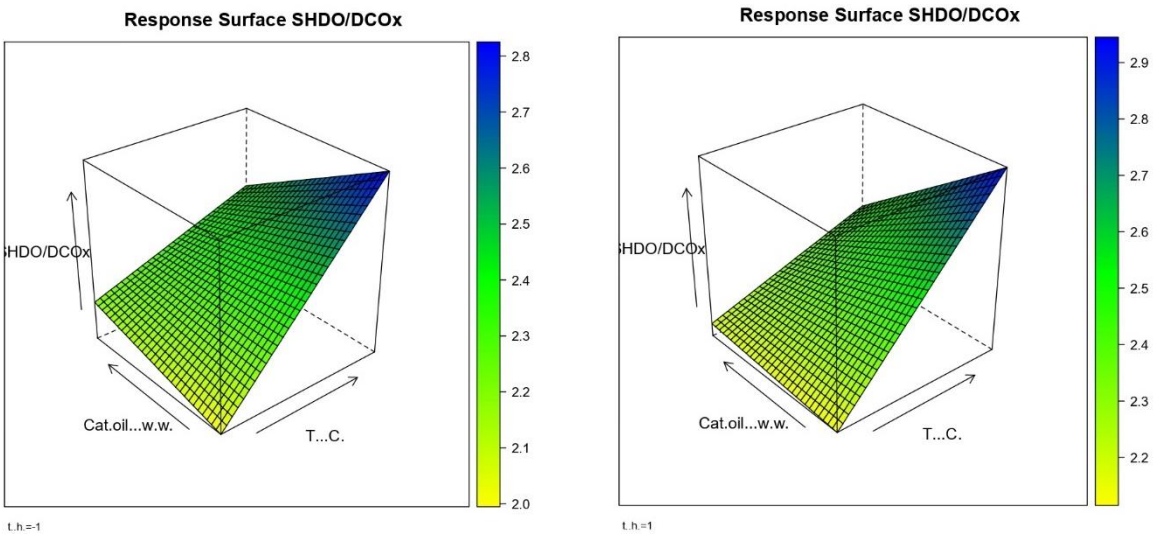
(**d**)


Response Surface Ydiesel
Ydiesel
Cat.oil...w.w.
T...C.
65
60
55
50
45
40
t..h.=-1

(**e**)

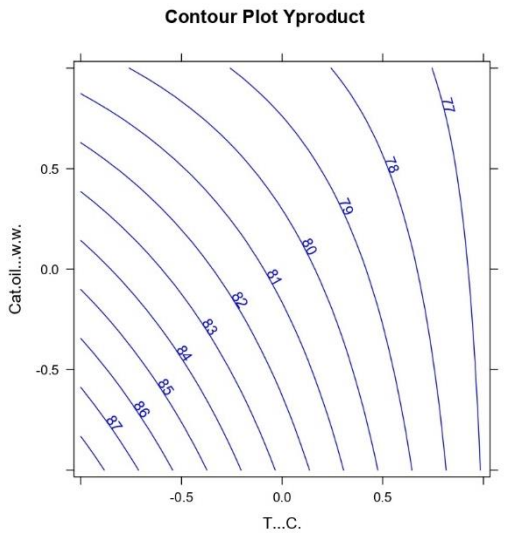

Response Surface Ydiesel
Ydiesel
Cat.oil...w.w.
T...C.
70
68
66
64
62
60
58
t..h.=1

(**f**)

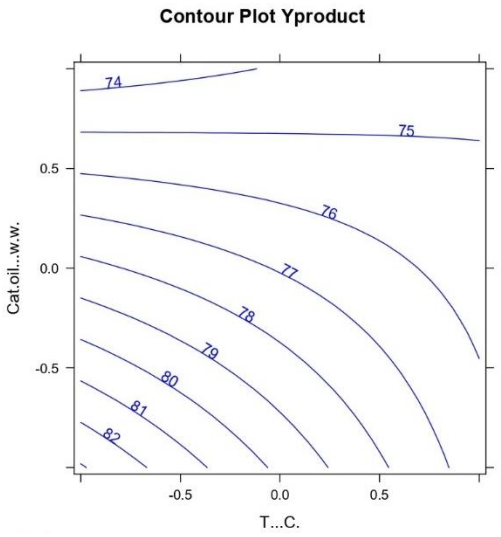


(**g**) (**h**)

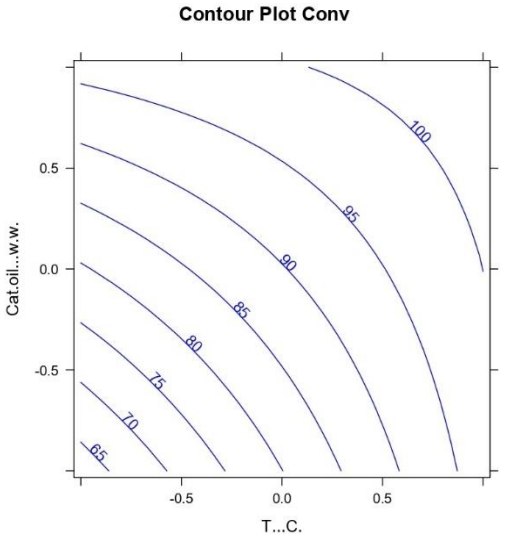
Figure D 5 Response surface of DO process parameters for ZnCoMo catalyst derived from the regression model of 2^3 experimental DoE, with coefficients in Table 20, at t=±1: (a) $Y_{product}$ (Equation 2.9) at t=-1; (b) $Y_{product}$ (Equation 2.9) at t=1; (c) χ (Equation 2.10) at t=-1; (d) χ (Equation 2.10) at t=1; (e) Y_{diesel} (Equation 2.11) at t=-1; (f) Y_{diesel} (Equation 2.11) at t=1; (g) $S_{HDO/DCOx}$ (Equation 2.12) at t=-1; (e) $S_{HDO/DCOx}$ (Equation 2.12) at t=1.


Contour Plot Yproduct
Cat.oil...w.w.
T...C.
77
78
79
80
81
82
83
84
85
86
87

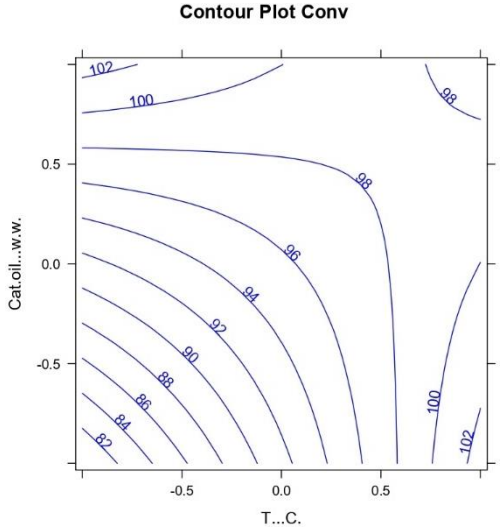
(**a**)


Contour Plot Yproduct
Cat.oil...w.w.
T...C.
74
75
76
77
78
79
80
81
82

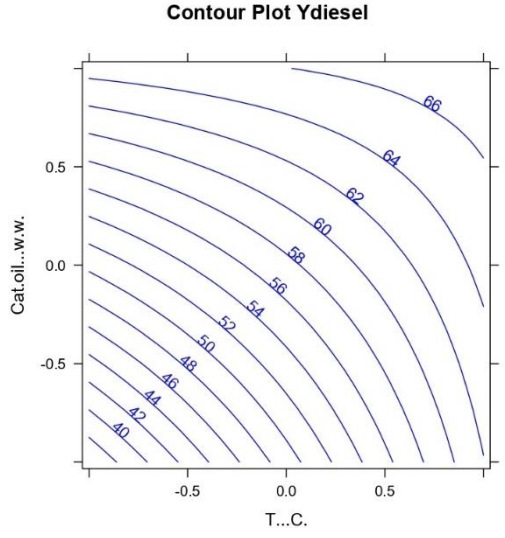
(**b**)


Contour Plot Conv
Cat.oil...w.w.
T...C.
100
95
90
85
80
75
70
65

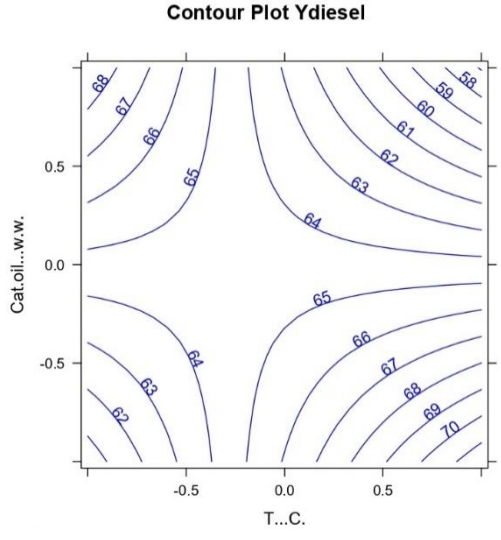
(**c**)


Contour Plot Conv
Cat.oil...w.w.
T...C.
102
100
98
96
94
92
90
88
86
84
82

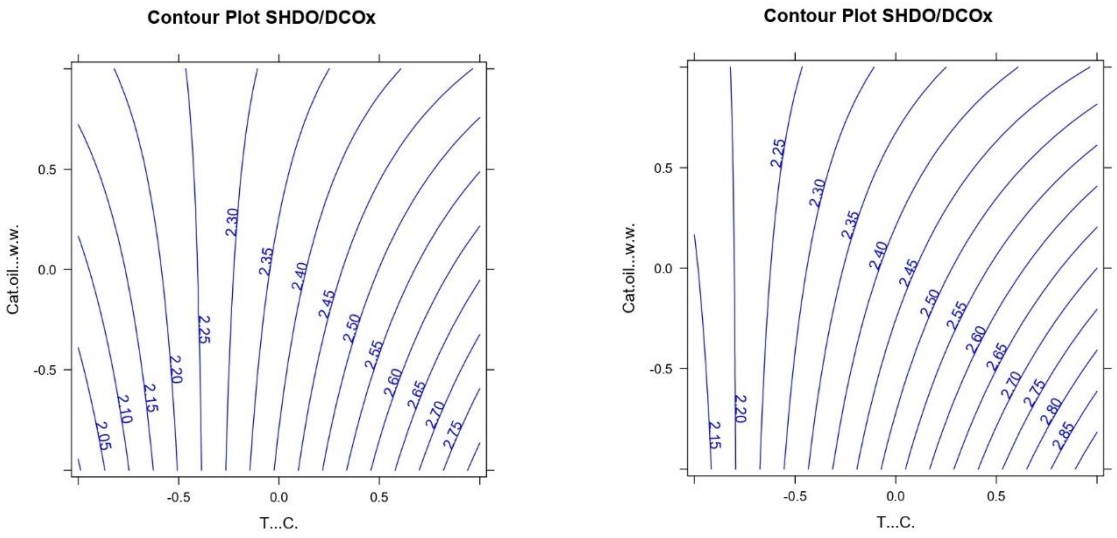
(**d**)


Contour Plot Ydiesel
Cat.oil...w.w.
T...C.
66
64
62
60
58
56
54
52
50
48
46
44
42
40

(**e**)

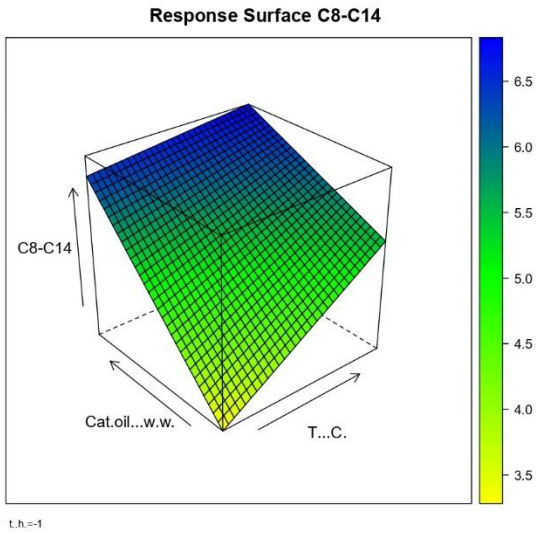

Contour Plot Ydiesel
Cat.oil...w.w.
T...C.
68
67
66
65
64
63
62
61
60
59
58
65
66
67
68
69
70

(**f**)

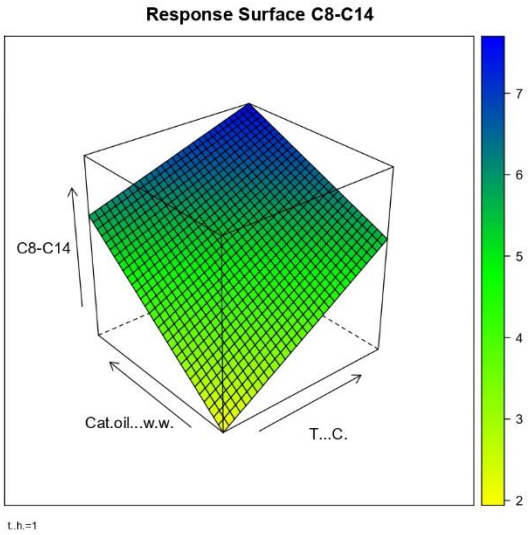


(**g**) (**h**)

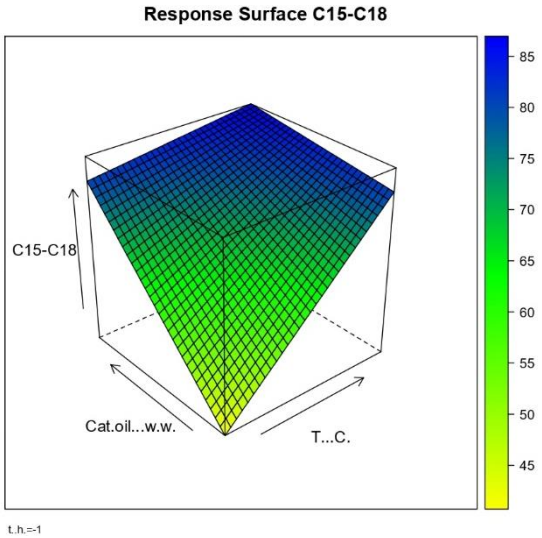
Figure D 6 Contour plots of DO process parameters for ZnCoMo catalyst derived from the regression model of 2^3 experimental DoE, with coefficients in Table 20, at t=±1: (a) $Y_{product}$ (Equation 2.9) at t=-1; (b) $Y_{product}$ (Equation 2.9) at t=1; (c) χ (Equation 2.10) at t=-1; (d) χ (Equation 2.10) at t=1; (e) Y_{diesel} (Equation 2.11) at t=-1; (f) Y_{diesel} (Equation 2.11) at t=1; (g) $S_{HDO/DCOx}$ (Equation 2.12) at t=-1; (e) $S_{HDO/DCOx}$ (Equation 2.12) at t=1.


Response Surface C8-C14
C8-C14
Cat.oil...w.w.
T...C.
6.5
6.0
5.5
5.0
4.5
4.0
3.5
t.h.=-1

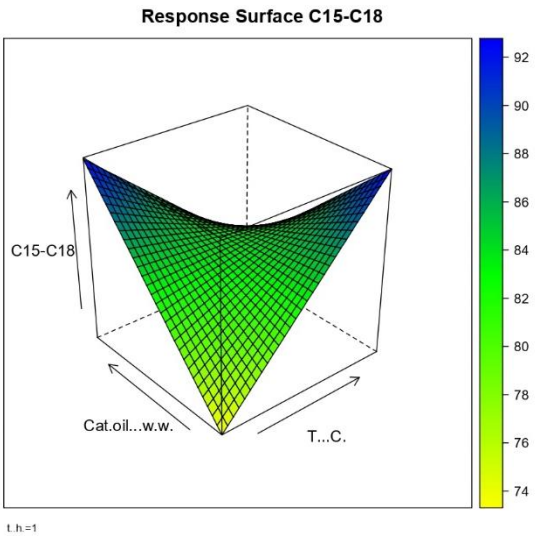
(**a**)


Response Surface C8-C14
C8-C14
Cat.oil...w.w.
T...C.
7
6
5
4
3
2
t.h.=1

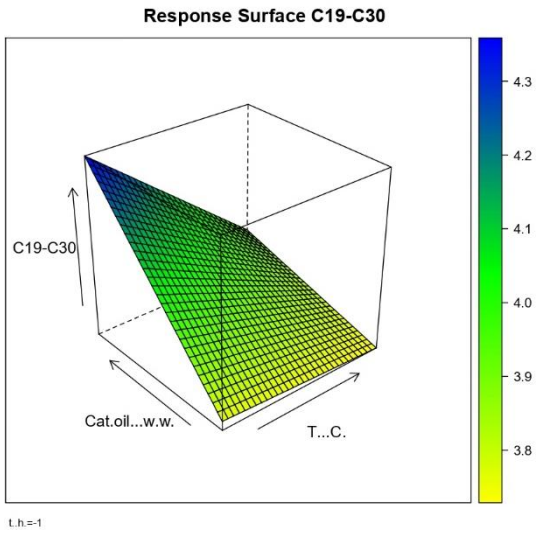
(**b**)


Response Surface C15-C18
C15-C18
Cat.oil...w.w.
T...C.
85
80
75
70
65
60
55
50
45
t.h.=-1

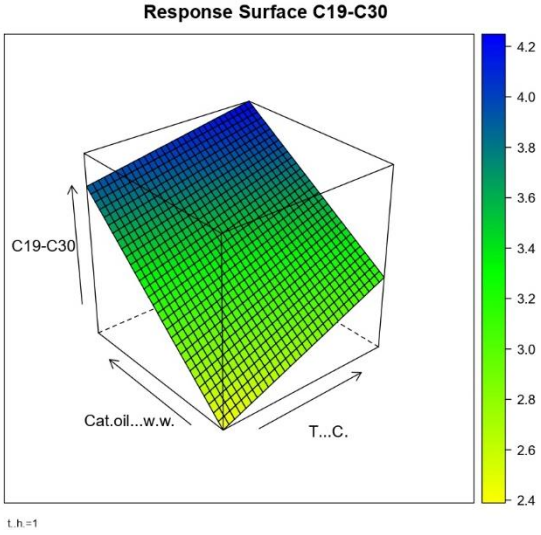
(**c**)


Response Surface C15-C18
C15-C18
Cat.oil...w.w.
T...C.
92
90
88
86
84
82
80
78
76
74
t.h.=1

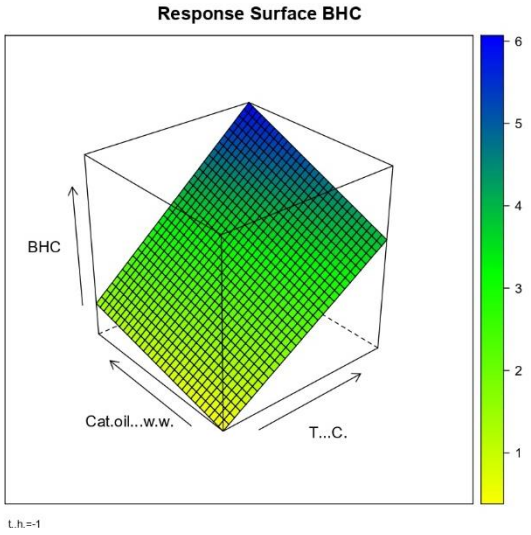
(**d**)


Response Surface C19-C30
C19-C30
Cat.oil...w.w.
T...C.
4.3
4.2
4.1
4.0
3.9
3.8
t.h.=-1

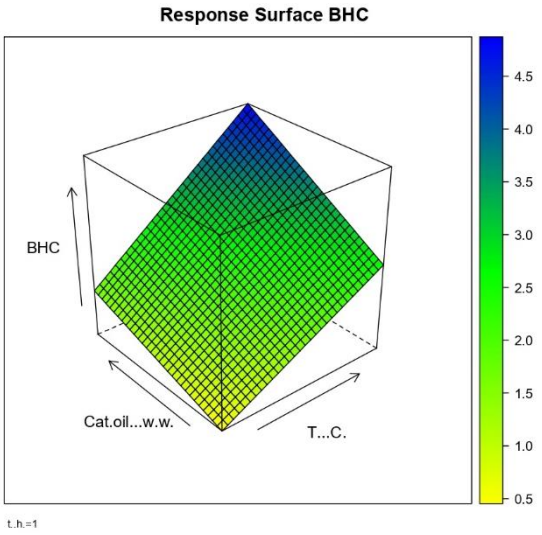
(**e**)


Response Surface C19-C30
C19-C30
Cat.oil...w.w.
T...C.
4.2
4.0
3.8
3.6
3.4
3.2
3.0
2.8
2.6
2.4
t.h.=1

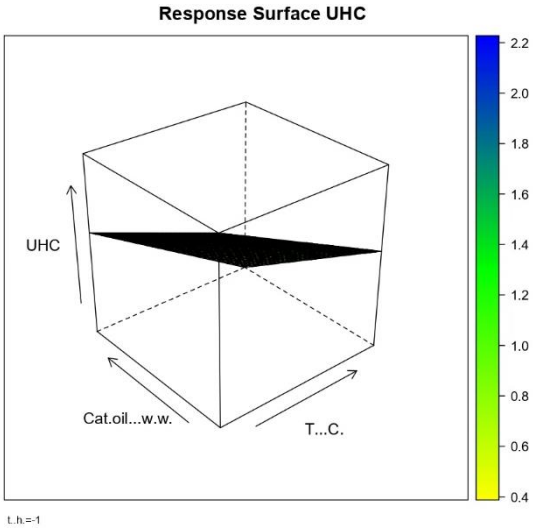
(**f**)


Response Surface BHC
BHC
Cat.oil...w.w.
T...C.
t.h.=-1
6
5
4
3
2
1

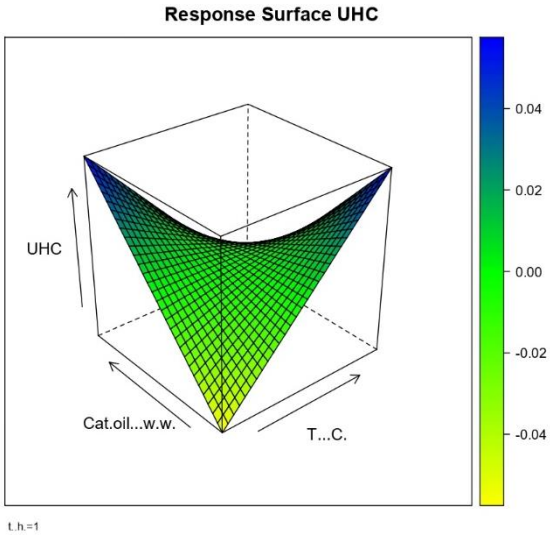
(g)


Response Surface BHC
BHC
Cat.oil...w.w.
T...C.
t.h.=1
4.5
4.0
3.5
3.0
2.5
2.0
1.5
1.0
0.5

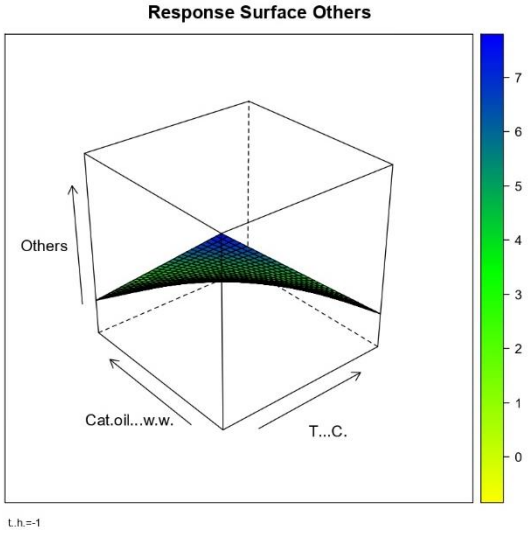
(h)


Response Surface UHC
UHC
Cat.oil...w.w.
T...C.
t.h.=-1
2.2
2.0
1.8
1.6
1.4
1.2
1.0
0.8
0.6
0.4

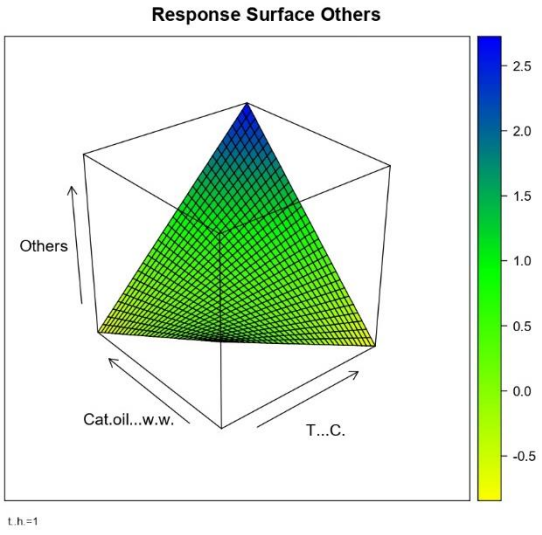
(i)


Response Surface UHC
UHC
Cat.oil...w.w.
T...C.
t.h.=1
0.04
0.02
0.00
-0.02
-0.04

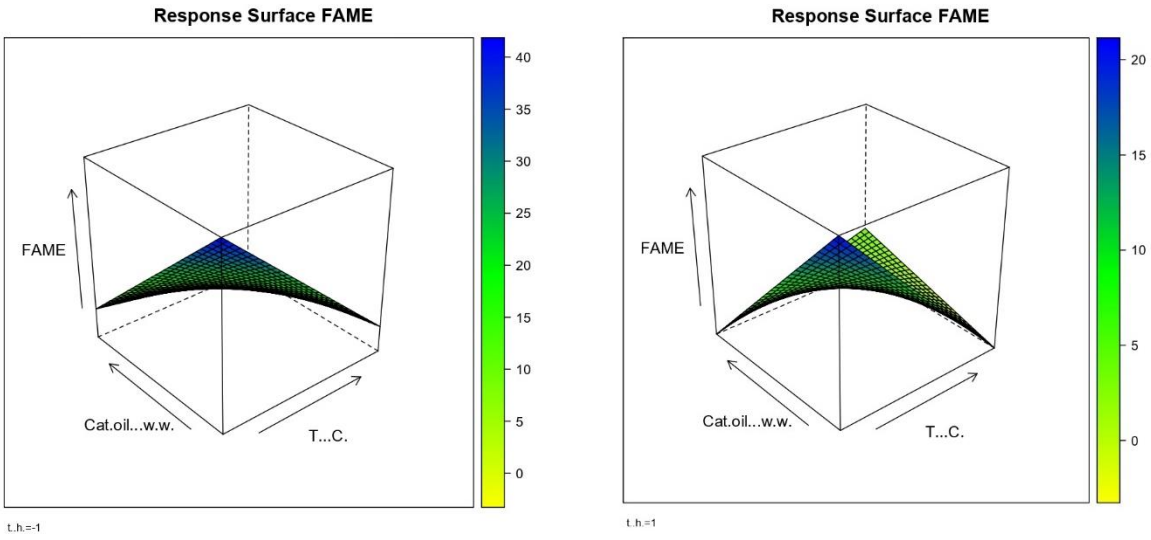
(l)


Response Surface Others
Others
Cat.oil...w.w.
T...C.
t.h.=-1
7
6
5
4
3
2
1
0

(m)

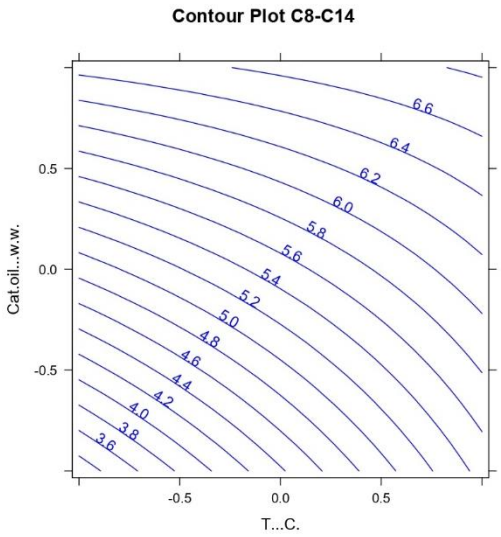

Response Surface Others
Others
Cat.oil...w.w.
T...C.
t.h.=1
2.5
2.0
1.5
1.0
0.5
0.0
-0.5

(n)

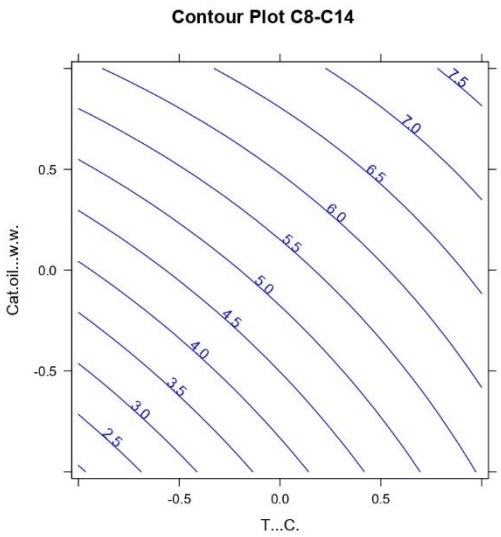


(**p**) (**q**)

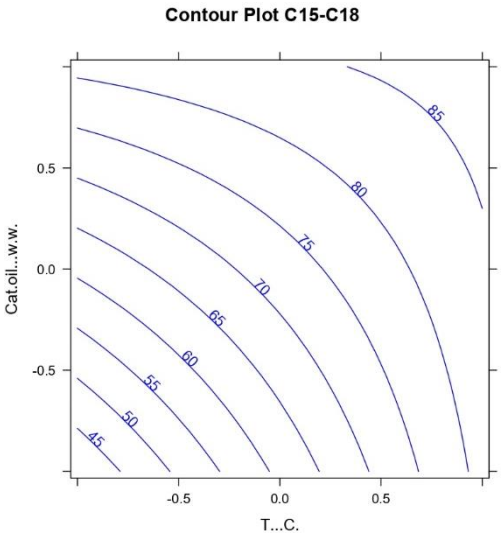
Figure D 7 Response surface of DO product composition for ZnCoMo catalyst derived from the regression model of 2^3 experimental DoE, with coefficients in Table 20, at t=±1: (a) $A\%_{Ci}$ (with $C_8 \leq i \leq C_{14}$) at t=-1; (b) $A\%_{Ci}$ (with $C_8 \leq i \leq C_{14}$) at t=1; (c) $A\%_{Ci}$ (with $C_{15} \leq i \leq C_{18}$) at t=-1; (d) $A\%_{Ci}$ (with $C_{15} \leq i \leq C_{18}$) at t=1; (e) $A\%_{Ci}$ (with $C_{19} \leq i \leq C_{30}$) at t=-1; (f) $A\%_{Ci}$ (with $C_{19} \leq i \leq C_{30}$) at t=1; (g) $A\%_{BHC}$ at t=-1; (h) $A\%_{BHC}$ at t=1; (i) $A\%_{UHC}$ at t=-1; (l) $A\%_{UHC}$ at t=1; (m) $A\%_{Others}$ at t=-1; (n) $A\%_{Others}$ at t=1; (p) $A\%_{FAME}$ at t=-1; (q) $A\%_{FAME}$ at t=1.


Contour Plot C8-C14
Cat.oil...w.w.
T...C.
6.6
6.4
6.2
6.0
5.8
5.6
5.4
5.2
5.0
4.8
4.6
4.4
4.2
4.0
3.8
3.6

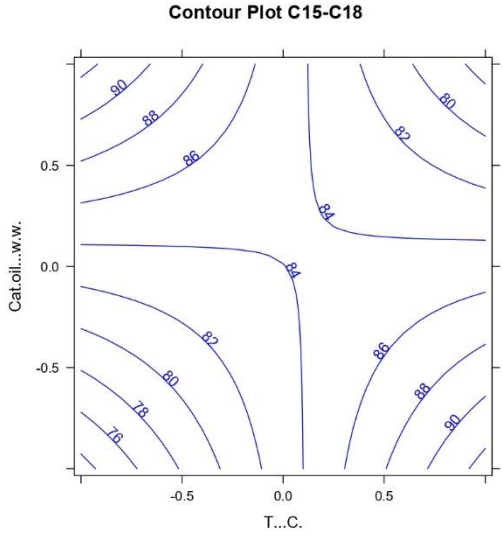
(**a**)


Contour Plot C8-C14
Cat.oil...w.w.
T...C.
7.5
7.0
6.5
6.0
5.5
5.0
4.5
4.0
3.5
3.0
2.5

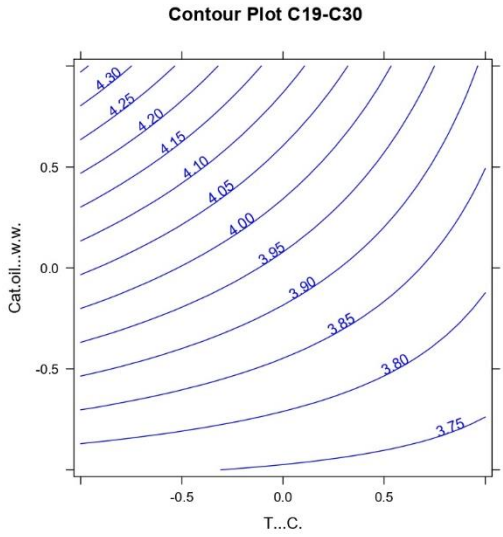
(**b**)


Contour Plot C15-C18
Cat.oil...w.w.
T...C.
85
80
75
70
65
60
55
50
45

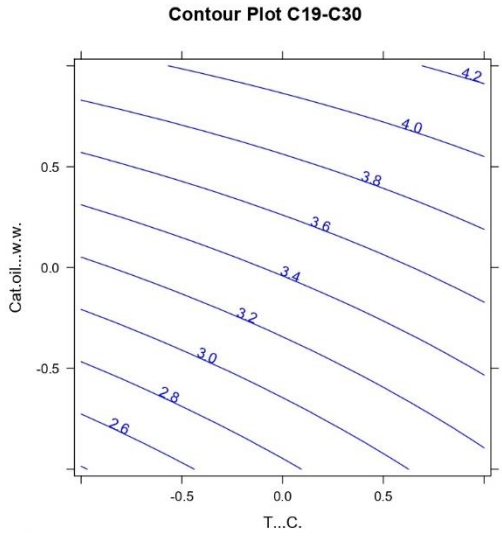
(**c**)


Contour Plot C15-C18
Cat.oil...w.w.
T...C.
90
88
86
84
82
80
78
76

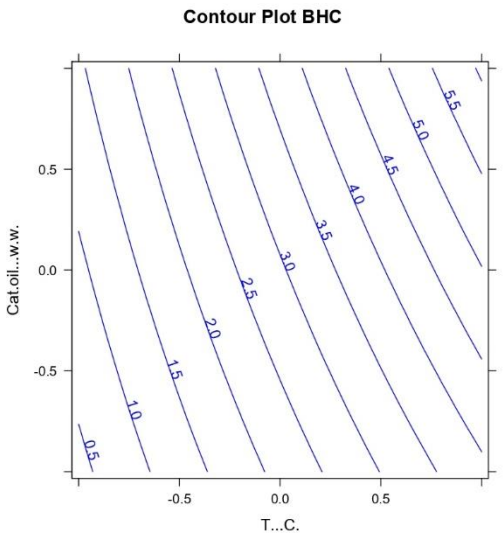
(**d**)


Contour Plot C19-C30
Cat.oil...w.w.
T...C.
4.30
4.25
4.20
4.15
4.10
4.05
4.00
3.95
3.90
3.85
3.80
3.75

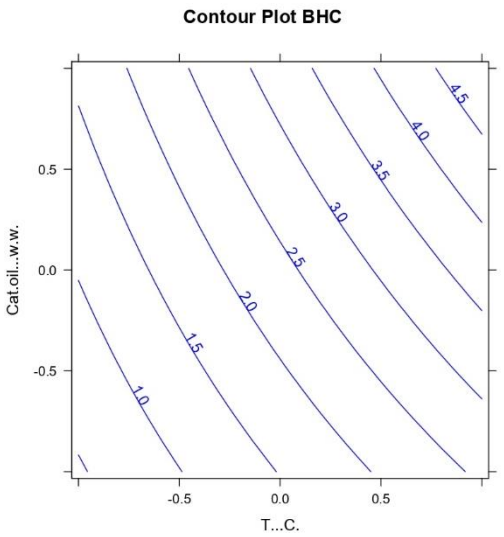
(**e**)


Contour Plot C19-C30
Cat.oil...w.w.
T...C.
4.2
4.0
3.8
3.6
3.4
3.2
3.0
2.8
2.6

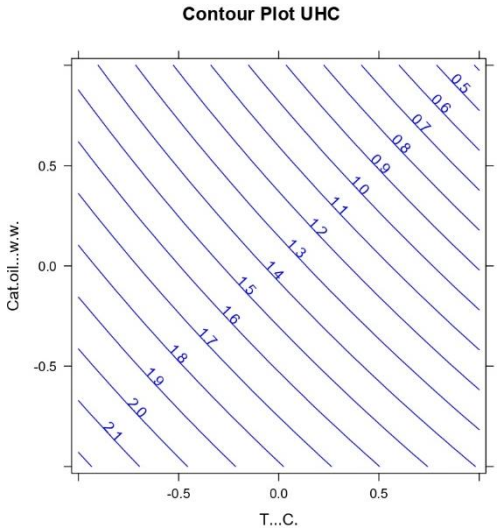
(**f**)


Contour Plot BHC
Cat.oil...w.w.
T...C.
0.5
0.0
-0.5
-0.5
0.0
0.5
0.5
1.0
1.5
2.0
2.5
3.0
3.5
4.0
4.5
5.0
5.5

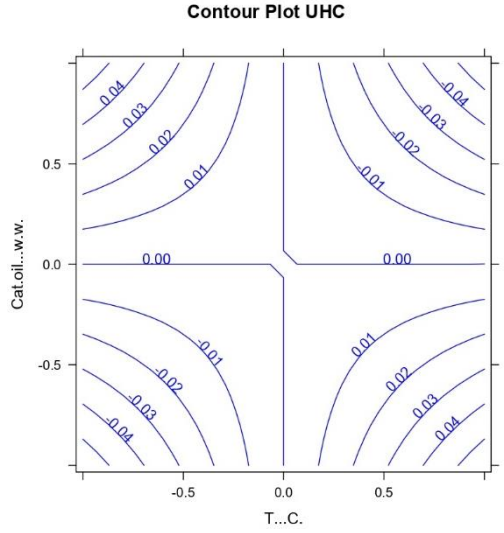
(g)


Contour Plot BHC
Cat.oil...w.w.
T...C.
0.5
0.0
-0.5
-0.5
0.0
0.5
1.0
1.5
2.0
2.5
3.0
3.5
4.0
4.5

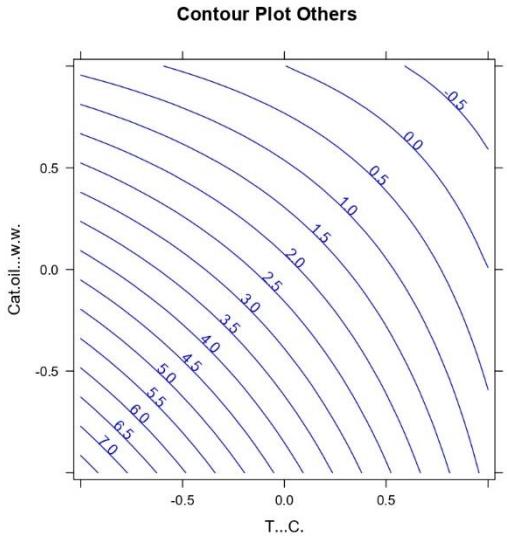
(h)


Contour Plot UHC
Cat.oil...w.w.
T...C.
0.5
0.0
-0.5
-0.5
0.0
0.5
0.5
0.6
0.7
0.8
0.9
1.0
1.1
1.2
1.3
1.4
1.5
1.6
1.7
1.8
1.9
2.0
2.1

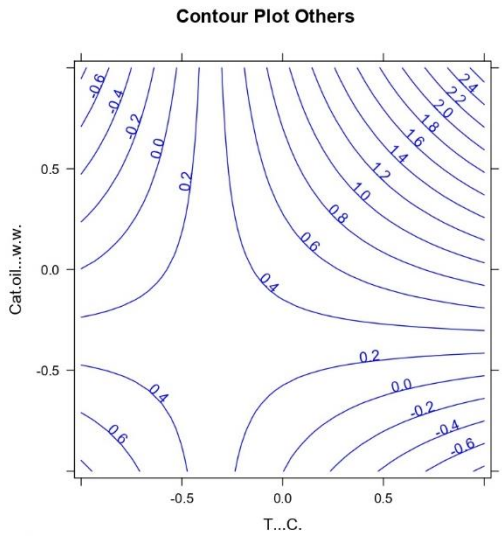
(i)


Contour Plot UHC
Cat.oil...w.w.
T...C.
0.5
0.0
-0.5
-0.5
0.0
0.5
0.04
0.03
0.02
0.01
0.00
-0.01
-0.02
-0.03
-0.04

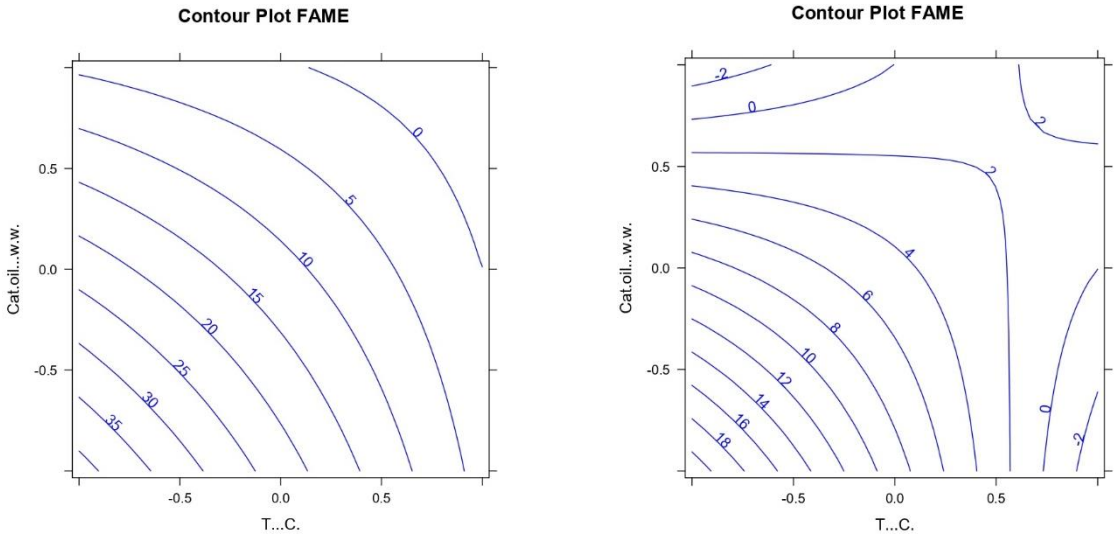
(l)


Contour Plot Others
Cat.oil...w.w.
T...C.
0.5
0.0
-0.5
-0.5
0.0
0.5
-0.5
0.0
0.5
1.0
1.5
2.0
2.5
3.0
3.5
4.0
4.5
5.0
5.5
6.0
6.5
7.0

(m)

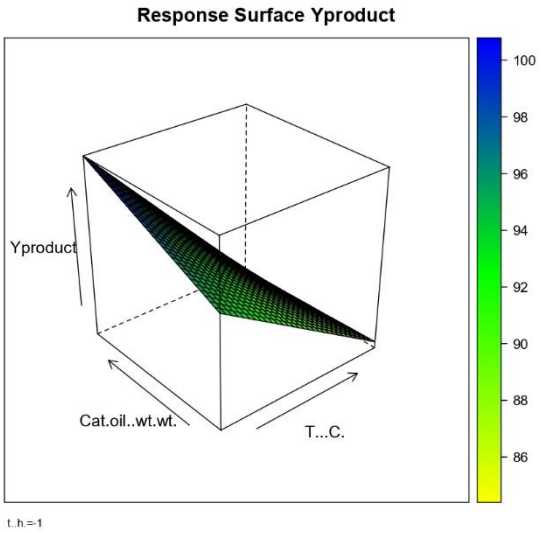

Contour Plot Others
Cat.oil...w.w.
T...C.
0.5
0.0
-0.5
-0.5
0.0
0.5
-0.6
-0.4
-0.2
0.0
0.2
0.4
0.6
0.8
1.0
1.2
1.4
1.6
1.8
2.0
2.2
2.4

(n)

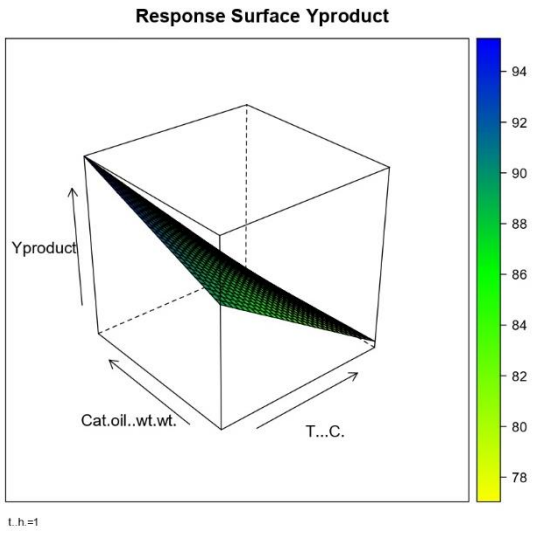


(**p**) (**q**)

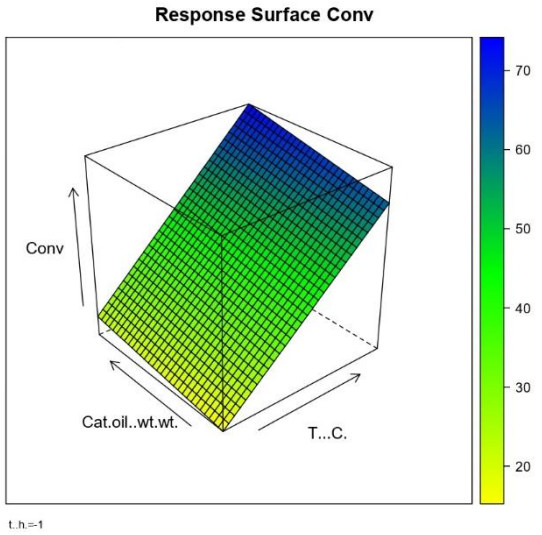
Figure D 8 Contour plots of DO product composition for ZnCoMo catalyst derived from the regression model of 2^3 experimental DoE, with coefficients in Table 20, at t=±1: (a) $A\%_{Ci}$ (with $C_8 \leq i \leq C_{14}$) at t=-1; (b) $A\%_{Ci}$ (with $C_8 \leq i \leq C_{14}$) at t=1; (c) $A\%_{Ci}$ (with $C_{15} \leq i \leq C_{18}$) at t=-1; (d) $A\%_{Ci}$ (with $C_{15} \leq i \leq C_{18}$) at t=1; (e) $A\%_{Ci}$ (with $C_{19} \leq i \leq C_{30}$) at t=-1; (f) $A\%_{Ci}$ (with $C_{19} \leq i \leq C_{30}$) at t=1; (g) $A\%_{BHC}$ at t=-1; (h) $A\%_{BHC}$ at t=1; (i) $A\%_{UHC}$ at t=-1; (l) $A\%_{UHC}$ at t=1; (m) $A\%_{Others}$ at t=-1; (n) $A\%_{Others}$ at t=1; (p) $A\%_{FAME}$ at t=-1; (q) $A\%_{FAME}$ at t=1.


Response Surface Yproduct
Yproduct
Cat.oil..wt.wt.
T...C.
t..h.=-1
100
98
96
94
92
90
88
86

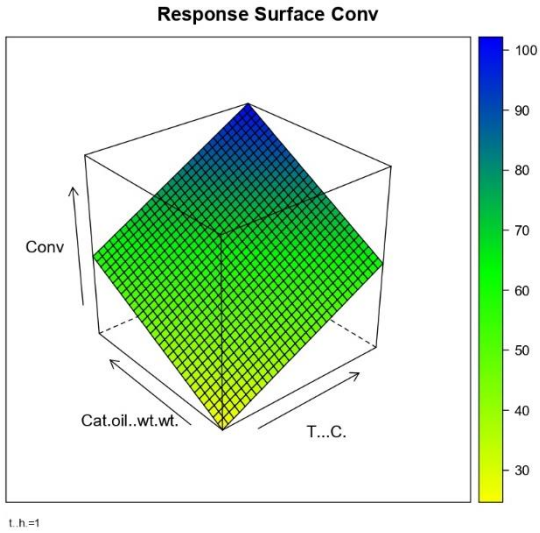
(**a**)


Response Surface Yproduct
Yproduct
Cat.oil..wt.wt.
T...C.
t..h.=1
94
92
90
88
86
84
82
80
78

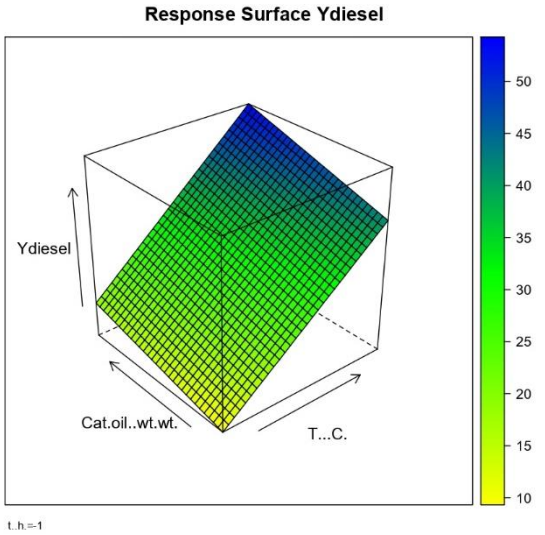
(**b**)


Response Surface Conv
Conv
Cat.oil..wt.wt.
T...C.
t..h.=-1
70
60
50
40
30
20

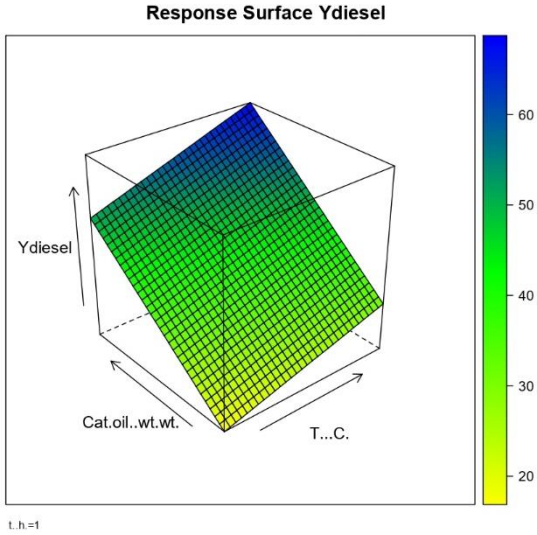
(**c**)


Response Surface Conv
Conv
Cat.oil..wt.wt.
T...C.
t..h.=1
100
90
80
70
60
50
40
30

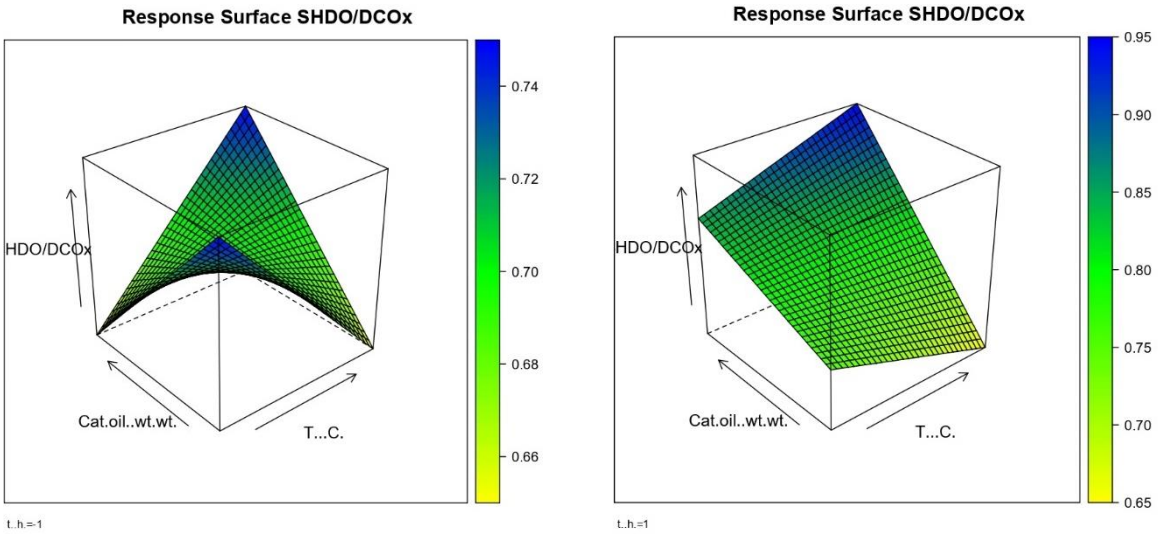
(**d**)


Response Surface Ydiesel
Ydiesel
Cat.oil..wt.wt.
T...C.
t..h.=-1
50
45
40
35
30
25
20
15
10

(**e**)

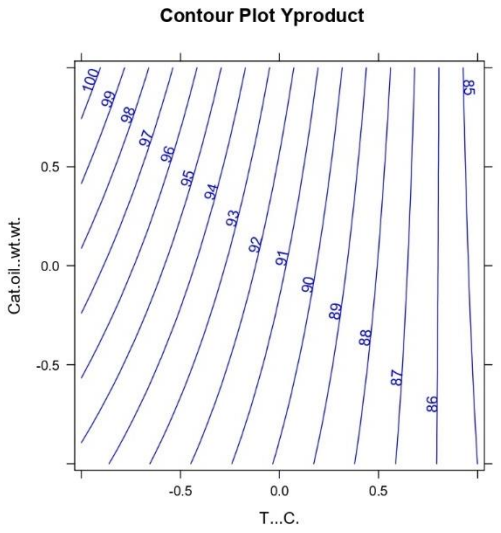

Response Surface Ydiesel
Ydiesel
Cat.oil..wt.wt.
T...C.
t..h.=1
60
50
40
30
20

(**f**)

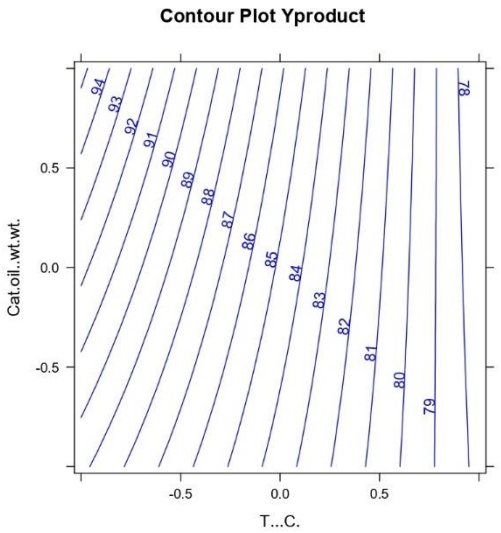


(**g**) (**h**)

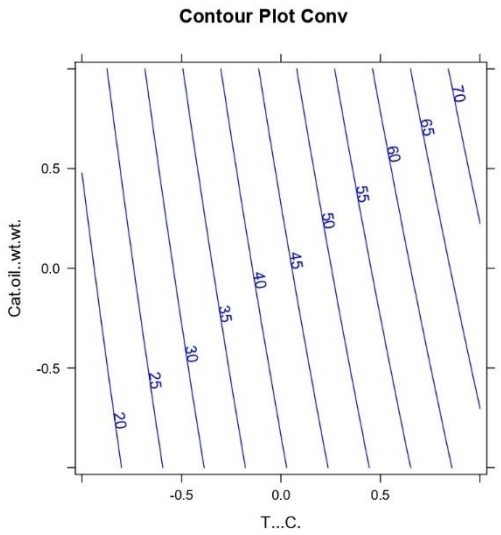
Figure D 9 Response surface of DO process parameters for Ni-Mo-Al catalyst derived from the regression model of 2^3 experimental DoE, with coefficients in Table 23, at t=±1: (a) $Y_{product}$ (Equation 2.9) at t=-1; (b) $Y_{product}$ (Equation 2.9) at t=1; (c) χ (Equation 2.10) at t=-1; (d) χ (Equation 2.10) at t=1; (e) Y_{diesel} (Equation 2.11) at t=-1; (f) Y_{diesel} (Equation 2.11) at t=1; (g) $S_{HDO/DCOx}$ (Equation 2.12) at t=-1; (e) $S_{HDO/DCOx}$ (Equation 2.12) at t=1.


Contour Plot Yproduct
Cat.oil..wt.wt.
T...C.
100
99
98
97
96
95
94
93
92
91
90
89
88
87
86
85

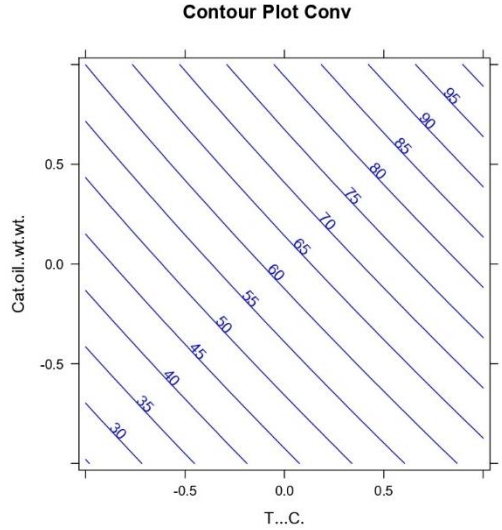
(**a**)


Contour Plot Yproduct
Cat.oil..wt.wt.
T...C.
94
93
92
91
90
89
88
87
86
85
84
83
82
81
80
79
78

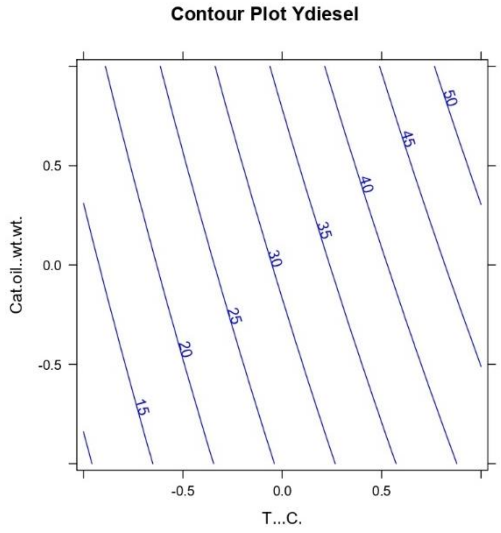
(**b**)


Contour Plot Conv
Cat.oil..wt.wt.
T...C.
70
65
60
55
50
45
40
35
30
25
20

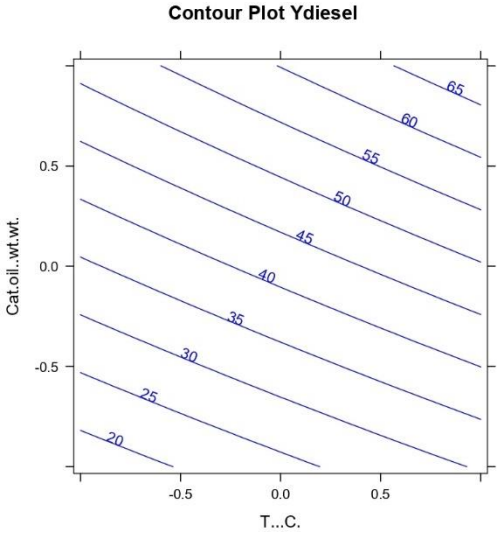
(**c**)


Contour Plot Conv
Cat.oil..wt.wt.
T...C.
95
90
85
80
75
70
65
60
55
50
45
40
35
30

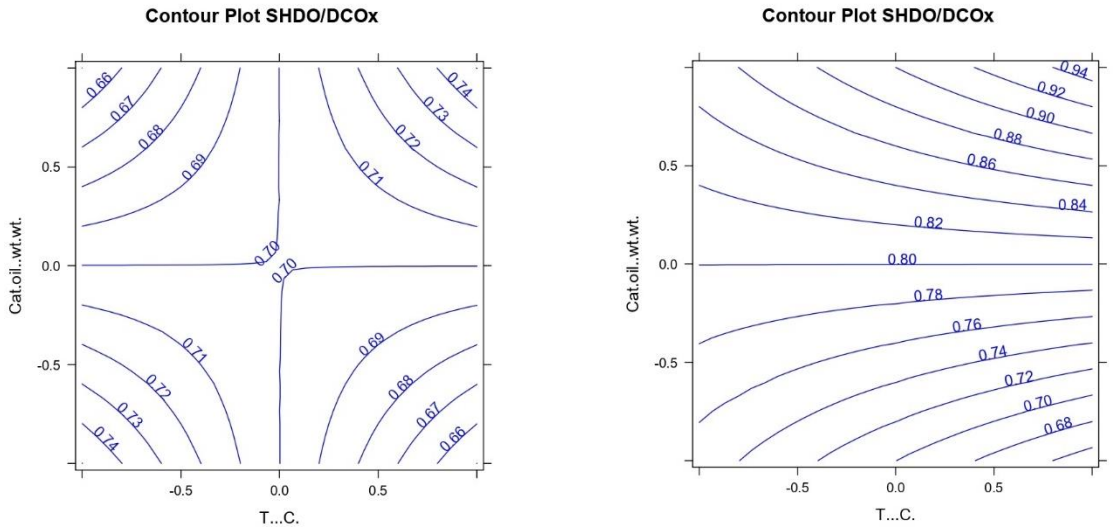
(**d**)


Contour Plot Ydiesel
Cat.oil..wt.wt.
T...C.
50
45
40
35
30
25
20
15

(**e**)

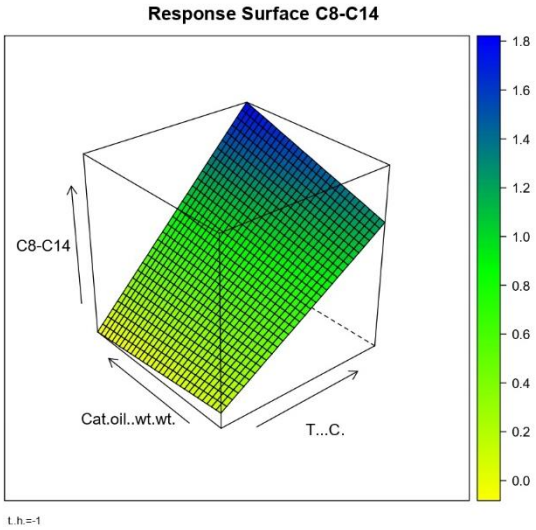

Contour Plot Ydiesel
Cat.oil..wt.wt.
T...C.
65
60
55
50
45
40
35
30
25
20

(**f**)

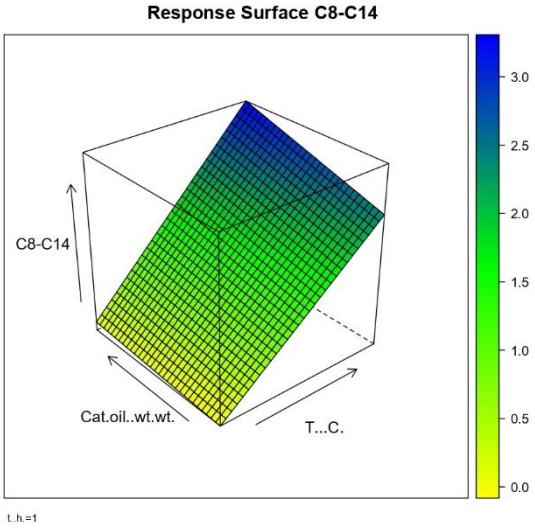


(**g**) (**h**)

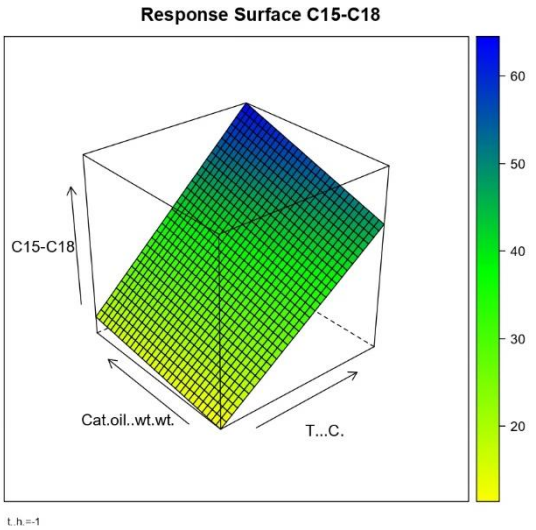
Figure D 10 Contour plots of DO process parameters for Ni-Mo-Al catalyst derived from the regression model of 2^3 experimental DoE, with coefficients in Table 23, at t=±1: (a) $Y_{product}$ (Equation 2.9) at t=-1; (b) $Y_{product}$ (Equation 2.9) at t=1; (c) χ (Equation 2.10) at t=-1; (d) χ (Equation 2.10) at t=1; (e) Y_{diesel} (Equation 2.11) at t=-1; (f) Y_{diesel} (Equation 2.11) at t=1; (g) $S_{HDO/DCOx}$ (Equation 2.12) at t=-1; (e) $S_{HDO/DCOx}$ (Equation 2.12) at t=1.


Response Surface C8-C14
C8-C14
Cat.oil..wt.wt.
T...C.
t.h.=-1
1.8
1.6
1.4
1.2
1.0
0.8
0.6
0.4
0.2
0.0

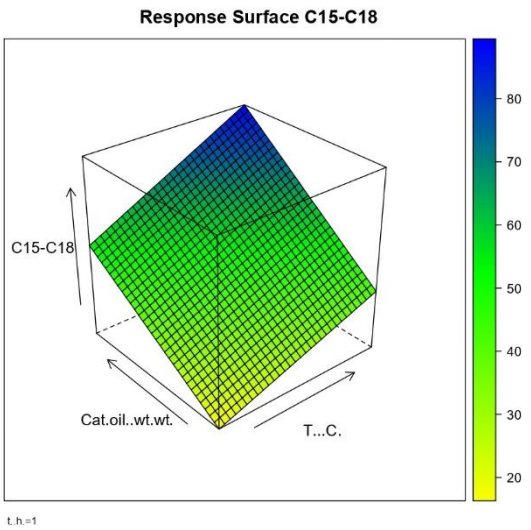
(**a**)


Response Surface C8-C14
C8-C14
Cat.oil..wt.wt.
T...C.
t.h.=1
3.0
2.5
2.0
1.5
1.0
0.5
0.0

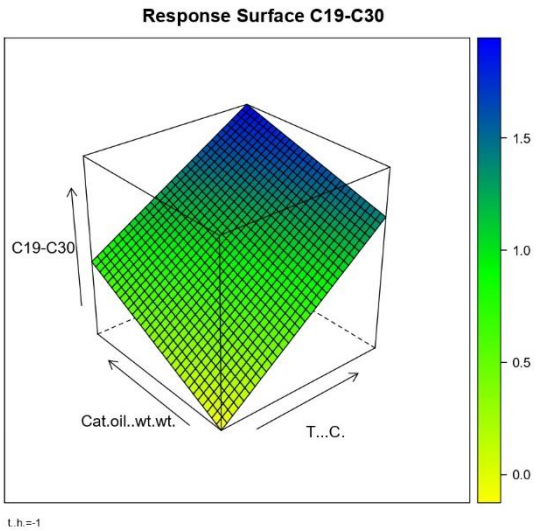
(**b**)


Response Surface C15-C18
C15-C18
Cat.oil..wt.wt.
T...C.
t.h.=-1
60
50
40
30
20

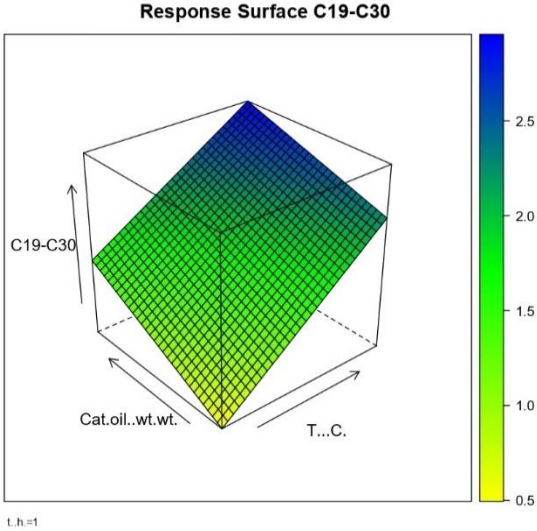
(**c**)


Response Surface C15-C18
C15-C18
Cat.oil..wt.wt.
T...C.
t.h.=1
80
70
60
50
40
30
20

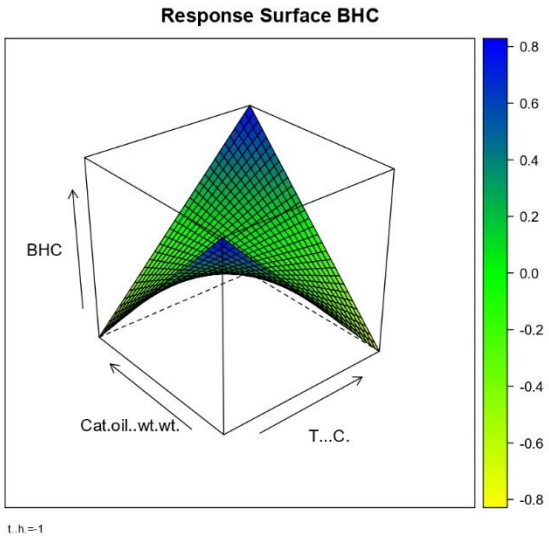
(**d**)


Response Surface C19-C30
C19-C30
Cat.oil..wt.wt.
T...C.
t.h.=-1
1.5
1.0
0.5
0.0

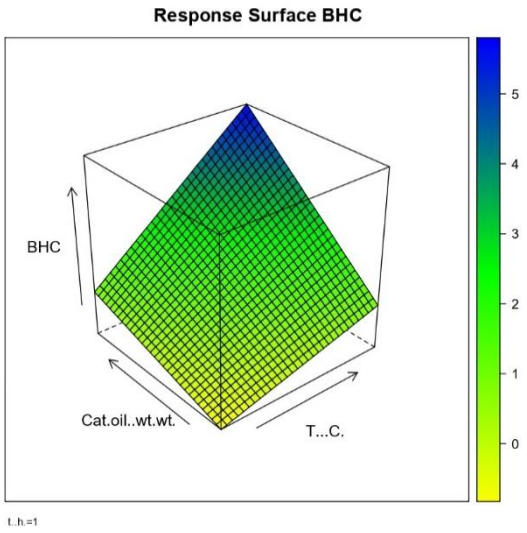
(**e**)


Response Surface C19-C30
C19-C30
Cat.oil..wt.wt.
T...C.
t.h.=1
2.5
2.0
1.5
1.0
0.5

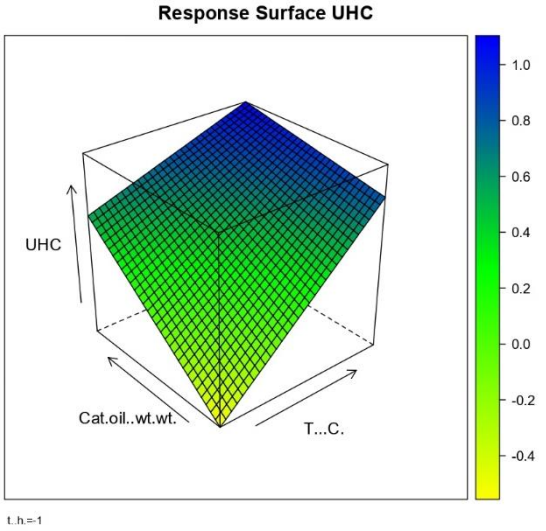
(**f**)


Response Surface BHC
BHC
Cat.oil..wt.wt.
T...C.
0.8
0.6
0.4
0.2
0.0
-0.2
-0.4
-0.6
-0.8
t..h.=-1

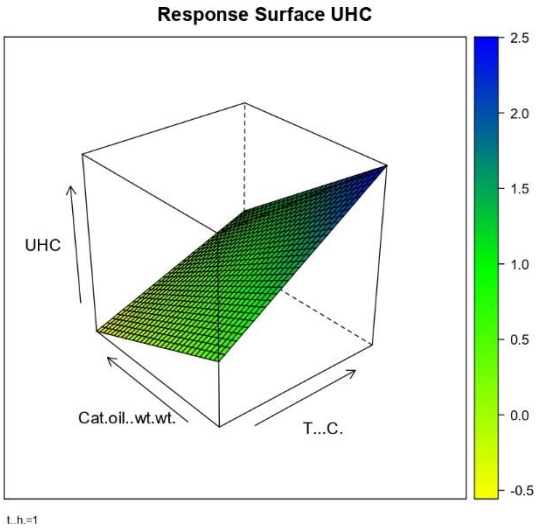
(g)


Response Surface BHC
BHC
Cat.oil..wt.wt.
T...C.
5
4
3
2
1
0
t..h.=1

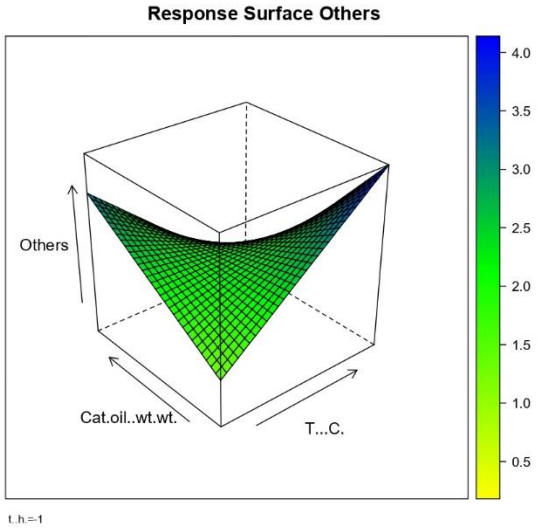
(h)


Response Surface UHC
UHC
Cat.oil..wt.wt.
T...C.
1.0
0.8
0.6
0.4
0.2
0.0
-0.2
-0.4
t..h.=-1

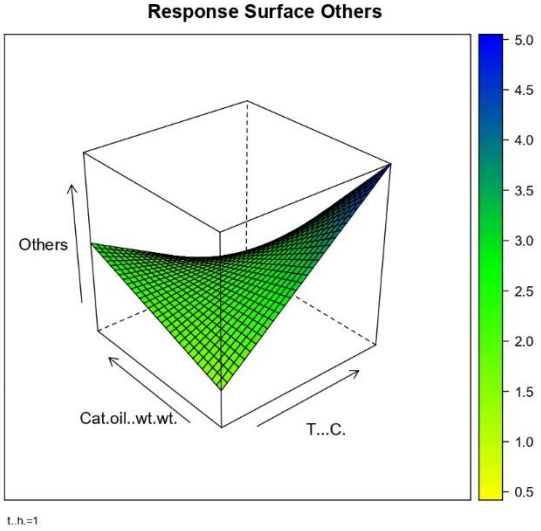
(i)


Response Surface UHC
UHC
Cat.oil..wt.wt.
T...C.
2.5
2.0
1.5
1.0
0.5
0.0
-0.5
t..h.=1

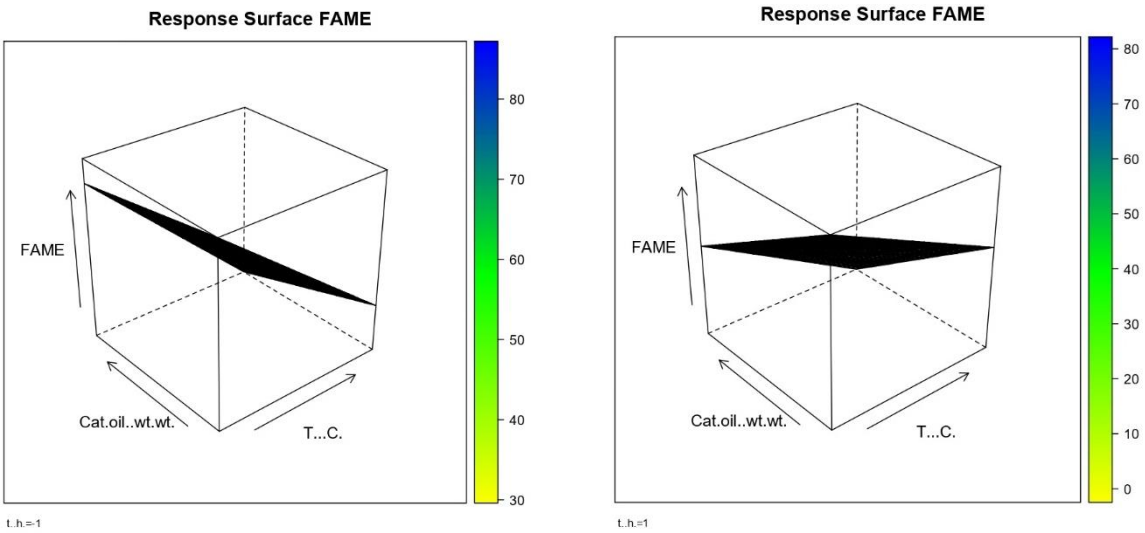
(l)


Response Surface Others
Others
Cat.oil..wt.wt.
T...C.
4.0
3.5
3.0
2.5
2.0
1.5
1.0
0.5
t..h.=-1

(m)

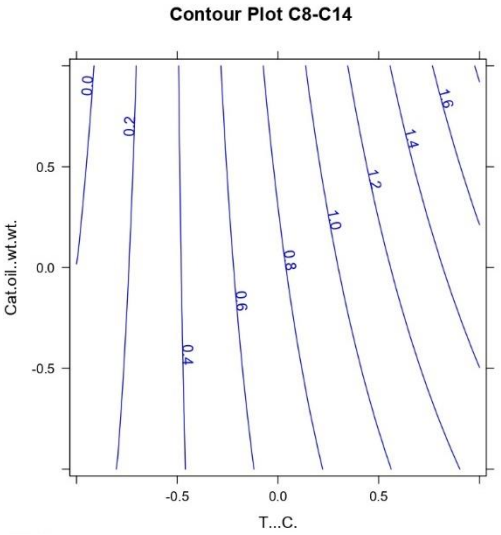

Response Surface Others
Others
Cat.oil..wt.wt.
T...C.
5.0
4.5
4.0
3.5
3.0
2.5
2.0
1.5
1.0
0.5
t..h.=1

(n)

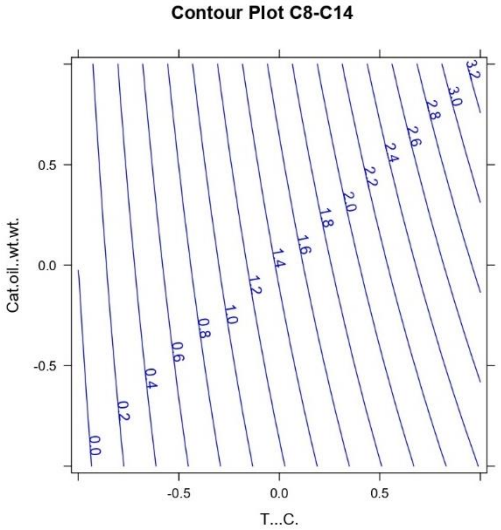


(**p**) (**q**)

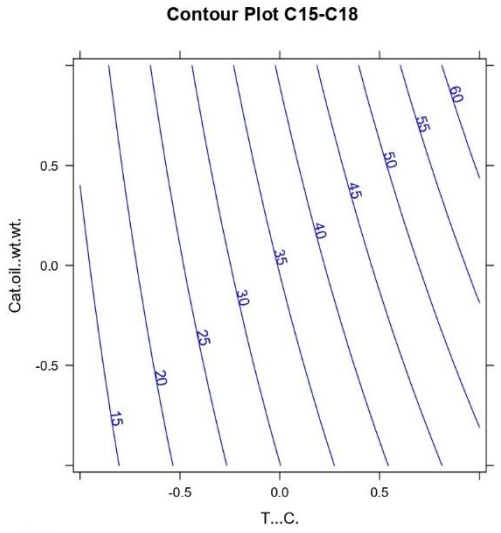
Figure D 11 Surface responses of DO product composition for Ni-Mo-Al catalyst derived from the regression model of 2^3 experimental DoE, with coefficients in Table 23, at t=±1: (a) $A\%_{Ci}$ (with $C_8 \leq i \leq C_{14}$) at t=-1; (b) $A\%_{Ci}$ (with $C_8 \leq i \leq C_{14}$) at t=1; (c) $A\%_{Ci}$ (with $C_{15} \leq i \leq C_{18}$) at t=-1; (d) $A\%_{Ci}$ (with $C_{15} \leq i \leq C_{18}$) at t=1; (e) $A\%_{Ci}$ (with $C_{19} \leq i \leq C_{30}$) at t=-1; (f) $A\%_{Ci}$ (with $C_{19} \leq i \leq C_{30}$) at t=1; (g) $A\%_{BHC}$ at t=-1; (h) $A\%_{BHC}$ at t=1; (i) $A\%_{UHC}$ at t=-1; (l) $A\%_{UHC}$ at t=1; (m) $A\%_{Others}$ at t=-1; (n) $A\%_{Others}$ at t=1; (p) $A\%_{FAME}$ at t=-1; (q) $A\%_{FAME}$ at t=1.


Contour Plot C8-C14
Cat.oil..wt.wt.
T...C.
0.0
0.2
0.4
0.6
0.8
1.0
1.2
1.4
1.6

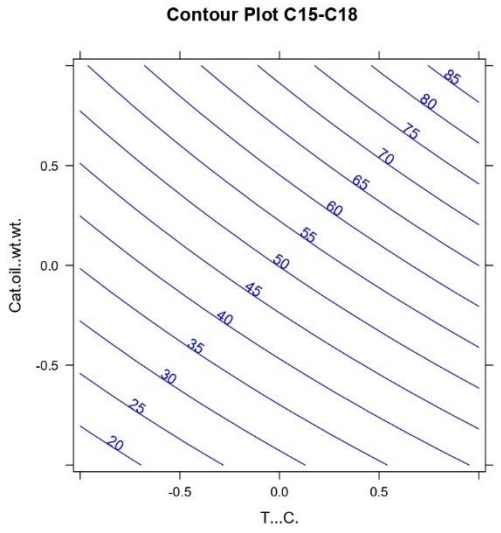
(**a**)


Contour Plot C8-C14
Cat.oil..wt.wt.
T...C.
0.0
0.2
0.4
0.6
0.8
1.0
1.2
1.4
1.6
1.8
2.0
2.2
2.4
2.6
2.8
3.0
3.2

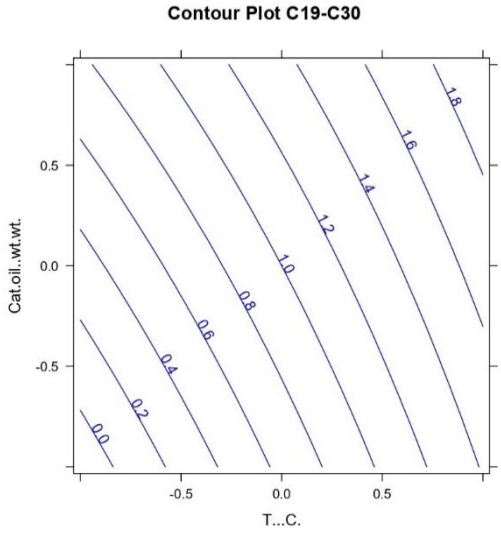
(**b**)


Contour Plot C15-C18
Cat.oil..wt.wt.
T...C.
15
20
25
30
35
40
45
50
55
60

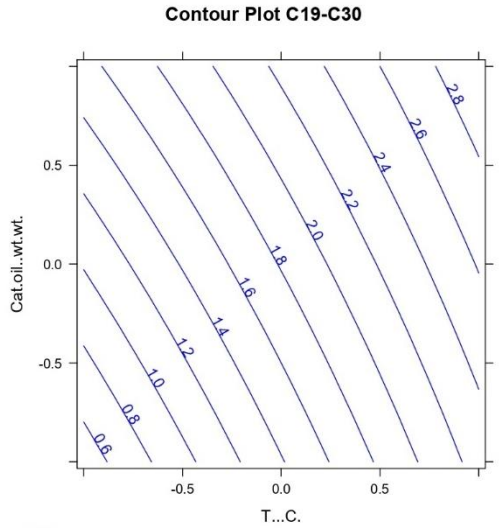
(**c**)


Contour Plot C15-C18
Cat.oil..wt.wt.
T...C.
20
25
30
35
40
45
50
55
60
65
70
75
80
85

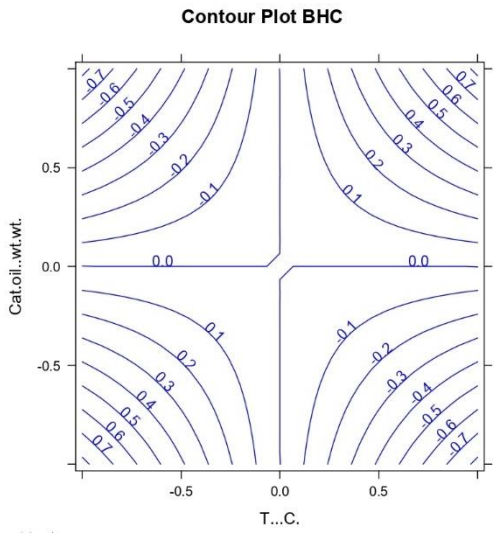
(**d**)


Contour Plot C19-C30
Cat.oil..wt.wt.
T...C.
0.0
0.2
0.4
0.6
0.8
1.0
1.2
1.4
1.6
1.8

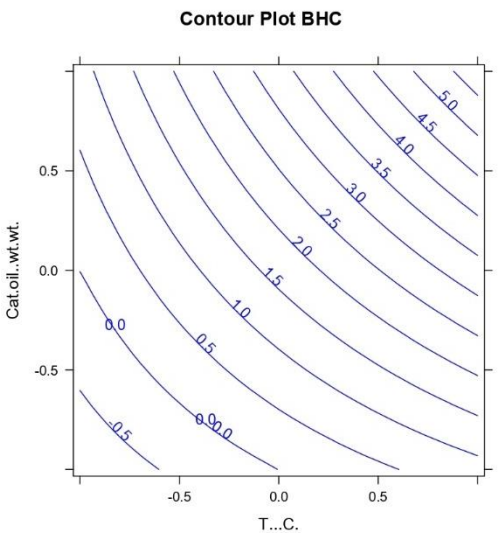
(**e**)


Contour Plot C19-C30
Cat.oil..wt.wt.
T...C.
0.6
0.8
1.0
1.2
1.4
1.6
1.8
2.0
2.2
2.4
2.6
2.8

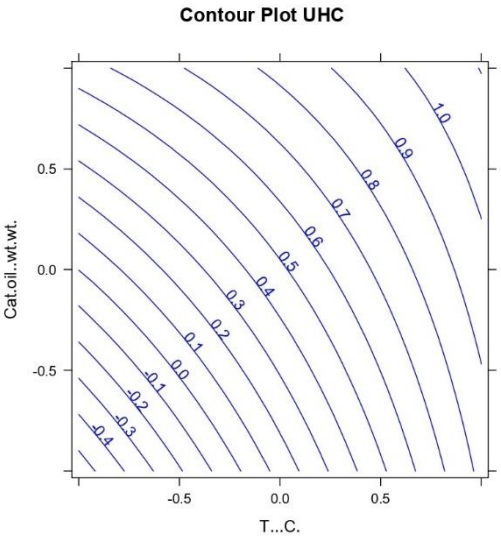
(**f**)


Contour Plot BHC
Cat.oil..wt.wt.
T...C.

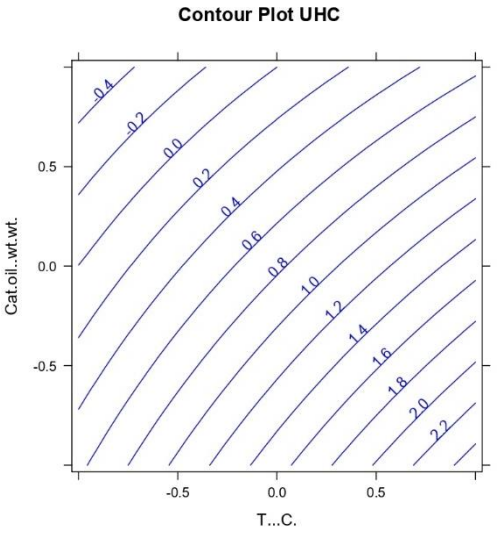
(g)


Contour Plot BHC
Cat.oil..wt.wt.
T...C.

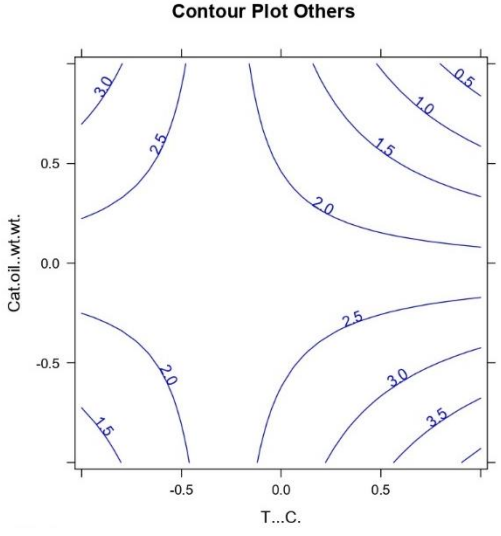
(h)


Contour Plot UHC
Cat.oil..wt.wt.
T...C.

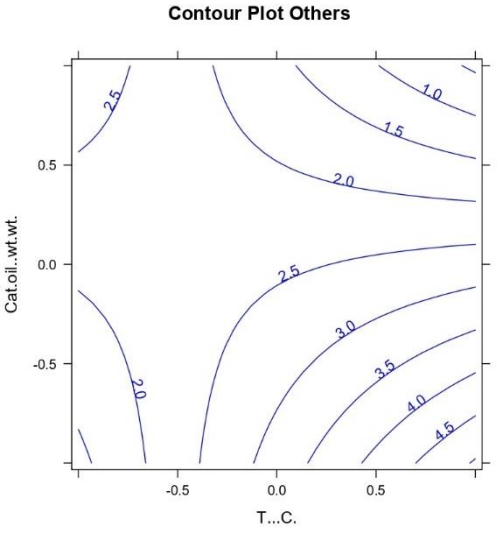
(i)


Contour Plot UHC
Cat.oil..wt.wt.
T...C.

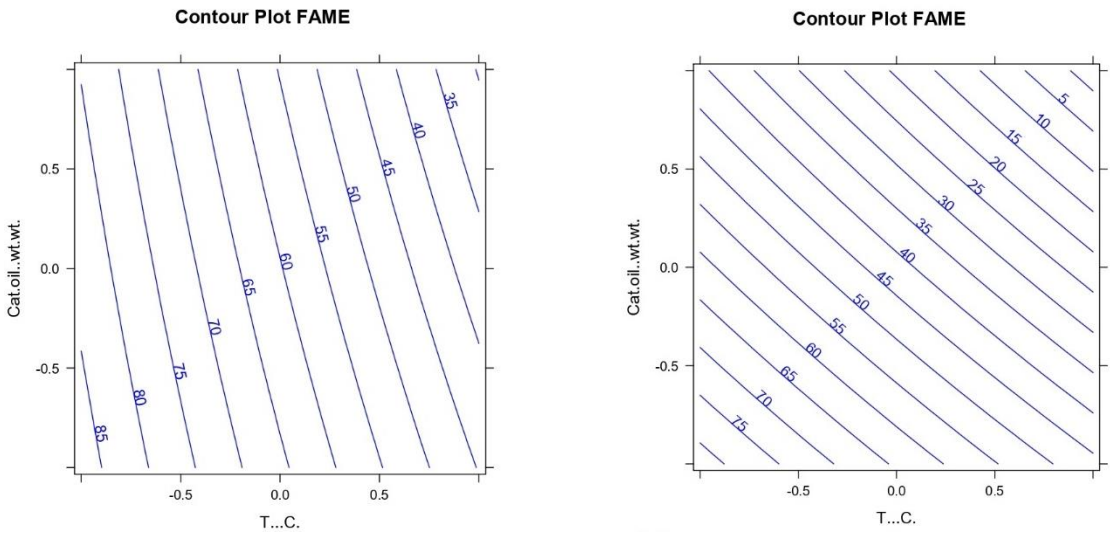
(l)


Contour Plot Others
Cat.oil..wt.wt.
T...C.

(m)

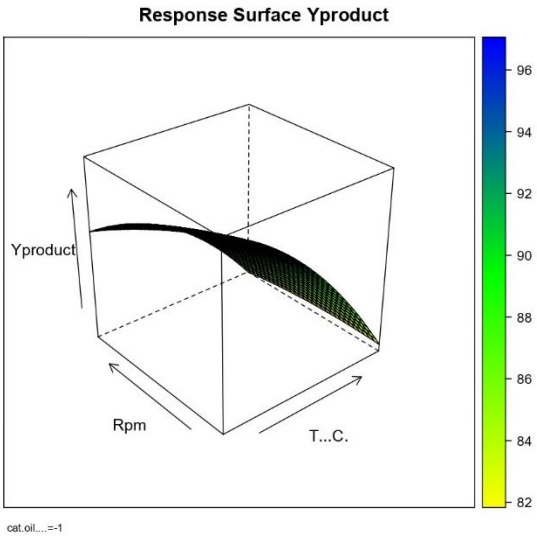

Contour Plot Others
Cat.oil..wt.wt.
T...C.

(n)

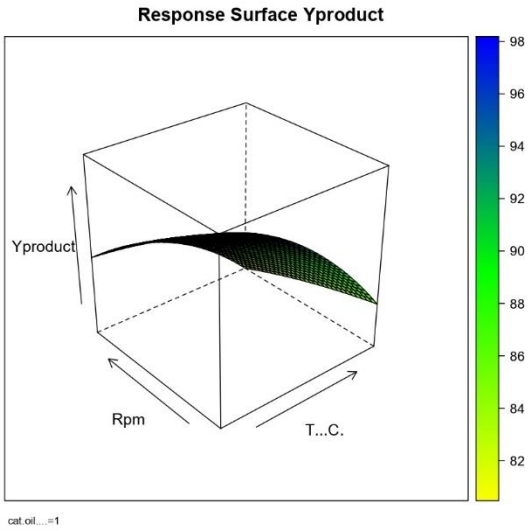


(**p**) (**q**)

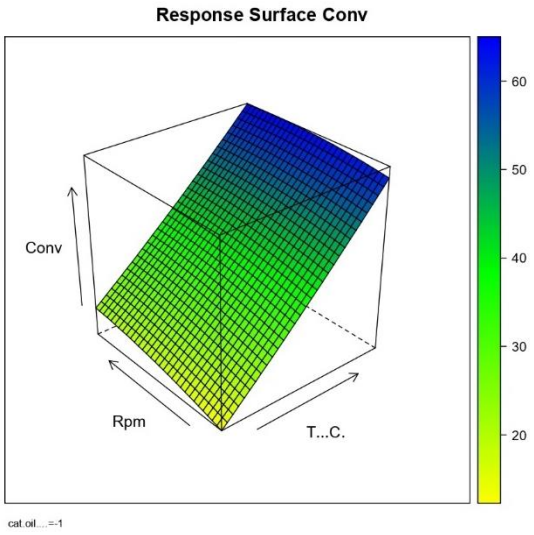
Figure D 12 Contour plots of DO product composition for Ni-Mo-Al catalyst derived from the regression model of 2^3 experimental DoE, with coefficients in Table 23, at t=±1: (a) $A\%_{Ci}$ (with $C_8 \leq i \leq C_{14}$) at t=-1; (b) $A\%_{Ci}$ (with $C_8 \leq i \leq C_{14}$) at t=1; (c) $A\%_{Ci}$ (with $C_{15} \leq i \leq C_{18}$) at t=-1; (d) $A\%_{Ci}$ (with $C_{15} \leq i \leq C_{18}$) at t=1; (e) $A\%_{Ci}$ (with $C_{19} \leq i \leq C_{30}$) at t=-1; (f) $A\%_{Ci}$ (with $C_{19} \leq i \leq C_{30}$) at t=1; (g) $A\%_{BHC}$ at t=-1; (h) $A\%_{BHC}$ at t=1; (i) $A\%_{UHC}$ at t=-1; (l) $A\%_{UHC}$ at t=1; (m) $A\%_{Others}$ at t=-1; (n) $A\%_{Others}$ at t=1; (p) $A\%_{FAME}$ at t=-1; (q) $A\%_{FAME}$ at t=1.


Response Surface Yproduct
Yproduct
Rpm
T...C.
96
94
92
90
88
86
84
82
cat.oil....=-1

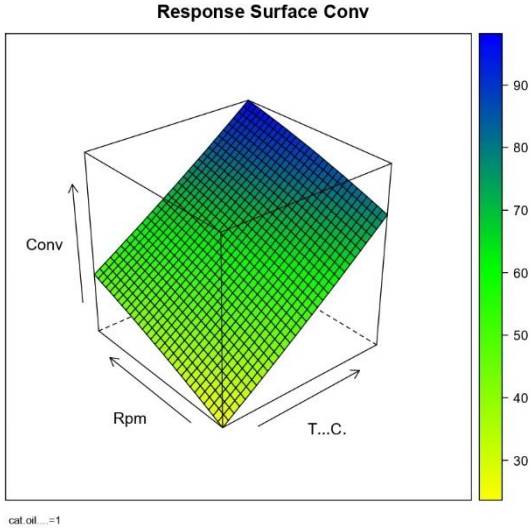
(**a**)


Response Surface Yproduct
Yproduct
Rpm
T...C.
98
96
94
92
90
88
86
84
82
cat.oil....=1

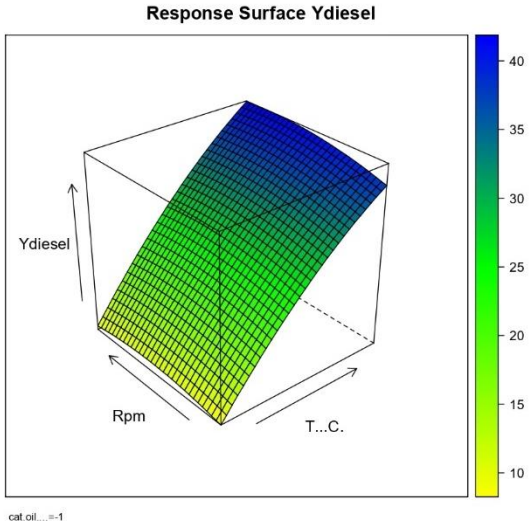
(**b**)


Response Surface Conv
Conv
Rpm
T...C.
60
50
40
30
20
cat.oil....=-1

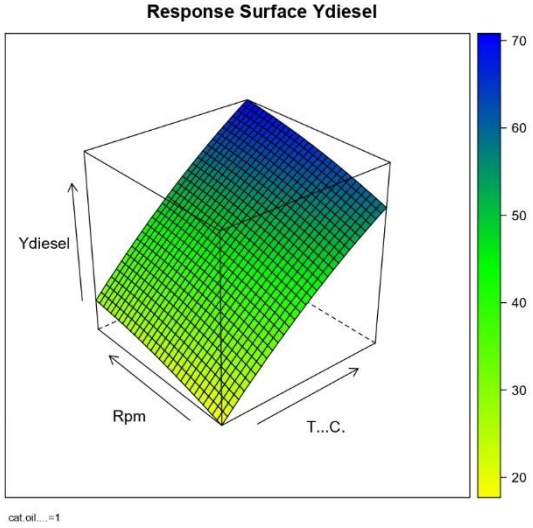
(**c**)


Response Surface Conv
Conv
Rpm
T...C.
90
80
70
60
50
40
30
cat.oil....=1

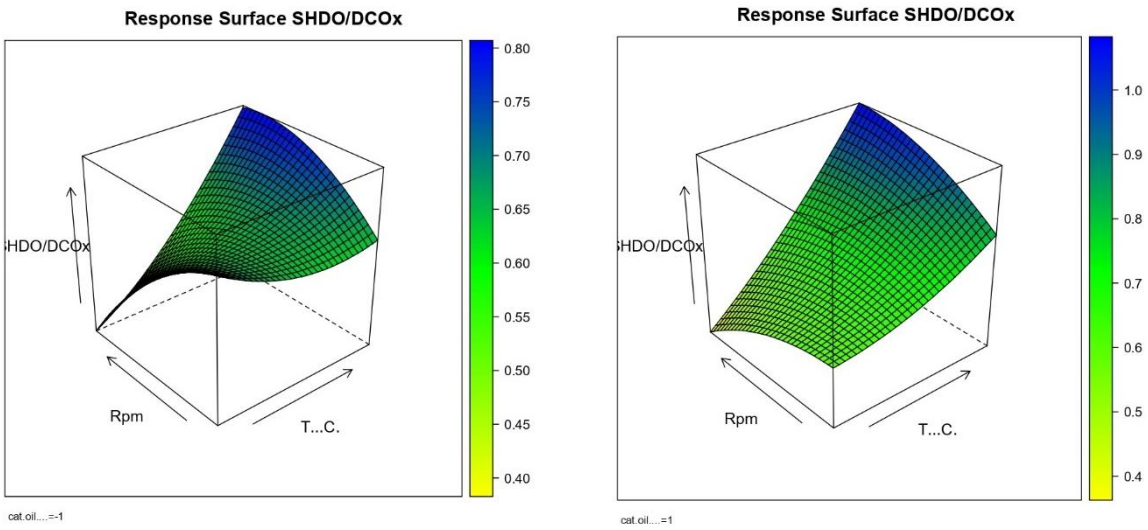
(**d**)


Response Surface Ydiesel
Ydiesel
Rpm
T...C.
40
35
30
25
20
15
10
cat.oil....=-1

(**e**)

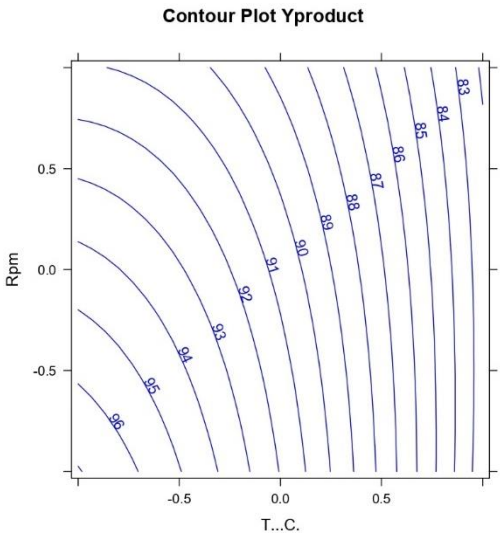

Response Surface Ydiesel
Ydiesel
Rpm
T...C.
70
60
50
40
30
20
cat.oil....=1

(**f**)

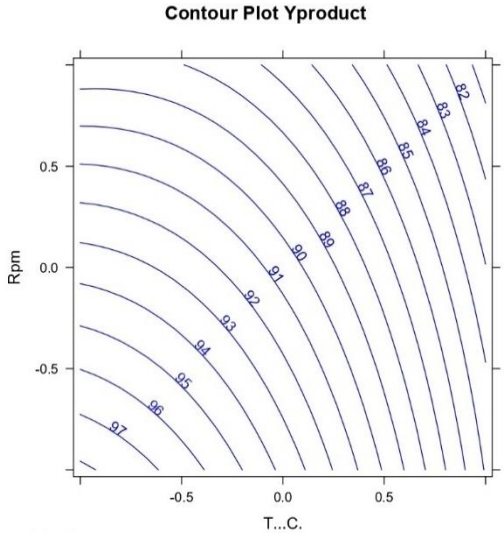


(**g**) (**h**)

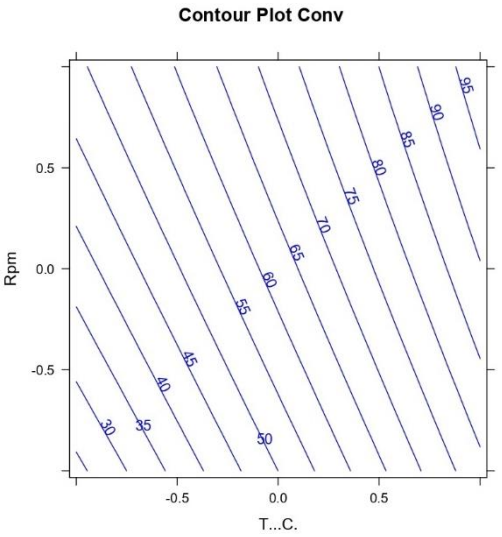
Figure D 13 Surface responses of DO process parameters for Ni-Mo-Al catalyst derived from the regression model of FCCCD, with coefficients in Table 26, at $\Upsilon=\pm1$: (a) $Y_{product}$ (Equation 2.9) at $\Upsilon=-1$; (b) $Y_{product}$ (Equation 2.9) at $\Upsilon=1$; (c) χ (Equation 2.10) at $\Upsilon=-1$; (d) χ (Equation 2.10) at $\Upsilon=1$; (e) Y_{diesel} (Equation 2.11) at $\Upsilon=-1$; (f) Y_{diesel} (Equation 2.11) at $\Upsilon=1$; (g) $S_{HDO/DCOx}$ (Equation 2.12) at $\Upsilon=-1$; (e) $S_{HDO/DCOx}$ (Equation 2.12) at $\Upsilon=1$.


Contour Plot Yproduct
Rpm
T...C.
-0.5
0.0
0.5
83
84
85
86
87
88
89
90
91
92
93
94
95
96

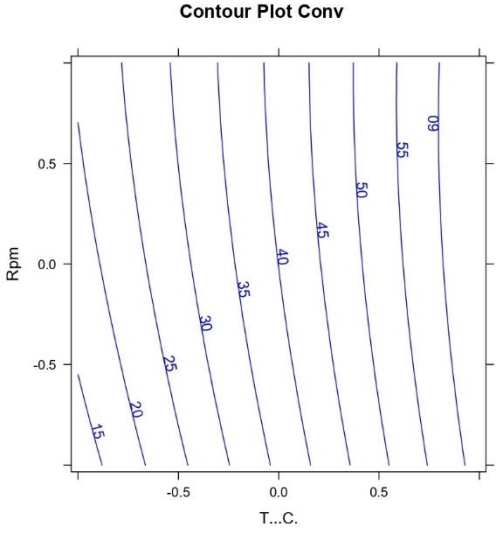
(**a**)


Contour Plot Yproduct
Rpm
T...C.
-0.5
0.0
0.5
82
83
84
85
86
87
88
89
90
91
92
93
94
95
96
97

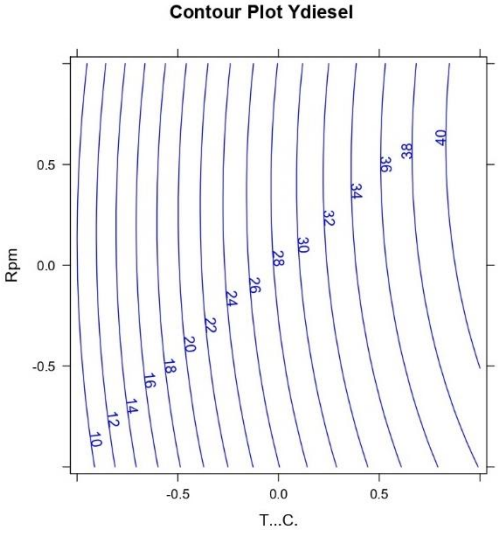
(**b**)


Contour Plot Conv
Rpm
T...C.
-0.5
0.0
0.5
30
35
40
45
50
55
60
65
70
75
80
85
90
95

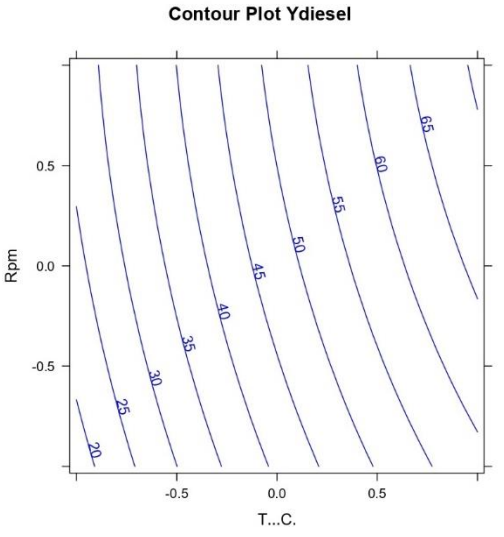
(**c**)


Contour Plot Conv
Rpm
T...C.
-0.5
0.0
0.5
15
20
25
30
35
40
45
50
55
60

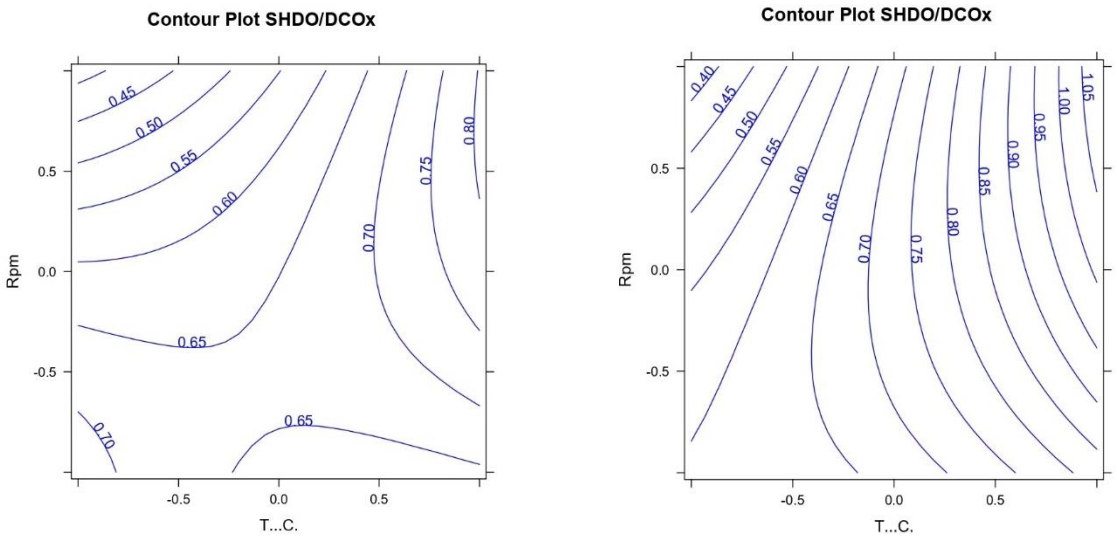
(**d**)


Contour Plot Ydiesel
Rpm
T...C.
-0.5
0.0
0.5
10
12
14
16
18
20
22
24
26
28
30
32
34
36
38
40

(**e**)

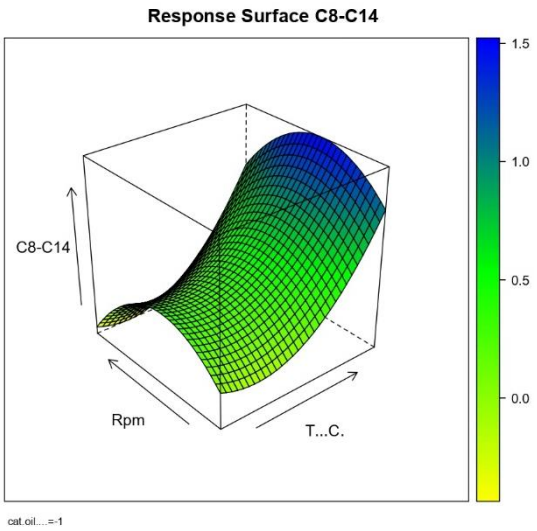

Contour Plot Ydiesel
Rpm
T...C.
-0.5
0.0
0.5
20
25
30
35
40
45
50
55
60
65

(**f**)

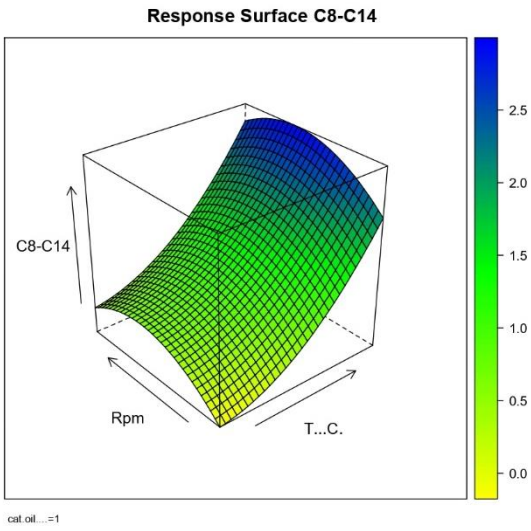


(**g**) (**h**)

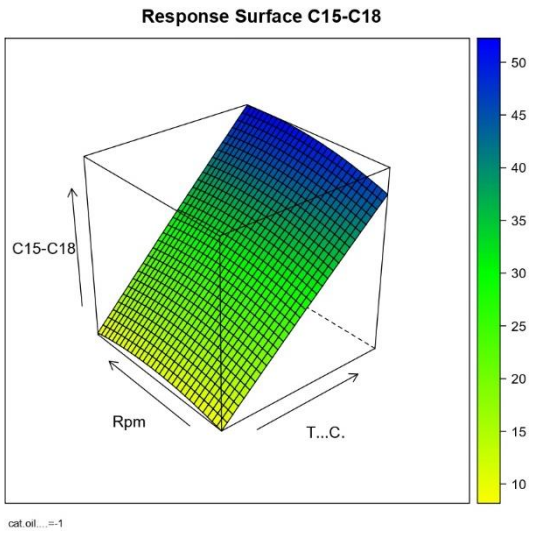
Figure D 14 Contour plots of DO process parameters for Ni-Mo-Al catalyst derived from the regression model of FCCCD, with coefficients in Table 26, at $\Upsilon=\pm1$: (a) $Y_{product}$ (Equation 2.9) at $\Upsilon=-1$; (b) $Y_{product}$ (Equation 2.9) at $\Upsilon=1$; (c) χ (Equation 2.10) at $\Upsilon=-1$; (d) χ (Equation 2.10) at $\Upsilon=1$; (e) Y_{diesel} (Equation 2.11) at $\Upsilon=-1$; (f) Y_{diesel} (Equation 2.11) at $\Upsilon=1$; (g) $S_{HDO/DCOx}$ (Equation 2.12) at $\Upsilon=-1$; (e) $S_{HDO/DCOx}$ (Equation 2.12) at $\Upsilon=1$.


Response Surface C8-C14
C8-C14
Rpm
T...C.
1.5
1.0
0.5
0.0
cat.oil....=-1

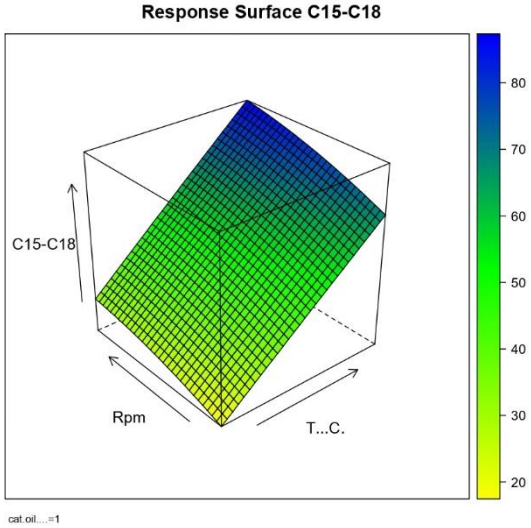
(**a**)


Response Surface C8-C14
C8-C14
Rpm
T...C.
2.5
2.0
1.5
1.0
0.5
0.0
cat.oil....=1

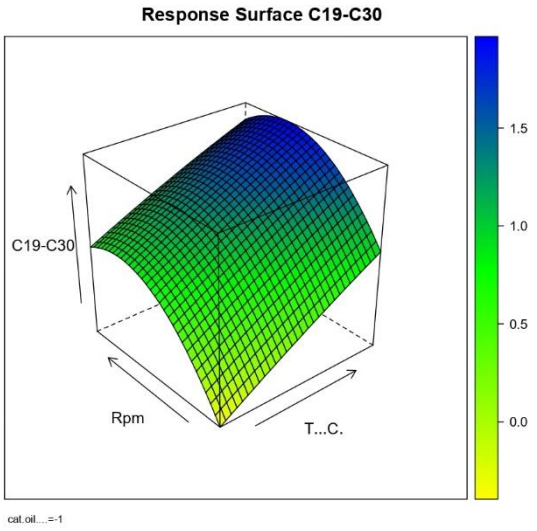
(**b**)


Response Surface C15-C18
C15-C18
Rpm
T...C.
50
45
40
35
30
25
20
15
10
cat.oil....=-1

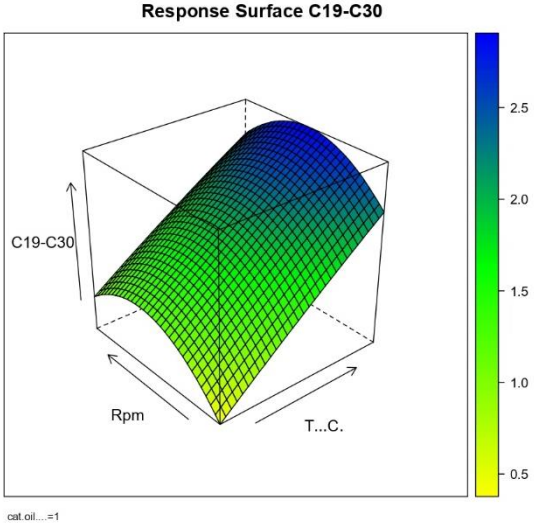
(**c**)


Response Surface C15-C18
C15-C18
Rpm
T...C.
80
70
60
50
40
30
20
cat.oil....=1

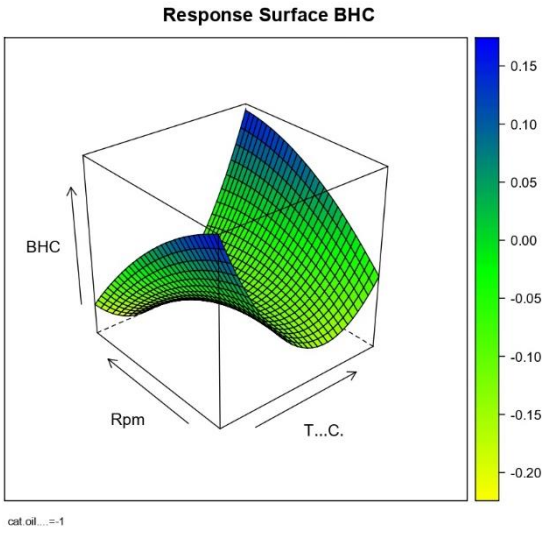
(**d**)


Response Surface C19-C30
C19-C30
Rpm
T...C.
1.5
1.0
0.5
0.0
cat.oil....=-1

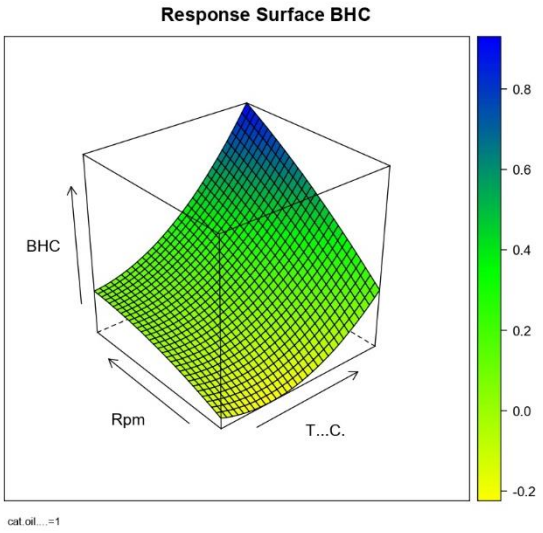
(**e**)


Response Surface C19-C30
C19-C30
Rpm
T...C.
2.5
2.0
1.5
1.0
0.5
cat.oil....=1

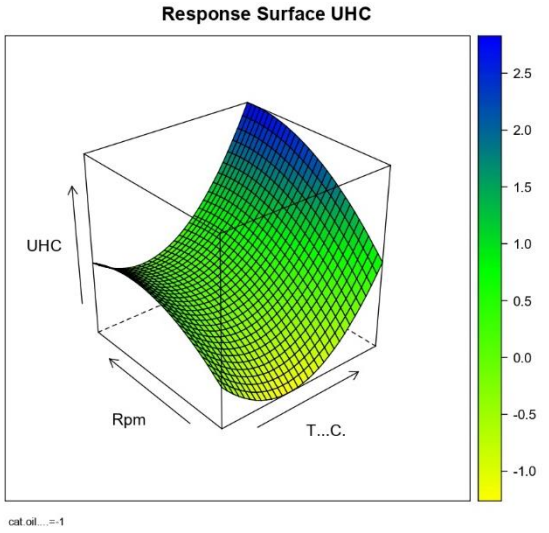
(**f**)


Response Surface BHC
BHC
Rpm
T...C.
0.15
0.10
0.05
0.00
-0.05
-0.10
-0.15
-0.20
cat.oil....=-1

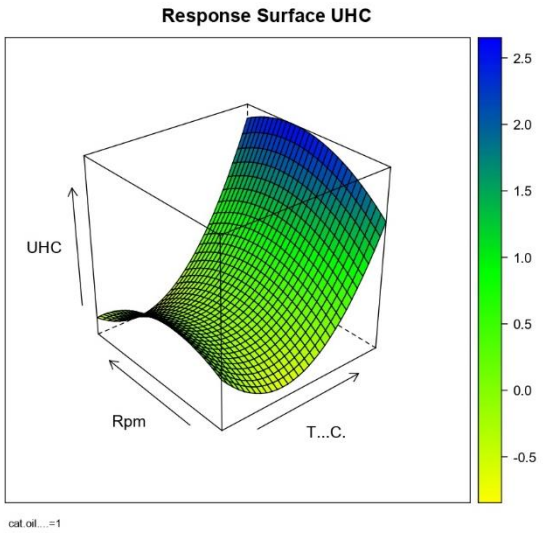
(**g**)


Response Surface BHC
BHC
Rpm
T...C.
0.8
0.6
0.4
0.2
0.0
-0.2
cat.oil....=1

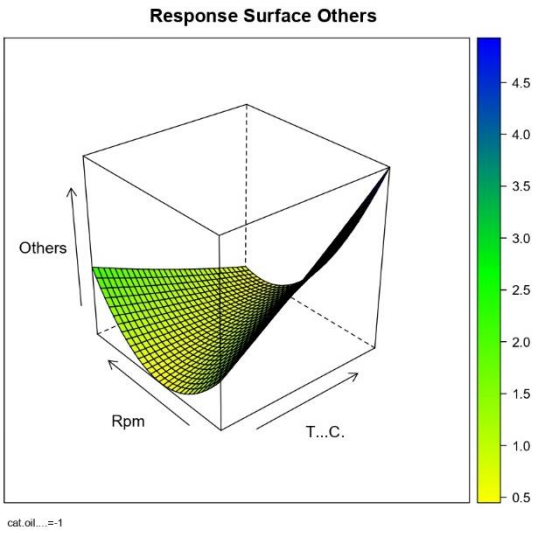
(**h**)


Response Surface UHC
UHC
Rpm
T...C.
2.5
2.0
1.5
1.0
0.5
0.0
-0.5
-1.0
cat.oil....=-1

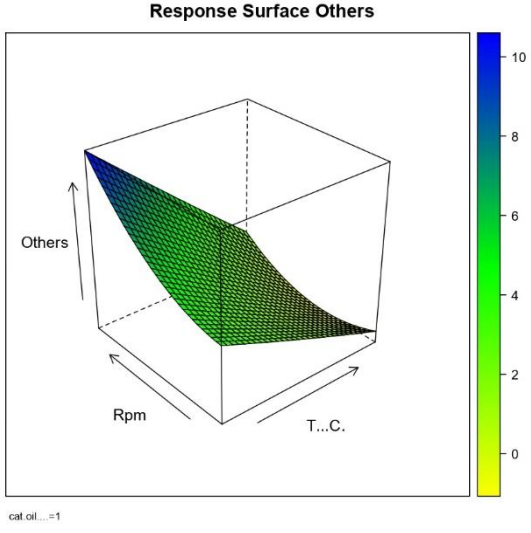
(**i**)


Response Surface UHC
UHC
Rpm
T...C.
2.5
2.0
1.5
1.0
0.5
0.0
-0.5
cat.oil....=1

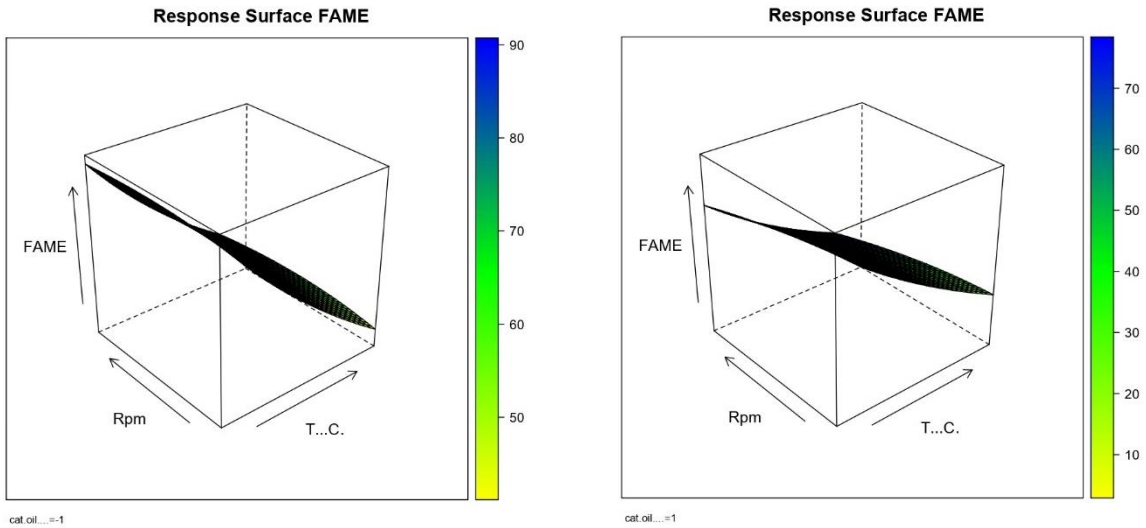
(**l**)


Response Surface Others
Others
Rpm
T...C.
4.5
4.0
3.5
3.0
2.5
2.0
1.5
1.0
0.5
cat.oil....=-1

(**m**)

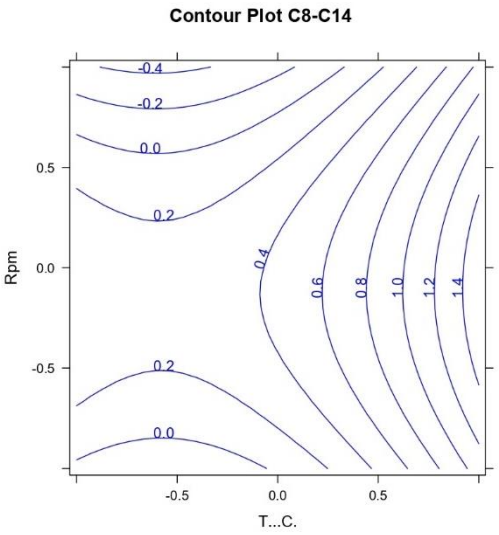

Response Surface Others
Others
Rpm
T...C.
10
8
6
4
2
0
cat.oil....=1

(**n**)

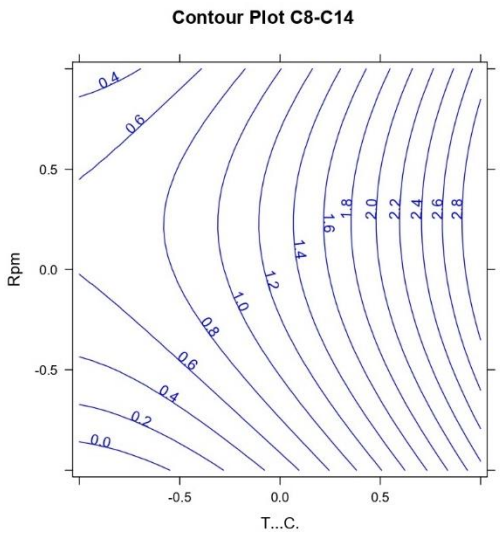


(**p**) (**q**)

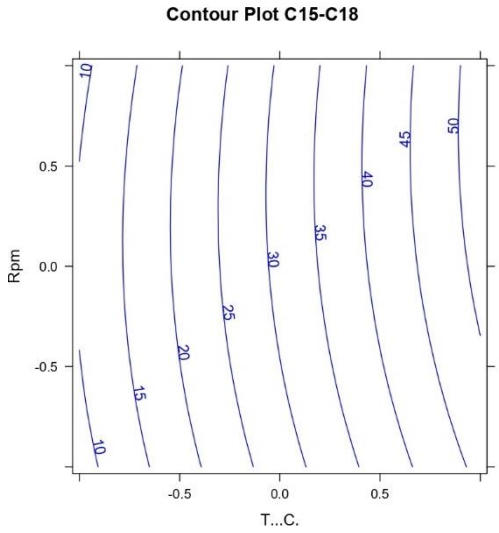
Figure D 15 Response surfaces of DO product composition for Ni-Mo-Al catalyst derived from the regression model of FCCCD, with coefficients in Table 26, at $\Upsilon=\pm1$: (a) $A\%_{Ci}$ (with $C_8 \leq i \leq C_{14}$) at $\Upsilon=-1$; (b) $A\%_{Ci}$ (with $C_8 \leq i \leq C_{14}$) at $\Upsilon=1$; (c) $A\%_{Ci}$ (with $C_{15} \leq i \leq C_{18}$) at $\Upsilon=-1$; (d) $A\%_{Ci}$ (with $C_{15} \leq i \leq C_{18}$) at $\Upsilon=1$; (e) $A\%_{Ci}$ (with $C_{19} \leq i \leq C_{30}$) at $\Upsilon=-1$; (f) $A\%_{Ci}$ (with $C_{19} \leq i \leq C_{30}$) at $\Upsilon=1$; (g) $A\%_{BHC}$ at $\Upsilon=-1$; (h) $A\%_{BHC}$ at $\Upsilon=1$; (i) $A\%_{UHC}$ at $\Upsilon=-1$; (l) $A\%_{UHC}$ at $\Upsilon=1$; (m) $A\%_{Others}$ at $\Upsilon=-1$; (n) $A\%_{Others}$ at $\Upsilon=1$; (p) $A\%_{FAME}$ at $\Upsilon=-1$; (q) $A\%_{FAME}$ at $\Upsilon=1$.


Contour Plot C8-C14
Rpm
T...C.

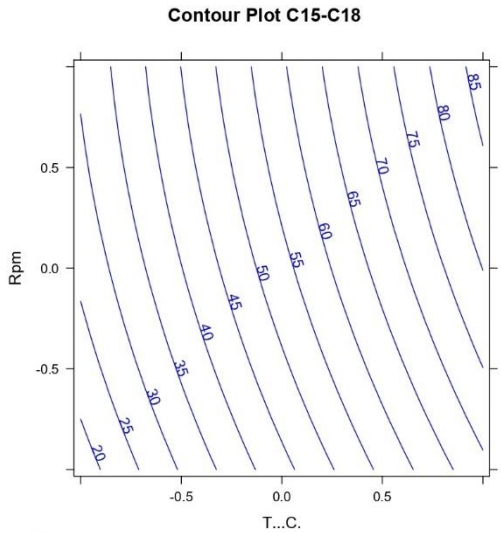
(**a**)


Contour Plot C8-C14
Rpm
T...C.

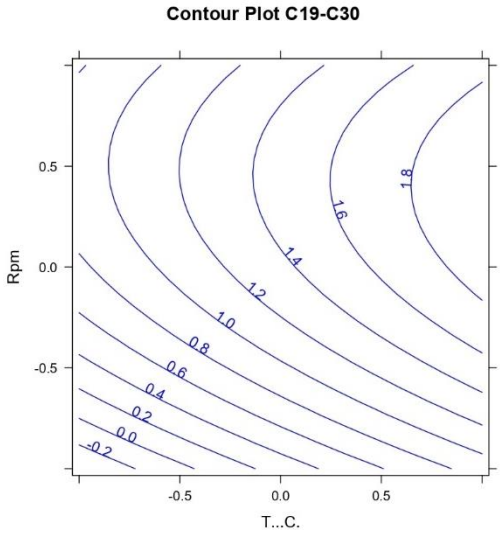
(**b**)


Contour Plot C15-C18
Rpm
T...C.

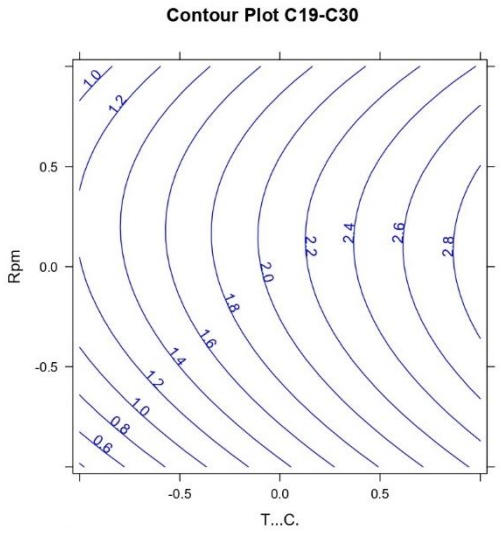
(**c**)


Contour Plot C15-C18
Rpm
T...C.

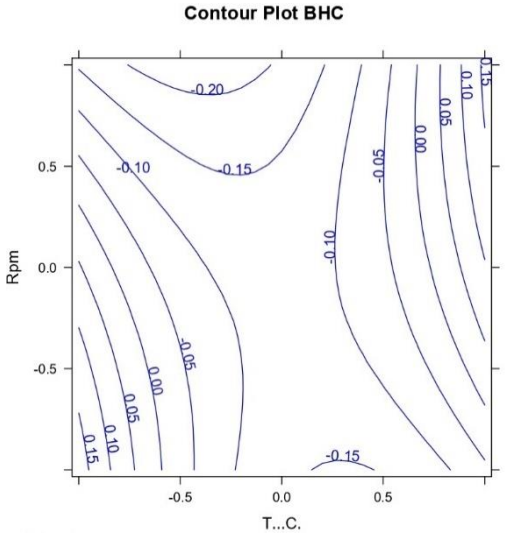
(**d**)


Contour Plot C19-C30
Rpm
T...C.

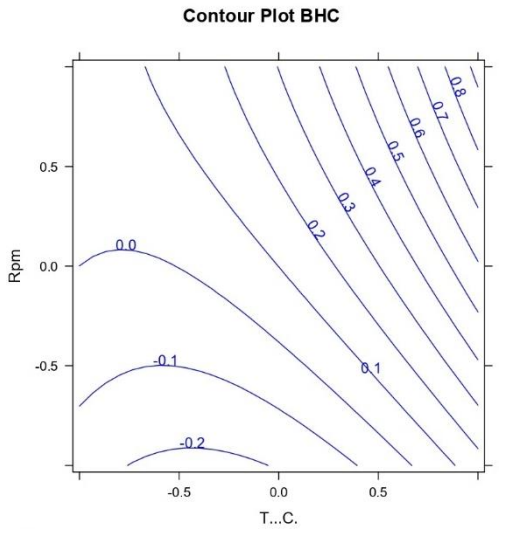
(**e**)


Contour Plot C19-C30
Rpm
T...C.

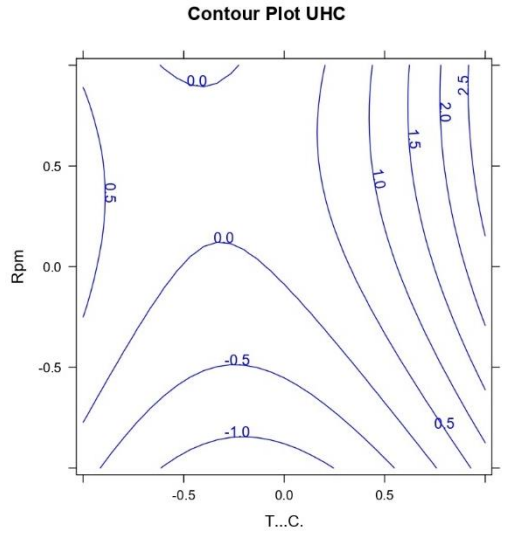
(**f**)


Contour Plot BHC
Rpm
T...C.

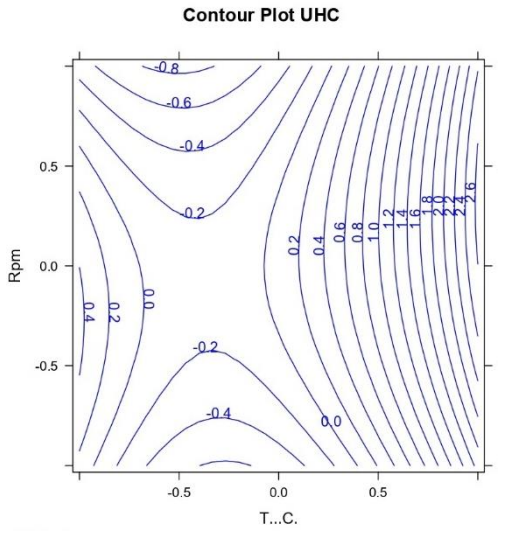
(g)


Contour Plot BHC
Rpm
T...C.

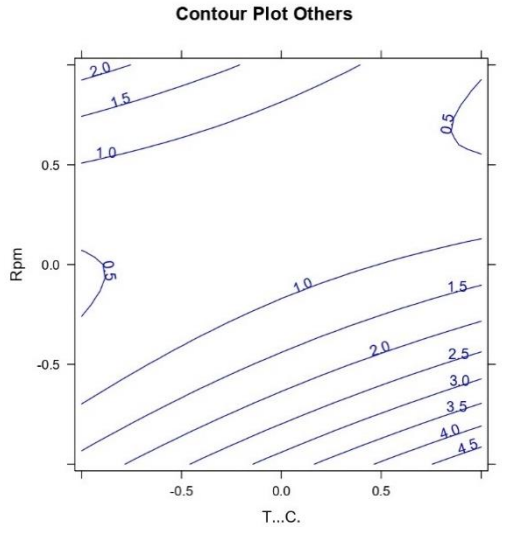
(h)


Contour Plot UHC
Rpm
T...C.

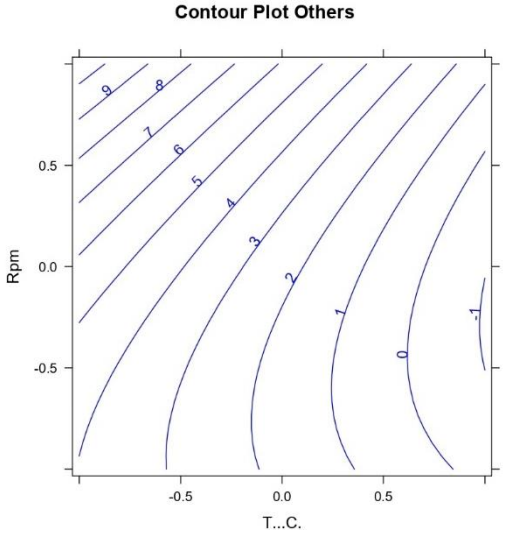
(i)


Contour Plot UHC
Rpm
T...C.

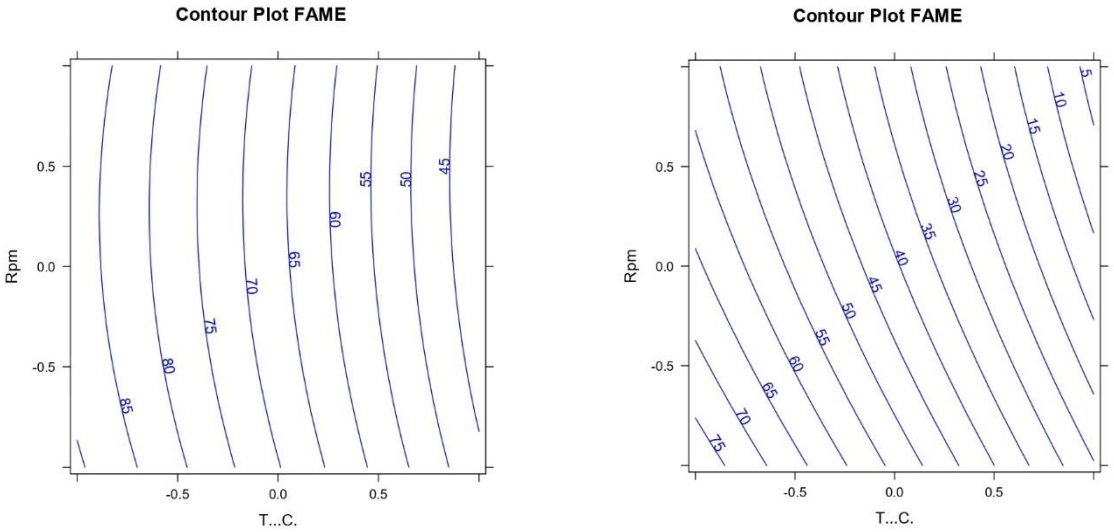
(l)


Contour Plot Others
Rpm
T...C.

(m)


Contour Plot Others
Rpm
T...C.

(n)



(**p**) (**q**)

Figure D 16 Contour plots of DO product composition for Ni-Mo-Al catalyst derived from the regression model of FCCCD, with coefficients in Table 26, at $\Upsilon=\pm1$: (a) $A\%_{Ci}$ (with $C_8 \leq i \leq C_{14}$) at $\Upsilon=-1$; (b) $A\%_{Ci}$ (with $C_8 \leq i \leq C_{14}$) at $\Upsilon=1$; (c) $A\%_{Ci}$ (with $C_{15} \leq i \leq C_{18}$) at $\Upsilon=-1$; (d) $A\%_{Ci}$ (with $C_{15} \leq i \leq C_{18}$) at $\Upsilon=1$; (e) $A\%_{Ci}$ (with $C_{19} \leq i \leq C_{30}$) at $\Upsilon=-1$; (f) $A\%_{Ci}$ (with $C_{19} \leq i \leq C_{30}$) at $\Upsilon=1$; (g) $A\%_{BHC}$ at $\Upsilon=-1$; (h) $A\%_{BHC}$ at $\Upsilon=1$; (i) $A\%_{UHC}$ at $\Upsilon=-1$; (l) $A\%_{UHC}$ at $\Upsilon=1$; (m) $A\%_{Others}$ at $\Upsilon=-1$; (n) $A\%_{Others}$ at $\Upsilon=1$; (p) $A\%_{FAME}$ at $\Upsilon=-1$; (q) $A\%_{FAME}$ at $\Upsilon=1$.

BIBLIOGRAPHY

1. Afifa, et al., *Air pollution and climate change as grand challenges to sustainability.* Science of the Total Environment, 2024. **928**.
2. Lu, C.W. and K. Wang, *Natural resource conservation outpaces and climate change: Roles of reforestation, mineral extraction, and natural resources depletion.* Resources Policy, 2023. **86**.
3. Shah, I.H., et al., *Comprehensive review: Effects of climate change and greenhouse gases emission relevance to environmental stress on horticultural crops and management.* Journal of Environmental Management, 2024. **351**.
4. Chidiogo Uzoamaka, A., et al., *Legislative Responses to Climate Change: A Global Review of Policies and Their Effectiveness.* International Journal of Applied Research in Social Sciences, 2024. **6**(3): p. 225-239.
5. Pörtner, H.O., Scholes, R. J., Agard, J., Archer, E., Arneth, A., Bai, X., ... & Ngo, *IPBES-IPCC Co-Sponsored Workshop Report on Biodiversity and Climate Change.* 2021.
6. Organization, W.H. *World Health Organization-Climate change*. 2023 [cited 2024 07-22]; Available from: https://www.who.int/health-topics/climate-change#tab=tab_1.
7. Hannah Ritchie, P.R.a.V.S. *Climate Change-How are global temperatures changing, and what are the impacts on sea level rise, sea ice, and ice sheets?* 2024 [cited 2024 07-22]; Available from: https://ourworldindata.org/climate-change#research-writing.
8. NASA. *Global Temperature*. 2024; Available from: https://climate.nasa.gov/vital-signs/global-temperature/?intent=121.
9. *Do scientists agree on climate change?* [cited 2024 09-16]; Available from: https://science.nasa.gov/climate-change/faq/do-scientists-agree-on-climate-change/.
10. Schwartz, S.E., *The whitehouse effect—Shortwave radiative forcing of climate by anthropogenic aerosols: an overview.* Journal of Aerosol Science, 1996. **27**(3): p. 359-382.

11. Filonchyk, M., et al., *Greenhouse gases emissions and global climate change: Examining the influence of CO2, CH4, and N2O.* Science of The Total Environment, 2024. **935**: p. 173359.
12. Berger, A. and C. Tricot, *The greenhouse effect.* Surveys in geophysics, 1992. **13**(6): p. 523-549.
13. Houghton, J., *Global warming: the complete briefing*. 2009: Cambridge university press.
14. Schmidt, G.A., et al., *Attribution of the present‐day total greenhouse effect.* Journal of Geophysical Research: Atmospheres, 2010. **115**(D20).
15. Hannah Ritchie, P.R.a.M.R. *Greenhouse gas emissions*. 2024 [cited 2024 07-22]; Available from: https://ourworldindata.org/greenhouse-gas-emissions.
16. Friedlingstein, P., et al., *Global Carbon Budget 2022.* Earth System Science Data, 2022. **14**(11): p. 4811-4900.
17. *What is the Kyoto Protocol?* [cited 2023 15/09]; Available from: https://unfccc.int/kyoto_protocol.
18. *The Paris Agreement*. Available from: https://unfccc.int/process-and-meetings/the-paris-agreement.
19. *UN Climate Change Conference - United Arab Emirates*. 2023 [cited 2024 07-22]; Available from: https://unfccc.int/cop28.
20. *The European Green Deal*. [cited 2024 07-22]; Available from: https://commission.europa.eu/strategy-and-policy/priorities-2019-2024/european-green-deal_en.
21. *European Climate Pact*. [cited 2024 07-22]; Available from: https://climate-pact.europa.eu/about_en.
22. Yang, F., X. Yang, and X. Li, *China's diverse energy transition pathways toward carbon neutrality by 2060.* Sustainable Production and Consumption, 2024. **47**: p. 236-250.
23. Joshi, A.K. and C. Negi, *Instruments for Addressing Climate Change in Renewable Energy Policy of India: A Review of Developments in Policy Research.* Journal of The Institution of Engineers (India): Series C, 2024. **105**(1): p. 233-240.
24. *President Biden's Historic Climate Agenda*. [cited 2024 09-17]; Available from: https://www.whitehouse.gov/climate/.
25. *London Environment Strategy*. 2018 [cited 2024 07-22]; Available from: https://www.london.gov.uk/sites/default/files/london_environment_strategy_0.pdf.
26. *Climate Mobilization Act*. 2019 [cited 2024 07-22]; Available from: https://council.nyc.gov/data/green/.
27. *Climate Change Mitigation Strategy*. 2020 [cited 2024 07-22]; Available from: https://www.melbourne.vic.gov.au/about-council/vision-goals/eco-city/Pages/climate-change-mitigation-strategy.aspx.
28. *Climate and Energy Strategy for Oslo*. 2020 [cited 2024 07-22]; Available from: https://gbcitalia.org/wp-content/uploads/attachments/Climate-and-Energy-Strategy-2016-English.pdf.

29. *One Less Nuclear Power Plant*. 2011 [cited 2024 07-22]; Available from: https://english.seoul.go.kr/wp-content/uploads/2016/08/Seoul-Sustainable-Energy-Action-Plan_report.pdf.
30. *CO_2 and Greenhouse Gas Emissions*. [cited 2024 07-22]; Available from: https://ourworldindata.org/co2-and-greenhouse-gas-emissions?insight=current-climate-policies-will-reduce-emissions-but-not-enough-to-keep-temperature-rise-below-2c#key-insights.
31. *Current World Population*. 2024 [cited 2024 07-23]; Available from: https://www.worldometers.info/world-population/#:~:text=World%20Population%20Clock%3A%208.1%20Billion,(LIVE%2C%202024)%20%2D%20Worldometer.
32. *Population, total*. 2024 [cited 2024 07-23]; Available from: https://data.worldbank.org/indicator/SP.POP.TOTL.
33. *Total energy consumption*. 2024 [cited 2024 07-23]; Available from: https://yearbook.enerdata.net/total-energy/world-consumption-statistics.html.
34. *Energy Mix*. 2023 [cited 2024 07-23]; Available from: https://ourworldindata.org/energy-mix.
35. Lucantonio, S., et al., *Green Diesel Production via Deoxygenation Process: A Review*. Energies, 2023. **16**(2).
36. 2018 [cited 2024 07-23]; Available from: https://eur-lex.europa.eu/legal-content/EN/TXT/?uri=CELEX%3A32018L2001.
37. *Sources of Greenhouse Gas Emissions*. [cited 2024 07-23]; Available from: https://www.epa.gov/ghgemissions/sources-greenhouse-gas-emissions.
38. *European overview of GHG emissions*. [cited 2024 07-23]; Available from: https://www.statistiques.developpement-durable.gouv.fr/edition-numerique/chiffres-cles-du-climat-2023/en/7-european-overview-of-ghg-emissions#:~:text=In%20the%20European%20Union%2C%20energy,2%25).
39. *Breakdown of carbon dioxide, methane and nitrous oxide emissions by sector*. 2024 [cited 2024 07-23]; Available from: https://ourworldindata.org/emissions-by-sector.
40. Mulvihill, M.J., et al., *Green chemistry and green engineering: a framework for sustainable technology development.* Annual review of environment and resources, 2011. **36**(1): p. 271-293.
41. Cathcart, C., *Green chemistry in the emerald isle.* Chemistry and Industry (London), 1990(21): p. 684-687.
42. Anastas, P.T. and T.C. Williamson, *Green chemistry: designing chemistry for the environment*. 1996: ACS Publications.
43. Anastas, P.T. and J.C. Warner, *Green chemistry: theory and practice*. 2000: Oxford university press.
44. de Marco, B.A., et al., *Evolution of green chemistry and its multidimensional impacts: A review*. Saudi Pharmaceutical Journal, 2019. **27**(1): p. 1-8.

45. Kreuder, A.D., et al., *A method for assessing greener alternatives between chemical products following the 12 principles of green chemistry.* ACS Sustain. Chem. Eng, 2017. **5**(4): p. 2927-2935.
46. Abdussalam-Mohammed, W., A.Q. Ali, and A. Errayes, *Green chemistry: principles, applications, and disadvantages.* Chem. Methodol, 2020. **4**(4): p. 408-423.
47. Gupta, M., S. Paul, and R. Gupta, *General aspects of 12 basic principles of green chemistry with applications.* Current Science, 2010: p. 1341-1360.
48. Ivanković, A., et al., *Review of 12 principles of green chemistry in practice.* International Journal of Sustainable and Green Energy, 2017. **6**(3): p. 39-48.
49. Anastas, P. and N. Eghbali, *Green chemistry: principles and practice.* Chemical Society Reviews, 2010. **39**(1): p. 301-312.
50. Erythropel, H.C., et al., *The Green ChemisTREE: 20 years after taking root with the 12 principles.* Green chemistry, 2018. **20**(9): p. 1929-1961.
51. Anastas, P.T. and J.B. Zimmerman, *Peer reviewed: design through the 12 principles of green engineering*, 2003, ACS Publications.
52. Anastas, P. and J. Zimmerman, *The twelve principles of green engineering as a foundation for sustainability*, in *Sustainability Science and Engineering*. 2006, Elsevier. p. 11-32.
53. McDonough, W., et al., *Peer reviewed: Applying the principles of green engineering to cradle-to-cradle design.* Environmental science & technology, 2003. **37**(23): p. 434A-441A.
54. Gałuszka, A., Z. Migaszewski, and J. Namieśnik, *The 12 principles of green analytical chemistry and the SIGNIFICANCE mnemonic of green analytical practices.* TrAC Trends in Analytical Chemistry, 2013. **50**: p. 78-84.
55. Ruiz-Mercado, G.J., A. Carvalho, and H. Cabezas, *Using green chemistry and engineering principles to design, assess, and retrofit chemical processes for sustainability.* ACS sustainable chemistry & engineering, 2016. **4**(11): p. 6208-6221.
56. Kirchhoff, M.M., *Promoting Green Engineering through Green Chemistry.* Environmental Science & Technology, 2003. **37**(23): p. 5349-5353.
57. *Biofuels*. [cited 2024 07-23]; Available from: https://energy.ec.europa.eu/topics/renewable-energy/bioenergy/biofuels_en.
58. Rial, R.C., *Biofuels versus climate change: Exploring potentials and challenges in the energy transition.* Renewable & Sustainable Energy Reviews, 2024. **196**.
59. Nolfi, G.D., K. Gallucci, and L. Rossi, *Green Diesel Production by Catalytic Hydrodeoxygenation of Vegetables Oils.* International Journal of Environmental Research and Public Health, 2021. **18**(24).
60. Velvizhi, G., et al., *Emerging trends and advances in valorization of lignocellulosic biomass to biofuels.* Journal of Environmental Management, 2023. **345**.

61. Yang, D.P., et al., *Biomass-Derived Carbonaceous Materials: Recent Progress in Synthetic Approaches, Advantages, and Applications.* Acs Sustainable Chemistry & Engineering, 2019. **7**(5): p. 4564-4585.
62. Hazeena, S.H., et al., *Lignocellulosic bio-refinery approach for microbial 2,3-Butanediol production.* Bioresource Technology, 2020. **302**.
63. Popp, J., et al., *Bioeconomy: Biomass and biomass-based energy supply and demand.* New Biotechnology, 2021. **60**: p. 76-84.
64. *Global biofuel production 2023, by select country*. [cited 2024 07-24]; Available from: https://www.statista.com/statistics/274168/biofuel-production-in-leading-countries-in-oil-equivalent/#:~:text=Global%20biofuel%20production%20has%20gradually,fuel%20sources%20or%20as%20additives.
65. Saladini, F., et al., *Guidelines for emergy evaluation of first, second and third generation biofuels.* Renewable & Sustainable Energy Reviews, 2016. **66**: p. 221-227.
66. Naik, S.N., et al., *Production of first and second generation biofuels: A comprehensive review.* Renewable & Sustainable Energy Reviews, 2010. **14**(2): p. 578-597.
67. Correa, D.F., et al., *Biodiversity impacts of bioenergy production: Microalgae vs. first generation biofuels.* Renewable & Sustainable Energy Reviews, 2017. **74**: p. 1131-1146.
68. Sims, R.E.H., et al., *An overview of second generation biofuel technologies.* Bioresource Technology, 2010. **101**(6): p. 1570-1580.
69. Mahapatra, S., et al., *Biofuels and their sources of production: A review on cleaner sustainable alternative against conventional fuel, in the framework of the food and energy nexus.* Energy Nexus, 2021. **4**.
70. Igwebuike, C.M., S. Awad, and Y. Andrès, *Renewable Energy Potential: Second-Generation Biomass as Feedstock for Bioethanol Production.* Molecules, 2024. **29**(7).
71. Singh, D., et al., *A review on feedstocks, production processes, and yield for different generations of biodiesel.* Fuel, 2020. **262**.
72. Leong, W.H., et al., *Third generation biofuels: A nutritional perspective in enhancing microbial lipid production.* Renewable & Sustainable Energy Reviews, 2018. **91**: p. 950-961.
73. Lam, M.K. and K.T. Lee, *Microalgae biofuels: A critical review of issues, problems and the way forward.* Biotechnology Advances, 2012. **30**(3): p. 673-690.
74. Zhou, W.G., et al., *Environment-enhancing algal biofuel production using wastewaters.* Renewable & Sustainable Energy Reviews, 2014. **36**: p. 256-269.
75. Daneshvar, E., et al., *Microalgal growth and nitrate removal efficiency in different cultivation conditions: Effect of macro and micronutrients and salinity.* Journal of Environmental Chemical Engineering, 2018. **6**(2): p. 1848-1854.

76. Abdullah, B., et al., *Fourth generation biofuel: A review on risks and mitigation strategies.* Renewable & Sustainable Energy Reviews, 2019. **107**: p. 37-50.
77. Hsieh, C.H. and W.T. Wu, *Cultivation of microalgae for oil production with a cultivation strategy of urea limitation.* Bioresource Technology, 2009. **100**(17): p. 3921-3926.
78. Aron, N.S.M., et al., *Sustainability of the four generations of biofuels - A review.* International Journal of Energy Research, 2020. **44**(12): p. 9266-9282.
79. Dell'Aversano, S., et al., *E-Fuels: A Comprehensive Review of the Most Promising Technological Alternatives towards an Energy Transition.* Energies, 2024. **17**(16): p. 3995.
80. Ueckerdt, F., et al., *Potential and risks of hydrogen-based e-fuels in climate change mitigation.* Nature Climate Change, 2021. **11**(5): p. 384-393.
81. Bharti, S., et al., *Potential of E-Fuels for Decarbonization of Transport Sector*, in *Greener and Scalable E-fuels for Decarbonization of Transport*, A.K. Agarwal and H. Valera, Editors. 2022, Springer Singapore: Singapore. p. 9-32.
82. Estevez, R., et al., *Internal Combustion Engines and Carbon-Neutral Fuels: A Perspective on Emission Neutrality in the European Union.* Energies, 2024. **17**(5): p. 1172.
83. *Standard Specification for Biodiesel Fuel Blend Stock (B100) for Middle Distillate Fuels*. [cited 2024 07-25]; Available from: https://www.astm.org/d6751-20a.html.
84. Knothe, G., *Biodiesel and renewable diesel: A comparison.* Progress in Energy and Combustion Science, 2010. **36**(3): p. 364-373.
85. *Automotive fuels - Fatty acid methyl esters (FAME) for diesel engines - Requirements and test methods*. [cited 2024 25-07]; Available from: https://standards.iteh.ai/catalog/standards/cen/d3475989-a401-45ea-a3b3-27c9b71ab152/en-14214-2008#:~:text=This%20European%20Standard%20specifies%20requirements,with%20the%20requirements%20of%20EN.
86. Yusuf, N., S.K. Kamarudin, and Z. Yaakub, *Overview on the current trends in biodiesel production.* Energy Conversion and Management, 2011. **52**(7): p. 2741-2751.
87. Babadi, A.A., et al., *Emerging technologies for biodiesel production: Processes, challenges, and opportunities.* Biomass & Bioenergy, 2022. **163**.
88. Freedman, B., E. Pryde, and T. Mounts, *Variables affecting the yields of fatty esters from transesterified vegetable oils.* Journal of the American Oil Chemists Society, 1984. **61**: p. 1638-1643.
89. Van Gerpen, J., *Biodiesel production technology*. 2004: USDA/NCAUR.
90. Szeto, W. and D.Y.C. Leung, *Is hydrotreated vegetable oil a superior substitute for fossil diesel? A comprehensive review on physicochemical properties, engine performance and emissions.* Fuel, 2022. **327**.

91. Knothe, G. and L.F. Razon, *Biodiesel fuels.* Progress in Energy and Combustion Science, 2017. **58**: p. 36-59.
92. Vonortas, A. and N. Papayannakos, *Comparative analysis of biodiesel versus green diesel.* Wiley Interdisciplinary Reviews-Energy and Environment, 2014. **3**(1): p. 3-23.
93. Mahdi, H.I., et al., *Catalytic deoxygenation of palm oil and its residue in green diesel production: A current technological review.* Chemical Engineering Research & Design, 2021. **174**: p. 158-187.
94. Julio, A.A.V., et al., *Techno-economic and environmental potential of Renewable Diesel as complementation for diesel and biodiesel in Brazil: A comprehensive review and perspectives.* Journal of Cleaner Production, 2022. **371**.
95. Yang, Z.Y., et al., *Characterization of renewable diesel, petroleum diesel and renewable diesel/biodiesel/petroleum diesel blends.* Renewable Energy, 2024. **224**.
96. Singh, D., K.A. Subramanian, and S.K. Singal, *Emissions and fuel consumption characteristics of a heavy duty diesel engine fueled with Hydroprocessed Renewable Diesel and Biodiesel.* Applied Energy, 2015. **155**: p. 440-446.
97. Orozco, L.M., et al., *Second-generation green diesel from castor oil: Development of a new and efficient continuous-production process.* Chemical Engineering Journal, 2017. **322**: p. 149-156.
98. Shi, H., et al., *Catalytic deoxygenation of methyl laurate as a model compound to hydrocarbons on nickel phosphide catalysts: Remarkable support effect.* Fuel Processing Technology, 2014. **118**: p. 161-170.
99. Douvartzides, S.L., et al., *Green Diesel: Biomass Feedstocks, Production Technologies, Catalytic Research, Fuel Properties and Performance in Compression Ignition Internal Combustion Engines.* Energies, 2019. **12**(5).
100. Loganathan, S., *Biohydro-fined diesel (BHD) and biodiesel (BOD) production process and property review*, in *Innovations in Fuel Economy and Sustainable Road Transport*. 2011, Woodhead Publishing. p. 97-107.
101. Ogunkoya, D., et al., *Investigation of the effects of renewable diesel fuels on engine performance, combustion, and emissions.* Fuel, 2015. **140**: p. 541-554.
102. Chua, S.Y., et al., *Biodiesel synthesis using natural solid catalyst derived from biomass waste — A review.* Journal of Industrial and Engineering Chemistry, 2020. **81**: p. 41-60.
103. Bezergianni, S., et al., *Hydrotreating of waste cooking oil for biodiesel production. Part II: Effect of temperature on hydrocarbon composition.* Bioresource Technology, 2010. **101**(19): p. 7658-7660.
104. Kalnes, T., T. Marker, and D.R. Shonnard, *Green diesel: a second generation biofuel.* International Journal of Chemical Reactor Engineering, 2007. **5**(1).
105. *Technology Readiness Levels*. [cited 2024 08-02]; Available from: https://www.nasa.gov/directorates/somd/space-communications-navigation-program/technology-readiness-levels/.

106. *What is Neste MY Renewable Diesel (HVO100)?* [cited 2024 08-06]; Available from: https://www.neste.com/products-and-innovation/neste-my-renewable-diesel/product-information.
107. *Diamond Green Diesel*. [cited 2024 08-06]; Available from: https://www.diamondgreendiesel.com/science-process.
108. *Ecofining™, a proprietary biofuel technology*. [cited 2024 08-06]; Available from: https://www.eni.com/en-IT/actions/energy-transition-technologies/biofuels/biomass-ecofining.html.
109. *Biofuels*. [cited 2024 08-06]; Available from: https://miningsolutions.totalenergies.com/renewables-and-low-carbon-energies/biofuels.
110. *UPM BioVerno advanced biofuels: sustainable alternatives to fossil fuels*. [cited 2024 08-06]; Available from: https://www.upmbiofuels.com/traffic-fuels/.
111. *EMRD™ Renewable Diesel Licensing*. [cited 2024 08-06]; Available from: https://www.exxonmobilchemical.com/en/catalysts-and-technology-licensing/emrd.
112. Razak, N.A.A., et al., *Production of green diesel via hydrogen-free and solventless deoxygenation reaction of waste cooking oil.* Journal of Cleaner Production, 2022. **366**.
113. Ameen, M., et al., *Catalytic hydrodeoxygenation of triglycerides: An approach to clean diesel fuel production.* Renewable and Sustainable Energy Reviews, 2017. **80**: p. 1072-1088.
114. Zhou, Y., et al., *Tuning the selectivity of natural oils and fatty acids/esters deoxygenation to biofuels and fatty alcohols: A review.* Green Energy & Environment, 2023. **8**(3): p. 722-743.
115. Rogers, K.A. and Y. Zheng, *Selective Deoxygenation of Biomass-Derived Bio-oils within Hydrogen-Modest Environments: A Review and New Insights.* Chemsuschem, 2016. **9**(14): p. 1750-1772.
116. Gosselink, R.W., et al., *Reaction pathways for the deoxygenation of vegetable oils and related model compounds.* ChemSusChem, 2013. **6**(9): p. 1576-94.
117. Kubička, D. and L. Kaluža, *Deoxygenation of vegetable oils over sulfided Ni, Mo and NiMo catalysts.* Applied Catalysis A: General, 2010. **372**(2): p. 199-208.
118. Fu, J., X.Y. Lu, and P.E. Savage, *Catalytic hydrothermal deoxygenation of palmitic acid.* Energy & Environmental Science, 2010. **3**(3): p. 311-317.
119. Monteiro, R.R.C., et al., *Production of Jet Biofuels by Catalytic Hydroprocessing of Esters and Fatty Acids: A Review.* Catalysts, 2022. **12**(2): p. 237.
120. Lin, D., et al., *Kinetic insights into deoxygenation of vegetable oils to produce second-generation biodiesel.* Fuel, 2023. **333**: p. 126416.
121. Choo, M.-Y., et al., *Recent progress in catalytic conversion of microalgae oil to green hydrocarbon: A review.* Journal of the Taiwan Institute of Chemical Engineers, 2017. **79**: p. 116-124.
122. Kiméné, A., et al., *Catalytic decarboxylation of fatty acids to hydrocarbons over non‑noble metal catalysts: the state of the art.*

Journal of Chemical Technology & Biotechnology, 2018. **94**(3): p. 658-669.
123. Long, F., et al., *State-of-the-art technologies for biofuel production from triglycerides: A review.* Renewable and Sustainable Energy Reviews, 2021. **148**: p. 111269.
124. de Klerk, A., *Fischer–Tropsch refining: technology selection to match molecules.* Green Chemistry, 2008. **10**(12): p. 1249-1279.
125. Tan, Y., et al., *Species and impacts of metal sites over bifunctional catalyst on long chain n-alkane hydroisomerization: A review.* Applied Catalysis A: General, 2021. **611**: p. 117916.
126. Dhar, A., R.L. Vekariya, and P. Bhadja, *n-Alkane isomerization by catalysis—a method of industrial importance: An overview.* Cogent Chemistry, 2018. **4**(1): p. 1514686.
127. Wei, C., et al., *Effect of metal–acid balance and textual modifications on hydroisomerization catalysts for n-alkanes with different chain length: A mini-review.* Fuel, 2022. **315**: p. 122809.
128. Tamizhdurai, P., et al., *Effect of acidity and porosity changes of dealuminated mordenite on n-pentane, n-hexane and light naphtha isomerization.* Microporous and Mesoporous Materials, 2019. **287**: p. 192-202.
129. Yang, Y., et al., *Controllable synthesis of SAPO-11/5 intergrowth zeolite for hydroisomerization of n-hexane.* Microporous and Mesoporous Materials, 2021. **313**: p. 110857.
130. Deldari, H., *Suitable catalysts for hydroisomerization of long-chain normal paraffins.* Applied Catalysis A: General, 2005. **293**: p. 1-10.
131. Fedyna, M., et al., *Composite of Pt/AlSBA-15+zeolite catalyst for the hydroisomerization of n-hexadecane: The effect of platinum precursor.* Microporous and Mesoporous Materials, 2020. **305**: p. 110366.
132. Saab, R., et al., *Synthesis and performance evaluation of hydrocracking catalysts: A review.* Journal of Industrial and Engineering Chemistry, 2020. **89**: p. 83-103.
133. Gunawan, M.L., et al., *Palm-oil transformation into green and clean biofuels: Recent advances in the zeolite-based catalytic technologies.* Bioresource Technology Reports, 2023. **23**: p. 101546.
134. Kim, T.-H., et al., *Effects of Fatty Acid Compositions on Heavy Oligomer Formation and Catalyst Deactivation during Deoxygenation of Triglycerides.* ACS Sustainable Chemistry & Engineering, 2018. **6**(12): p. 17168-17177.
135. Huang, X., S. Dong, and X. Yang, *Refining lipid for aviation biofuel at the molecular level.* Renewable Energy, 2022. **201**: p. 148-159.
136. Baik, Y., K. Lee, and M. Choi, *Catalytic conversion of triglycerides into diesel, jet fuel, and lube base oil.* Chinese Journal of Catalysis, 2024. **58**: p. 15-24.
137. Hongloi, N., P. Prapainainar, and C. Prapainainar, *Review of green diesel production from fatty acid deoxygenation over Ni-based catalysts.* Molecular Catalysis, 2022. **523**: p. 111696.

138. Wang, F., et al., *Effect of Pd promotion and catalyst support on the Ni-catalyzed deoxygenation of tristearin to fuel-like hydrocarbons.* Renewable Energy, 2022. **195**: p. 1468-1479.
139. Karmakar, A., S. Karmakar, and S. Mukherjee, *Properties of various plants and animals feedstocks for biodiesel production.* Bioresource Technology, 2010. **101**(19): p. 7201-7210.
140. Ambat, I., V. Srivastava, and M. Sillanpää, *Recent advancement in biodiesel production methodologies using various feedstock: A review.* Renewable and Sustainable Energy Reviews, 2018. **90**: p. 356-369.
141. Arun, N., R.V. Sharma, and A.K. Dalai, *Green diesel synthesis by hydrodeoxygenation of bio-based feedstocks: Strategies for catalyst design and development.* Renewable & Sustainable Energy Reviews, 2015. **48**: p. 240-255.
142. Sharma, S., et al., *Feedstocks for Green Diesel*, in *Green Diesel: An Alternative to Biodiesel and Petrodiesel*, M. Aslam, S. Shivaji Maktedar, and A.K. Sarma, Editors. 2022, Springer Nature Singapore: Singapore. p. 41-53.
143. Pattanaik, B.P. and R.D. Misra, *Effect of reaction pathway and operating parameters on the deoxygenation of vegetable oils to produce diesel range hydrocarbon fuels: A review.* Renewable & Sustainable Energy Reviews, 2017. **73**: p. 545-557.
144. Hosseinzadeh-Bandbafha, H., et al., *Managing the hazardous waste cooking oil by conversion into bioenergy through the application of waste-derived green catalysts: A review.* Journal of Hazardous Materials, 2022. **424**: p. 127636.
145. Douvartzides, S.L., et al. *Green Diesel: Biomass Feedstocks, Production Technologies, Catalytic Research, Fuel Properties and Performance in Compression Ignition Internal Combustion Engines*. Energies, 2019. **12**, DOI: 10.3390/en12050809.
146. Oparanti, S.O., et al., *Canola oil: A renewable and sustainable green dielectric liquid for transformer insulation.* Industrial Crops and Products, 2024. **215**: p. 118674.
147. Patel, R.L. and C.D. Sankhavara, *Biodiesel production from Karanja oil and its use in diesel engine: A review.* Renewable and Sustainable Energy Reviews, 2017. **71**: p. 464-474.
148. Zhang, Y., L. Duan, and H. Esmaeili, *A review on biodiesel production using various heterogeneous nanocatalysts: Operation mechanisms and performances.* Biomass and Bioenergy, 2022. **158**: p. 106356.
149. [cited 2024 08-06]; Available from: https://www.foodmanufacture.co.uk/Article/2024/03/18/edible-oils-price-index-exclusive-report.
150. Lee, C.-P. and W.-C. Wang, *The production of hydroprocessed renewable diesel with a catalyst regenerated using supercritical carbon dioxide (SCCO2).* Energy, 2022. **246**: p. 123402.
151. Morgan, A.S., et al., *ScCO2 decarboxylation of oleic acid to green diesel.* The Journal of Supercritical Fluids, 2024. **205**: p. 106120.

152. Maki-Arvela, P., et al., *Catalytic deoxygenation of tall oil fatty acid over palladium supported on mesoporous carbon.* Energy & Fuels, 2011. **25**(7): p. 2815-2825.
153. Kubička, D., M. Bejblová, and J. Vlk, *Conversion of vegetable oils into hydrocarbons over CoMo/MCM-41 catalysts.* Topics in catalysis, 2010. **53**: p. 168-178.
154. Wang, W.-C., W.L. Roberts, and L.F. Stikeleather, *Hydrocarbon fuels from gas phase decarboxylation of hydrolyzed free fatty acid.* 2012.
155. Hebish, A.A., et al., *The impact of operating conditions on H2-free catalytic deoxygenation of triglycerides for bio-jet fuel synthesis: A step towards sustainable aviation.* Applied Catalysis O: Open, 2024. **190**: p. 206926.
156. Srifa, A., et al., *Roles of monometallic catalysts in hydrodeoxygenation of palm oil to green diesel.* Chemical Engineering Journal, 2015. **278**: p. 249-258.
157. Jęczmionek, Ł. and K. Porzycka-Semczuk, *Hydrodeoxygenation, decarboxylation and decarbonylation reactions while co-processing vegetable oils over NiMo hydrotreatment catalyst. Part II: Thermal effects – Experimental results.* Fuel, 2014. **128**: p. 296-301.
158. Asikin-Mijan, N., et al., *Towards sustainable green diesel fuel production: Advancements and opportunities in acid-base catalyzed H2-free deoxygenation process.* Catalysis Communications, 2023. **182**: p. 106741.
159. Shi, F., et al., *Green diesel-like hydrocarbon production by H2-free catalytic deoxygenation of oleic acid via Ni/MgO-Al2O3 catalysts: Effect of the metal loading amount.* Journal of Environmental Chemical Engineering, 2023. **11**(5): p. 110520.
160. Safa-Gamal, M., et al., *Catalytic deoxygenation by H2-free single-step conversion of free fatty acid feedstock over a Co-Ag carbon-based catalyst for green diesel production.* Journal of Analytical and Applied Pyrolysis, 2021. **160**: p. 105334.
161. Choo, M.-Y., et al., *Deoxygenation of triolein to green diesel in the H2-free condition: Effect of transition metal oxide supported on zeolite Y.* Journal of Analytical and Applied Pyrolysis, 2020. **147**: p. 104797.
162. Nugraha, R.E., et al., *Lewis acid Ni/Al-MCM-41 catalysts for H2-free deoxygenation of Reutealis trisperma oil to biofuels††Electronic supplementary information (ESI) available. See DOI: 10.1039/d1ra03145g.* RSC Advances, 2021. **11**(36): p. 21885-21896.
163. Santillan‐Jimenez, E. and M. Crocker, *Catalytic deoxygenation of fatty acids and their derivatives to hydrocarbon fuels via decarboxylation/decarbonylation.* Journal of Chemical Technology & Biotechnology, 2012. **87**(8): p. 1041-1050.
164. Snåre, M., et al., *Catalytic deoxygenation of unsaturated renewable feedstocks for production of diesel fuel hydrocarbons.* Fuel, 2008. **87**(6): p. 933-945.
165. Kubičková, I., et al., *Hydrocarbons for diesel fuel via decarboxylation of vegetable oils.* Catalysis Today, 2005. **106**(1-4): p. 197-200.

166. Asikin-Mijan, N., et al., *Production of green diesel via cleaner catalytic deoxygenation of Jatropha curcas oil.* Journal of Cleaner Production, 2017. **167**: p. 1048-1059.
167. Han, J., et al., *Palladium-catalyzed decarboxylation of higher aliphatic esters: Towards a new protocol to the second generation biodiesel production.* Green Chemistry, 2010. **12**(3): p. 463-467.
168. Li, Y. and M.A. El-Sayed, *The effect of stabilizers on the catalytic activity and stability of Pd colloidal nanoparticles in the Suzuki reactions in aqueous solution.* The Journal of Physical Chemistry B, 2001. **105**(37): p. 8938-8943.
169. Hermida, L., A.Z. Abdullah, and A.R. Mohamed, *Deoxygenation of fatty acid to produce diesel-like hydrocarbons: A review of process conditions, reaction kinetics and mechanism.* Renewable & Sustainable Energy Reviews, 2015. **42**: p. 1223-1233.
170. Xin, H., et al., *Production of high-grade diesel from palmitic acid over activated carbon-supported nickel phosphide catalysts.* Applied Catalysis B: Environmental, 2016. **187**: p. 375-385.
171. Ardiyanti, A.R., et al., *Catalytic hydrotreatment of fast-pyrolysis oil using non-sulfided bimetallic Ni-Cu catalysts on a δ-Al2O3 support.* Applied Catalysis B: Environmental, 2012. **117-118**: p. 105-117.
172. Nolfi, G.D.V. *New Catalysts for the Synthesis of Green Diesel by Deoxygenation of Vegetable oils*. 2023 [cited 2024 08-30]; Available from: https://ricerca.univaq.it/handle/11697/208539?mode=complete.
173. Sonthalia, A. and N. Kumar, *Hydroprocessed vegetable oil as a fuel for transportation sector: A review.* Journal of the Energy Institute, 2019. **92**(1): p. 1-17.
174. Bezergianni, S., et al., *Toward Hydrotreating of Waste Cooking Oil for Biodiesel Production. Effect of Pressure, H2/Oil Ratio, and Liquid Hourly Space Velocity.* Industrial & Engineering Chemistry Research, 2011. **50**(7): p. 3874-3879.
175. Lam, J.E., et al., *Palm fatty acid distillate derived biofuels via deoxygenation: Properties, catalysts and processes.* Fuel Processing Technology, 2022. **236**: p. 107394.
176. Khan, S., et al., *A review on deoxygenation of triglycerides for jet fuel range hydrocarbons.* Journal of Analytical and Applied Pyrolysis, 2019. **140**: p. 1-24.
177. Yao, X., et al., *Catalytic hydrothermal deoxygenation of lipids and fatty acids to diesel-like hydrocarbons: a review.* Green Chemistry, 2021. **23**(3): p. 1114-1129.
178. Kamaruzaman, M.F., Y.H. Taufiq-Yap, and D. Derawi, *Green diesel production from palm fatty acid distillate over SBA-15-supported nickel, cobalt, and nickel/cobalt catalysts.* Biomass and Bioenergy, 2020. **134**: p. 105476.
179. Rakmae, S., et al., *Defining nickel phosphides supported on sodium mordenite for hydrodeoxygenation of palm oil.* Fuel Processing Technology, 2020. **198**: p. 106236.

180. Kim, S.K., et al., *Production of renewable diesel by hydrotreatment of soybean oil: Effect of reaction parameters.* Chemical Engineering Journal, 2013. **228**: p. 114-123.
181. Sotelo-Boyás, R., Y. Liu, and T. Minowa, *Renewable Diesel Production from the Hydrotreating of Rapeseed Oil with Pt/Zeolite and NiMo/Al2O3 Catalysts.* Industrial & Engineering Chemistry Research, 2010. **50**(5): p. 2791-2799.
182. Immer, J.G., M.J. Kelly, and H.H. Lamb, *Catalytic reaction pathways in liquid-phase deoxygenation of C18 free fatty acids.* Applied Catalysis A: General, 2010. **375**(1): p. 134-139.
183. Mäki-Arvela, P., et al., *Continuous decarboxylation of lauric acid over Pd/C catalyst.* Fuel, 2008. **87**(17-18): p. 3543-3549.
184. Bouras, H., et al., *CFD modeling of mass transfer in Gas-Liquid-Solid catalytic reactors.* Chemical Engineering Science, 2021. **233**: p. 116378.
185. Hachemi, I., et al., *Comparative study of sulfur-free nickel and palladium catalysts in hydrodeoxygenation of different fatty acid feedstocks for production of biofuels.* Catalysis Science & Technology, 2016. **6**(5): p. 1476-1487.
186. Bischoff, K., *An extension of the general criterion for importance of pore diffusion with chemical reactions.* Chemical Engineering Science, 1967. **22**(4): p. 525-530.
187. Zhou, L. and A. Lawal, *Kinetic study of hydrodeoxygenation of palmitic acid as a model compound for microalgae oil over Pt/γ-Al2O3.* Applied Catalysis A: General, 2017. **532**: p. 40-49.
188. Arora, P., et al., *Kinetic study of hydrodeoxygenation of stearic acid as model compound for renewable oils.* Chemical Engineering Journal, 2019. **364**: p. 376-389.
189. Hafriz, R.S.R.M., et al., *Comparative, reusability and regeneration study of potassium oxide-based catalyst in deoxygenation reaction of WCO.* Energy Conversion and Management: X, 2022. **13**: p. 100173.
190. Papageridis, K.N., et al., *Effect of operating parameters on the selective catalytic deoxygenation of palm oil to produce renewable diesel over Ni supported on Al2O3, ZrO2 and SiO2 catalysts.* Fuel Processing Technology, 2020. **209**: p. 106547.
191. Kopli, F.Z., et al., *Synthesizing and Performance Testing of Zn Promoted Ni Catalyst With γ-Al2O3 Support in The Process of Hydrotreating Used Cooking Oil into Green Diesel.* Jurnal Riset Teknologi Pencegahan Pencemaran Industri, 2024. **15**(1): p. 41-49.
192. Moreira, J.d.B.D., D.B. de Rezende, and V.M.D. Pasa, *Deoxygenation of Macauba acid oil over Co-based catalyst supported on activated biochar from Macauba endocarp: a potential and sustainable route for green diesel and biokerosene production.* Fuel, 2020. **269**: p. 117253.
193. Ameen, M., et al., *The effect of metal loading over Ni/γ-Al2O3 and Mo/γ-Al2O3 catalysts on reaction routes of hydrodeoxygenation of rubber seed oil for green diesel production.* Catalysis Today, 2020. **355**: p. 51-64.

194. Papanikolaou, G., et al., *Highly selective bifunctional Ni zeo-type catalysts for hydroprocessing of methyl palmitate to green diesel.* Catalysis Today, 2020. **345**: p. 14-21.
195. Safa-Gamal, M., et al., *Catalytic deoxygenation by H2-free single-step conversion of free fatty acid feedstock over a Co-Ag carbon-based catalyst for green diesel production.* Journal of Analytical and Applied Pyrolysis, 2021. **160**: p. 105334.
196. Liu, P., et al., *Metal–organic framework-derived Ni-based catalyst for the hydrotreatment of triolein into green diesel.* Sustainable Energy & Fuels, 2021. **5**(6): p. 1809-1820.
197. Nikolopoulos, I., et al., *Waste cooking oil transformation into third generation green diesel catalyzed by nickel–alumina catalysts.* Molecular Catalysis, 2020. **482**: p. 110697.
198. Jeon, K.-W., et al., *Deoxygenation of non-edible fatty acid for green diesel production: Effect of metal loading amount over Ni/MgO–Al2O3 on the catalytic performance and reaction pathway.* Fuel, 2022. **311**: p. 122488.
199. Nikolopoulos, I., et al., *Cobalt–alumina coprecipitated catalysts for green diesel production.* Industrial & Engineering Chemistry Research, 2021. **60**(51): p. 18672-18683.
200. Papadopoulos, C., et al., *W promoted Ni-Al2O3 co-precipitated catalysts for green diesel production.* Fuel Processing Technology, 2021. **217**: p. 106820.
201. Gousi, M., et al., *Green diesel production over nickel-alumina nanostructured catalysts promoted by copper.* Energies, 2020. **13**(14): p. 3707.
202. Lin, M., et al., *Hydrothermal hydrogenation/deoxygenation of palmitic acid to alkanes over Ni/activated carbon catalyst.* Chinese Journal of Chemical Engineering, 2024. **66**: p. 8-18.
203. Zhang, M., et al., *Catalytic HDO of pyrolysis oil in supercritical ethanol with CoMoP and CoMoW catalysts supported on different carbon materials using formic acid as in-situ hydrogen sources.* Biomass and Bioenergy, 2023. **174**: p. 106814.
204. Zhao, S. and K. Wang, *Regulation of the Reaction Route in Hydrogenation of Renewable Palm Oil Using NiMo Bimetallic Catalyst.* Energy & Fuels, 2023. **37**(23): p. 18899-18910.
205. Aiamsiri, P., et al., *Biohydrogenated Diesel from Palm Oil Deoxygenation over Unsupported and gamma-Al2O3 Supported Ni-Mo Catalysts.* Energy & Fuels, 2021. **35**(18): p. 14793-14804.
206. Thongkumkoon, S., et al., *Catalytic activity of trimetallic sulfided Re-Ni-Mo/γ-Al2O3 toward deoxygenation of palm feedstocks.* Renewable Energy, 2019. **140**: p. 111-123.
207. Srifa, A., et al., *Catalytic behaviors of Ni/gamma-Al2O3 and Co/gamma-Al2O3 during the hydrodeoxygenation of palm oil.* Catalysis Science & Technology, 2015. **5**(7): p. 3693-3705.
208. Cao, X., et al., *Chemoselective decarboxylation of higher aliphatic esters to diesel-range alkanes over the NiCu/Al2O3 bifunctional catalyst under mild reaction conditions.* Renewable Energy, 2021. **180**: p. 1-13.

209. Kaewmeesri, R., et al., *Deoxygenation of Waste Chicken Fats to Green Diesel over Ni/Al2O3: Effect of Water and Free Fatty Acid Content.* Energy & Fuels, 2015. **29**(2): p. 833-840.
210. Krár, M., et al., *Fuel purpose hydrotreating of sunflower oil on CoMo/Al2O3 catalyst.* Bioresour Technol, 2010. **101**(23): p. 9287-93.
211. Oh, M., et al., *Importance of pore size and Lewis acidity of Pt/Al2O3 for mitigating mass transfer limitation and catalyst fouling in triglyceride deoxygenation.* Chemical Engineering Journal, 2022. **439**: p. 135530.
212. Zharova, P., et al., *Original Pt-Sn/Al2O3 catalyst for selective hydrodeoxygenation of vegetable oils.* Energy, 2019. **172**: p. 18-25.
213. Asikin-Mijan, N., et al., *Pyrolytic-deoxygenation of triglycerides model compound and non-edible oil to hydrocarbons over SiO2-Al2O3 supported NiO-CaO catalysts.* Journal of Analytical and Applied Pyrolysis, 2018. **129**: p. 221-230.
214. Sotelo-Boyas, R., Y. Liu, and T. Minowa, *Renewable diesel production from the hydrotreating of rapeseed oil with Pt/Zeolite and NiMo/Al2O3 catalysts.* Industrial & Engineering Chemistry Research, 2011. **50**(5): p. 2791-2799.
215. Janampelli, S. and S. Darbha, *Selective and reusable Pt-WOx/Al2O3 catalyst for deoxygenation of fatty acids and their esters to diesel-range hydrocarbons.* Catalysis Today, 2018. **309**: p. 219-226.
216. Vázquez-Garrido, I., et al., *Synthesis of NiMo catalysts supported on Mn-Al2O3 for obtaining green diesel from waste soybean oil.* Catalysis Today, 2021. **365**: p. 327-340.
217. Hengsawad, T., et al., *Synergistic effect of oxygen vacancies and highly dispersed Pd nanoparticles over Pd-loaded TiO2 prepared by a single-step sol–gel process for deoxygenation of triglycerides.* Applied Catalysis A: General, 2018. **566**: p. 74-86.
218. Di, L., et al., *Robust ruthenium catalysts for the selective conversion of stearic acid to diesel-range alkanes.* Applied Catalysis B: Environmental, 2017. **201**: p. 137-149.
219. Janampelli, S. and S. Darbha, *Highly efficient Pt-MoOx/ZrO2 catalyst for green diesel production.* Catalysis Communications, 2019. **125**: p. 70-76.
220. Konwar, L.J. and J.-P. Mikkola, *Carbon support effects on metal (Pd, Pt and Ru) catalyzed hydrothermal decarboxylation/deoxygenation of triglycerides.* Applied Catalysis A: General, 2022. **638**: p. 118611.
221. Malins, K., *Synthesis of renewable hydrocarbons from vegetable oil feedstock by hydrotreatment over selective sulfur-free SiO2-Al2O3 supported monometallic Pd, Pt, Ru, Ni, Mo and bimetallic NiMo catalysts.* Fuel, 2021. **285**: p. 119129.
222. Janampelli, S. and S. Darbha, *Effect of support on the catalytic activity of WOx promoted Pt in green diesel production.* Molecular Catalysis, 2018. **451**: p. 125-134.
223. Kim, S.K., et al., *Production of renewable diesel via catalytic deoxygenation of natural triglycerides: Comprehensive understanding of reaction intermediates and hydrocarbons.* Applied energy, 2014. **116**: p. 199-205.

224. Tan, K.B., et al., *Catalytic deoxygenation of stearic acid into olefins over Pt catalysts supported on MOF-derived metal oxides.* Catalysis Science & Technology, 2024.
225. Nepomnyashchii, A., et al., *Combined Deoxygenation and Isomerization of Sunflower Oil Fatty Acid Triglycerides on Pt/Al2O3-Zeolite Catalysts.* Catalysis in Industry, 2024. **16**(2): p. 170-177.
226. Wan Khalit, W.N.A., et al., *One-pot decarboxylation and decarbonylation reaction of waste cooking oil over activated carbon supported nickel-zinc catalyst into diesel-like fuels.* Journal of Analytical and Applied Pyrolysis, 2022. **164**: p. 105505.
227. Chang, H., et al., *Development of porous MIL-101 derived catalyst application for green diesel production.* Fuel, 2024. **355**: p. 129459.
228. Wang, F., et al., *Hydrotreatment of vegetable oil for green diesel over activated carbon supported molybdenum carbide catalyst.* Fuel, 2018. **216**: p. 738-746.
229. Sari, E., et al., *A highly active nanocomposite silica-carbon supported palladium catalyst for decarboxylation of free fatty acids for green diesel production: Correlation of activity and catalyst properties.* Applied Catalysis A: General, 2013. **467**: p. 261-269.
230. Gamal, M.S., et al., *Effective catalytic deoxygenation of palm fatty acid distillate for green diesel production under hydrogen-free atmosphere over bimetallic catalyst CoMo supported on activated carbon.* Fuel Processing Technology, 2020. **208**: p. 106519.
231. Jermy, B.R., et al., *Crude oil conversion to chemicals over green synthesized ZSM-5 zeolite.* Fuel Processing Technology, 2023. **241**: p. 107610.
232. Nur Azreena, I., et al., *Hydro-processing of palm fatty acid distillate for diesel-like hydrocarbon fuel production using La-zeolite beta catalyst.* Industrial Crops and Products, 2024. **218**: p. 118907.
233. Kang, Y.-H., et al., *Green and effective catalytic hydroconversion of an extractable portion from an oil sludge to clean jet and diesel fuels over a mesoporous Y zeolite-supported nickel catalyst.* Fuel, 2021. **287**: p. 119396.
234. Wu, Y., et al., *Synthesis of Ni/SAPO-11-X zeolites with graded secondary pore structure and its catalytic performance for hydrodeoxygenation-isomerization of FAME for green diesel production.* Renewable Energy, 2023. **218**: p. 119372.
235. Putra, R., et al., *Fe/Indonesian Natural Zeolite as Hydrodeoxygenation Catalyst in Green Diesel Production from Palm Oil.* 2018, 2018: p. 11.
236. Sotelo-Boyás, R., Y. Liu, and T. Minowa, *Renewable Diesel Production from the Hydrotreating of Rapeseed Oil with Pt/Zeolite and NiMo/Al2O3 Catalysts.* Industrial & Engineering Chemistry Research, 2011. **50**(5): p. 2791-2799.
237. Sousa, F.P., et al., *Simultaneous deoxygenation, cracking and isomerization of palm kernel oil and palm olein over beta zeolite to produce biogasoline, green diesel and biojet-fuel.* Fuel, 2018. **223**: p. 149-156.

238. Choo, M.Y., et al., *Deoxygenation of triolein to green diesel in the H-2-free condition: Effect of transition metal oxide supported on zeolite Y.* Journal of Analytical and Applied Pyrolysis, 2020. **147**.
239. Naqvi, S.R., et al., *Recent progress in catalytic deoxygenation of biomass pyrolysis oil using microporous zeolites for green fuels production.* Fuel, 2023. **333**.
240. Yenumala, S.R., et al., *Production of green diesel from karanja oil (Pongamia pinnata) using mesoporous NiMo-alumina composite catalysts.* Bioresource Technology Reports, 2019. **7**: p. 100288.
241. Sharma, R.K., et al., *Jatropha-oil conversion to liquid hydrocarbon fuels using mesoporous titanosilicate supported sulfide catalysts.* Catalysis Today, 2012. **198**(1): p. 314-320.
242. Asikin-Mijan, N., et al., *Promoting deoxygenation of triglycerides via Co-Ca loaded SiO2-Al2O3 catalyst.* Applied Catalysis A: General, 2018. **552**: p. 38-48.
243. Liu, Y., et al., *Hydrotreatment of Jatropha Oil to Produce Green Diesel over Trifunctional Ni–Mo/SiO2–Al2O3 Catalyst.* Chemistry Letters, 2009. **38**(6): p. 552-553.
244. Toba, M., et al., *Hydrodeoxygenation of waste vegetable oil over sulfide catalysts.* Catalysis Today, 2011. **164**(1): p. 533-537.
245. Wang, F., et al., *Fe-promoted Ni catalyst with extremely high loading and oxygen vacancy for lipid deoxygenation into green diesel.* Renewable Energy, 2022. **197**: p. 40-49.
246. Li, X., et al., *Heterogeneous sulfur-free hydrodeoxygenation catalysts for selectively upgrading the renewable bio-oils to second generation biofuels.* Renewable and Sustainable Energy Reviews, 2018. **82**: p. 3762-3797.
247. Cheah, K.W., et al., *Recent advances in the catalytic deoxygenation of plant oils and prototypical fatty acid models compounds: Catalysis, process, and kinetics.* Molecular Catalysis, 2022. **523**: p. 111469.
248. Lycourghiotis, S., et al., *Transformation of residual fatty raw materials into third generation green diesel over a nickel catalyst supported on mineral palygorskite.* Renewable Energy, 2021. **180**: p. 773-786.
249. Hachemi, I., et al., *Sulfur-free Ni catalyst for production of green diesel by hydrodeoxygenation.* Journal of Catalysis, 2017. **347**: p. 205-221.
250. Cherstiouk, O.V., et al., *Electrocatalysis of the hydrogen oxidation reaction on carbon-supported bimetallic NiCu particles prepared by an improved wet chemical synthesis.* Journal of Electroanalytical Chemistry, 2016. **783**: p. 146-151.
251. Hafriz, R., et al., *Effect of Ni/Malaysian dolomite catalyst synthesis technique on deoxygenation reaction activity of waste cooking oil.* Renewable Energy, 2021. **178**: p. 128-143.
252. Si, Z., et al., *An overview on catalytic hydrodeoxygenation of pyrolysis oil and its model compounds.* Catalysts, 2017. **7**(6): p. 169.
253. Kordulis, C., et al., *Development of nickel based catalysts for the transformation of natural triglycerides and related compounds into*

green diesel: a critical review. Applied Catalysis B: Environmental, 2016. **181**: p. 156-196.

254. Balakos, M.W. and E.E. Hernandez, *Catalyst characteristics and performance in edible oil hydrogenation.* Catalysis Today, 1997. **35**(4): p. 415-425.
255. Ooi, X.Y., et al., *Overview on catalytic deoxygenation for biofuel synthesis using metal oxide supported catalysts.* Renewable and Sustainable Energy Reviews, 2019. **112**: p. 834-852.
256. Khalit, W.N.A.W., et al., *Development of bimetallic nickel-based catalysts supported on activated carbon for green fuel production.* RSC advances, 2020. **10**(61): p. 37218-37232.
257. Mahene, W.L., T. Kivevele, and R. Machunda, *The role of textural properties and surface chemistry of activated carbon support in catalytic deoxygenation of triglycerides into renewable diesel.* Catalysis Communications, 2023. **181**: p. 106737.
258. Safa Gamal, M., et al., *Solvent-free catalytic deoxygenation of palm fatty acid distillate over cobalt and manganese supported on activated carbon originating from waste coconut shell.* Journal of Analytical and Applied Pyrolysis, 2019. **144**: p. 104690.
259. Velasquez, J., et al., *Propane Oxidative Dehydrogenation on ZnCoMo and NiCoMo Catalysts Obtained from ϕy and ϕx Precursors.* Industrial & Engineering Chemistry Research, 2013. **52**(16): p. 5582-5586.
260. A. Di Giuliano, K.G., S .Lucantonio, L. Rossi, G. Di Vito Nolfi, *Catalizzatore solido a base di ossidi di nichel, molibdeno e alluminio, per deossigenazione catalitica eterogenea di trigliceridi di origine biologica a formare idrocarburi, e suo metodo di sintesi senza solventi*: Italy.
261. Smolakova, L., et al., *Precursors of active Ni species in Ni/Al2O3 catalysts for oxidative dehydrogenation of ethane.* Chinese Journal of Catalysis, 2013. **34**(10): p. 1905-1913.
262. Pacewska, B. and M. Keshr, *Thermal transformations of aluminium nitrate hydrate.* Thermochimica Acta, 2002. **385**(1-2): p. 73-80.
263. Shaheen, W.M. and M.M. Selim, *Thermal decompositions of pure and mixed manganese carbonate and ammonium molybdate tetrahydrate.* Journal of Thermal Analysis and Calorimetry, 2000. **59**(3): p. 961-970.
264. Aceto, M., *The use of ICP-MS in food traceability*, in *Advances in food traceability techniques and technologies*. 2016, Elsevier. p. 137-164.
265. Griffiths, P.R., *Fourier transform infrared spectrometry.* Science, 1983. **222**(4621): p. 297-302.
266. Li, H., et al., *Experimental methods in chemical engineering: particle size distribution by laser diffraction—PSD.* The Canadian Journal of Chemical Engineering, 2019. **97**(7): p. 1974-1981.
267. Doroszkowski, A., *Particle size and size measurement.* Paint and Surface Coatings: Theory and Practice, 1999: p. 243.

268. Epp, J., *X-ray diffraction (XRD) techniques for materials characterization*, in *Materials characterization using nondestructive evaluation (NDE) methods*. 2016, Elsevier. p. 81-124.
269. Giacovazzo, C., *Fundamentals of crystallography*. Vol. 7. 2002: Oxford university press, USA.
270. *Britannica, The Editors of Encyclopaedia. "Bragg law"*. Encyclopedia Britannica 9 Aug. 2024; Available from: https://www.britannica.com/science/Bragg-law.
271. ALHAJ YOUSSEF, R. *Processi di deidrogenazione/deossigenazione catalitici su oli vegetali per ottenere bioprodotti e green diesel*. 2021 [cited 2024 08-28]; Available from: https://hdl.handle.net/11697/167473.
272. Thommes, M., et al., *Physisorption of gases, with special reference to the evaluation of surface area and pore size distribution (IUPAC Technical Report).* Pure and applied chemistry, 2015. **87**(9-10): p. 1051-1069.
273. Bardestani, R., G.S. Patience, and S. Kaliaguine, *Experimental methods in chemical engineering: specific surface area and pore size distribution measurements—BET, BJH, and DFT.* The Canadian Journal of Chemical Engineering, 2019. **97**(11): p. 2781-2791.
274. Keenan, A., *The relation between the BET and Langmuir multilayer adsorption equations.* Journal of Chemical Education, 1948. **25**(12): p. 666.
275. Brunauer, S., P.H. Emmett, and E. Teller, *Adsorption of gases in multimolecular layers.* Journal of the American chemical society, 1938. **60**(2): p. 309-319.
276. Włodarczyk-Stasiak, M. and J. Jamroz, *Specific surface area and porosity of starch extrudates determined from nitrogen adsorption data.* Journal of food engineering, 2009. **93**(4): p. 379-385.
277. Barrett, E.P., L.G. Joyner, and P.P. Halenda, *The determination of pore volume and area distributions in porous substances. I. Computations from nitrogen isotherms.* Journal of the American Chemical society, 1951. **73**(1): p. 373-380.
278. Goldstein, J.I., et al., *Scanning electron microscopy and X-ray microanalysis*. 2017: springer.
279. Echlin, P., et al., *Advanced scanning electron microscopy and X-ray microanalysis*. 2013: Springer Science & Business Media.
280. Kohl, H. and L. Reimer, *Transmission electron microscopy.* Springer Series in Optical Sciences, 2008. **36**.
281. Reiche, M.A., M. Maciejewski, and A. Baiker, *Characterization by temperature programmed reduction.* Catalysis Today, 2000. **56**(4): p. 347-355.
282. Pirola, C., F. Galli, and G.S. Patience, *Experimental methods in chemical engineering: Temperature programmed reduction—TPR.* The Canadian Journal of Chemical Engineering, 2018. **96**(11): p. 2317-2320.
283. Imelik, B. and J.C. Vedrine, *Catalyst characterization: physical techniques for solid materials*. 2013: Springer Science & Business Media.

284. AOAC. *AOAC 969.33-1969(1997), Fatty acids in oils and fats. Preparation*. 1997 [cited 2024 08-30]; Available from: http://www.aoacofficialmethod.org/index.php?main_page=product_info&products_id=1733.
285. Montgomery, D.C., *Design and analysis of experiments*. 2017: John wiley & sons.
286. Harmain, G. and I. Amin, *An assessment of erosive wear of hydro-turbine steel using statistical modeling and optimization.* 2020.
287. Qiu, F., et al., *Biodiesel production from mixed soybean oil and rapeseed oil.* Applied Energy, 2011. **88**(6): p. 2050-2055.
288. Zenkevich, I.G., *Kovats retention index system.* Encyclopedia of Chromatography, 3rd ed.; Cazes, J., Ed, 2002: p. 1304-1310.
289. Ameen, M., et al., *Catalytic hydrodeoxygenation of rubber seed oil over sonochemically synthesized Ni-Mo/γ-Al₂O₃ catalyst for green diesel production.* Ultrasonics Sonochemistry, 2019. **51**: p. 90-102.
290. Kaewchada, A., et al., *Production of bio-hydrogenated diesel from palm oil using Rh/HZSM-5 in a continuous mini fixed-bed reactor.* Chemical Engineering and Processing-Process Intensification, 2021. **168**.
291. Ruangudomsakul, M., et al., *Hydrodeoxygenation of palm oil to green diesel products on mixed-phase nickel phosphides.* Molecular Catalysis, 2022. **523**.
292. Huber, G.W., P. O'Connor, and A. Corma, *Processing biomass in conventional oil refineries: Production of high quality diesel by hydrotreating vegetable oils in heavy vacuum oil mixtures.* Applied Catalysis A: General, 2007. **329**: p. 120-129.
293. Draper, N.R. and H. Smith, *Applied regression analysis*. Vol. 326. 1998: John Wiley & Sons.
294. Pazzi, M., et al., *Statistical Optimization of Urinary Organic Acids Analysis by a Multi-Factorial Design of Experiment.* Analytica—A Journal of Analytical Chemistry and Chemical Analysis, 2020. **1**(1): p. 14-23.
295. Dismuke, C. and R. Lindrooth, *Ordinary least squares.* Methods and designs for outcomes research, 2006. **93**(1): p. 93-104.
296. Wasserstein, R.L. and N.A. Lazar, *The ASA statement on p-values: context, process, and purpose*, 2016, Taylor & Francis. p. 129-133.
297. Neter, J., et al., *Applied linear statistical models.* 1996.
298. Bates, S., T. Hastie, and R. Tibshirani, *Cross-validation: what does it estimate and how well does it do it?* Journal of the American Statistical Association, 2024. **119**(546): p. 1434-1445.
299. Wong, T.-T., *Performance evaluation of classification algorithms by k-fold and leave-one-out cross validation.* Pattern recognition, 2015. **48**(9): p. 2839-2846.
300. Hastie, T., et al., *The elements of statistical learning: data mining, inference, and prediction*. Vol. 2. 2009: Springer.
301. Levenspiel, O., *Chemical reaction engineering*. 1998: John wiley & sons.

302. Thommes, M., et al., *Physisorption of gases, with special reference to the evaluation of surface area and pore size distribution (IUPAC Technical Report).* Pure and Applied Chemistry, 2015. **87**(9-10): p. 1051-1069.
303. Ravikovitch, P.I. and A.V. Neimark, *Characterization of nanoporous materials from adsorption and desorption isotherms.* Colloids and Surfaces A: Physicochemical and Engineering Aspects, 2001. **187**: p. 11-21.
304. Rouquerol, J., et al., *Recommendations for the characterization of porous solids (Technical Report).* Pure and applied chemistry, 1994. **66**(8): p. 1739-1758.
305. Sing, K.S., *Reporting physisorption data for gas/solid systems with special reference to the determination of surface area and porosity (Recommendations 1984).* Pure and applied chemistry, 1985. **57**(4): p. 603-619.
306. Shozi, M.L., et al., *An investigation of Cu-Re-ZnO catalysts for the hydrogenolysis of glycerol under continuous flow conditions.* Sustainable Energy & Fuels, 2017. **1**(6): p. 1437-1445.
307. Brito, J.L. and A.L. Barbosa, *Effect of phase composition of the oxidic precursor on the HDS activity of the sulfided molybdates of Fe(II), Co(II), and Ni(II).* Journal of Catalysis, 1997. **171**(2): p. 467-475.
308. Gowtham, B., et al., *MoO3 overview: hexagonal plate-like MoO3 nanoparticles prepared by precipitation method.* Journal of Materials Science: Materials in Electronics, 2018. **29**(8): p. 6835-6843.
309. Fogler, H.S., *Elements of chemical reaction engineering*. Fourth Edition ed. 2006.
310. Estellé, J., et al., *Comparative study of the morphology and surface properties of nickel oxide prepared from different precursors.* Solid State Ionics, 2003. **156**(1-2): p. 233-243.
311. Mohammed, A. and H. Atta, *Synthesis Of Nano Ni-Mo/γ-Al2O3 Catalyst.* Iraqi Journal of Chemical and Petroleum Engineering, 2016. **17**.
312. Yang, X.H., et al., *Mechanism and kinetics of decomposition reaction of ultrafine ammonium molybdate for preparing ultrafine MoO3 powder.* Materials Chemistry and Physics, 2023. **302**.
313. Manukyan, K.V., et al., *Nickel Oxide Reduction by Hydrogen: Kinetics and Structural Transformations.* Journal of Physical Chemistry C, 2015. **119**(28): p. 16131-16138.
314. Arnoldy, P., J.C.M. Dejonge, and J.A. Moulijn, *TEMPERATURE-PROGRAMMED REDUCTION OF MOO3 AND MOO2.* Journal of Physical Chemistry, 1985. **89**(21): p. 4517-4526.
315. Ameen, M., et al., *Physicochemical Properties of Ni-Mo/γ-Al2O3 Catalysts Synthesized via Sonochemical Method.* Procedia Engineering, 2016. **148**: p. 64-71.
316. Zhang, H., et al., *Catalytic cracking of n-decane over NiO–MoO3 modified Pt/ZrO2–TiO2–Al2O3 catalyst with different Al2O3 ratios.* Petroleum Chemistry, 2017. **57**(8): p. 666-672.

317. Ma, Y., et al., *Cooperation Between Active Metal and Basic Support in Ni-Based Catalyst for Low-Temperature CO2 Methanation.* Catalysis Letters, 2020. **150**(5): p. 1418-1426.
318. Li, H., et al., *Ni/SBA-15 catalysts for CO methanation: effects of V, Ce, and Zr promoters.* RSC advances, 2015. **5**(117): p. 96504-96517.
319. Gunstone, F., *Vegetable oils in food technology: composition, properties and uses*. 2011: John Wiley & Sons.
320. Choe, E. and D. Min, *Chemistry of deep‐fat frying oils.* Journal of food science, 2007. **72**(5): p. R77-R86.
321. Chen, J., et al., *The formation, determination and health implications of polar compounds in edible oils: Current status, challenges and perspectives.* Food Chemistry, 2021. **364**: p. 130451.
322. Fullana, A., Á.A. Carbonell‐Barrachina, and S. Sidhu, *Volatile aldehyde emissions from heated cooking oils.* Journal of the Science of Food and Agriculture, 2004. **84**(15): p. 2015-2021.
323. Zhou, L. and A. Lawal, *Hydrodeoxygenation of microalgae oil to green diesel over Pt, Rh and presulfided NiMo catalysts.* Catalysis Science & Technology, 2016. **6**(5): p. 1442-1454.
324. Hafriz, R., et al., *The catalytic deoxygenation reaction temperature and N2 gas flow rate influence the conversion of soybean fatty acids into Green Diesel.* Journal of the Taiwan Institute of Chemical Engineers, 2024. **165**: p. 105700.
325. Draper, N., *Applied regression analysis*. 1998: McGraw-Hill. Inc.
326. Bruice, P.Y., *Organic chemistry*. 2017: Pearson.
327. Lin, D., et al., *Catalyst Design Strategies for Deoxygenation of Vegetable Oils to Produce Second-Generation Biodiesel.* Industrial & Engineering Chemistry Research, 2023. **62**(32): p. 12462-12481.
328. Wang, W., et al., *Amorphous Co–Mo–B catalyst with high activity for the hydrodeoxygenation of bio-oil.* Catalysis Communications, 2011. **12**(6): p. 436-440.
329. Wu, K., et al., *In-situ preparation of MnFeCoNiCu/C for the sustainable co-production of bio-jet fuel and green diesel under solvent-free and low hydrogen pressure conditions.* Energy Conversion and Management, 2024. **318**: p. 118875.

RINGRAZIAMENTI

Desidero esprimere la mia profonda gratitudine ai miei tutor, Dott. Andrea Di Giuliano e Prof.ssa Katia Gallucci, per il supporto e la disponibilità che mi hanno dimostrato durante il percorso di dottorato. Grazie per aver condiviso con me la vostra esperienza, il vostro entusiasmo per la ricerca e la vostra passione per la conoscenza, che hanno reso questo percorso non solo una sfida intellettuale, ma anche una preziosa occasione di crescita personale.

Desidero ringraziare anche il Professor Leucio Rossi, che, pur non essendo mio tutor, ha avuto un ruolo fondamentale nel mio percorso. La sua disponibilità nel condividere le sue conoscenze e il tempo dedicato a rispondere ai miei dubbi hanno arricchito il mio lavoro e mi hanno permesso di approfondire aspetti essenziali di questa tesi.

Il ringraziamento più grande va al Dottor Giuseppe Di Vito Nolfi, o meglio Peppe (Yosef, Jusuf, Josef e quanti altri soprannomi dati in questi anni), guida fondamentale, senza il quale NON sarebbe stato possibile conseguire i risultati ottenuti. Nei momenti di maggiore sconforto sei stato un grande amico, più che un collega, aiutandomi con tutte le forze possibili, anche nei momenti meno opportuni. Peppe, senza te tutto sarebbe stato molto ma molto più complicato.

Desidero ringraziare sinceramente tutte le persone con cui ho avuto il privilegio di collaborare durante questo percorso. Ognuno di voi ha

contribuito a rendere questa esperienza unica, arricchendola con le proprie competenze, idee e supporto.

Un ringraziamento senza pari va ai miei genitori Luigi e Gabriella, pilastri fondamentali della mia esistenza. Voi che avete sempre appoggiato le mie scelte, senza mai mettere bocca su nulla, siete un supporto fondamentale, unico e prezioso.

Un grazie speciale va a Stefano, compagno incredibile di mille avventure, che con la sua pazienza e la sua dolcezza ha saputo guidarmi anche nei momenti più bui. Nessuno, tranne lui, sa quanto è stato difficile e complesso questo percorso. Non mi hai mai fatto sentire sola, mi hai spronato sempre a fare di meglio e ad essere la persona sorridente e solare che sono sempre stata. Il tuo supporto è stato un altro pilastro fondamentale, senza il quale non sarei di certo qui. Il tuo amore incondizionato è stato e sarà sempre una guida preziosa e necessaria.

A nonno Sergio e nonna Antonia vorrei dire grazie, ma oggi purtroppo non siete con noi. Vi immagino seduti in prima fila, a sentire cose che nonostante non capireste, sapreste dire che sono il lavoro più ben fatto che sia mai stato condotto. Vi immagino prepararvi di mattina (rigorosamente alle ore 6) e sento dire "Su Sé, muoviti, che la bella stella di nonna oggi diventa nuovamente Ingegnere. Fammi piglià la borsa và". E immagino nonno seduto sul divano, col sorriso, ad aspettare il grande momento "Su Antò, sennò fecem tardi". Vi immagino, fieri e felici per tutti i traguardi che tutti noi abbiamo raggiunto. Vi ringrazio e vi ringrazierò sempre per tutto quello che avete fatto per me, e per gli altri nipoti.
Così come ringrazio gli altri due nonni, nonna Maria e nonno Pasquale, che non hanno potuto godere, quanto voi, dei traguardi dei loro nipoti.

Un grazie particolare a mio Fratello Valerio, a Serena, a Gabriele, alle Zie, allo Zio, a Tina e Giovanni, e a tutti coloro che in un modo o nell'altro mi hanno supportato in questi tre anni, con gesti o parole che hanno riscaldato le giornate meno calde.

Ai miei amici di sempre, Eleonora, Lucrezia, Gianmario, Lorenzo, Francesca e Ponte, perché nonostante tutto ci siete sempre stati, e so che ci sarete sempre. Non servono parole per descrivere il nostro rapporto, perché già sapete tutto.

Un grazie, non di poca importanza, a tutti i miei colleghi "Coppitani", che sono diventati degli amici più che colleghi. Grazie per avermi accolta sin dal primo giorno, come se ci conoscessimo da anni, e per non avermi mai fatto sentire sola.

Grazie anche ai miei colleghi "Roiani", in particolare alla mia unica e inimitabile compagna di "viaggio" Barbi. Nelle nostre avventure sempre insieme, anche se distanti.

Infine, un sentito ringraziamento a tutti coloro che ho incontrato in questo percorso complesso ma tanto, tanto, gratificante.

Per concludere, vorrei rassicurare tutti Voi che questa sarà ufficialmente la mia ultima tesi, promesso!!!!